

AD _____

Award Number: DAMD17-01-1-0635

TITLE: Combining Electron with Intensity Modulated Photon Beams
for Breast Cancer

PRINCIPAL INVESTIGATOR: Lei Xing, Ph.D.

CONTRACTING ORGANIZATION: The Leland Stanford Jr. University
Stanford, California 94305-5401

REPORT DATE: July 2003

TYPE OF REPORT: Final

PREPARED FOR: U.S. Army Medical Research and Materiel Command
Fort Detrick, Maryland 21702-5012

DISTRIBUTION STATEMENT: Approved for Public Release;
Distribution Unlimited

The views, opinions and/or findings contained in this report are
those of the author(s) and should not be construed as an official
Department of the Army position, policy or decision unless so
designated by other documentation.

20040105 128

REPORT DOCUMENTATION PAGE

Form Approved
OMB No. 074-0188

Public reporting burden for this collection of information is estimated to average 1 hour per response, including the time for reviewing instructions, searching existing data sources, gathering and maintaining the data needed, and completing and reviewing this collection of information. Send comments regarding this burden estimate or any other aspect of this collection of information, including suggestions for reducing this burden to Washington Headquarters Services, Directorate for Information Operations and Reports, 1215 Jefferson Davis Highway, Suite 1204, Arlington, VA 22202-4302, and to the Office of Management and Budget, Paperwork Reduction Project (0704-0188), Washington, DC 20503.

1. AGENCY USE ONLY (Leave blank)	2. REPORT DATE July 2003	3. REPORT TYPE AND DATES COVERED Final (1 Jul 2001 - 30 Jun 2003)
4. TITLE AND SUBTITLE Combining Electron with Intensity Modulated Photon Beams for Breast Cancer		5. FUNDING NUMBERS DAMD17-01-1-0635
6. AUTHOR(S) Lei Xing, Ph.D.		
7. PERFORMING ORGANIZATION NAME(S) AND ADDRESS(ES) The Leland Stanford Jr. University Stanford, California 94305-5401 E-Mail: lei@reyes.stanford.edu		8. PERFORMING ORGANIZATION REPORT NUMBER
9. SPONSORING / MONITORING AGENCY NAME(S) AND ADDRESS(ES) U.S. Army Medical Research and Materiel Command Fort Detrick, Maryland 21702-5012		10. SPONSORING / MONITORING AGENCY REPORT NUMBER
11. SUPPLEMENTARY NOTES		
12a. DISTRIBUTION / AVAILABILITY STATEMENT Approved for Public Release; Distribution Unlimited		12b. DISTRIBUTION CODE
13. ABSTRACT (Maximum 200 Words) A hybrid breast cancer treatment technique using electron and intensity modulated photon was developed. The technique took advantage of the useful features of the two types of beams and showed significant promise to improve the current breast irradiation technique. Technically, the weight of the electron beam and the fluence profiles of the IMRT beams were optimized simultaneously with the goal of generating a uniform composite dose distribution in the target volume. We have (i) developed an effective algorithm for the hybrid optimization with the regional dose modifiable by a regional penalty scheme; (ii) explored the feasibility of further improving the technique by intensity- and energy-modulate the electron beam; (iii) developed software to incorporate MLC transmission and head scatter into IMRT delivery to ensure accurate dose delivery; (iv) demonstrated the dosimetric advantage of the hybrid approach; (v) evaluated the matching of electron and IMRT beams against the setup errors; and (vi) explored the feasibility of combining intensity- and energy-modulate electron beam and IMRT for breast irradiation. The development provides a viable alternative for clinically difficult breast cases. Using the technique, the high doses to the lung and heart were markedly reduced with minimal increase in the dose to other normal structures.		
14. SUBJECT TERMS Breast cancer		15. NUMBER OF PAGES 192
		16. PRICE CODE
17. SECURITY CLASSIFICATION OF REPORT Unclassified	18. SECURITY CLASSIFICATION OF THIS PAGE Unclassified	19. SECURITY CLASSIFICATION OF ABSTRACT Unclassified
		20. LIMITATION OF ABSTRACT Unlimited

Table of Contents

Cover.....	1
SF 298.....	2
Table of Contents.....	3
Introduction.....	4
Body.....	4
Key Research Accomplishments.....	11
Reportable Outcomes.....	12
Conclusions.....	14
References.....	15
Appendices.....	16

I. INTRODUCTION

This Concept Award was awarded to the principal investigator (PI) for the period of July 1, 2001—June 30, 2002. An one-year no-cost extension was applied because of the late arrival of the postdoctoral fellow for the project and was granted. This is the final report of the project.

This project was aimed at developing a hybrid treatment method of electron and intensity modulated photon beams for breast cancer and exploring the potential benefit of the approach. The specific aims of the proposal are: (1) to demonstrate that the combination of the two modalities can lead to more conformal dose distributions that would not otherwise be possible for breast cancer treatment; and (2) to show that substantially improved dose distributions can be realized in practice. Under the generous support from the U.S. Army Medical Research and Materiel Command (USAMRMC), we have applied physics and engineering knowledge to breast cancer radiotherapy and successfully demonstrated the potential impact of the proposed hybrid treatment technique. Several conference abstracts and peer-reviewed papers have been resulted from the support. The data obtained under the support of the grant has also enabled the PI to start new research initiatives and significantly advanced his academic career. In the following, our research activities over the last two years are described in details.

II. RESEARCH AND ACCOMPLISHMENTS

Breast cancer is the most common cancer in women, more than 180,000 cases are diagnosed per year in US. As an indispensable treatment for breast cancer, radiation therapy aims to deliver a uniform dose to the breast tumor target while minimizing the damages to the adjacent normal structures such as the lung and heart (in case of left breast irradiation)(1-3). Because of the special location and shape of the breast target volume, it is often difficult to achieve a desired dose distribution using the conventional opposed lateral photon beams. As thus, breast irradiation has been associated with a number of potential complications, which include radiation pneumonitis, necrosis, cardiac toxicity, and radiation-induced secondary cancer (4-6). Adjuvant treatment with chemotherapy further aggravates these effects.

Many approaches have been proposed to improve the current tangential-field treatment technique (7-9). Hong *et al* form Memorial Sloan Kettering Cancer Center (10) have replaced the tangential fields by intensity modulated beams and showed notable improvement in the dose distributions. Our group has examined the feasibility of using multiple (3~7) intensity-modulated

beams for breast cancer(11). The technique can treat the breast target as well as nodal sites with a single set of IMRT fields, which simplifies the treatment when the regional lymph nodes (supraclavicular, axillary and internal mammary nodes) are involved and eliminates the potential overdosing/underdosing caused by the field matching. While there is no doubt that IMRT improves the dose inhomogeneity in the breast target volume, the doses to the sensitive structures are not reduced significantly and photon beam alone does not seem to be the optimal method for breast irradiation. When only photon beams are used, because of the half-moon shape of the breast target, it is inevitable that part of the lung (and part of the heart for left breast irradiation) will be in the treatment fields regardless of intensity modulation or not.

Clinically, electron has been widely used for treating shallow tumors and has a sharp falloff beyond its range. A logical approach to overcome the above limitation is to combine photon with electron to take advantage of the desirable features of the two modalities. The attempt to combine the conventional electron and photon beams for breast cancer has, however, been hindered by distinctly

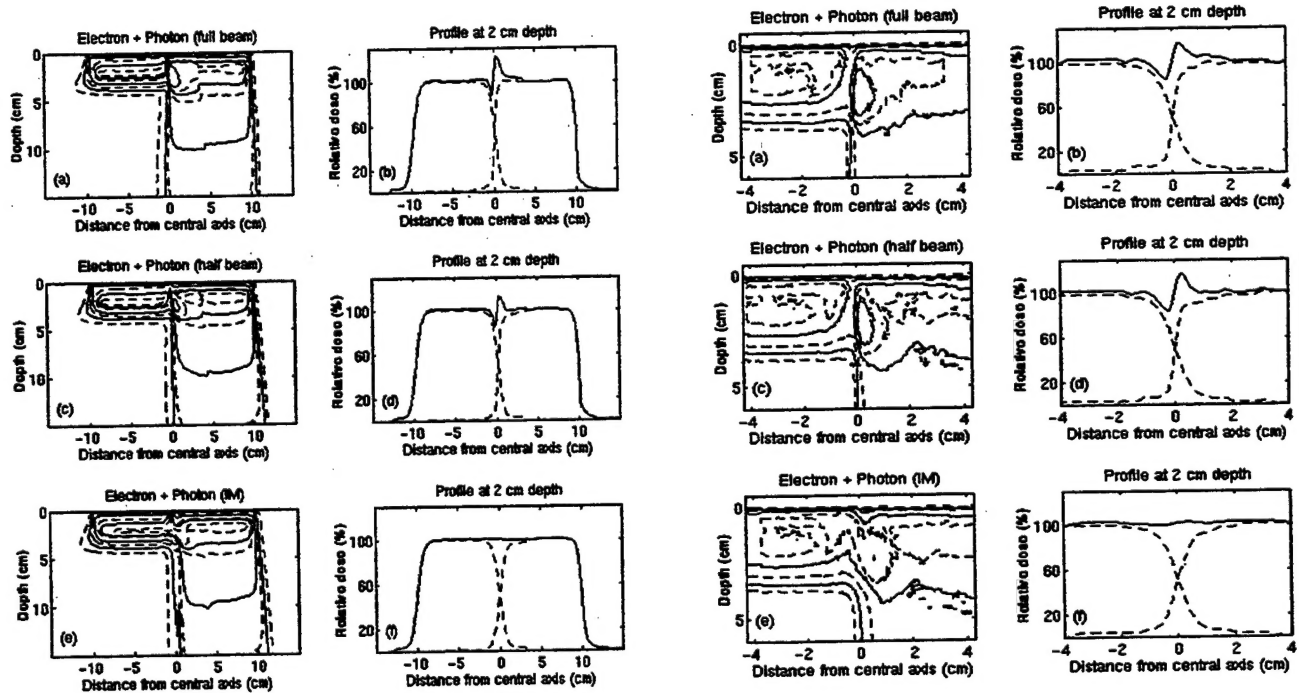


Fig. 1 Matching of electron-photon fields. The left two columns are theoretical calculations and the right two columns are film measurements. A divergent (full-beam), non-divergent (half beam) and intensity modulated photon beams were used in obtaining the results shown in the first, second and the third rows. As indicated by the first two rows, there are always hot/cold spots (over 20%) in the abutting region when we match a conventional photon beam (without intensity modulation) with an electron beam. A perfect match at 2cm depth is achieved using intensity modulated photon beam. The dynamic MLC serves as a photon penumbra generator, effectively broadening the photon penumbra and complementing the electron penumbra.

different penumbra characteristics of the two modalities. Excessive hot/cold spots exist in the match-line region and the match is extremely sensitive to the patient setup error and organ motion. Intensity-modulation can significantly improve the matching because it allows one to deliver a predetermined (not necessarily uniform) radiation field. Our strategy is to irradiate the shallow part of a breast tumor in the medial region using an anterior (enface) electron beam (<15 MeV) and then to add doses to the remaining target volume using intensity-modulated photons. In Fig. 1, we show that by properly designing the photon fluence profile in the abutting region it is possible to achieve a perfect match at a certain depth. In addition, the matching becomes significantly less sensitive to a set-up error or organ motion(12).

We have developed an effective dose optimization algorithm to simultaneously optimize the IMRT beam profiles and the electron beam weight. The treatment planning was done with the PLUNC treatment planning system (University of North Carolina). The goal of the optimization was to obtain a uniform dose of 100% to the target. A quadratic objective function defined by

$$Obj = \frac{1}{N} \sum_{n=1}^N r_\sigma [D_c(n) - D_0(n)]^2 \quad (1)$$

was used for all the optimization calculations, where N is the total number of grid points, $D_0(n)$ is the prescribed dose of 100% to the target volume and 0% to normal structures, $D_c(n)$ is the calculated dose, and r_σ is a relative importance factor, which was unity for the target and 0.5% for the critical structures. The optimization algorithm searches the functional space iteratively and generated the optimal weight of the electron field and the beam profiles of the intensity-modulated photon beams.

In Fig. 2 we show a comparison of a tangential field treatment, IMRT treatment, and a composite plan obtained using an electron and intensity modulated photon beams for a left-sided



Figure 2 Comparison of the isodose distributions of the treatment plans in the transverse section of the left-sided breast cancer patient using the tangential field technique (a), IMRT (b), and the combined electron and IMRT technique (c). Target volume includes the whole breast and the internal mammary nodes. Isodose levels are shown at 100%, 90%, 70%, 50%, 30%, and 10%, with 100% = 5600 cGy.

breast cancer patient. The corresponding dose-volume histograms (DVHs) are plotted in Fig. 3. As discussed in the Introduction, two major concerns in breast radiotherapy are the radiation dose to the heart and the lung. Typically, between 4%~10% of the heart volume is inevitably included in the tangential fields (left panel of Fig. 2), resulting in a high radiation dose to this small volume of the heart. For the particular patient in Fig. 2, it was also difficult to exclude the contralateral breast from the tangential field without overdosing the lateral chest wall, resulting in a hot spot in the medial part of the contralateral breast. The IMRT treatment plan (middle panel of Fig. 2) reduced the high dose to the ipsilateral lung, the heart, and the contralateral breast. However, larger volumes of these structures as well as the contralateral lung received low doses of radiation. For example, for the ipsilateral lung, 40% of the volume received doses of more than 1,400 cGy, compared with ~17% of the volume for the tangential field plan. The volumes of the critical structures receiving low doses of radiation were significantly reduced with the combined electron and IMRT technique (right panel of Fig. 2), as well as reduction in the high dose to the ipsilateral lung, the heart, and the contralateral breast when compared with the tangential field plan. For the ipsilateral lung, the volume receiving doses of more than 1,400 cGy was reduced to 15%, and the reduction in the maximum dose was similar to that achieved with IMRT.

Figure 4 compares the isodose curves in the transverse section of a right-sided breast cancer patient for the treatment plans using the tangential field technique, IMRT, and the combined electron

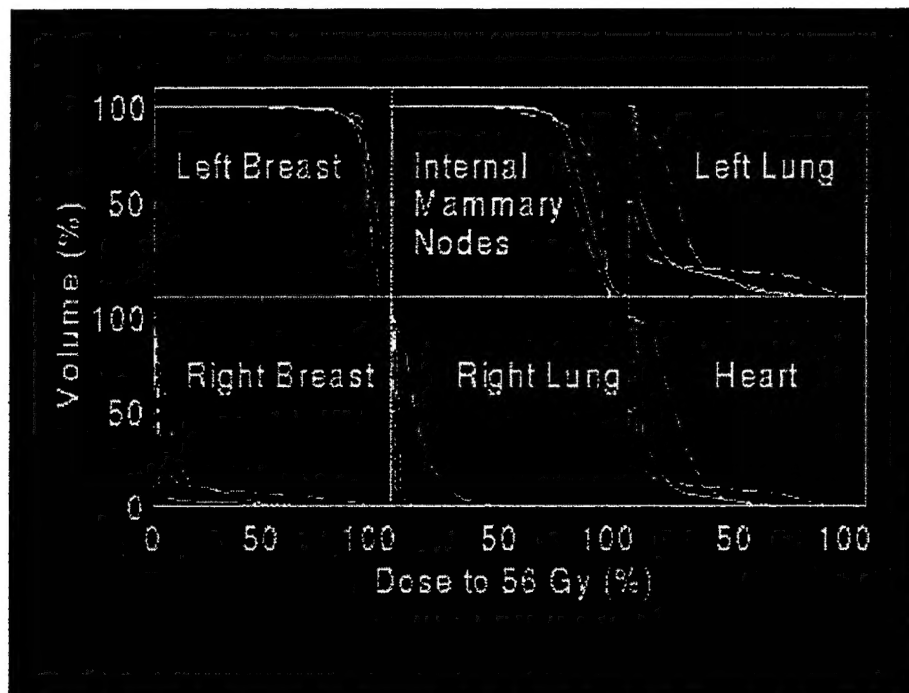


Figure 3 Dose-volume histograms for the targets and normal structures for the treatment plans of the left-sided breast cancer patient as shown in Fig. 3. Dash-dotted lines: tangential field plan. Dashed lines: IMRT plan. Solid lines: combined electron and IMRT plan.



Figure 4 Comparison of the isodose distributions of the treatment plans in the transverse section of the left-Comparison of the isodose distributions of the treatment plans in the transverse section of the right-sided breast cancer patient using the tangential field technique (a), IMRT (b), and the combined electron and IMRT technique (c). Isodose levels are shown at 100%, 90%, 70%, 50%, 30%, and 10%, with 100% = 5600 cGy.

and IMRT technique. The heart, contralateral lung, and the contralateral breast received minimal dose with the tangential technique, as these structures were excluded from the tangential fields (Fig. 4a). However, about 10% of the right lung were included in the tangential fields, resulting in this part of the lung receiving full dose of ~5,000 cGy. This high radiation dose to the lung was reduced by almost 30% using IMRT, together with some improvement in the dose homogeneity to the target volume. This was achieved at the cost of giving low radiation dose to larger volumes of the lungs, heart, and the contralateral breast. IMRT effectively spread the entrance/exit dose of the photon beams to a larger volume. With the combined electron and IMRT technique, the reduction in the high radiation dose to the right lung was comparable to that achieved with IMRT. This is apparent by an examination of the isodose distribution of Fig. 4c, where the 90% isodose line is more conformal to the target than that in Fig. 4a. In addition, minimal increase in the volume of the right lung receiving lower radiation dose was seen. Doses to the heart, the contralateral lung, and the contralateral breast were also kept to a minimum. Therefore, the combined technique achieved significant reduction in high radiation dose to the ipsilateral lung with minimal increase in either dose to the normal structures or volumes of the normal structures receiving low dose of radiation.

Figure 5 shows the minima attained by the objective function as a function of the weight of the electron beam for the case. Here the optimized electron beam weight was 0.8. The behavior of the objective function minima in Fig. 5 can be understood as follows: when the weight of the electron beam was small (~0), the treatment plan approached a conventional tangential field technique, with a high dose region in the ipsilateral lung along the chest wall. As the weight of the electron beam was increased, the high dose to the ipsilateral lung was reduced, resulting in the

decrease in the objective function minima until the lowest was reached. Beyond this point, further increase in the electron beam weight resulted in an increase in the dose inhomogeneity in the target volume as there was less room for the photon beams to compensate for the dose inhomogeneity of the electron beam. Therefore, the behavior of the objective function in Fig. 5 reflects a tradeoff between a uniform dose to the target and a low radiation dose to the ipsilateral lung.

One of the problems we have encountered in the development of hybrid treatment technique was how to get a clinically acceptable solution efficiently. The currently available dose optimization is intractable due to the existence of multiple free parameters (e.g., the prescribed doses to the target and sensitive structures, the importance factors of various structures) and the lack of an explicit relation between these parameters and the final dose distribution. The

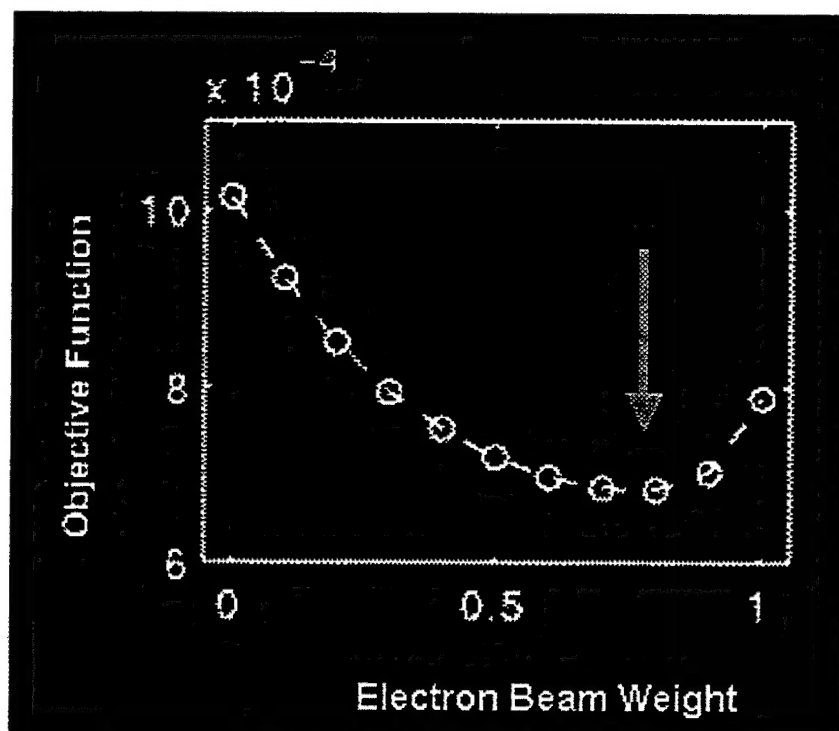


Figure 5. The objective function as a function of the electron beam weight for the combined electron and IMRT treatment plans of the right-sided breast cancer patient.

determination of these parameters is essentially a “guessing” game since the dose modification can only be achieved by adjusting structure dependent system parameters (e.g., prescription, importance factors) in the dose optimization process. The influence of the free parameters on the final solution is not known until the optimization is performed. The lack of a mechanism to fine-tune the doses has been known as a major deficiency of inverse planning and makes the hybrid treatment planning labor intensive. On one hand, our plan selection decision-making is based on the visual evaluation of the isodose distribution or DVHs. On the other hand, in order to modify the dose at a region or to change the shape of a DVH curve, we need to go back to the beginning of plan optimization process and modify some parameters whose role to the dose in the region of interest is known only vaguely. In

reality, it is this vagueness or ambiguity that makes the inverse planning process difficult to control and tedious. If we proceed along the above procedure, the best we can achieve is to lower/increase the overall dose to a structure.

In practice, ranking of treatment plans is variable and subjective, reflecting different criteria among physicians and patient and implying that an “optimal” plan may need to be “tweaked” in a clinical setting. For instance, in breast treatment one may wish to shift the high dose region away from the lung or heart to reduce the influence of breathing motion and avoid potential complication. We have, for the first time, pointed out that the local dosimetric behavior should be controlled by introducing a regional penalty scheme and demonstrated the utility of the approach (13, 14). The technique greatly facilitates the dose optimization process of the hybrid treatment of IMRT and electron. Knowing the region(s) that is “hot” or “cold” for a given solution, or knowing the part of a DVH curve that we wish to modify, the newly developed regional penalty scheme allows us to directly identify the responsible parties in the parameter space and vary them accordingly so that the dose distribution is improved toward our expectation. The new scheme provides us more latitude to fine-tune the local doses and enables us to adaptively search for plans that would be otherwise impossible to obtain. A US patent has been filed by the Office of Technology Licensing of Stanford University for this technique.

On the delivery side, we have incorporated the MLC head scatter into the MLC leaf sequencing algorithm (15) and make it possible to actually achieving the planned hybrid dose distribution in a clinical environment. In general, transmission and head scatter play important roles in the dosimetric behavior of IMRT delivery. Using our model, the deviations between the desired fluence maps and the ones calculated using the corrected leaf sequence files were found to be less than 1.0% for all cases tested. The experimental data showed that both absolute and relative dose distributions delivered by the corrected leaf sequences agree with the desired ones within 2.5% of the maximum dose or 2mm in high dose gradient regions. The head scatter has also been included in the quality assurance software for independent monitor unit check of the IMRT and the hybrid treatment plans (16).

We have recently also implemented an genetic algorithm for dose optimization(17). Different from the conventional beamlet-based optimization, the technique permits us to pre-specify a desired number of segments for the intensity modulated fields and then optimizes the shapes and weights of the involved segments with or without the presence of the electron field. The algorithm has the

potential to further improve the hybrid dose optimization described earlier. Finally, we have also explored the feasibility of combining intensity- and energy-modulate electron beam (18) and IMRT for breast irradiation(19). The added degree of freedom shows further improvement in target coverage and sensitive structures sparing (19). We are currently seeking for extramural funding to continue the new initiative resulted from the research.

The Concept Award for Breast Cancer from US Army Medical Research and Materiel Command has also greatly advanced the PI's academic career. He is in the process of being promoted from Assistant Professor to Associate Professor at Department of Radiation Oncology of Stanford University. Based, in part, on the preliminary data generated from this Concept Award, he submitted a NIH R01 grant proposal, which was ranked in the top 1.5% in the Radiation Study Section and was recommended for funding recently. The PI wishes to take this opportunity to thank USAMRMC once again for the generous support which has enabled the PI gain experience in breast cancer research and to advance our knowledge in breast cancer management.

III. KEY RESEARCH ACCOMPLISHMENTS

- Developed an effective inverse planning algorithm for optimizing the photon beam profiles and electron beam weight.
- Provided a mechanism for fine-tuning the final dose distributions by using voxel-dependent penalty.
- Extended the beamlet-based inverse planning to segment-based optimization.
- Demonstrated the dosimetric advantage of hybrid breast treatment using IMRT and conventional electron.
- Incorporated the MLC head scatter into leaf sequencing process, which makes it possible to accurately deliver the optimal treatment plans.
- Performed dosimetric measurements to evaluate the sensitivity against the setup errors in hybrid treatment of IMRT and electron.
- Explored the feasibility of combining intensity- and energy-modulate electron beam and IMRT for breast irradiation.

IV. REPORTABLE OUTCOMES

The following is a list of publications resulted from the grant support. Copies of the publication materials are enclosed with this report.

Refereed publication:

1. Cotrutz C and Xing L, "Segment-Based Inverse Planning Using Genetic Algorithm". *Physics in Medicine and Biology* 48, in press, 2003.
2. Cotrutz C and Xing L: "Using Voxel Dependent Importance Factors for DVH-Based Interactive Planning", *Physics in Medicine and Biology* 47, 1659-69, 2002.
3. Lian J, Cotrutz C and Xing L, "Inverse Planning with Probabilistic Dose Prescription". *Medical Physics* 30, 655-666, 2003.
4. Yang Y and Xing L, "Incorporating Leaf Transmission and Head Scatter Corrections into Step-and-Shoot Leaf Sequences for IMRT". *International Journal of Radiation Oncology, Biology, Physics* 55, 1121-1134, 2003.
5. Cotrutz C and Xing L, "IMRT Dose Shaping with Regionally Variable Penalty Scheme". *Medical Physics* 30, 544-551, 2003.
6. Song Y, Boyer A, Pawlicki T, Xing L, Lee M, Jiang S, Yan Y, Ma C, Modulated Electron Radiation Therapy: A Comparative Dosimetric Study of MERT and IMRT for Parotid Cancer, *Technology in Cancer Research and Treatment*, accepted.
7. Yang Y and Xing L, "Using the Volumetric Effect of a Finite-Sized Detector for Routine Quality Assurance of MLC Leaf Positioning ". *Medical Physics* 30, 433-442, 2003.
8. Yang Y and Xing L, "Independent Dosimetric Calculation with Inclusion of Head Scatter and MLC Transmission". *Medical Physics*, accepted.
9. Pugachev A and Xing L: "Incorporating Prior Knowledge into IMRT Beam Orientation Optimization", *International Journal of Radiation Oncology, Biology, Physics*, 54, 1565-1574, 2002.
10. Xing L, Pawlicki T, Yuen L, Crooks S, Dugan J, Li C, Halberg F, Cotrutz C, Lehmann J, Donaldson S, Luxton G, Boyer A, Goffinet D: "A comprehensive method of breast-conserving radiation therapy using forward multiple segment planning and step-and-shoot delivery", *Journal of Applied Clinical Medical Physics*, in preparation.

Book Chapter:

1. Xing L, Yang Y, Li J, Chen Y, Luxton G, Boyer A (2003): Monitor Unit Calculation and IMRT plan Validation. In: Intensity Modulated Radiation Therapy, Palta J and Mackie RT (Editors). Medical Physics Publishing, Madison, Wisconsin,.

Published Abstracts:

The PI's group has also been active in disseminating our research results. The following are some relevant presentations given in various national/international meetings.

Xing L YY, L J, Song Y, Pawlicki T., Boyer AL, Le Q. Dose Matching of an IMRT plan with an Electron or 3D Conformal Treatment plan. 2003 World Congress on Medical Physics and Biomedical Engineering. Sydney, Australia, 2003.

Lo A SY, Boyer A.L., Pawlicki T., Xing L. Combining IMRT and Modulated Electron Radiation Therapy for Breast-Conserving Radiation Therapy. Oral presentation in 2003 RSNA Annual Meeting. Chicago, IL, 2003.

Cotrutz C, Xing L. Segment-Based Dose Optimization Using a Genetic Algorithm. Oral presentation in 2003 AAPM Annual Meeting, San Diego, CA.

L. Xing, J.G. Li, Y. Song, D.Y. Yang, D. Goffinet, A.L. Boyer, "Combining electron with intensity modulated photon beams for breast cancer", the Era of Hope 2002 DOD Breast Cancer Research Program Meeting, Orlando, Florida, September 25-28, 2002.

L Xing, T. Pawlicki, L Yuen, C. Cotrutz, J. Dogan, C. Li, F. Halberg, A. Boyer, G. Luxton, D. Goffinet, "Multiple Segment Radiation Therapy for Breast Cancer Treatment After Breast-Conserving Surgery", poster presentation in 2001 Annual Meeting of American Society of Therapeutic Radiology and Oncology (ASTRO), San Francisco, CA.

Y Yang, L Xing, "An Algorithm to Incorporate Leaf Transmission and Head Scatter Corrections Into Step-And-Shoot Leaf Sequences for IMRT", oral presentation in 2002 American Association of Physicists in Medicine (AAPM) Annual Meeting, Montreal, Canada.

C Cotrutz, L Xing, "Inverse Treatment Planning with Interactively Variable Voxel-Dependent Importance Factors", oral presentation in 2002 AAPM Annual Meeting, Montreal, Canada.

A Pugachev, L Xing, "Incorporating Prior Knowledge into Beam Orientation Optimization in IMRT", oral presentation in 2002 AAPM Annual Meeting, Montreal, Canada.

L Xing, J Lian, C Cotrutz, Y Yang, G Luxton, A Boyer, "Inverse Treatment Planning with Inclusion of Model Parameter Uncertainty", oral presentation in 2002 AAPM Annual Meeting, Montreal, Canada.

C Cotrutz, L Xing, "IMRT Dose Shaping Using a Regional Penalty Scheme", oral presentation in 2002 ASTRO Annual Meeting, New Orleans, LA.

US Patent:

Cotrutz C. and Xing L., *Fine-tuning a dose distribution after dose optimization*, US Provisional Patent Application filed in March 2002. Stanford Office of Technology Reference #: S01-261 (pending).

Invited talks:

The PI has been invited as abstract review and session chair in several national/international meetings and has given a number of invited talks. The following is a partial list of the relevant activities in last year.

- *Clinical issues in Breast IMRT treatment*, invited guest speaker, the 12th Annual Scientific Meeting of the Singapore Radiological Society, Singapore, Feb., 2003.
- *Dose Matching of an IMRT plan with an Electron or 3D Conformal Treatment Plan*, World Congress on Medical Physics and Biomedical Engineering, Sydney, Australia, Aug., 2003.

- Inverse Treatment Planning, the 1st International Workshop of Operational Research in Radiation Oncology, Fort Lauderdale, FL, Jan., 2003.
- IMRT Quality Assurance, IMRT Practicum of ASTRO, San Diego, CA, Feb., 2003.
- *Clinical IMRT treatment planning*, International Workshop on Intensity Modulated Radiation Therapy, Rio de Janeiro, Brazil, Feb., 2003.
- Monitor Unit Calculation and IMRT plan Validation. AAPM Summer School on Intensity Modulated Radiation Therapy, Colorado Springs, CO, June, 2003.
- Inverse Treatment Planning, 7th International Symposium on 3D Conformal Radiation Therapy and IMRT, San Francisco, CA, April, 2003.
- *Integration of Functional Imaging into Radiation Therapy Planning*, Workshop on Image Guided Radiotherapy, Lake Tahoe, Sept., 2003.
- *Recent Progress in Inverse Treatment Planning*, invited speaker, Symposium entitled "Inverse Treatment Planning & IMRT", 2002 AAPM Annual Meeting, July, 2002, Montreal, Canada.
- *Current status and future directions of IMRT*, invited speaker, annual meeting of AAPM Missouri-Valley Chapter, Nov., 2002.
- *IMRT and its Combination with Electron for Breast Cancer*, invited talk in 2002 Northern California Society of Radiation Therapists conference, Greenbrae, CA.
- *Multiple Segment Radiation Therapy for Breast Cancer*, in 2002 Stanford IMRT Course.
- *Fast Optimization and the Selection of Beam Angles*, invited speaker, NCI-NSF Sponsored Workshop—Operations Research Applied to Radiation Therapy, 2002, Bethesda, MD.

V. CONCLUSIONS

A combined electron and IMRT technique has been developed and evaluated for the treatment of breast cancer. The electron beam was used to treat the bulk of the tumor volume, whereas intensity modulated photon beams were used to improve target dose homogeneity. The weight of the electron beam as well as the beam fluence profiles of the intensity modulated photon beams were optimized simultaneously. It was found that high doses to the ipsilateral lung and, in the case of the left-breast cancer patient, the heart were markedly reduced with minimal increase in the dose to other normal structures when compared with treatment plans generated using the tangential field technique. A segment-based dose optimization algorithm was also developed to further improve the performance of the inverse planning system. In addition, technique of incorporating MLC head scatter has been developed to ensure that the accuracy of IMRT delivery and an effective method of fine-tuning a planned dose distribution has been established. It is expected these tools will greatly facilitate the planning, delivery, and quality assurance of the hybrid breast treatment. Finally, the utility of combining the intensity- and energy-modulated electron with IMRT has also been investigated.

References

1. Perez CA, Brady LW. Principles and Practice of Radiation Oncology. Philadelphia: Lippincott Williams & Wilkins, 1998.
2. Asrari F, Gage I. Radiation therapy in management of breast cancer. Current Opinion in Oncology 1999; 11 (6): 463.
3. Fisher B, Redmond C, Poisson R, et al. Eight-year results of a randomized clinical trial comparing total mastectomy and lumpectomy with or without irradiation in the treatment of breast cancer [published erratum appears in N Engl J Med 1994 May 19;330(20):1467] [see comments]. Comment in: N Engl J Med 1989 Sep 7;321(10):689-90. New England Journal of Medicine 1989; 320 (13): 822.
4. Arbetter KR, Prakash UB, Tazelaar HD, Douglas WW. Radiation-induced pneumonitis in the "nonirradiated" lung. Mayo Clinic Proceedings 1999; 74 (1): 27.
5. Boice JD, Jr., Harvey EB, Blettner M, Stovall M, Flannery JT. Cancer in the contralateral breast after radiotherapy for breast cancer. New England Journal of Medicine 1992; 326 (12): 781.
6. Dobbs HJ. Radiation therapy for breast cancer at the millennium. Radiotherapy & Oncology 2000; 54: 191.
7. Phaisangittisakul N, Ma L. Range-Modulated Electron Radiotherapy with Longitudinal Magnetic Field Collimation. 2002 Annual Meeting of AAPM. Montreal, Canada, 2002.
8. Hyodynmaa S, Gustafsson A, Brahme A. Optimization of conformal electron beam therapy using energy- and fluence-modulated beams. Medical Physics 1996; 23 (5): 659.
9. Ma CM, Pawlicki T, Lee MC, et al. Energy- and intensity-modulated electron beams for radiotherapy. Physics in Medicine & Biology 2000; 45 (8): 2293.
10. Hong L, Hunt M, Chui C, et al. Intensity-modulated tangential beam irradiation of the intact breast. International Journal of Radiation Oncology, Biology, Physics 1999; 44 (5): 1155.
11. Williams SS, Xing L, Boyer AL, Goffinet D. Intensity modulated treatment of breast cancer with inclusion of supraclavicular and internal mammary lymph nodes. International Journal Radiation Oncology, Biology, Physics 1998; 42 (1): 370.
12. Xing L YY, L J, Song Y, Pawlicki T., Boyer AL, Le Q. Dose Matching of an IMRT plan with an Electron or 3D Conformal Treatment plan. 2003 World Congress on Medical Physics and Biomedical Engineering. Sydney, Australia, 2003: to be delivered.
13. Cotrutz C, Xing L. Using voxel-dependent importance factors for interactive DVH-based dose optimization. Physics in Medicine & Biology 2002; 47 (5): 1659.
14. Cotrutz C, Xing L. IMRT dose shaping using regionally variable penalty scheme. Medical Physics 2002; 30: 544.
15. Yang Y, Xing L. Incorporating leaf transmission and header scatter corrections into MLC leaf sequences for IMRT. International Journal of Radiation Oncology, Biology, Physics 2003; 55: 1121.
16. Xing L, Yang Y, Li J, et al. Monitor Unit Calculation and Plan Validation for IMRT. In: Palta JR, Mackie TR, eds. Intensity-Modulated Radiation Therapy: The State of the Art: Medical Physics Publishing, 2003: 3567.
17. Cotrutz C, Xing L. Segment-Based Dose Optimization Using a Genetic Algorithm. Physics in Medicine & Biology 2003; 48: in press.
18. Song Y, Boyer A, Pawlicki T, Xing L., et al. Modulated Electron Radiation Therapy: A Comparative Dosimetric Study of MERT and IMRT for Parotid Cancer. Technology in Cancer Research and Treatment 2003; in press.

19. Lo A SY, Boyer A.L., Pawlicki T., Xing L. Combining IMRT and Modulated Electron Radiation Therapy for Breast-Conserving Radiation Therapy. Oral presentation in 2003 RSNA Annual Meeting. Chicago, IL, 2003: to be delivered.

List of personnel receiving pay from the research effort: 10% of PI's salary was supported by the grant during the funding period. In addition, 65% of Dr. David Yong Yang (Postdoctoral fellow)'s effort was supported by the grant. There are no other personnel who receive pay from the research effort.

Appendices: Copies of manuscripts

List of Enclosed Materials:

1. Cotrutz C and Xing L, "Segment-Based Inverse Planning Using Genetic Algorithm". *Physics in Medicine and Biology* 48, in press, 2003.
2. Cotrutz C and Xing L: "Using Voxel Dependent Importance Factors for DVH-Based Interactive Planning", *Physics in Medicine and Biology* 47, 1659-69, 2002.
3. Lian J, Cotrutz C and Xing L, "Inverse Planning with Probabilistic Dose Prescription". *Medical Physics* 30, 655-666, 2003.
4. Yang Y and Xing L, "Incorporating Leaf Transmission and Head Scatter Corrections into Step-and-Shoot Leaf Sequences for IMRT". *International Journal of Radiation Oncology, Biology, Physics* 55, 1121-1134, 2003.
5. Cotrutz C and Xing L, "IMRT Dose Shaping with Regionally Variable Penalty Scheme". *Medical Physics* 30, 544-551, 2003.
6. Song Y, Boyer A, Pawlicki T, Xing L, Lee M, Jiang S, Yan Y, Ma C, Modulated Electron Radiation Therapy: A Comparative Dosimetric Study of MERT and IMRT for Parotid Cancer, *Technology in Cancer Research and Treatment*, accepted.
7. Yang Y and Xing L, "Independent Dosimetric Calculation with Inclusion of Head Scatter and MLC Transmission". *Medical Physics*, accepted.
8. Pugachev A and Xing L: "Incorporating Prior Knowledge into IMRT Beam Orientation Optimization", *International Journal of Radiation Oncology, Biology, Physics*, 54, 1565-1574, 2002.
9. Xing L, Pawlicki T, Yuen L, Crooks S, Dugan J, Li C, Halberg F, Cotrutz C, Lehmann J, Donaldson S, Luxton G, Boyer A, Goffinet D: "A comprehensive method of breast-conserving radiation therapy using forward multiple segment planning and step-and-shoot delivery", *Journal of Applied Clinical Medical Physics*, in preparation.
10. Xing L, Yang Y, Li J, Chen Y, Luxton G, Boyer A (2003): Monitor Unit Calculation and IMRT plan Validation. In: Intensity Modulated Radiation Therapy, Palta J and Mackie RT (Editors). Medical Physics Publishing, Madison, Wisconsin.
11. Xing L, L J, Song Y, Pawlicki T., Boyer AL, Le Q. Dose Matching of an IMRT plan with an Electron or 3D Conformal Treatment plan. 2003 World Congress on Medical Physics and Biomedical Engineering. Sydney, Australia, 2003.
12. Lo A SY, Boyer A.L., Pawlicki T., Xing L. Combining IMRT and Modulated Electron Radiation Therapy for Breast-Conserving Radiation Therapy. Oral presentation in 2003 RSNA Annual Meeting. Chicago, IL, 2003.

US Patent:

Cotrutz C. and Xing L, *Fine-tuning a dose distribution after dose optimization*, US Provisional Patent Application filed in March 2002. Stanford Office of Technology Reference #: S01-261 (pending).

Segment-based dose optimization using a genetic algorithm

Cristian Cotrutz and Lei Xing

Department of Radiation Oncology, Stanford University School of Medicine, 300 Pasteur Drive, Stanford, CA 94305-5304, USA

E-mail: lei@reyes.stanford.edu

Received 3 March 2003, accepted for publication 18 July 2003

Published DD MMM 2003

Online at stacks.iop.org/PMB/48/1

Abstract

Intensity modulated radiation therapy (IMRT) inverse planning is conventionally done in two steps. Firstly, the intensity maps of the treatment beams are optimized using a dose optimization algorithm. Each of them is then decomposed into a number of segments using a leaf-sequencing algorithm for delivery. An alternative approach is to pre-assign a fixed number of field apertures and optimize directly the shapes and weights of the apertures. While the latter approach has the advantage of eliminating the leaf-sequencing step, the optimization of aperture shapes is less straightforward than that of beamlet-based optimization because of the complex dependence of the dose on the field shapes, and their weights. In this work we report a genetic algorithm for segment-based optimization. Different from a gradient iterative approach or simulated annealing, the algorithm finds the optimum solution from a population of candidate plans. In this technique, each solution is encoded using three chromosomes: one for the position of the left-bank leaves of each segment, the second for the position of the right-bank and the third for the weights of the segments defined by the first two chromosomes. The convergence towards the optimum is realized by crossover and mutation operators that ensure proper exchange of information between the three chromosomes of all the solutions in the population. The algorithm is applied to a phantom and a prostate case and the results are compared with those obtained using beamlet-based optimization. The main conclusion drawn from this study is that the genetic optimization of segment shapes and weights can produce highly conformal dose distribution. In addition, our study also confirms previous findings that less segments are generally needed to generate plans that are comparable with the plans obtained using beamlet-based optimization. Thus the technique may have useful application in facilitating IMRT treatment planning.

1. Introduction

Intensity modulated radiation therapy (IMRT) inverse planning aims to conform the high dose of radiation to the planning target volume (PTV) while reducing as much as possible the doses to the organs at risk (OARs) and normal tissue. During an inverse planning calculation the fluence maps are changed iteratively under the guidance of an objective function until the optimum dose distribution is obtained. After the dose optimization, each fluence map is transformed into a set of MLC-shaped segments by using a leaf-sequencing algorithm (Convery and Rosenbloom 1992, Bortfeld *et al* 1994, Spirou and Chui 1994, Stein *et al* 1994, Xia and Verhey 1998, Crooks *et al* 2002). The above approach separates the dose optimization and MLC leaf-sequencing processes and often requires a large number of segments (typically, 20–150, depending on the complexity of the fluence map) to produce the obtained fluence maps and the optimal dose distributions. Physical characteristics of the MLC (e.g., intra-leaf leakage of the MLC, head scatter and tongue-and-groove effect) are considered in the leaf-sequencing process (Yang and Xing 2003) or during the dose optimization (Siebers *et al* 2002).

An alternative approach is to optimize directly the objective function with respect to the shapes and weights of the segmented fields (Bednarz *et al* 2002, De Gersem *et al* 2001, Shepard *et al* 2002). The number of segments for each incident beam is pre-specified in the so-called aperture-based dose optimization. Along this line, Bednarz *et al* used mixed-integer programming to optimize the weights of some pre-defined field segments. A special segmentation tool was used to create a pool of allowable delivery segments. In the same category one can also include the work of Cotrutz *et al* (2000), who developed an aperture-based optimization method for intensity modulated arc therapy (IMAT). De Gersem *et al* (2001) implemented a technique in which the MLC leaf positions of each segment and the segment weights are adjusted iteratively. The initial segments are determined by using an anatomy-based segmentation tool. At each iteration step, a trial configuration is accepted only if it leads to a reduction of the objective function. Recently, Shepard *et al* (2002) reported a direct aperture optimization (DAO) algorithm, in which the leaf positions are initialized to match the beam's eye view of the target. The aperture shapes and weights are optimized using a simulated annealing technique. Generally speaking, it is more computationally involved to optimize an objective function with respect to the segment shapes and weights because of the nonlinear dependence of the dose on the leaf coordinates.

The present paper describes the implementation of a genetic algorithm for the optimization of both segment shapes and weights. Genetic algorithm is a class of search techniques inspired from the biological process of evolution by means of natural selection. It has been used to construct numerical optimization techniques that perform robustly on problem characterized by ill-behaved search spaces (Michalewicz 1996). The main advantage of the method over the simulated annealing algorithm lies in the fact that, instead of randomly sampling the trial solutions, the probability of a given solution being selected to survive is proportional to its fitness; better trial solutions have higher probabilities to survive. In our implementation, the system variables consist of the coordinates of the MLC leaves, and the weights of the MLC-defined segments. We do not impose restrictions on the topological shape of the segments as long as they are permissible by the delivery system (for instance, for Varian's MLC, a segment can be composed of two or more topologically disconnected apertures). A hypothetical phantom and a prostate case are used to illustrate the feasibility of the segment-based optimization algorithm.

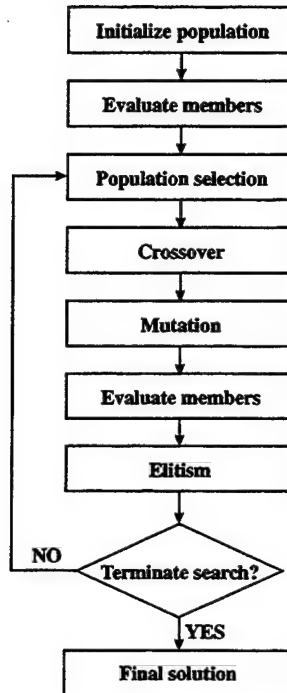


Figure 1. Flow chart of the genetic algorithm for segmented dose optimization.

2. Method and materials

2.1. Genetic algorithms for radiation therapy dose optimization

Genetic algorithms (GAs) have been successfully used to optimize the weights of open/wedged beams (Ezzell 1996, Wu and Zhu 2000) and the beam orientations (Haas *et al* 1998) in conformal 3D radiation therapy, and the dwell times of the HDR sources in brachytherapy (Lahanas *et al* 1999). The algorithms encode potential solutions in chromosome-like data structures and apply different recombination operators to explore the search space but meanwhile to preserve critical information. The fittest individuals sexually recombine and born descendants that keep the same characteristics as their parents. Due to the natural environment conditions some of the individuals can suffer mutations that can lead to individuals with better adaptive qualities to the environment. Most of the mutations will lead to individuals that are not fit and will therefore disappear. Eventually the whole population of solutions (individuals) converge towards the fittest configuration.

As shown in figure 1, the following features usually characterize the genetic algorithms: (i) a representation of potential solutions to the problem; (ii) a specific method for initializing the whole population of solutions; (iii) an evaluation function that ranks the quality of each solution (individual) and (iv) genetic operators (crossover and mutation) that determine the information exchange between the individuals of the population. The genetic algorithms search for a solution in a parallel fashion. Instead of using a single searcher as in the calculus-based methods, a population of solutions is used to 'scan' the solution space. Similar to the

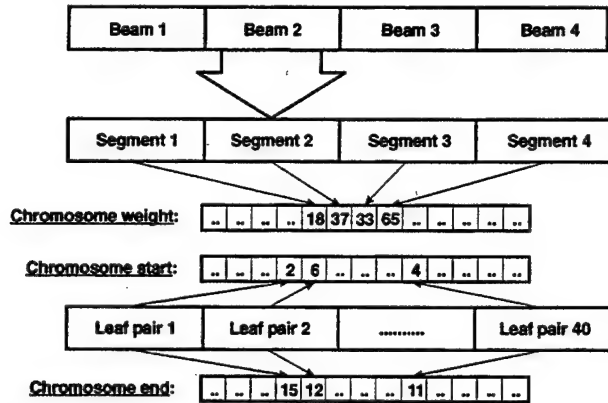


Figure 2. Diagram depicting the integer encoding of the variables used by the genetic optimization algorithm. The aperture shapes are encoded in two chromosomes: the first chromosome encodes the position of the left leaves, while the second chromosome encodes the position of the right leaves. The aperture weights are encoded in a separate chromosome.

simulated annealing algorithms, a GA is stochastic in nature and less likely to be trapped in local minima. However, instead of randomly sampling the trial solutions, the probability of a given solution being selected to survive depends on its fitness; better trial solutions have higher probabilities to survive.

2.2. Segment shape and weight encoding

The GA used for segment-based optimization is shown in figure 1. The variables that need to be optimized include the weights of the segments and the corresponding leaf positions of the involved leaf pairs of the segments. These variables are encoded in three chromosome-like structures for each potential solution (individual). The weights of the apertures are represented in integer format, by the concatenation of the individual weights of each segment. Figure 2 shows the weight encoding for a potential solution formed out of four beams, each with four apertures. The total length of such a weight chromosome will then be 16.

The variables defining a segment are encoded using two chromosomes. The first chromosome encodes the position of the left leaves, while the second one the position of the right leaves. This is schematically represented in figure 2, where for each of the considered segments, the positions of the left and right leaves are shown for each of the 40 Varian leaf pairs. Therefore, each of the leaf-position chromosomes will have a length of 4(beams) \times 4(segments/beam) \times 40(leaves/segments) = 640. The encoding of any leaf position is realized in integer format, and represents the index of the first open beamlet for the segment start and last open beamlet for the segment end. The dimension of a beamlet projected at the isocentre plane is usually 0.5 \times 1 cm.

The GA optimization starts with the initialization step where for each member of the solution population, the aperture shapes and weights are initialized to random values. The size of the population can differ from case to case, typically ranging from 100 to 200 members. The physical constraints of MLC leaf positions are considered in the initialization and subsequent optimization process.

2.3. Fitness evaluation

The quality of a solution i is evaluated according to its fitness F_i , which is defined as

$$F_i = \frac{1}{O_i} \quad (1)$$

$$O_i = \sum_{\sigma=1}^{N_{Struct}} w_{\sigma} \sum_{n=1}^{N_{\sigma}} \frac{g(d_n^{\sigma})(d_n^{\sigma} - d_0^{\sigma})^2}{N_{\sigma} d_0^{\sigma 2}} \quad (2)$$

where O_i is the conventional quadratic objective function, w_{σ} is the importance factor of a structure σ (Xing *et al* 1999, Starkschall *et al* 2001), d_n^{σ} and d_0^{σ} are the calculated and prescribed doses for the structure σ and N_{σ} is the number of voxels of structure σ . In equation (2), for an OAR, $g(d_n^{\sigma})$ is a step function defined as

$$g(d_n^{\sigma}) = \begin{cases} 1 & \text{if } d_n^{\sigma} > d_0^{\sigma} \\ 0 & \text{if } d_n^{\sigma} \leq d_0^{\sigma} \end{cases}$$

For PTV, $g(d_n^{\sigma})$ takes unit value. The dose to a voxel n of the structure σ , d_n^{σ} , is calculated as a weighted sum of the doses d_n^{BS} produced by each individual segment S of beam B . w_{BS} represents the weight of the segments BS :

$$d_n^{\sigma} = \sum_{B=1}^{N_{beams}} \sum_{S=1}^{N_{seg}} w_{BS} d_n^{BS}. \quad (3)$$

A detailed description of the dose calculation is described in a previous publication (Cotrutz *et al* 2001).

2.4. Fitness-based selection

The fitness is evaluated for every encoded solution (chromosome-triplet) in the population. The selection process is based on the principle of ‘survival of the fittest’ and critically determines the convergence properties of the GA. The chance of a particular solution characterized by fitness F_i to be part of the next generation population is proportional to its survival probability defined by

$$P_{S_i} = \frac{F_i}{\sum_{i=1}^{Pop} F_i} \quad (4)$$

where $\sum_{i=1}^{Pop} F_i$ is the total fitness of the considered population. A more fit solution has a higher probability of being selected for the next generation. The new population is then selected by simulating the spinning of a suitable roulette wheel, N times, where N equals the number of the solutions in the current generation (Michalewicz 1996). In addition to the fitness-based selection process the best members of the current population are allowed to be copied automatically into the next generation. This process called *elitism* leads to a faster convergence and keeps track of the best solutions obtained at each iteration.

2.5. Genetic operators

The solutions chosen in the fitness-based selection process serve as progenitors for a new generation of solutions. Several recombination techniques such as crossover and mutation are applied to the selected solutions in order to exchange information and create new, improved solutions. The genetic operators are applied three times for each pair of selected solutions,

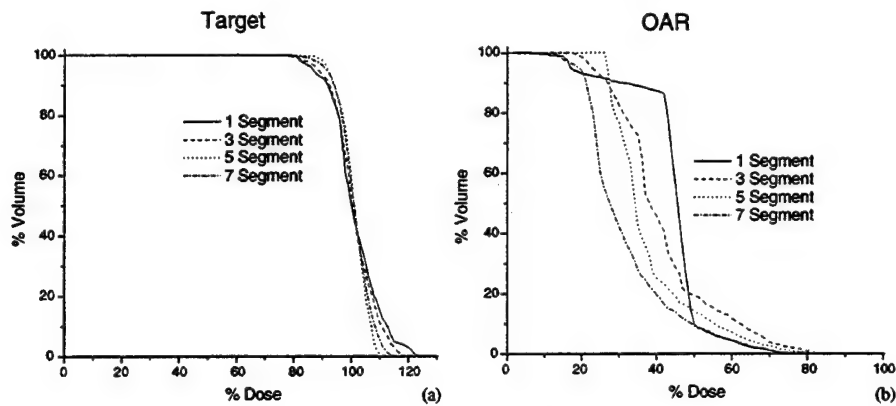


Figure 3. DVH plots of the C-shape tumour (a) and the OAR (b) for the segment-based optimization with one, three, five and seven segments per beam.

firstly for the chromosomes encoding the position of the left leaves, then for those encoding the position of the right leaves and finally for the weight encoding chromosomes.

The one-point crossover operator (Michalewicz 1996) used in our GA seeks to construct better segment shapes and weights by combining the features of the surviving ones. Initially the entire population is paired off at random to give $N/2$ potential parents. Following, each pair of solutions is chosen to undergo crossover with probability P_C , which is defined at the beginning of the optimization. The crossover probability P_C usually takes values of 0.80–0.95. If the probability condition is met, a randomly chosen crossing point is selected for each of the corresponding chromosomes. The offspring solutions are formed by swapping the genes (bits) located past the break-up point.

The purpose of mutation operator is to ensure the diversity of the potential solutions and prevent the loss of genetic information that occurs when only crossover recombination is used. The mutation operator usually produces solutions far apart from those considered the best and usually occurs with very low probability P_M (of the order of 0.03 or less). The role of these mutated solutions is to ensure a large range search of the solution space. Like the crossover operator, mutation occurs on both the segment shape and weight encoding chromosomes. In the latter case, a selected gene is replaced by a new value, which is randomly chosen within the interval 0, maxweight , where maxweight is the maximum allowed segment weight. The mutation mechanism is also applied to the aperture shape encoding chromosomes. The mutation results in either opening or closing the leaf gaps, which are assigned with equal probabilities, in order to avoid biasing the algorithm towards large or small apertures.

3. Results and discussion

3.1. C-shape tumour

The performance of the newly developed GA is first tested using a synthetic case. The geometry of the phantom, the C-shape PTV and circularly shaped OAR are shown in figure 4. Nine 6 MV equispaced beams were used to irradiate the tumour. The optimization was carried out successively for one, three, five and seven segments per beam. Figure 3 shows the

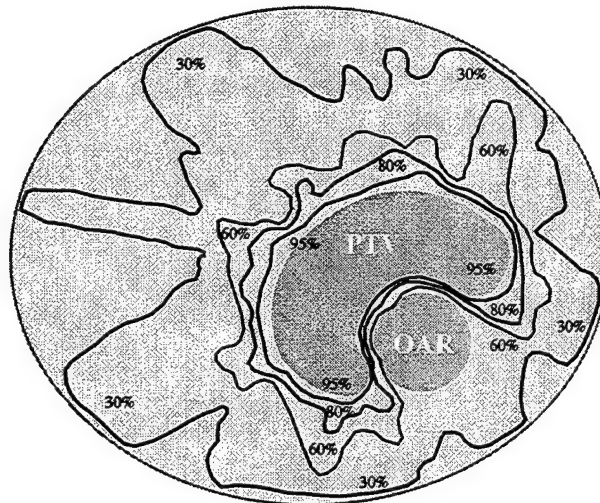


Figure 4. Isodose distribution for the C-shape tumour optimized using seven apertures per beam. Nine 6 MV equispaced photon beams were used.

dose–volume histograms (DVHs) for the target and critical structure when different numbers of segments are employed.

It is clear from these DVHs that as the number of segments per beam increases, better PTV dose coverage and OAR dose sparing are achieved. This is consistent with our intuition because an increase of the number of apertures enhances the degree of intensity modulation. It is remarkable though that by using only three to five apertures per beam one can get very good results. The general observation here is in accordance with previous studies that used simulated annealing algorithms (Shepard *et al* 2002). Figure 4 shows the dose distribution obtained with seven apertures per beam. The dose conformation to the tumour is very good, and furthermore, the dose gradient in the region proximal to the OAR is steep, ensuring thus a good OAR protection.

Using the same phantom, we also investigated the convergence properties of the genetic algorithm. Figure 5 shows the fitness of the best member in the population as a function of iteration step for the plans with three and seven apertures per beam. For both runs we used the same parameters for the population size (150 members) and crossover ($P_C = 0.95$) and mutation ($P_M = 0.03$) probabilities. A rapid increase in the fitness is observed in the first 1500 iterations for both runs. Following, the convergence slope decreases until a plateau region is reached. We note that the optimization run performed with seven segments per beam converges more slowly than that when only three apertures per beam are used, which is explainable considering that the number of variables in the latter case is much less than the former one.

3.2. Prostate patient

The genetic algorithm was applied to plan an IMRT prostate treatment. Seven 6 MV equispaced beams were used with three apertures per beam. The OARs in this case included the rectum, bladder and the two femoral heads.

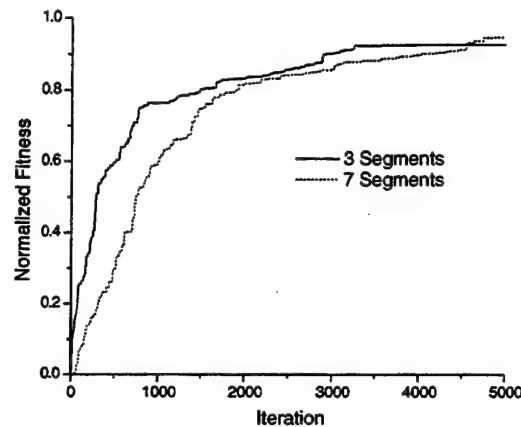


Figure 5. Plot showing the convergence behaviour of the genetic optimization algorithm when three and seven segments per beam are used.



Figure 6. Axial slice of the final dose distribution optimized with seven equispaced 6 MV photon beams, each with three segments. The isodose lines shown are 30, 60, 80 and 95%.

Figure 6 shows an axial slice of the final dose distribution. It is seen that even with as little as three segments per beam, the 95% isodose line can encompass the prostate and the seminal vesicles. The bladder and rectum are also spared nicely. The femoral heads receive less than 45% of the prescribed dose. Figure 7 shows the DVHs of the prostate, bladder and rectum and femoral heads for this plan.

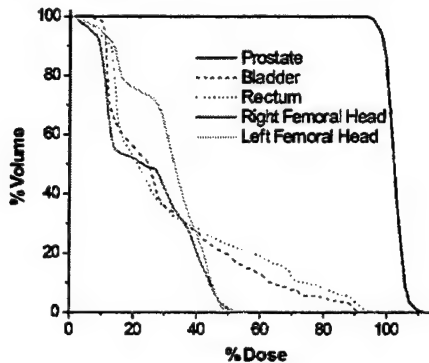


Figure 7. DVHs for the three segments per beam prostate case.

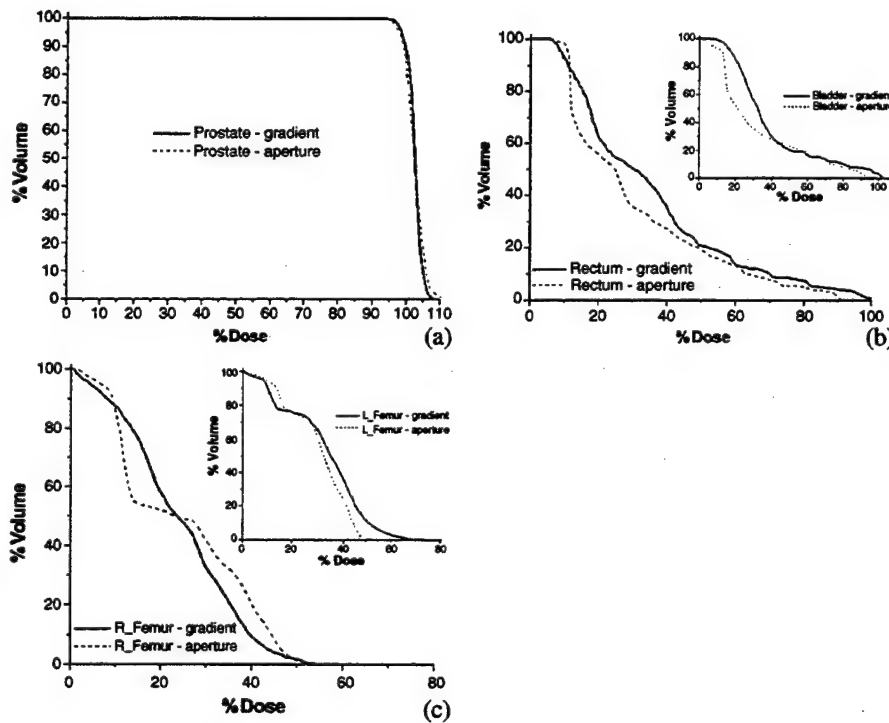


Figure 8. DVHs comparison for a prostate case optimized with a segment and beamlet-based dose optimization engines: (a) prostate; (b) rectum and bladder; (c) femoral heads.

We compared the segment-based optimization with a beamlet-based optimization algorithm described in a previous publication (Cotruț *et al* 2001). The same organ tolerances were used in both calculations. To have a more meaningful comparison, we chose the structure importance factors in the segment-based optimization in such way that similar prostate dose coverage and comparable DVHs for the rectum and bladder were obtained. Figures 8(a)–(c)

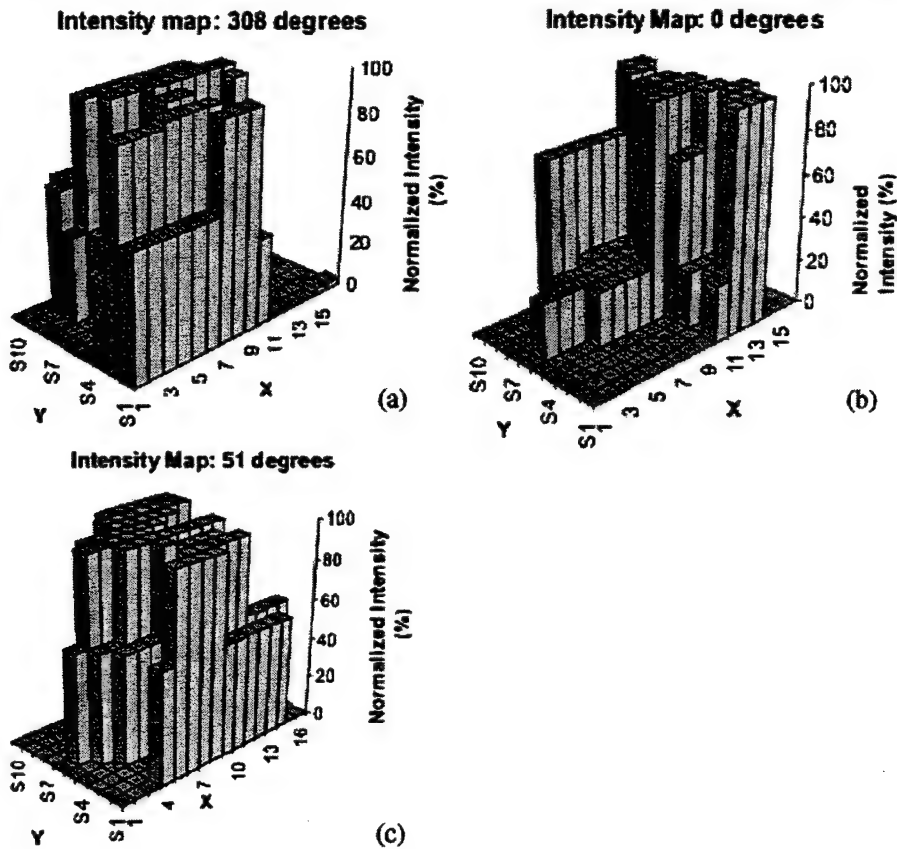


Figure 9. Three intensity maps for the anterior (180°) and antero-lateral beams (308° and 51°) used for the prostate patient.

show the DVHs of the prostate (a), bladder and rectum (b) and femoral heads (c), for the two optimization approaches. As can be seen from figure 8, there is no clear-cut conclusion on which plan is better. While the prostate is better coved in beamlet-based optimization, the segment-based approach performs equally or better for the rest of the structures. The rectum and bladder DVHs in figure 8(b) show a reduction of approximately 8% of the maximum dose for the segment-based optimized plan, whereas for the right femoral head, the volumes receiving high doses are increased as compared to the beamlet-based optimized plan. Generally speaking, a segment-based optimization represents a special case of the beamlet-based optimization and the plan obtained using the former approach should therefore be equal or less conformal in comparison with the general beamlet-based approach. In practice, however, there are many parameters (such as beamlet size, number of intensity levels, etc) in the beamlet-based optimization that may influence the quality of the final plan and even revert the above statement in some unfavourable situations.

We have also planned the patient using five and seven segments per beam, and a similar trend as described for the synthetic phantom case (section 3.1) was observed. In general,

it seems true that for relatively simple cases, such as the prostate case studied here, three to seven segments per beam are sufficient to produce a clinically acceptable IMRT plan. A technique with beam specific number of segments instead of uniform number of segments for all treatment fields could be easily implemented.

Note that in this study we do not restrict a segment to be topologically connected. The three intensity maps shown in figure 9 correspond to the anterior and anterior-lateral beams used for the prostate plan. The intensity maps are topologically connected, and could be deliverable by any MLC. If topologically disconnected segments would result following the optimization, beams would be deliverable by a Varian MLC, but not by a Siemens or an Elekta accelerator, because the interdigitation of the adjacent leaves is not allowed. In general, the MLC constraints of the treatment machine should be considered in the segment-based optimization process.

4. Conclusions

A simple genetic algorithm is developed to simultaneously optimize the segment shapes and their weights for IMRT. The segment-based genetic optimization exploits a number of trial solutions in a variety of directions based on genetic selection rules. Application of the new technique to two test cases shows that with only a small number of segments per beam, it can produce plans comparable to those obtained with conventional beamlet-based algorithm. Another advantage of the segment-based optimization is that it eliminates the intermediate leaf-sequencing process, leading to a solution that is directly deliverable.

Acknowledgments

This work was supported in part by a Research Scholar Grant Award from the American Cancer Society (RSG-01-022-01-CCE) and Research Grant from the US Department of Defense (BC021705).

References

- Bednarz G, Michalski D, Houser C, Huq M S, Xiao Y, Rani Anne P and Galvin J M 2002 The use of mixed-integer programming for inverse treatment planning with pre-defined field segments *Phys. Med. Biol.* **47** 2235–45
Bortfeld T R, Kahler D L, Waldron T J and Boyer A L 1994 X-ray field compensation with multileaf collimators *Int. J. Radiat. Oncol. Biol. Phys.* **28** 723–30
Convery D J and Rosenblom M E 1992 The generation of intensity-modulated fields for conformal radiotherapy by dynamic collimation *Phys. Med. Biol.* **37** 1359–74
Cotruzz C, Kappas C and Webb S 2000 Intensity modulated arc therapy (IMAT) with centrally blocked rotational fields *Phys. Med. Biol.* **45** 2185–206
Cotruzz C, Lahanas M, Kappas C and Baltas D 2001 A multiobjective gradient-based dose optimization algorithm for external beam conformal radiotherapy *Phys. Med. Biol.* **46** 2161–75
Crooks S M, McAven L, Robinson D and Xing L 2002 Minimizing delivery time and monitor units in static IMRT by leaf-sequencing *Phys. Med. Biol.* **47** 3105–16
De Gersem W, Claus F, De Wagter C, Van Duyse B and De Neve W 2001 Leaf position optimization for step-and-shoot IMRT *Int. J. Radiat. Oncol. Biol. Phys.* **51** 1371–88
Ezzell G A 1996 Genetic and geometric optimization of three-dimensional radiation therapy treatment planning *Med. Phys.* **23** 293–305
Haas O C, Burnham K J and Mills J A 1998 Optimization of beam orientation in radiotherapy using planar geometry *Phys. Med. Biol.* **43** 2179–93
Lahanas M, Baltas D and Zamboglou N 1999 Anatomy-based three-dimensional dose optimization in brachytherapy using multiobjective genetic algorithms *Med. Phys.* **26** 1904–18
Michalewicz Z 1996 *Genetic Algorithms + Data Structures = Evolution Programs* (Berlin: Springer)

- Shepard D M, Earl M A, Naqvi S and Yu C 2002 Direct aperture optimization: a turnkey solution for step-and-shoot IMRT *Med. Phys.* **29** 1007–18
- Siebers J V, Lauterbach M, Keall P J and Mohan R 2002 Incorporating multi-leaf collimator leaf sequencing into iterative IMRT optimization *Med. Phys.* **29** 952–9
- Spirou S V and Chui C S 1994 Generation of arbitrary intensity profiles by dynamic jaws or multileaf collimators *Med. Phys.* **21** 1031–41
- Starkschall G, Pollak A and Stevens C 2001 Treatment planning using a dose-volume feasibility search algorithm **49** 1419–27 See endnote 1
- Stein J, Bortfeld T, Dorschel B and Schlegel W 1994 Dynamic X-ray compensation for conformal radiotherapy by means of multi-leaf collimation *Radiat. Oncol.* **32** 163–73
- Wu X and Zhu Y 2000 A mixed-encoding genetic algorithm with beam constraint for conformal radiotherapy treatment planning *Med. Phys.* **27** 2508–16
- Xia P and Verhey L J 1998 Multileaf collimator leaf sequencing algorithm for intensity modulated beams with multiple static segments *Med. Phys.* **25** 1424–34
- Xing L, Li J G, Donaldson S, Le Q T and Boyer A L 1999 Optimization of importance factors in inverse planning *Phys. Med. Biol.* **44** 2525–36
- Yang Y and Xing L 2003 Incorporating leaf transmission and head scatter corrections into step-and-shoot leaf sequences for IMRT **55** 1121–34

Using voxel-dependent importance factors for interactive DVH-based dose optimization*

Cristian Cotrutz and Lei Xing

Department of Radiation Oncology, Stanford University School of Medicine, 300 Pasteur Drive, Stanford CA 94305-5304, USA

E-mail: cristian@reyes.stanford.edu and lei@reyes.stanford.edu

Received 11 January 2002

Published 2 May 2002

Online at stacks.iop.org/PMB/47/1659

Abstract

Intensity modulated radiation therapy (IMRT) inverse planning is usually performed by pre-selecting parameters such as beam modality, beam configuration and importance factors and then optimizing the fluence profiles or beamlet weights. In reality, the IMRT dose optimization problem may be ill-conditioned and there may not be a physical solution to account for the chosen parameters and constraints. Planner intervention is often required to conduct a multiple trial-and-error process where several parameters are sequentially varied until an acceptable compromise is achieved. The resulting solution reflects a balance between the conflicting requirements of the target and the sensitive structures. A major problem of the conventional inverse planning formalism is that there exists no effective mechanism for a planner to fine-tune the dose distribution on a local level or to differentially modify the dose–volume histograms (DVHs) of the involved structures. In this paper we introduce a new inverse planning scheme with voxel-dependent importance factors and demonstrate that it provides us with an effective link between the system parameters and the dosimetric behaviour at a local level. The planning proceeds in two steps. After a conventional trial-and-error inverse planning procedure is completed, we identify the dose interval at which the fractional volume on the DVH curve needs to be changed. The voxels that receive dose in the selected range are then located and their voxel-dependent importance factors are adjusted accordingly. The fine-tuning of the DVHs is iterative in nature and, using widely available computer graphic software tools, the process can be made graphically interactive. The new IMRT planning scheme is applied to two test cases and the results indicate that our control over the differential shapes of the DVHs of the involved structures is greatly enhanced. Thus the technique may have significant practical implications in facilitating the IMRT treatment planning process.

* US Patent pending.

1. Introduction

IMRT represents one of the most important advancements in radiation therapy, and aims at delivering high radiation doses to the target volumes while maximally sparing the adjacent critical structures. The beam profiles of an IMRT treatment are usually obtained using inverse planning systems that employ various approaches for dose optimization (Webb 1989, Bortfeld *et al* 1990, Rosen *et al* 1995, Morrill *et al* 1995, Xing and Chen 1996, Olivera *et al* 1998, Spirou and Chui 1998, Wu and Mohan 2000, Gopal and Starkshall 2001, Cotrutz *et al* 2001). Most inverse planning algorithms developed to date require dose-volume prescriptions. At the dose optimization level, these algorithms can be categorized into two classes: (i) minimization of a dose-volume histogram (DVH)-based objective function (Togane *et al* 1998, McGary 2001) and (ii) minimization of a quadratic objective function with dose-volume constraints (Cho *et al* 1998, Spirou and Chui 1998, Bortfeld 1999, Wu and Mohan 2000). The latter approach attempts to satisfy the dose-volume constraints either by constantly penalizing those voxels that exceed the permitted fractional volume (Spirou and Chui 1998) or by adopting a volume sensitive variable penalization scheme (Cho *et al* 1998) of the same voxels. The final solution is determined by the choice of DVH prescriptions and the structure specific importance factors that prioritize the relative importance of the clinical goals of the involved structures. In general, the optimized plan complies to a certain degree with the prescriptions and constraints set to the target and critical structures, but hardly meets all the requirements. Therefore, several trial-and-error adjustments of the system parameters are often necessary to achieve a good compromise solution.

A main problem of the currently available inverse planning systems is that there is no explicit way to fine-tune the shapes of the final DVHs. While the shape of the optimized DVH curve of a given structure often differs from the desired one, at which dose bin(s) the fractional volume exceeds the expected value(s) is somewhat random and out of the user's control. There is no explicit way for a user to differentially modify the DVH curves according to the clinical requirement after a trial optimization is completed. When the need arises, the user often refers to the prescribed DVHs and/or the structure-specific importance factors, hoping that the resulting solution will be more consistent with his/her expectation.

In this work, we report an effective method for interactively controlling the shapes of the final DVHs of the target and sensitive structures. We introduce the concept of voxel-dependent importance factors and relate it to the local dosimetric behaviour of the system. After an optimal solution is reached by using the conventional approach, further refinement of the dose distribution is accomplished by modifying the importance factors of user-defined voxels. This process proceeds interactively driven by the user's clinical judgement.

In section 2 we introduce the concept of local importance factors and describe in detail the interactive planning procedure. Also, the technique is exemplified using two test cases. Our physical insight on the approach is given along with the presentation of the results. We conclude in section 4.

2. Method

2.1. Local importance factors

The inverse radiotherapy problem is to determine a vector of beamlet weights, \mathbf{w} , with the goal of achieving a prescribed dose distribution or DVHs. In a vectorial form, the dose to the points in the treatment region depends upon the beamlet weights as

$$\mathbf{D}_c = \mathbf{d} \cdot \mathbf{w} \quad (1)$$

where d represents the dose deposition coefficient matrix, expressing the dose deposited to any calculation point when irradiated with a set of unit weight beamlets.

A commonly used method to find the optimal solution of the inverse IMRT problem is to minimize a quadratic objective function (Webb 1989, Bortfeld *et al* 1990, Mageras and Mohan 1993, Xing and Chen 1996) defined by

$$F = \frac{1}{N} \sum_n r_\sigma [D_c(n) - D_0(n)]^2 \quad (2)$$

where D_c and D_0 are the calculated and prescribed doses, respectively, N is the total number of voxels within a structure σ , n is the voxel index and r_σ is the importance factor that controls the relative importance of a structure σ . Different sets of importance factors result in different 'optimal' solutions and multiple trial-and-error are often needed to find a set of clinically acceptable values. Several methods have been proposed to use the computer to facilitate the trial-and-error determination of the importance factors (Xing *et al* 1999a, 1999b, Cotruzz *et al* 2001, Wu and Zhu 2001).

While the inverse planning formalism with structure-specific importance factors can provide us with acceptable solutions, there is no mechanism for the user to differentially modify the shapes of the DVHs of the final solution or the regional dose within a structure when a such clinical need arises. To give an example, imagine the behaviour of a system comprising two very closely located anatomical structures, e.g. planning target volume (PTV) and one critical structure volume (CSV). In the most probable instance, neither the PTV, nor CSV prescription doses will be met at the common boundary region. Therefore, it would be less advisable to penalize the voxels in the high-gradient region with the same importance factor as for those located in the bulk of the structures. Here we propose a general inverse planning framework with non-uniform importance factors. In this new formalism, the importance at a voxel n is expressed as a product of two factors, r_σ and r_n (see equation (3)), where r_σ characterizes the importance of the structure σ as an entity relative to other structures, and r_n modulates the importance in obtaining an optimal solution at a regional level of the structure. The voxel-specific importance factor provides an effective means for us to prioritize the inner structural importance. The objective function now reads

$$F = \sum_{\sigma=1}^{n_\sigma} \left[\frac{1}{N_\sigma} \sum_{n=1}^{N_\sigma} r_\sigma r_n [D_c(n) - D_0(n)]^2 \right] \quad (3)$$

where N_σ represents the total number of voxels of a structure. In equation (3), $D_0(n)$ is the prescription dose. Note that conventional inverse planning scheme represents a special case of the more general formalism proposed here when all the r_n have unit values.

2.2. Strategy of the optimization process

The overall planning process is schematically shown in the flow chart of figure 1. The operations included within rectangle I are part of the conventional inverse planning process, where system parameters, such as structure-specific importance factors and beam angles, are determined through trial-and-error. For each trial, the optimization results are assessed using dose distributions and DVH tools. This process can be realized by any inverse planning system.

After the conventional IMRT plan is obtained, we proceed to the next stage of interactive planning shown in rectangle II of figure 1. The flow of operations follows the same pattern as in the case of conventional planning (rectangle I), but the adjusting parameters are now the

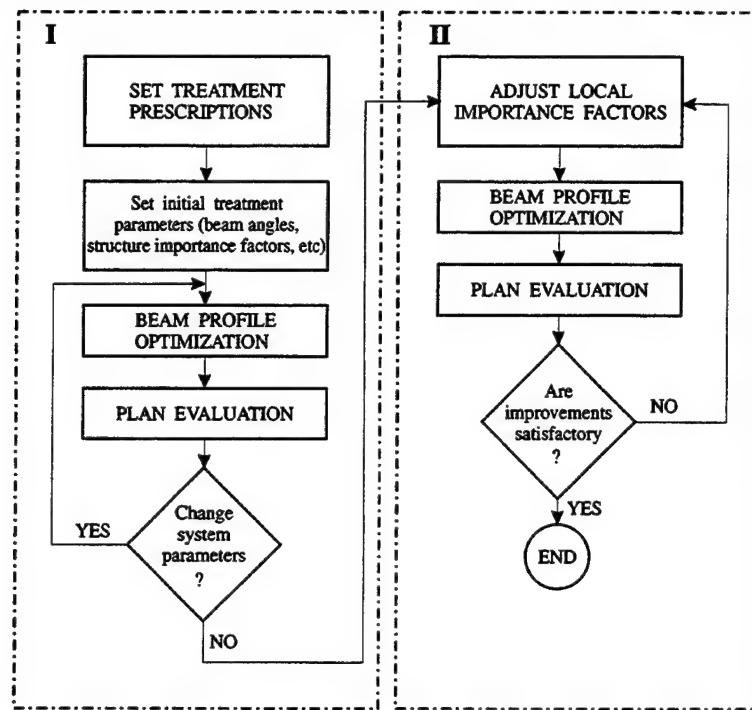


Figure 1. Flow chart depicting the strategy followed by the interactive inverse planning algorithm with voxel-dependent importance factors. The operations incorporated in the left rectangle define the classical inverse planning process. Further refinement of dose distributions and DVHs is achieved by interactively modifying the voxel-dependent importance factors. This latter process is schematically shown in the right rectangle.

local importance factors. Every cycle of this iterative procedure begins with the assessment of the dose distributions and DVHs resulted from the precedent loop.

The planner selects the dose interval(s) for which further refinement of structure DVH(s) is sought. The indices of the voxels belonging to the selected dose interval(s) are automatically detected and 'turned on.' The local importance factors of these voxels are then increased or decreased accordingly. Obviously, increasing the values of the local importance factors will increase the penalization level at the considered voxels and generally lead to better compliance of the resulting dose distribution with the prescription in that region. Conversely, decreasing the importance factors will have an opposite effect and relax the compliance. The amount of change in the importance factors is empirical and we usually proceed by assigning a value 15–50% higher/lower than their previous values after the corresponding voxels are identified. For every change in the importance factors, the dose is re-optimized and the plan is then re-evaluated. The planning process proceeds in an iterative fashion, as shown in figure 1.

The introduction of the local importance factors makes it possible for us to identify the system parameters that are most responsible for the dosimetric behaviour at a local level. Once this link is established, the dose distribution can be fine-tuned more directly. The adjustment of the local importance factors can be performed sequentially or simultaneously

for a few structures. According to our experience, two to three iterations are often sufficient to significantly improve the final solution.

2.3. Beam profile optimization and voxel selection

The algorithm used for beam profile optimization belongs to the gradient-based methods and has been extensively described elsewhere (Cotruț *et al* 2001). The dose calculation engine is based on a radiological pathlength algorithm (Cotruț *et al* 1998). The system was modified to take into account the voxel-based importance factors defined in relation (3). The capability for a user to graphically identify one or more regions on a DVH curve of interest was added as a new feature of the planning system. Alternatively, dose distribution layouts can be used to guide the user to geometrically select the regions where the dose(s) need to be modified by changing the local importance factors.

Subsequent to user's selection of the DVH dose interval of interest (or the outlined volumes of interest) the indices of the voxels receiving a dose in that range are identified and the corresponding values of the voxel-specific importance factors are ready to be assigned with a new value. The plan is re-optimized after the importance factors are updated. The above procedure is performed interactively until the best possible solution is obtained.

3. Results and discussion

Two test cases were used to assess the dose optimization approach proposed in this paper. The first was an elliptical phantom case with a C-shaped tumour and an abutting circular critical structure. The second one was a nasopharynx tumour. The considered critical structures included the eyes, optic chiasm and the brain stem.

3.1. The C-shaped tumour case

The configuration of the C-shaped tumour case is shown in figure 2. Nine 6 MV equispaced beams were used in the treatment (0° , 40° , 80° , 120° , 160° , 200° , 240° , 280° and 320° —respecting the IEC convention). The prescribed dose to the PTV was set to 100 arbitrary dose units and 20 units were assigned as tolerance dose of the critical structure volume (CSV).

Using the conventional inverse planning procedure, we found that the values of the structure-specific importance factors were $r_{PTV} = 0.8$ and $r_{CSV} = 0.2$. This set of importance factors provided a reasonable overall trade-off between dose coverage of the tumour and the protection of the critical structure. The black lines in figure 3 show the tumour and critical structure DVHs for the plan optimized with this set of structure-specific importance factors.

Assuming that our clinical concern was the dose to the CSV, we wanted to lower the maximum dose and the fractional volume receiving dose in the interval AB shown in figure 3. To accomplish this, we first identified the responsible voxels by analysing the dose distribution in the critical structure. These voxels represent $\sim 25\%$ of the structure volume and are marked in figure 2 by plain dots. Their distribution is along the periphery of the CSV's contour, with a larger density within the part proximal to the PTV. In a first attempt, the local importance factors for these voxels labelled by the plain dots were increased from 1.00 to 1.35, while the importance factors of the rest of the CSV voxels remained unchanged and fixed at unit value. Upon re-optimization of the system, the new DVHs are shown in grey lines in figure 3. The target coverage remains practically unchanged, but the CSV sparing is greatly improved. In particular, the maximum dose is decreased by almost 8 dose units as compared to the plan performed with only structure-specific importance factors. With the use of the local

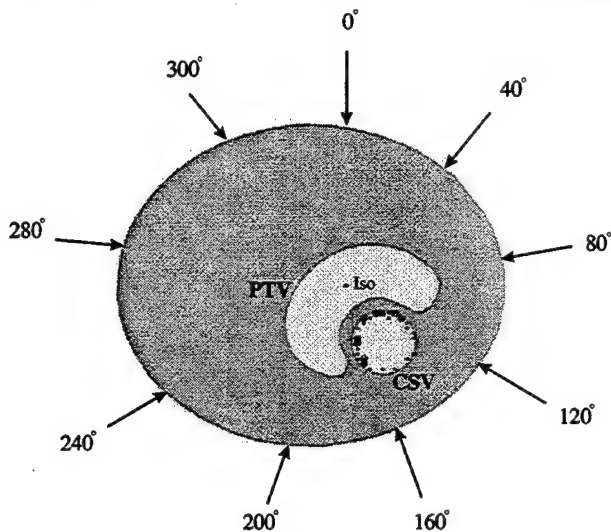


Figure 2. Sketch of the C-shaped tumour test case and the nine-beam set-up used for dose optimization. Dose prescription is set 100 dose units (arbitrary units) to the tumour (PTV) and 20 units to the circular critical structure (CSV).

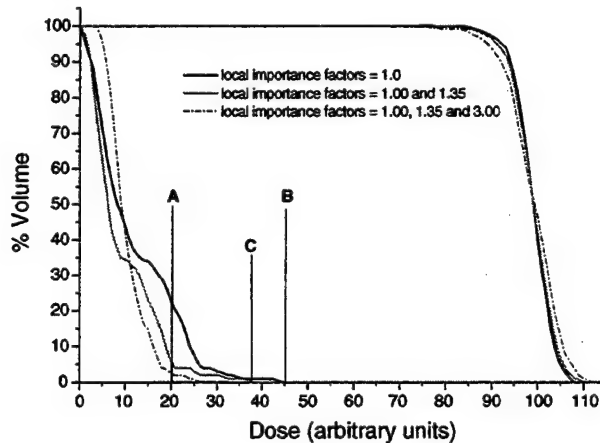


Figure 3. DVHs corresponding to three optimization runs, with different values of the local importance factors. Dose is normalized to the mean target dose.

importance factors, the number of voxels that received a dose exceeding the tolerance level was greatly reduced. These voxels can now be found only at the boundary region with the PTV, as represented by open circles in figure 2.

Further decrease of the fractional volume in the dose range A and C (see figure 3) was sought in our attempt to improve the dose to the CSV. Therefore we assigned a new local importance value of 3.0 to the voxels labelled with open circles in figure 2 and then repeated the above procedure. The importance factors of the remaining voxels were kept at the same

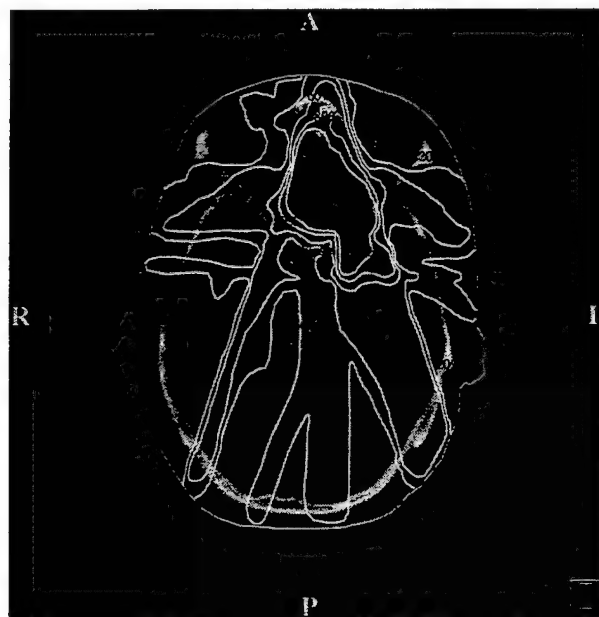


Figure 4. A transverse slice showing the anatomical structures delineated for the nasopharynx tumour and the corresponding optimized dose distribution for local importance factors of unit value. The doses are normalized to the mean target value.

values that were used in the previous optimization (i.e. 1.35 for the voxels labelled by the plain dots and 1.0 for the voxels that are not labelled by circles or dots). The DVHs of the new plan corresponding to this distribution of the importance factors are shown as dotted lines in figure 3. The maximum dose of the CSV drops by 20 dose units compared to the initial optimization result. The increased importance values for the CSV voxels lead to an increased dose inhomogeneity within the target. This is not surprising because of the trade-off nature of the problem. The important point here is that, when local importance factors are used, the trade-off is accentuated at a regional level and our control over the shapes of the final DVHs is greatly enhanced.

3.2. The nasopharynx tumour case

The second test case was a nasopharynx tumour. The prescription dose to the tumour was 60 Gy, and the tolerance doses were 10 Gy for the eyes, 35 Gy for the brain stem and 45 Gy for the optic chiasm, respectively. Nine beams were placed at the following angular positions: 10°, 80°, 120°, 160°, 180°, 200°, 240°, 270° and 355°. The size of the pencil beam defined at the isocenter was 0.5 cm.

A reasonable plan was obtained with the following set of structure-specific importance factors: 0.40 for the tumour, 0.32 for the right eye, 0.10 for the left eye, 0.04 for the brain stem 0.04 for the optic chiasm and 0.1 for the normal tissue, respectively. Figure 4 shows the resulting isodose distribution in a transverse slice of the skull. In this case, we found that the 95% isodose line covers acceptably well the PTV. The DVHs of the optimized plan are plotted with plain lines in figure 5.

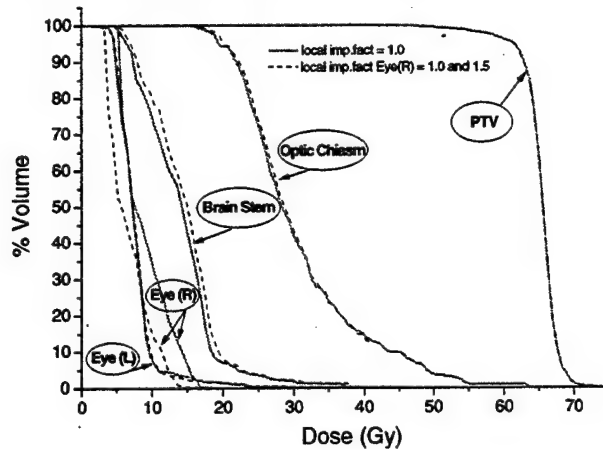


Figure 5. DVHs for plans optimized with unit value local importance factors (the plain lines) versus optimized using higher value of local importance factors for the right eye (the dashed lines).

In a first instance we were concerned with lowering the dose to the right eye. We located the voxels with a dose exceeding the 10 Gy tolerance level and increased their importance from 1.0 to 1.5. The beam profile optimization was performed again and the resulting DVHs are shown with dashed lines in figure 5. The results show no degradation of the target coverage and a significant reduction of the dose to the right eye accompanied by a reduction in the maximum dose by almost 5 Gy. While the DVH curve for the other eye remains the same, an insignificant degradation is observed for the brain stem and optic chiasm.

As an exercise, we further tried to increase the values of the local importance factors to 1.5 for those voxels receiving a dose higher than 10 Gy in both eyes. The dashed curves in figure 6 represent the corresponding DVHs of various structures after dose optimization. As in the previous case, the dose-volume characteristics of both eyes are improved significantly. Interestingly, the dose homogeneity in the PTV is also improved slightly. Only the dose to the optic chiasm unambiguously deteriorates in this case.

In order to understand the planning tool more extensively, we tested whether any improvement could be achieved in the optic chiasm dose after the significant improvement was made in sparing the two eyes. From figure 6 it is seen that 15% of the optic chiasm receives a dose greater than 40 Gy. We wondered whether this volume could be lowered and whether the maximum optic chiasm dose could be reduced, and if yes, at what cost. For this purpose, we found the overdosed voxels in the optic chiasm and assigned them with a new importance value of 1.4. The importance factor distributions in both eyes and other structures were kept the same as in the previous case. The DVHs corresponding to this new arrangement of the importance factors are plotted in figure 7. While the optic chiasm DVH was significantly improved, the dose inhomogeneity within the tumour increased. In addition, the level of improvement in the eyes resulted from the last trial has decreased, even though it did not go back to the original plan shown as the plain curves in figure 7. This result suggests that the order in which the critical structures are considered in the dose-tuning process may play a role. If a critical structure is closely located to the target, the boundary region is usually in the overlap area of several beamlets coming from different beams. In general, the dose in this type of structures is more strongly correlated with that of other structures. It is also instructive

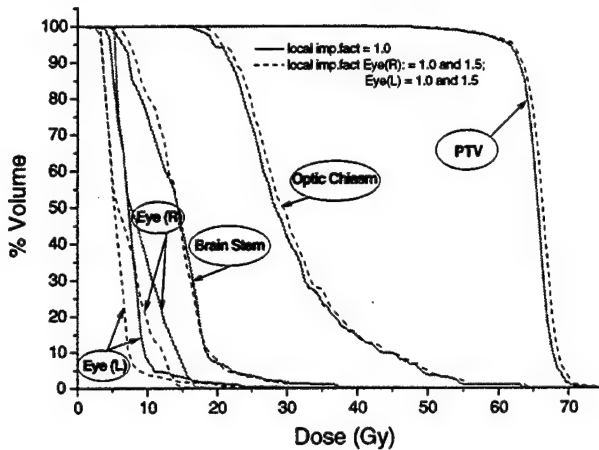


Figure 6. DVHs for plans optimized with unit value local importance factors (the plain lines) versus optimized using higher value of local importance factors for both the eye structures (the dashed lines).

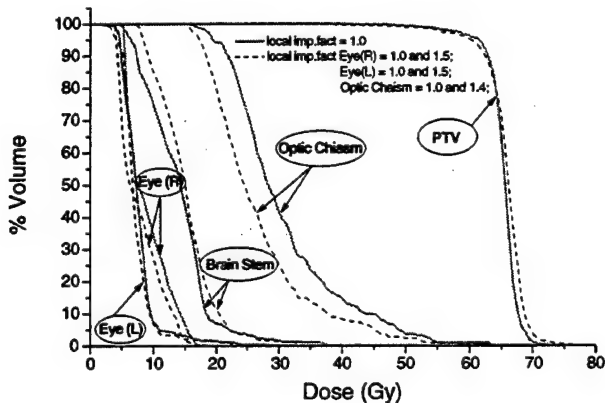


Figure 7. DVHs for plans optimized with unit value local importance factors (the plain lines) versus optimized using higher value of local importance factors for both the eye structures and the optic chiasm (the dashed lines).

to point out that the whole dose-volume curve of the optic chiasm was improved in figure 7 instead of only the dose bins above 40 Gy. This revealed the role of correlation between different voxels within the same structure, which is most pronounced for a structure like optic chiasm because of its small volume.

The above planning procedure is fairly straightforward. After an IMRT plan is obtained using a conventional inverse planning procedure, the system is already in the vicinity of the optimal solution. The plan at this point is usually at a stage of 'mostly satisfactory' except that one or a few sub-volumes in the target or some sensitive structures are overdosed/underdosed. The focus of using local importance factors is directed towards meeting the clinical goals for these disadvantaged regions. Because of the strong correspondence between the regional

dose and the local importance factor, we found that one or two trials are typically sufficient to improve the DVH shape of a structure and to come up with a better compromise solution. Even when the DVHs of the multiple structures need to be modified, we found that the process is not unmanageable, at least not as bad as it appears. One could proceed to change the local importance factors of different structures sequentially or simultaneously. Given the rapid advancement in computer hardware, the computing here should be made easier and easier with years to come.

4. Conclusions

An interactive DVH-based optimization tool for IMRT treatment planning is presented. The most important feature of the new planning environment is the introduction of voxel-dependent importance factors as an effective means for modifying the local doses and for adaptive planning. The system allows us to differentially fine-tune the shapes of the DVH curves of various structures according to clinical requirements and provides an invaluable tool to 'paint' and 'sculpt' IMRT dose. This new mechanism has been implemented in an existing inverse planning system. Application of the new planning technique to two test cases showed that the tool can significantly improve the plans obtained using currently available inverse planning techniques and affords a flexible means to meet diverse clinical needs. Upon clinical implementation we anticipate that the tool will have widespread application and make it possible to maximally utilize the efficacy of the IMRT technique.

Finally we mention that using variable local importance factors is not the only way to accomplish a voxel-dependent penalty scheme. Similar control could also be achieved by using a 'tunable' voxel-dependent objective function. This work is still in progress and will be reported elsewhere.

Acknowledgments

This work was supported in part by a Research Scholar Grant Award from the American Cancer Society and research grants from the Whitaker Foundation, the US Department of Defense and the Information Technology Systems and Services of Stanford University.

References

- Bortfeld T 1999 Optimized planning using physical objectives and constraints *Semin. Radiat. Oncol.* **9** 20–34
- Bortfeld T, Burkhardt J, Boesecke R and Schlegel W 1990 Methods of image reconstruction from projections applied to conformation radiotherapy *Phys. Med. Biol.* **35** 1423–34
- Cho P S, Lee S, Marks R J II, Oh S, Sutlief S G and Phillips M H 1998 Optimization of intensity modulated beams with volume constraints using two methods: cost function minimization and projections onto convex sets *Med. Phys.* **25** 435–43
- Cotrutz C, Kappas C, Theodorakos Y, Makris C and Mohan R 1998 Development in a Windows environment of a radiation treatment planning system for personal computers *Comput. Methods Progr. Biomed.* **56** 261–72
- Cotrutz C, Lahanas M, Kappas C and Baltas D 2001 A multiobjective gradient-based dose optimization algorithm for external beam conformal radiotherapy *Phys. Med. Biol.* **46** 2161–75
- Gopal R and Stark-Schall G 2001 Plan space: representation of treatment plans in multidimensional space *Med. Phys.* **28** 1227
- Mageras G S and Mohan R 1993 Application of fast simulated annealing to optimization of conformal radiation treatments *Med. Phys.* **20** 639–47
- McGary J E 2001 Corvus optimization algorithm and IMRT planning process *3-D Conformal and IMRT: Physics & Clinical Applications* ed J A Purdy, J R Paita, E B Butler and C A Perez (Madison, WI: Advanced Medical Publishing) pp 263–75

- Morrill S M, Lam K S, Lane R G, Langer M and Rosen I I 1995 Very fast simulated reannealing in radiation therapy treatment plan optimization *Int. J. Radiat. Oncol. Biol. Phys.* **31** 179–88
- Olivera G H, Shepard D M, Reckwerdt P J, Ruchala K, Zachman J, Fitchard E E and Mackie T R 1998 Maximum likelihood as a common computational framework in tomotherapy *Phys. Med. Biol.* **43** 3277–94
- Rosen I I, Lam K S, Lane R G, Langer M and Morrill S M 1995 Comparison of simulated annealing algorithms for conformal therapy treatment planning *Int. J. Radiat. Oncol. Biol. Phys.* **33** 1091–9
- Spiro S V and Chui C S 1998 A gradient inverse planning algorithm with dose–volume constraints *Med. Phys.* **25** 321–33
- Togane D, Hamilton R J, Boyer A L and Xing L 1998 Dose volume histogram based optimization for intensity modulated radiation therapy *Med. Phys.* **25** A118
- Webb S 1989 Optimization of conformal radiotherapy dose distributions by simulated annealing *Phys. Med. Biol.* **34** 1349–70 (Erratum: 1990 *Phys. Med. Biol.* **35** 297)
- Wu Q and Mohan R 2000 Algorithms and functionality of an intensity modulated radiotherapy optimization system *Med. Phys.* **27** 701–11
- Wu X and Zhu Y 2001 An optimization method for importance factors and beam weights based genetic algorithms for radiotherapy treatment planning *Phys. Med. Biol.* **46** 1085–99
- Xing L and Chen G T Y 1996 Iterative algorithms for inverse treatment planning *Phys. Med. Biol.* **41** 2107–23
- Xing L, Li J G, Donaldson S, Le Q T and Boyer A L 1999a Optimization of importance factors in inverse planning *Phys. Med. Biol.* **44** 2525–36
- Xing L, Li J G, Pugachev A, Le Q T and Boyer A L 1999b Estimation theory and model parameter selection for therapeutic treatment plan optimization *Med. Phys.* **26** 2348–58

Therapeutic treatment plan optimization with probability density-based dose prescription

Jun Lian, Cristian Cotrutz, and Lei Xing^{a)}

Department of Radiation Oncology, Stanford University School of Medicine, 300 Pasteur Drive, Stanford, California 94305-5304

(Received 18 September 2002; accepted for publication 29 January 2003; published 26 March 2003)

The dose optimization in inverse planning is realized under the guidance of an objective function. The prescription doses in a conventional approach are usually rigid values, defining in most instances an ill-conditioned optimization problem. In this work, we propose a more general dose optimization scheme based on a statistical formalism [Xing *et al.*, Med. Phys. 21, 2348–2358 (1999)]. Instead of a rigid dose, the prescription to a structure is specified by a preference function, which describes the user's preference over other doses in case the most desired dose is not attainable. The variation range of the prescription dose and the shape of the preference function are predesigned by the user based on prior clinical experience. Consequently, during the iterative optimization process, the prescription dose is allowed to deviate, with a certain preference level, from the most desired dose. By not restricting the prescription dose to a fixed value, the optimization problem becomes less ill-defined. The conventional inverse planning algorithm represents a special case of the new formalism. An iterative dose optimization algorithm is used to optimize the system. The performance of the proposed technique is systematically studied using a hypothetical C-shaped tumor with an abutting circular critical structure and a prostate case. It is shown that the final dose distribution can be manipulated flexibly by tuning the shape of the preference function and that using a preference function can lead to optimized dose distributions in accordance with the planner's specification. The proposed framework offers an effective mechanism to formalize the planner's priorities over different possible clinical scenarios and incorporate them into dose optimization. The enhanced control over the final plan may greatly facilitate the IMRT treatment planning process. © 2003 American Association of Physicists in Medicine.

[DOI: 10.1118/1.1561622]

Key words: IMRT, dose optimization, inverse planning, statistical analysis

I. INTRODUCTION

Inverse planning is used in intensity modulated radiation therapy (IMRT) for deriving the optimal beam intensity profiles that produce the best possible dose distribution for a given patient.^{1–16} The dose optimization process is usually performed under the guidance of an objective function, which measures the “distance” between the physical and the prescribed dose distributions.^{8,17–20} One of the common objective functions for inverse planning is the quadratic objective function,^{3,21,22} with importance factors assigned to the involved structures to prioritize their relative importance during the optimization process.^{23–25} The objective function is defined as a global quantity based on general physical considerations. When the desired dose distribution is not attainable during optimization, a compromise solution is found using the algorithm's ranking. The compromise dose distribution, however, is often not what the planner wants and multiple trial and errors are needed to obtain a clinically acceptable IMRT plan.

A main problem of the existing IMRT planning algorithms is the lack of an effective mechanism for incorporating prior knowledge into inverse planning.³¹ In the past, there have been many attempts to introduce soft/hard constraints to steer the dose optimization process toward the

clinically desired solutions.^{26–30,36} However, the constraints are introduced in an *ad hoc* fashion and do not fully utilize the partial information available from years of clinical investigations because of their phenomenological nature. On a more fundamental level, the constraints are imposed *a posteriori* and controls the optimization passively. Our purpose in this paper is to develop a statistical analysis-based inverse planning formalism to more effectively utilize the prior knowledge. Instead of specifying a rigid prescription dose, the formalism allows us to use a dose distribution as the input prescription to the system, providing a natural way for us to take advantage of the existing information of the system variables and promising to make the optimization outcome more predictable and controllable.

In the next section we present the details of the new dose optimization algorithm after a brief introduction of the concept of preference function. The formalism is then applied to a synthetic phantom case with C-shaped tumor target and a prostate case. Our results indicate that the statistical analysis-based formalism provides a general framework for inverse planning and is capable of producing conformal IMRT dose distribution. Coupled with the capability of the preference function in customizing/formalizing our prior clinical knowledge, it is expected that the proposed technique will have a

broad implication and potential to greatly facilitate an IMRT planning process.

II. MATERIAL AND METHODS

A. Theoretical background

In a vectorial form, the dose to the points in the treatment region depend upon the beamlet weights w as

$$\mathbf{D}_c = \mathbf{d} \cdot \mathbf{w}, \quad (1)$$

where \mathbf{d} represents the dose deposition matrix, expressing the dose deposited to any point in the patient when irradiated with a unit weight beamlet vector. The inverse problem as posed for IMRT is to find a set of beamlet weights that produce the optimal dose distribution by minimizing a therapeutic objective function. The most used objective function has a quadratic form and reads³² as

$$F = \frac{1}{N} \sum_{n=1}^N r_\sigma [D_c(n) - D_p(n)]^2, \quad (2)$$

where N is the total number of voxels, r_σ is the importance factor that controls the relative importance of a structure σ , and D_p and D_c are prescribed and calculated doses, respectively.

In inverse planning algorithm based on the quadratic objective function [Eq. (2)], the dose prescription to the target or sensitive structure takes a rigid value. The minimization of the objective function is realized by various algorithms like simulated annealing, gradient methods, etc.^{17,26,32,33} Independent of the used dose optimization algorithms, we will call these methods throughout the text conventional IMRT optimization procedures. The problem is usually ill-posed and may lead to negative fluence unless hard constraints are introduced.³ Practically, it is not uncommon that the plans computed by what are called optimization systems are not consistent with the expectation of the planner and that several trial-and-error adjustments of the system parameters might be required to achieve a clinically acceptable plan. Given a patient, the obtained plan can vary widely from one planer to the next, even within a department. In the following we describe a more adaptable and "intelligent" statistical inverse planning formalism based on the concept of a preference function to better deal with the dilemma.

B. Preference function

In a recent paper, Xing *et al.*³¹ introduced the concept of preference function to weaken the rigid dose prescription commonly seen in the existing inverse planning algorithms. Its role is to allow a dose distribution to be considered instead of just a single value, and to quantify the degree of our willingness to accept a prescription dose D_p in that range. The preference function can be constructed heuristically from clinical considerations.³¹ The defined preference function states that the most favorable prescription dose for a voxel n is $D_p(n)$ and that a different prescription dose is also acceptable, but with a smaller preference level. For illustration, in Fig. 1 we show a sketch of the preference functions

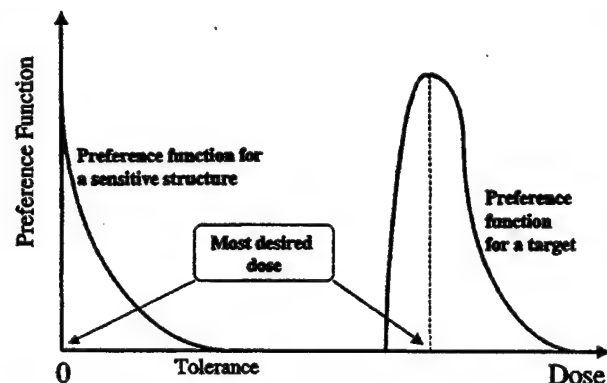


FIG. 1. A sketch of preference functions for a target and a sensitive structure.

for a target and sensitive structure. The most desirable dose for a sensitive structure should generally be set to zero. The conventional prescription scheme represents a special case of the general approach proposed here with the step function form of the preference function. That is,

$$P_n(D_p) = \begin{cases} 1, & \text{if } D_p = D_p^0, \\ 0, & \text{if } D_p \neq D_p^0. \end{cases} \quad (3)$$

To give another example, we write down the Gaussian preference function for a voxel n

$$P_n(D_p) = P_{0n} \exp\{-\gamma_n [D_p(n) - D_p^0(n)]^2\}, \quad (4)$$

where P_{0n} is a normalization constant and γ_n represents the Gaussian parameter. For a system comprising N voxels, the total preference is given by a product of the preference functions of all voxels:

$$P = \prod_n P_n(D_p) = \prod_n P_{0n} \exp\{-\gamma_n [D_p(n) - D_p^0(n)]^2\}. \quad (5)$$

When a maximum likelihood estimator is used, it has been demonstrated that the maximization of the logarithmic function of P or minimization of $\ln(1/P)$, is equivalent to the minimization of the conventional quadratic objective function.^{31,34} In this case, the Gaussian parameter γ_n in Eq. (5), which commands the "spread" of the Gaussian around D_p^0 , is equivalent to the importance factor that controls the relative importance of the structure and parametrizes the clinical trade-off strategy.

C. Probability density-based dose prescription and inverse planning

The objective function defined in Eq. (2) uses a rigid dose, D_p . Since in most instances an ideal dose prescription is not physically attainable, we resort to an expansion of the prescription dose, over a certain interval. That is, we allow the prescription dose to take a "probabilistic" distribution around the most desired dose as specified by the preference function. For computational purpose, we divide the permis-

sible prescription dose into a number of discretized values, $\{D_p^i\}$, where i is the index of a possible prescription dose and $i=0$ represents the most desirable dose. The preference distribution prescription is usually normalized to unity.

In order to utilize the probability information characterized by the preference function, we formulate the conventional dose optimization into a statistical analysis problem. To proceed, let us take the quadratic objective function as an example. We rewrite the traditional quadratic objective function (2) into

$$f(D_c) = f_0 \prod_n \exp\{-r_o [D_c(n) - D_p(n)]^2\}. \quad (6)$$

where f_0 is a normalization constant. For a given prescribed dose distribution, Eq. (6) measures the goodness of a calculated dose distribution using an exponential scale, as compared with Eq. (2). Equation (6) can be interpreted as a conditional probability and formally rewritten as

$$f(D_c|D_p) = f_0 \prod_n \exp\{-r_o [D_c(n) - D_p(n)]^2\}. \quad (7)$$

When the prescription dose is no longer a rigid dose, it is conceivable that there are a number of optimum solutions, each corresponding to a sample of prescription doses. Mathematically, we now have two "probability" distribution functions. One is the preference function that characterizes our *a priori* preference over different prescription doses $P(D_p)$, and the other is Eq. (6) that ranks a calculated dose for a given prescribed dose, D_p . Our task is to find the solution that is statistically optimal with consideration of the variable prescription. For this purpose, we introduce the "joint probability" of the two "probability" distributions defined by Eqs. (5) and (7). The function at a voxel n can be written as

$$P_n(D_c) = \sum_i f_n(D_c|D_p^i) P_n(D_p^i). \quad (8)$$

The total preference function of the system is given by

$$P = \prod_n P_n(D_c). \quad (9)$$

D. Optimization strategy

Having the rigid prescription D_p in (2) replaced by a range of prescribed doses, $\{D_p^i\}$, the total preference function is now given by Eqs. (8) and (9). For convenience, we define objective function $F = \ln(1/P)$ and derive the optimal solution by minimizing the F , which is equivalent to maximize the preference function (9). The objective function now reads as

$$F = \ln(1/P)$$

$$= -\ln \prod_n P_n = -\sum_n \ln \sum_i f_n(D_c|D_p^i) \cdot P_n(D_p^i). \quad (10)$$

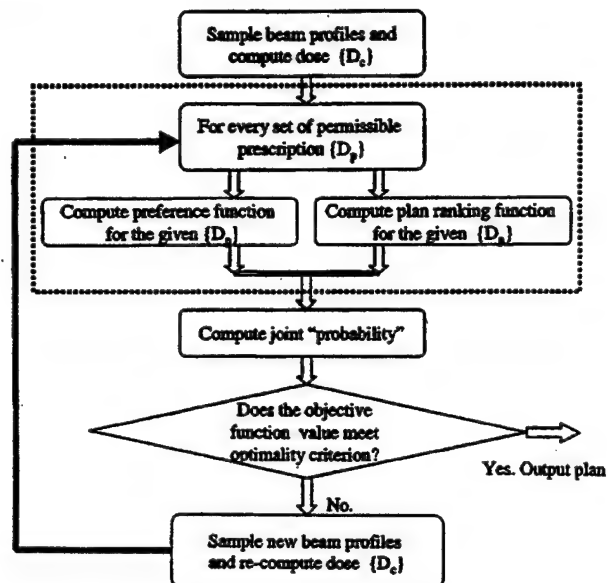


FIG. 2. A flow chart of the optimization process with the inclusion of pre-designed preference function information.

Note that the conventional quadratic objective function is a special case of the above general objective function when the prescription takes a rigid value for each structure, as described by Eq. (3).

The optimization process is schematically shown in a flow chart (Fig. 2). The beam profile is determined by minimizing the above objective function using a conjugate gradient optimization algorithm. The details of the algorithm have been discussed in a previous paper.³³ Briefly, the calculation consists of three major steps: (i) assume an initial intensity profile for each incident beam; (ii) compute the "joint probability" given by Eqs. (8) and (9). For this purpose, we need to sample all combinations of the prescription doses of different structures and compute the function given in Eqs. (5) and (7) for each of these combinations; and (iii) optimization of the multidimensional "joint probability" function. The second step is fairly computationally intensive because we must compute the two functions for every sampling of the prescription doses. In our calculation, we typically assign four to seven discrete possible prescription doses for each structure. A finer discretization of the prescription dose did not seem lead to further improvement but would greatly increase the computation time. All calculations presented here are performed on a Personal Computer (PC) with an Intel Pentium® III 1-GHz-CPU (Intel Corporation, Sunnyvale, CA). The computation time needed to obtain an optimal solution for a given set of system parameters (including beam configuration, preference function, importance factors) is typically less than ten minutes.

III. RESULTS AND DISCUSSION

A. A synthetic phantom case with a C-shaped tumor

To systematically study the performance of the statistical analysis-based inverse planning algorithm, we applied the

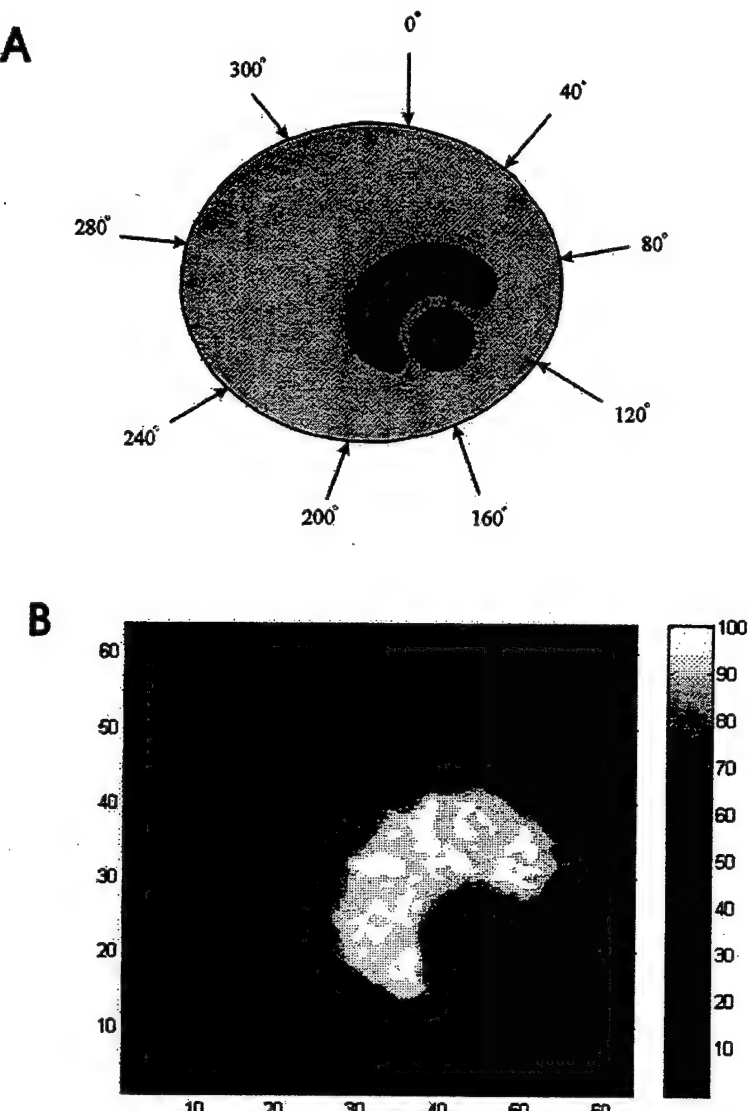


FIG. 3. (a) A sketch of a phantom case with a C-shaped tumor. The dose prescription is set 100 (arbitrary units) to the PTV and 0 to the circular OAR and normal tissue. (b) Dose distribution obtained using the "probabilistic" prescription shown in Fig. 4(a).

technique to a C-shaped tumor case [Fig. 3(a)] with a variety of preference functions and compared the results with that obtained using the conventional approach with a fixed dose prescription. Nine equally spaced 6 MV beams beginning at 0° (IEC) were used in this study. The prescription doses to the PTV and OAR in the conventional IMRT plans were 100 and 0 (the dose is in an arbitrary unit), respectively.

We first assigned three sets of symmetrical Gaussian distributions to the target while keeping the prescription to the sensitive structure at zero (Fig. 4). The Gaussian preference functions were represented by three sets of preference levels at seven discrete values (80, 87, 94, 100, 106, 113, and 120). The center of the Gaussian functions was set at 100. The preference levels for the seven doses are shown in Fig. 4 for each of the three situations studied here. The transverse dose distribution obtained using the statistical inverse planning formalism for the case shown in Fig. 4(a) is plotted in Fig. 3(b). As expected, target inhomogeneity increases as we

loosen the constraint of the rigid dose prescription. This can be better demonstrated by using the differential DVH for each situation. As seen from the differential DVH plots (the right column of Fig. 4), the width of the differential function gradually increases, from 26.72, 28.59–30.39, as we gradually increase the acceptance levels for the doses different from the most desirable dose (100). This series of calculations provides us with preliminary evidence that the final dose distribution can be steered by varying the preference function.

Next, we constructed six sets of asymmetric preference functions for the target (Fig. 5 and Fig. 6). When higher preference levels were assigned to the doses higher than 100, we found that the target DVH is shifted to the high dose region. Interestingly, even when an extremely low preference (for instance, 1%) was assigned to the doses less than 100 [Fig. 5(b)], a noticeable underdosing relative to the conventional result was resulted. A similar phenomenon can also be

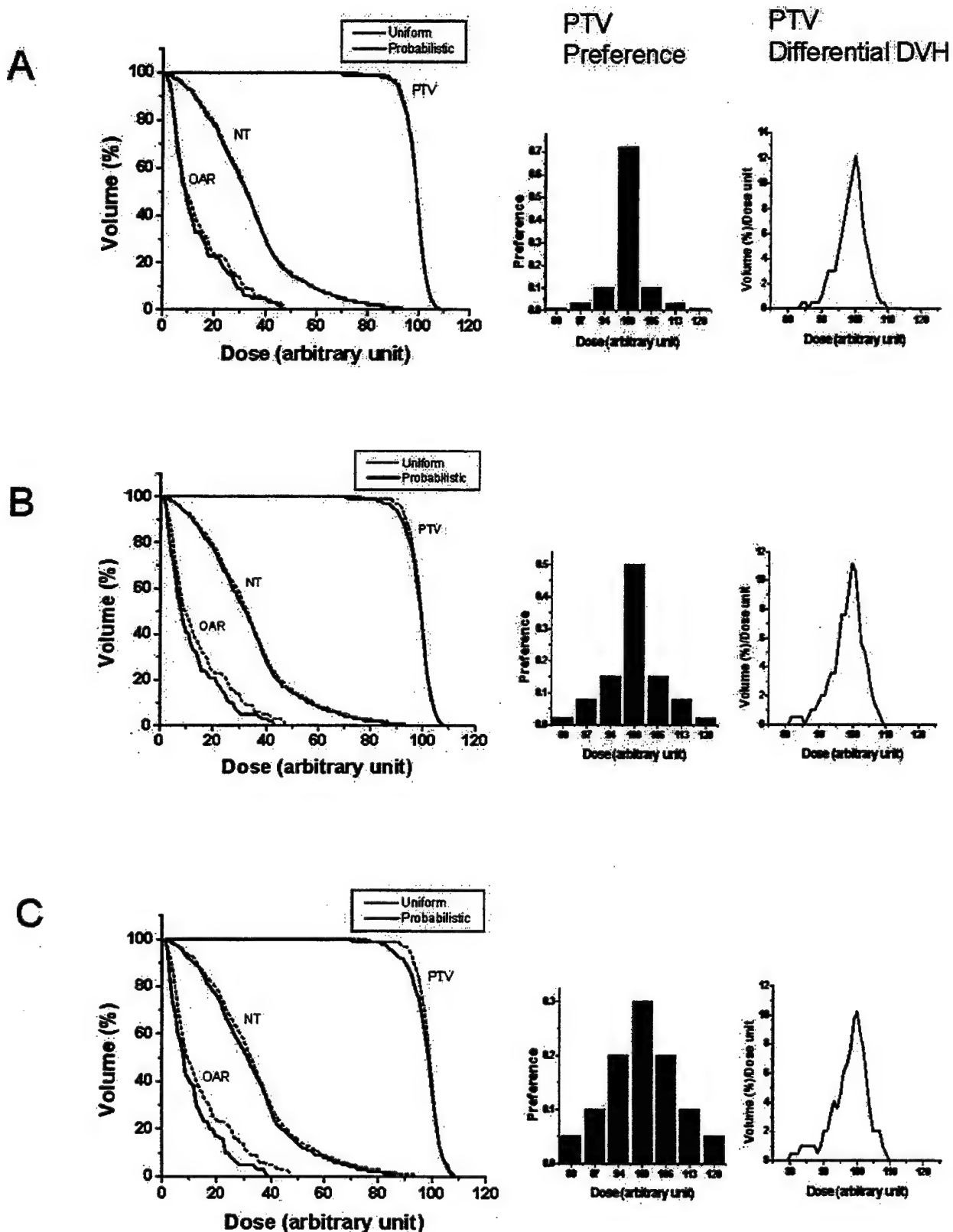


FIG. 4. DVHs of the PTV, OAR, and normal tissue (NT) obtained using the conventional rigid dose prescription (dotted line) and the "probabilistic" prescription (solid line). The Gaussian preference functions with different variances are shown in the middle panel. The right panel shows the differential DVHs for the target.

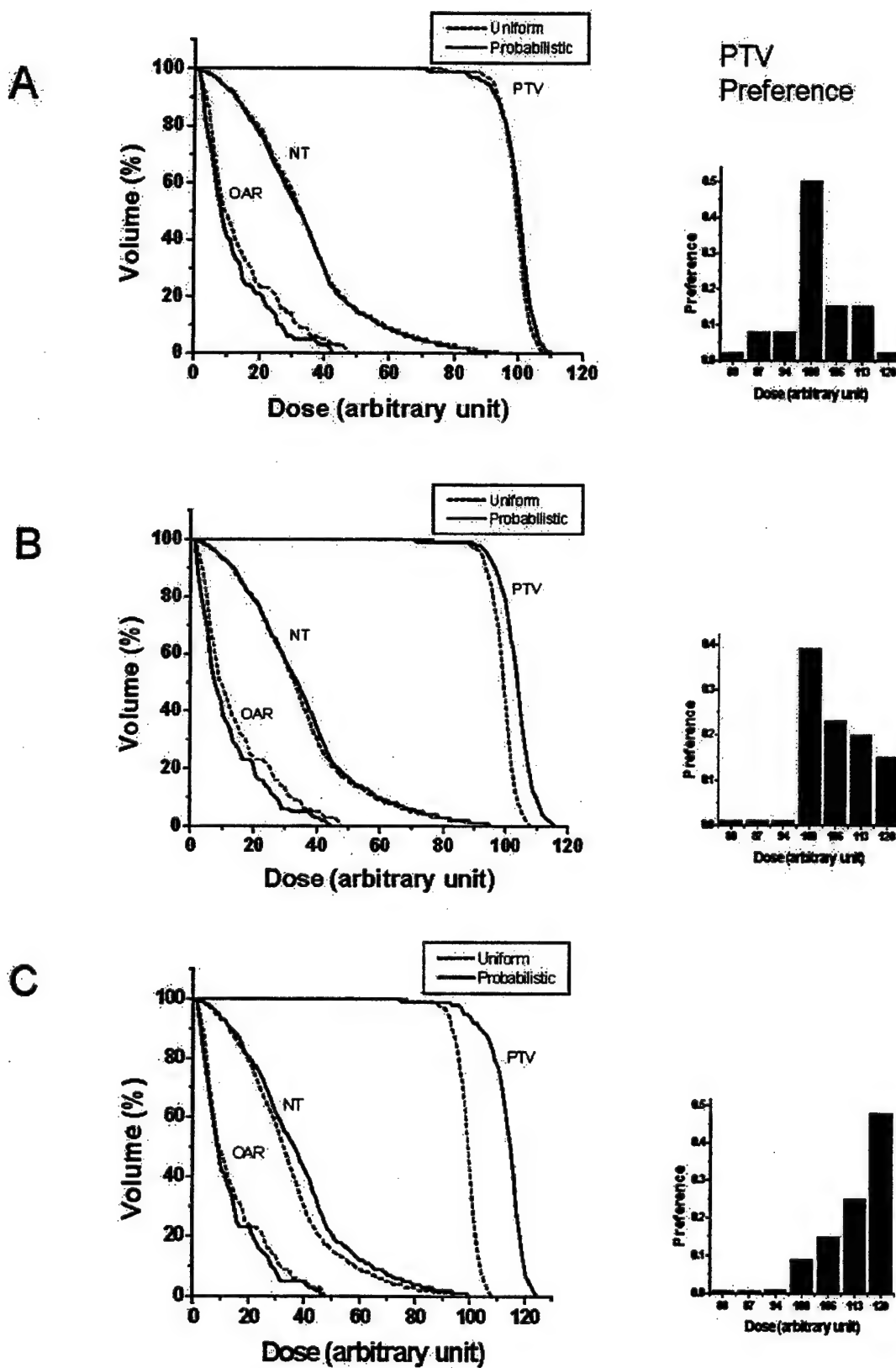


FIG. 5. DVHs of the PTV, OAR, and normal tissue (NT) obtained with the conventional rigid dose prescription (dotted line) and with the "probabilistic" prescription (solid line). The bar charts on right show the asymmetrical preference functions.

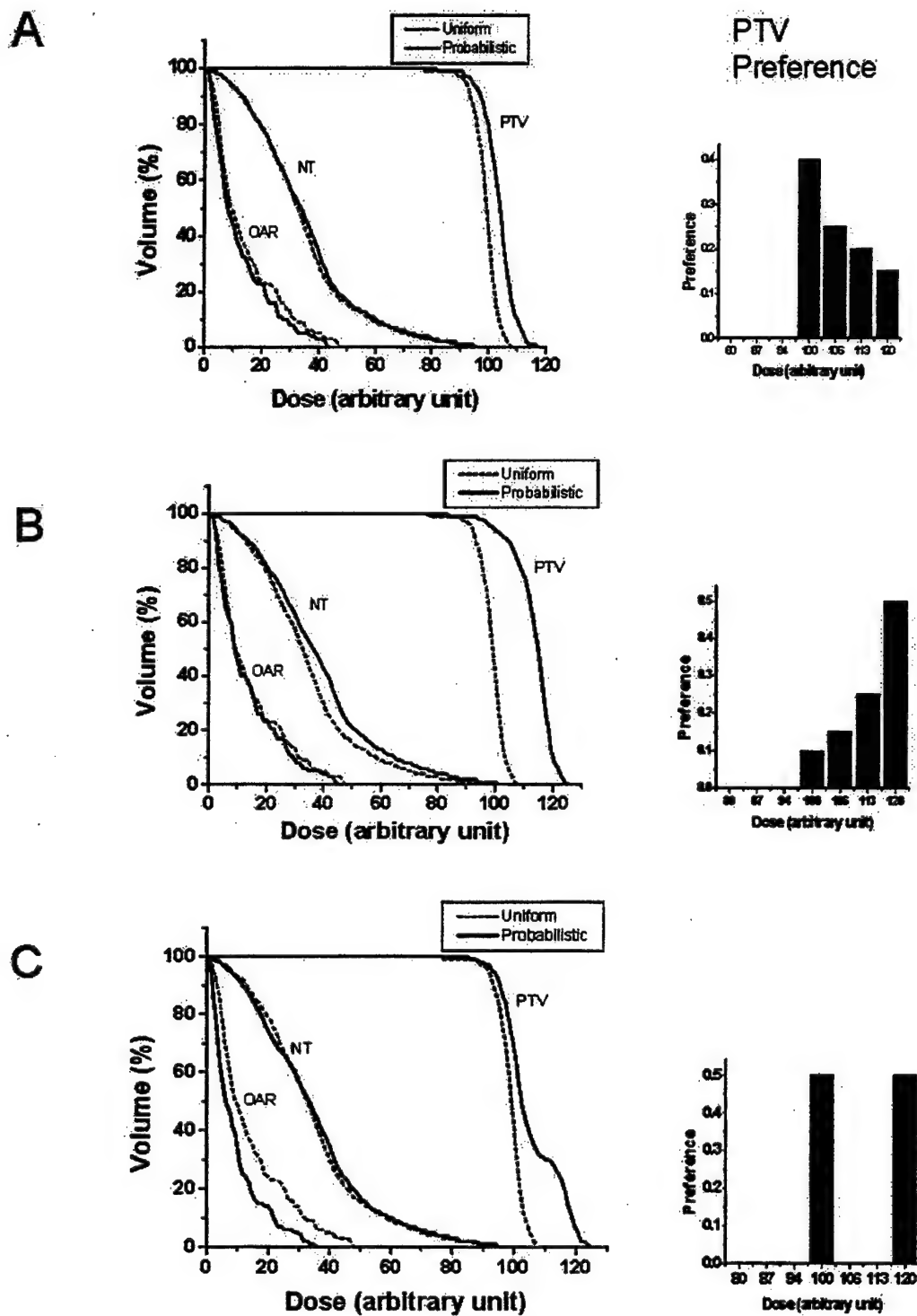


FIG. 6. DVHs of the PTV, OAR, and normal tissue (NT) obtained using the conventional rigid dose prescription (dotted line) and the new statistical inverse planning method for a variety of preference functions shown on the right panel (solid line).

seen from the result shown in Fig. 5(c), where only 0.5%, 0.7%, and 1% of preference levels were assigned to the dose values of 80, 87, and 94. This observation seems to indicate that the influence of the assigned preference level at a low

dose plays an important role. In Fig. 6, we set the preference levels for the doses less than 100 to be 0 and only assign nonzero preference levels for the doses higher than 100. It is seen that in all these situations the minimum target dose is

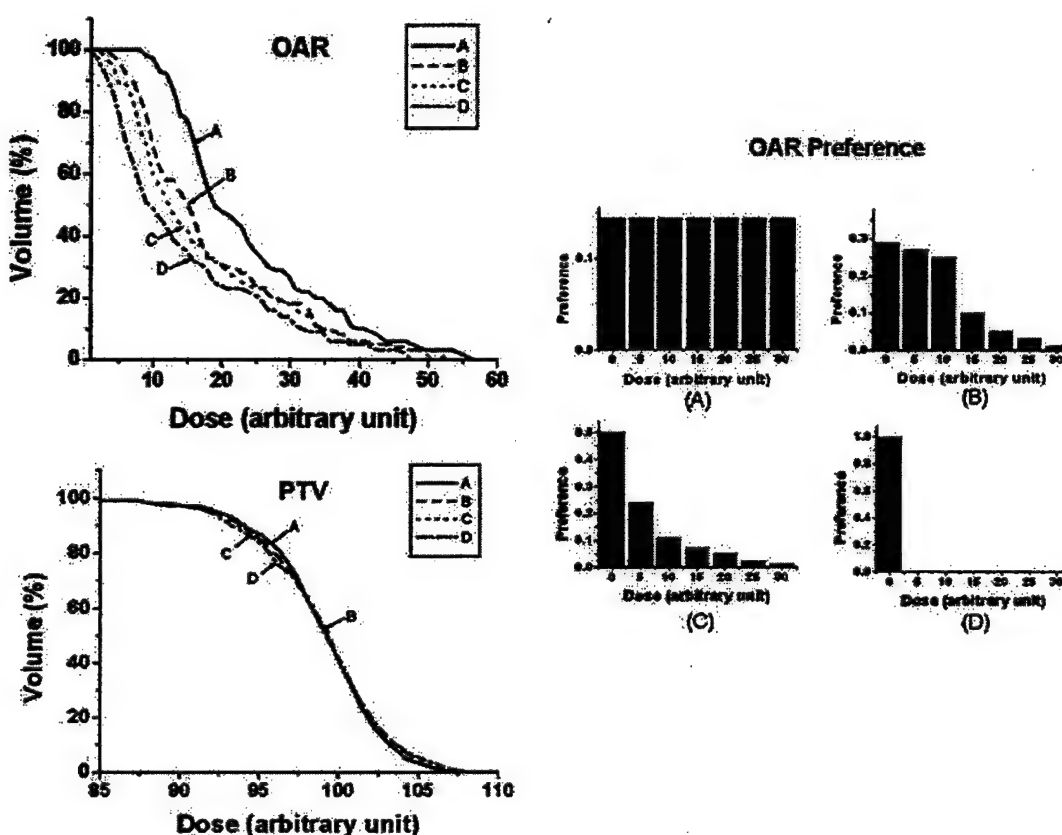


FIG. 7. DVHs of the OAR and PTV when the prescription dose to the OAR is modeled by (a) a uniform distribution, (b) a bell-shaped function, (c) an exponential decay function, and (d) a rigid value.

higher than that of the conventional plan. As a result of our preference over higher doses, the fractional volume at any dose less than 100 is improved in comparison to that of the conventional IMRT plan. In Fig. 6(c), we further exemplify the statistical analysis based inverse planning method by simplifying our preference to two doses (100 and 120), each with 50% preference levels. In this situation, in addition to that the doses in the target are shifted toward higher values, the target DVH exhibits a stepwise behavior: a plateau appears at around 110, which is in the middle of the two prescribed doses.

It is interesting to point out that the OAR sparing is improved as compared with the conventional IMRT plan in most cases studied in Figs. 5 and 6, even when the target dose is escalated. That is, the DVH of the OAR is not always shifted toward higher doses, as would occur if a higher dose is prescribed in a conventional inverse planning system. Instead, the dose to the OAR remained unchanged or even lowered in some cases. A reasonable explanation for the observed phenomenon is that, when a rigid dose prescription is replaced by a range of doses, the system is given more freedom for self-adjustment. As a benefit, a solution with a higher integral target dose and reduced OAR dose can be obtained from the expanded solution space.

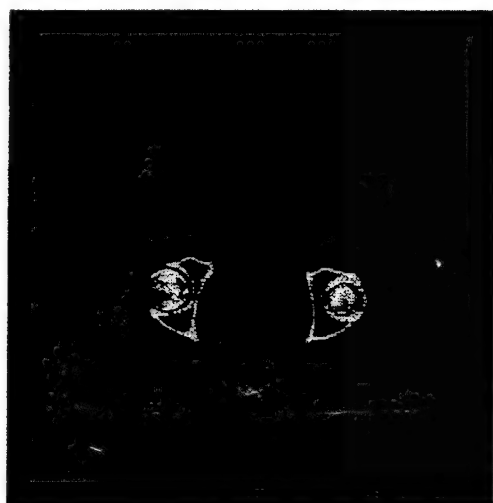
We have also studied the behavior of the system when a range of doses is prescribed to the OAR. In this investigation, we kept the target prescription to 100 and allowed the

OAR dose to take seven values: 0, 5, 10, 15, 20, 25, and 30 with the acceptance levels sampled from three different types of prescription distribution: uniform [Fig. 7(a)], bell-shaped [Fig. 7(b)], and exponential [Fig. 7(c)] functions. Figure 7(d) represents the conventional case with zero prescription to the OAR. The corresponding OAR and PTV DVHs are plotted in the left panel of Fig. 7. When the preference was uniformly sampled in the dose interval from 0 to 30, the resultant dose to the OAR was found to be the highest, as indicated by curve A in Fig. 7. The best target dose coverage was achieved in this situation. If the preference to a high dose was reduced, the DVH was gradually shifted to the low dose direction (curves B and C). It is not surprising that the best OAR sparing was achieved in the conventional case where a zero dose was prescribed to the OAR. The target dose homogeneity was slightly improved in all cases when a probabilistic prescription was given to the OAR. Similar to that described in the last paragraph, the results clearly demonstrate that the "probabilistic" prescription allows us to control the OAR dose distribution and indicate the usefulness of the statistic analysis approach.

B. The prostate case

The new inverse planning algorithm was also applied to study a six filed IMRT prostate treatment [Fig. 8(a)]. Four plans with different types of preference functions were gen-

A



B

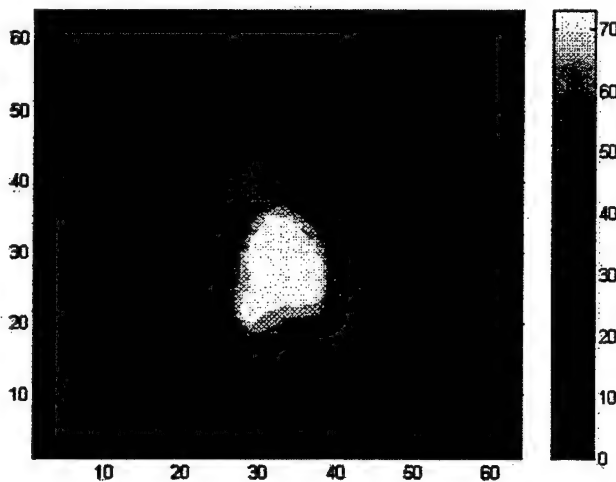


FIG. 8. A transverse slice showing the anatomical structures delineated for the prostate tumor (a) and (b) the dose distribution obtained using the "probabilistic" prescription shown in Fig. 9(a).

erated. In addition, a plan with rigid prescription (74 Gy on the target, 60 Gy on the bladder, and 40 Gy on the rectum) is also generated. The DVHs for this plan is plotted as dotted lines in Fig. 9 and is used as a reference for comparison. In all treatment plans, six beams were placed at the following angular positions: 0° , 55° , 135° , 180° , 225° , and 305° . The size of the pencil beam defined at the isocenter was 0.5 cm.

The DVH and preference functions for four different plans are schematically shown in Fig. 9. In the study shown in Figs. 9(a)–9(b), we kept the preference function of the sensitive structures unchanged and only varied the form of the preference function of the target. In Fig. 9(a), we assumed that target could take seven discrete values (74, 76, 78, 80, 82, 84, and 86 Gy) sampled from an exponential distribution. Compared with the dotted lines, the target DVH was shifted toward the high dose direction. The dose distribution corresponding to the preference function is shown in Fig. 8(b). The target DVH was shifted even further toward

the high dose region [Fig. 9(b)] when a bell-shaped preference function was used with more emphasis on the target receiving doses at 74, 76, and 78 Gy. In both cases, doses to the rectum and bladder did not change significantly.

In Fig. 9(c) we show the DVHs when the preference function to the rectum deviates from the uniform distribution. As a result, the rectum dose was significantly lowered in all dose levels and the maximum dose was reduced from 66 to 57 Gy. Because of the proximity of the rectum to the prostate target, the maximum rectum dose was not restricted to 30 Gy, as specified in the preference function. We emphasize that the improvement in rectum and bladder sparing was achieved at cost of higher dose inhomogeneity in the prostate target. This reminds us that, in dose optimization, there is a dosimetric compromise. That is, the improvement in the dose to a structure is often accompanied by dosimetrically adverse effect(s) at other points in the same or different structures. The important point that one should note is that from the clinical point

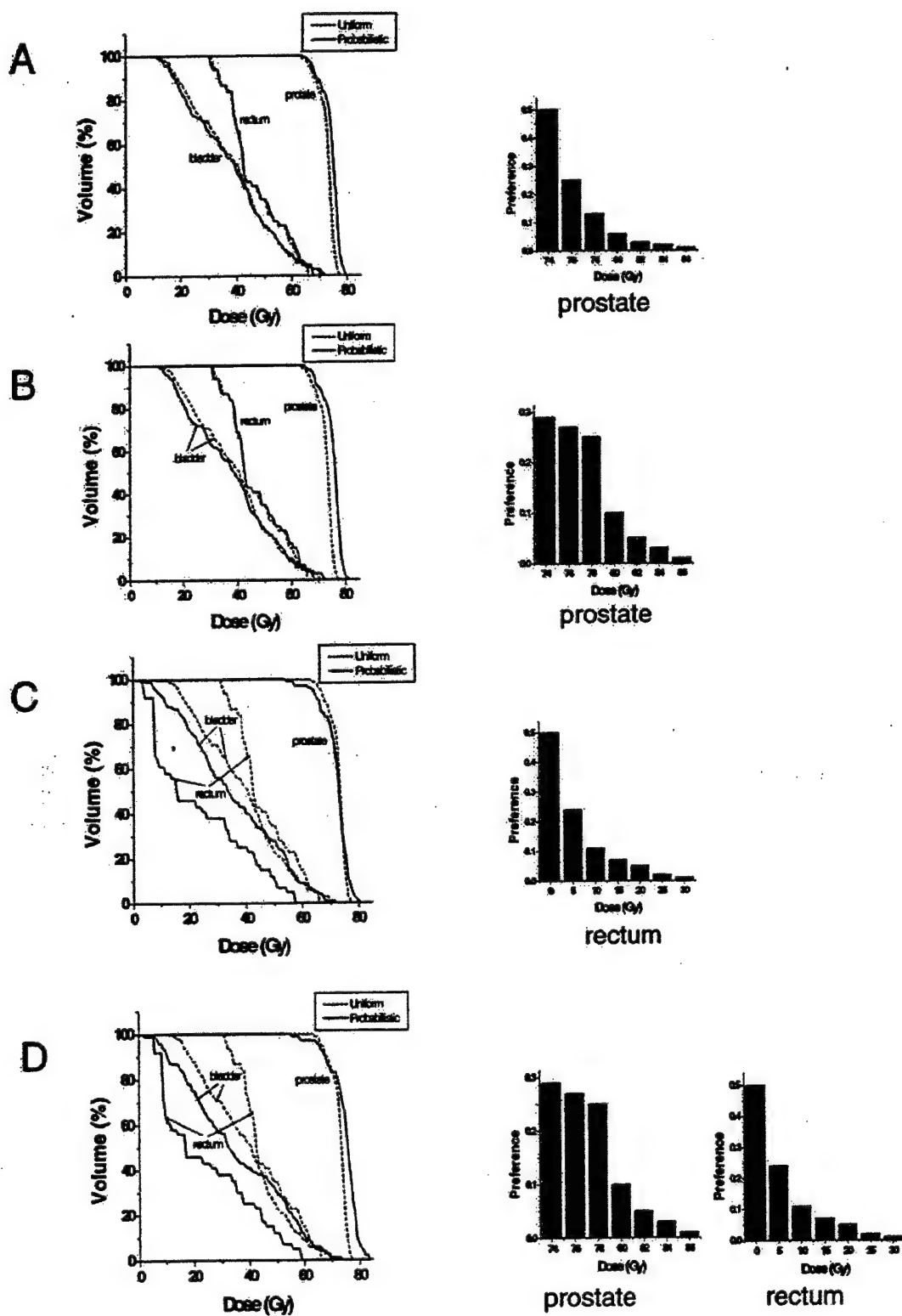


FIG. 9. A comparison of the DVHs obtained using the "probabilistic" prescription (solid line) and conventional rigid dose prescription (dotted line). The prostate and rectum prescriptions are represented on the right bar charts.

of view, some dose distributions are more acceptable than others and our goal is to find the solution that improves the plan to the largest possible extent, but with a clinically insignificant or acceptable sacrifice in OAR sparing. In order to achieve this, it is necessary to have a reasonable amount of controllability over the final dose distribution. In this sense we believe that the proposed formalism is valuable.

In addition, we varied the preference functions for both target and rectum [Fig. 9(d)]. The preference function for the rectum was the same as that in Fig. 9(c). Compared to the results shown in Fig. 9(c), we found that the target dose inhomogeneity was slightly improved.

IV. CONCLUSIONS

The formalism we derived here provides a general starting point for the study of a system with a probability density-based dose prescription. The inclusion of the partial information into the plan selection process represents a significant change from the conventional approaches. The proposed technique can be categorized into the general Bayesian decision-making theory,³¹ which is a useful tool to deal with a system with "statistical" inference. In image analysis and many other fields of science and engineering, it has proven extremely useful to include the prior knowledge of the system variables into the estimation process.³¹ The preference function proposed for radiotherapy optimization here serves as *a priori* probability density function in standard Bayesian statistics. The role of the preference function is to indicate our "bias" on the values of the system variables. By utilizing the partial information of the system variables, one can more effectively search the solution space and eliminate some unnecessary uncertainties in the optimization process.

In conclusion, we have developed a statistical analysis-based inverse planning algorithm to include preference and expert knowledge into the dose optimization process. Instead of a rigid dose prescription, the new approach allows us to prescribe a range of doses with predetermined preference levels. The technique represents a novel application of the general Bayesian decision-making theory³¹ for dealing with statistical inference and is valuable for deriving a statistically optimal solution in the presence of uncertainties in system parameters. The method was demonstrated for a system with modulating prescriptions but can be easily extended to solve many other related problems (e.g., in biologically based dose optimization, one can incorporate the uncertainties of various radiobiology parameters into the inverse planning process using the frameset developed in this work³⁵). The ill conditioning of the problem was improved because of the use of a less restrictive prescription and, as a result, new solutions that are otherwise inaccessible can be obtained naturally. It is demonstrated that the obtained solutions using the new approach strongly correlate with the preference function, suggesting that the planning process is controllable and predictable by the proposed method.

ACKNOWLEDGMENTS

We wish to thank Dr. A. Pugachev, Dr. J. G. Li, Dr. S. M. Crooks, Dr. Y. Yang, and Dr. A. L. Boyer for useful discussions. This work was partly supported by a Research Scholar Award from the American Cancer Society (RSG-01-022-01-CCE) and a research grant from the Department of Defense (BC996645). This work was presented in the 44th Annual AAPM Meeting, Montreal, 2002 and in the 44th Annual ASTRO Meeting, New Orleans, 2002.

- ¹Author to whom correspondence should be addressed. Stanford University School of Medicine, Department of Radiation Oncology, 300 Pasteur Drive, Stanford, California 94305-5304. Electronic mail: lei@reyes.stanford.edu; phone: (650) 498 7896; fax: (650) 498 4015.
- ²T. Bortfeld, W. Schlegel, C. Dykstra, S. Levegrun, and K. Preiser, "Physical vs. biological objectives for treatment plan optimization," *Radiother. Oncol.* **40**, 185–187 (1996).
- ³T. Bortfeld, J. Stein, and K. Preiser, "Clinically relevant intensity modulation optimization using physical criteria," in *Proceedings of the XII International Conference on the Use of Computers in Radiation Therapy*, Salt Lake City, UT, 1997.
- ⁴L. Xing and G. T. Chen, "Iterative methods for inverse treatment planning," *Phys. Med. Biol.* **41**, 2107–2123 (1996).
- ⁵P. S. Cho, S. Lee, R. J. Marks II, S. Oh, S. G. Sutlief, and M. H. Phillips, "Optimization of intensity modulated beams with volume constraints using two methods: cost function minimization and projections onto convex sets," *Med. Phys.* **25**, 435–443 (1998).
- ⁶B. S. Teh, S. Y. Woo, and E. B. Butler, "Intensity modulated radiation therapy (IMRT): a new promising technology in radiation oncology," *Oncologist* **4**, 433–442 (1999).
- ⁷Y. Xiao, J. Galvin, M. Hossain, and R. Valicenti, "An optimized forward-planning technique for intensity modulated radiation therapy," *Med. Phys.* **27**, 2093–2099 (2000).
- ⁸S. M. Crooks and L. Xing, "Linear algebraic methods applied to intensity modulated radiation therapy," *Phys. Med. Biol.* **46**, 2587–2606 (2001).
- ⁹G. Starkshall, A. Pollack, and C. W. Stevens, "Treatment planning using a dose-volume feasibility search algorithm," *Int. J. Radiat. Oncol., Biol., Phys.* **49**, 1419–1427 (2001).
- ¹⁰A. Brahmé, "Optimized radiation therapy based on radiobiological objectives," *Semin. Radiat. Oncol.* **9**, 35–47 (1999).
- ¹¹M. Langer, "Application of coloring theory to reduce intensity modulated radiotherapy dose calculations," *Med. Phys.* **27**, 2077–2083 (2000).
- ¹²I. C. W. Group, "Intensity-modulated radiotherapy: current status and issues of interest," *Int. J. Radiat. Oncol., Biol., Phys.* **51**, 880–914 (2001).
- ¹³G. A. Ezzell, "Genetic and geometric optimization of three-dimensional radiation therapy treatment planning," *Med. Phys.* **23**, 293–305 (1996).
- ¹⁴C. B. Saw, K. M. Ayyangar, W. Zhen, M. Yoe-Sein, S. Pillai, and C. A. Enke, "Clinical implementation of intensity-modulated radiation therapy," *Med. Dosim.* **27**, 161–169 (2002).
- ¹⁵K. S. Chao, F. J. Wippold, G. Ozigit, B. N. Tran, and J. F. Dempsey, "Determination and delineation of nodal target volumes for head-and-neck cancer based on patterns of failure in patients receiving definitive and postoperative IMRT," *Int. J. Radiat. Oncol., Biol., Phys.* **53**, 1174–1184 (2002).
- ¹⁶S. Webb, "Optimisation of conformal radiotherapy dose distributions by simulated annealing," *Phys. Med. Biol.* **34**, 1349–1370 (1989).
- ¹⁷G. S. Mageras and R. Mohan, "Application of fast simulated annealing to optimization of conformal radiation treatments," *Med. Phys.* **20**, 639–647 (1993).
- ¹⁸X. H. Wang, R. Mohan, A. Jackson, S. A. Leibel, Z. Fuks, and C. C. Ling, "Optimization of intensity-modulated 3D conformal treatment plans based on biological indices," *Radiother. Oncol.* **37**, 140–152 (1995).
- ¹⁹L. Jones and P. Hoban, "A method for physically based radiotherapy

- optimization with intelligent tissue weight determination," *Med. Phys.* **29**, 26–37 (2002).
- ²¹R. P. Li and F. F. Yin, "Optimization of inverse treatment planning using a fuzzy weight function," *Med. Phys.* **27**, 691–700 (2000).
- ²²Y. Chen, D. Michalski, C. Houser, and J. M. Galvin, "A deterministic iterative least-squares algorithm for beam weight optimization in conformal radiotherapy," *Phys. Med. Biol.* **47**, 1647–1658 (2002).
- ²³L. Xing, J. G. Li, S. Donaldson, Q. T. Le, and A. L. Boyer, "Optimization of importance factors in inverse planning," *Phys. Med. Biol.* **44**, 2525–2536 (1999).
- ²⁴X. Wu and Y. Zhu, "An optimization method for importance factors and beam weights based on genetic algorithms for radiotherapy treatment planning," *Phys. Med. Biol.* **46**, 1085–1099 (2001).
- ²⁵C. Cotrutz and L. Xing, "Using voxel-dependent importance factors for interactive DVH-based dose optimization," *Phys. Med. Biol.* **47**, 1659–1669 (2002).
- ²⁶S. V. Spirou and C. S. Chui, "A gradient inverse planning algorithm with dose-volume constraints," *Med. Phys.* **25**, 321–333 (1998).
- ²⁷A. Niemierko, M. Uriel, and M. Goitein, "Optimization of 3D radiation therapy with both physical and biological end points and constraints," *Int. J. Radiat. Oncol., Biol., Phys.* **23**, 99–108 (1992).
- ²⁸C. De Wagter, C. O. Colle, L. G. Fortan, B. B. Van Duyse, D. L. Van den Berge, and W. J. De Neve, "3D conformal intensity-modulated radiotherapy planning: interactive optimization by constrained matrix inversion," *Radiother. Oncol.* **47**, 69–76 (1998).
- ²⁹S. M. Morrill, R. G. Lane, J. A. Wong, and I. I. Rosen, "Dose-volume considerations with linear programming optimization," *Med. Phys.* **18**, 1201–10 (1991).
- ³⁰S. M. Morrill, K. S. Lam, R. G. Lane, M. Langer, and I. I. Rosen, "Very fast simulated annealing in radiation therapy treatment plan optimization," *Int. J. Radiat. Oncol., Biol., Phys.* **31**, 179–188 (1995).
- ³¹L. Xing, J. G. Li, A. Pugachev, Q. T. Le, and A. L. Boyer, "Estimation theory and model parameter selection for therapeutic treatment plan optimization," *Med. Phys.* **26**, 2348–2358 (1999).
- ³²Q. Wu and R. Mohan, "Algorithms and functionality of an intensity modulated radiotherapy optimization system," *Med. Phys.* **27**, 701–711 (2000).
- ³³C. Cotrutz, M. Lahanas, C. Kappas, and D. Baltas, "A multiobjective gradient-based dose optimization algorithm for external beam conformal radiotherapy," *Phys. Med. Biol.* **46**, 2161–2175 (2001).
- ³⁴J. Liacer, "Inverse radiation treatment planning using the Dynamically Penalized Likelihood method," *Med. Phys.* **24**, 1751–1764 (1997).
- ³⁵L. Xing, J. Lian, and C. Cotrutz, "Inverse treatment planning with inclusion of model parameter uncertainty," in the 44th Annual AAPM Meeting, Montreal, 2002.
- ³⁶R. B. Altman and R. Tombrouopoulos, "Probabilistic constraint satisfaction: application to radiosurgery," in the 18th Annual Symposium on Computer Applications in Medical Care, Washington, DC, 1994.

**PHYSICS CONTRIBUTION****INCORPORATING LEAF TRANSMISSION AND HEAD SCATTER CORRECTIONS INTO STEP-AND-SHOOT LEAF SEQUENCES FOR IMRT**

YONG YANG, PH.D., AND LEI XING, PH.D.

Department of Radiation Oncology, Stanford University School of Medicine, Stanford, CA

Purpose: Leaf transmission and head scatter are two important factors that influence intensity-modulated radiation therapy (IMRT) delivery and should be correctly taken into account when generating multileaf collimator (MLC) sequences. Significant discrepancies between the desired and delivered intensity profiles could otherwise result. The purpose of this article is to propose a reliable algorithm to minimize the dosimetric effects caused by the two factors in step-and-shoot mode.

Methods and Materials: The goal of the algorithm is to minimize the difference between the desired fluence map and the fluence map actually delivered. For this purpose, an error function, defined as the least-square difference between the desired and the delivered fluence maps, is introduced. The effects of transmission and head scatter are minimized by adjusting the fractional monitor units (MUs) in the initial MLC sequences, created by using the desired fluence map without inclusion of the contributions from the two factors. Computationally, a downhill simplex optimization method is used to minimize the error function with respect to the fractional MUs. A three-source model is used to evaluate the relative head scatter distribution for each segment at the beginning of the calculation. The algorithm has been assessed by comparing the dose distributions delivered by the corrected leaf sequence files and the theoretic predication, calculated by Monte Carlo simulation using the desired fluence maps, for an intuitive test field and several clinical IMRT cases.

Results: The deviations between the desired fluence maps and those calculated using the corrected leaf sequence files are <0.3% of the maximum MU for the test field and <1.0% for the clinical IMRT cases. The experimental data show that both absolute and relative dose distributions delivered by the corrected leaf sequences agree with the desired ones within 2.5% of the maximum dose or 2 mm in high-dose gradient regions. Compared with the results obtained by using the leaf sequences in which only the transmission or none of the two effects is corrected, significant improvements in the fluence and dose distributions have been observed.

Conclusions: Transmission and head scatter play important roles in the dosimetric behavior of IMRT delivery. A larger error may result if only one factor is considered because of the opposite effects of the two factors. We noted that the influence of the two effects is more pronounced in absolute dose than in the relative dose. The algorithm proposed in this work accurately corrects for these two effects in step-and-shoot delivery and provides a reliable tool for clinical IMRT application. © 2003 Elsevier Science Inc.

MLC, Head scatter, Step-and-shoot mode, Leaf sequences, IMRT.

INTRODUCTION

Intensity-modulated radiation therapy (IMRT) can be effectively delivered using a multileaf collimator (MLC), either in segmental mode (SMLC, also called step-and-shoot mode) (1–4) or in dynamic mode (DMLC) (5–8). In the SMLC mode, each intensity-modulated beam is delivered by a sequence of segments of different shapes formed by the MLC leaves; the beam is off while the leaves move from one segment to another. In the DMLC mode, however, the intensity-modulated beam is delivered by the continuous movement of the leaves at variable speed while the beam is on. The advantage of DMLC is that it is able to deliver the

desired intensity profile with a high fidelity; the advantage of SMLC is that it is relatively simple and easy to implement and verify (9).

An IMRT planning process usually includes two important steps. First, the best possible fluence maps, which are generally called the “desired intensity maps”, are generated by the optimization module. The desired intensity maps are then converted into MLC leaf sequences (or MLC trajectories) as a function of monitor units (MUs). Many leaf-sequencing algorithms (1–8) have been developed to achieve the second step, with the mechanical constraints, such as tongue-and-groove effects and collision constraints

Reprint requests to: Lei Xing, Ph.D., Department of Radiation Oncology, Stanford University School of Medicine, 300 Pasteur Drive, A0-40, Stanford, CA 94305-5301. Tel.: (650) 498-7896; Fax: (650) 498-4015; E-mail: lei@reyes.stanford.edu

Supported by a Research Scholar Award from the American Cancer Society (RSG-01-022-01-CCE) and a research grant from

the Department of Defense (BC996645).

Acknowledgments—We wish to thank Drs. M. Lee, M. Murphy, J. Kung, J. G. Li, and Arthur Boyer for useful discussions.

Received May 13, 2002, and in revised form Nov 4, 2002.

Accepted for publication Nov 12, 2002.

for adjoining leaf pairs, taken into account. However, most algorithms, especially the step-and-shoot algorithms, have assumed an ideal MLC and have ignored the influence of MLC transmission and head scatter, which may lead to significant discrepancies between the desired and actually delivered intensity maps. Some recent studies based on dynamic delivery with Varian accelerator (10) or step-and-shoot delivery using Electa (11) or Siemens (12) accelerators have indicated that these factors might cause more than 5% mean dosimetric error to planning target volume (PTV) for a typical IMRT plan for a pelvic tumor if they are not correctly accounted for.

The problem of correcting the effects of transmission and head scatter is less intractable for DMLC than for SMLC. When these effects are included, in general, the final working intensity profile (13) corresponding to the leaf sequences used for treatment is different from the desired one. In the case of dynamic delivery, because the working intensity profile is continuous, it can be updated iteratively to account for the effects of transmission and head scatter. At the end of the iterative calculation, the best working profile can be found and used to generate the final leaf sequences (13–19). In contrast, the same approach cannot easily be implemented in the SMLC mode because the working intensity profile is discretized and cannot be updated in the iterative fashion. This has been discussed extensively by Chui *et al.* (13). An effective method to correct the effects of transmission and head scatter for the SMLC mode is highly desirable. In addition, in many available treatment planning systems, transmission or head scatter has been neglected or poorly corrected. An accurate postplan correction of these effects may be valuable.

The purpose of this article is to develop an effective algorithm to minimize the dosimetric influence of MLC leaf transmission and head scatter in the SMLC delivery mode. The algorithm can be integrated into a treatment planning system to minimize the effects of transmission and head scatter in leaf sequences. It can also be treated as an independent module to make postplan correction and repair of the leaf sequences produced by a treatment planning system in which transmission or head scatter have been neglected or poorly corrected. In the next section, we first summarize some theoretic aspects related to the MLC leaf sequencing and IMRT fluence map calculation; in particular, the three-source model used for the calculation of relative head scatter distributions of MLC segments. We then introduce an error function, defined as the least-square difference between the desired and computed fluence maps, and formulate the problem into the minimization of the error function with respect to the fractional MUs in the MLC leaf sequence file. The algorithm is assessed using an intuitive test field and several clinical IMRT cases.

METHODS AND MATERIALS

Head scatter

An algorithm based on a three-source model is used to calculate the head scatter factor of each beamlet in each seg-

ment. In this algorithm, the photon radiation to the point of calculation is treated from three effective sources: one source for the primary photons from the target and two extrafocal photon sources for the scattered photons from the primary collimator and the flattening filter, respectively. The scatter source intensity distributions, different source positions, and the off-axis difference of the scatter radiation are taken into account in the calculation model. We assume that the primary source is a point source located at the rotational central axis of the collimator in the exit plane of the target and that its source intensity does not change with the jaw settings. In addition, the extrafocal photon source for the scatter radiation from the primary collimator is represented by a planar annulus source; that for the scatter radiation from the flattening filter can be described by a planar disk source. Source parameters are determined by the data of Monte Carlo simulation (20) and by fitting the head scatter factors for the symmetric square fields, which were measured in air using a PTW Farmer 0.6 cm³ ion chamber with a 3-mm-thick brass buildup cap for the Varian Clinic 2300C/D 15 MV photon beam (Varian Oncology System, Palo Alto, CA). Head scatter factor is calculated by integrating the radiation contributed from areas (determined by the detector's eye view) in the two scatter sources (21). In addition, to reduce the calculation time and save computer memory, we use the head scatter factor of the centered beamlet in each opened leaf pair of a segment to represent the head scatter factors of all other beamlets in the same leaf pair of the segment; the errors arising from such approximation are less than 1.0% in most situations. However, the calculation time and required computer memory are greatly reduced.

To verify the accuracy of the algorithm for small irregular fields, head scatter factors were measured at different positions for several clinical segments. All the measurements were performed at an isocenter plane using a film measurement technique proposed by LoSasso *et al.* (10), in which Kodak XV2 film in ready pack was used, and lead disks (6 mm in diameter and 3 mm in thickness) were placed at the measurement points upstream and downstream in contact with the film jacket to achieve sufficient buildup for 15-MV X-rays. The calibration curve for the used films was determined by optical densities measured at $d_{\max} = 3.0$ cm for different MU irradiation in the field center of a 10 × 10 cm² field with source to skin distance (SSD) = 100 cm in solid water. The optical densities of measurement points were converted to dose, and head scatter factor was then obtained. All the measured data were normalized to unity for a symmetric 10 × 10 cm² field at the isocenter. We used the following formula to obtain head scatter factor for the beamlet (i,j) in a segment:

$$S_{c,m}(i,j) = \frac{D_m(i,j)}{D_m(10,10,\text{isocenter})OAR(r)}, \quad (1)$$

where $S_{c,m}(i,j)$ is the measured head scatter factor for the beamlet (i,j) in a segment; $D_m(i,j)$ is the dose measured at the center of beamlet (i,j); $D_m(10, 10, \text{isocenter})$ is the dose

measured at isocenter for reference field (symmetric $10 \times 10 \text{ cm}^2$ field); and r is the distance between isocenter and the center of beamlet (i,j) . OAR (r) is the primary off-axis ratio measured at the isocenter plane for the center of beamlet (i,j) in air.

Calculation of fluence map

The fluence of a given IMRT field can be divided into a grid of beamlets (9). For an IMRT leaf sequence file with K segments, the delivered fluence map in the isocenter plane, $\phi(i,j)$, can be calculated by summing the contributions of all segments:

$$\Phi(i, j) = \sum_k f_k \varphi_k(i, j), \quad (2)$$

where f_k is the fractional MU of the k -th segment in the leaf sequence file and $\varphi_k(i,j)$ is the fluence per unit MU from the k -th segment in the beamlet (i,j) . If we denote the boundary of the k -th segment by A_k and introduce a notation:

$$\delta_{ij, A_k} = \begin{cases} 1 & \text{beamlet}(i, j) \in A_k \\ 0 & \text{beamlet}(i, j) \notin A_k \end{cases}, \quad (3)$$

the fluence per unit MU from the k -th segment for beamlet (i,j) can be written as:

$$\varphi_k(i, j) = S_{c,k}(i, j) \delta_{ij, A_k} + \alpha S'_c (1 - \delta_{ij, A_k}), \quad (4)$$

where $S_{c,k}(i,j)$ is the head scatter factor of the beamlet (i,j) in k th segment and is calculated by the three-source model described earlier, S'_c is the head scatter factor for the rectangular field defined by the jaws. For a Varian machine, S'_c is field-specific constant because the jaw settings do not change during the whole irradiation process of an IMRT field. In addition, we assume that all the beamlets in a rectangular field have the same S'_c . Such an approximation is reasonable because S'_c is involved only in the transmission fluence calculation. α in Eq. 4 is the average transmission factor, representing the amount of radiation passing through the MLC leaves (on average) as a percentage of the radiation of an open field defined by the jaws. It can be measured using an ion chamber or films (10, 22). For our Varian Clinic 2300C/D 15 MV photon beam, the average transmission factor for an 80-leaf standard MLC was determined to be 1.74%.

Error function and minimization calculation

It is usually impossible to produce the exactly desired fluence map using step-and-shoot mode with realistic MLC, but an optimum solution is feasible. Our strategy was to minimize the difference between the desired fluence map and the actually delivered fluence map. For this purpose, an error function was constructed according to the least-square

difference between the desired and the deliverable fluence map:

$$F = \sum_{i,j} [\Phi(i, j) - \Phi_d(i, j)]^2, \quad (5)$$

where $\Phi(i,j)$ and $\Phi_d(i,j)$ are the calculated and the desired fluences of beamlet (i,j) , respectively. In Eq. 5, only the beamlets with nonzero fluences in the desired intensity map are considered. The beamlets that received transmission radiation only were not included because we could not physically produce a beamlet with zero fluence.

We then added a correction factor to the fractional MU of each segment. The effects of transmission and head scatter were minimized by iteratively adjusting the correction factors in the MLC leaf sequences. The corrected fractional MU of the k -th segment, f'_k , can be expressed as,

$$f'_k = f_k^0 - \Delta f_k \quad (6)$$

where f_k^0 is the fractional MU of the k -th segment in the leaf sequence file generated from the desired intensity profile without considering the transmission and head scatter, and Δf_k is the correction factor for the k -th segment.

The calculation started with the MLC leaf sequence file derived from the desired fluence map without considering the transmission and head scatter. The desired intensity maps came from the optimization module of a commercial treatment planning system (CORVUS, NOMOS Corporation, Sewickley, PA) (23), and were output in the form of a grid of beamlet intensities. The initial leaf sequences were generated using the algorithm proposed by Bortfeld *et al.* (1). But any other step-and-shoot leaf sequence algorithm could also be used here (2, 4, 24, 25). The procedure of the algorithm is shown in Fig. 1. A downhill simplex algorithm was employed to minimize the error function and search the optimum correction factors. The starting vertices for downhill simplex algorithm can be chosen randomly before the optimization process. In our work, from the initial uncorrected delivered fluence, a -1.0% correction of the total MU was added to the fractional MU of a segment each time, whereas other correction factors remained as zero, thus $M + 1$ vertices were generated and used as the starting vertices of the algorithm. The iteration process stopped when the tolerance value or a preset maximum iteration number was reached. In our calculation, the tolerance value was set as 0.00001, and the maximum iteration number was set to 8000.

Dosimetric verification

The algorithm was verified by an intuitive test field and some clinical IMRT fields of prostate treatments using the Varian Clinic 2300C/D 15-MV photon beam. The dose distributions delivered by the leaf sequence files correcting for head scatter and transmission were measured using Kodak XV2 films at different depths in solid water. In the measurements,

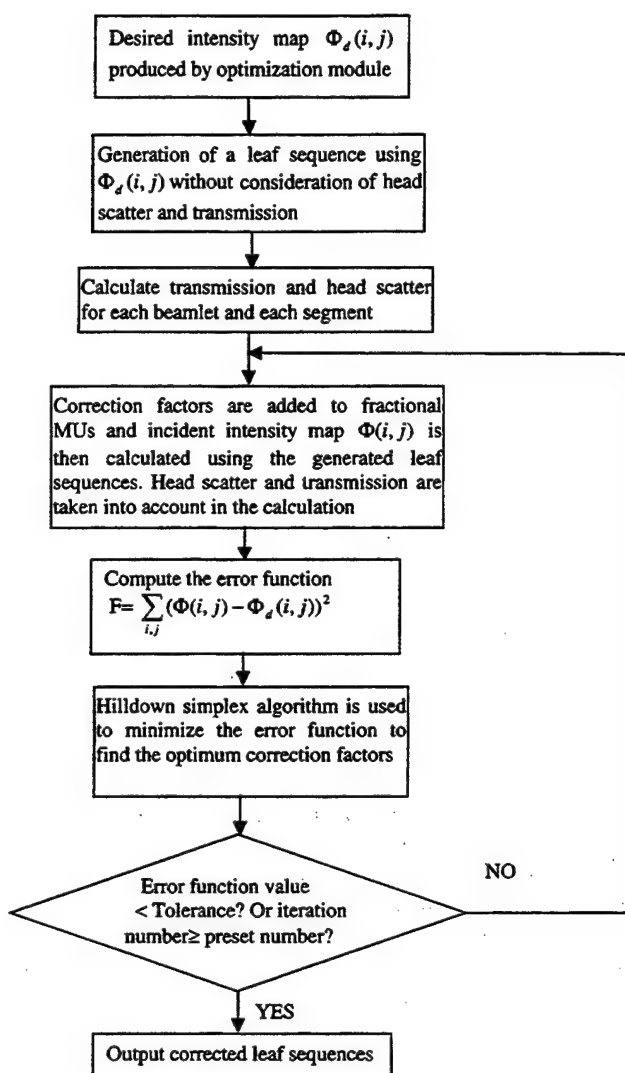


Fig. 1. The procedure of correcting the effects of head scatter and transmission in step-and-shoot leaf sequences.

radiographic films were placed in the isocenter plane perpendicular to the beam. The optical densities were converted to doses by the method described previously. The absolute doses were also measured with a PTW Farmer 0.6 cm³ ion chamber in a relatively flat part of the intensity maps to normalize the relative dose distributions obtained by the film measurements. The measured results were compared with the theoretic prediction calculated by Monte Carlo simulation (26–28) using the desired fluence maps. The verification process is schematically illustrated in Fig. 2.

The intuitive test field consisted of five consecutive 2.0 × 10 cm² segments (Fig. 3) aiming to produce a 10 × 10 cm² uniform open beam. This type of an intuitive example is best suited for illustrating our algorithm because its absolute dose distribution can be easily determined. Three step-and-shoot leaf sequence files were generated: (1) no corrections for transmission and head scatter, (2) corrections for both transmission and head scatter, and (3) only correction for transmission. The film measurements were made in isocenter plane at

depth 5.0 cm in a solid water phantom for the beams defined by the leaf sequence files. In addition, a measurement for a single-segment 10 × 10 cm² open field shaped by MLC with the same jaw settings was also performed.

IMRT fields from clinical prostate cases were also used to further test our algorithm. The plans were generated using the CORVUS system. The dose distributions were measured in the isocenter plane at a depth of 3.0 cm in a solid water phantom. Three MLC leaf sequence files with different correction schemes similar to those described previously were generated and delivered for each IMRT field. The dose distributions corresponding to these cases were measured and compared.

RESULTS

Head scatter factor

Figure 4 shows the measured and calculated head scatter factors for square fields from 4 cm to 40 cm at isocenter for the 15 MV beam. The line is the calculated values; the scattered solid circles represent the measured ones. The agreement between these two groups of data is within 0.3% for all measurement fields. Table 1 lists the measured and calculated head scatter factors for eight different beamlets in four randomly chosen segments of a clinical prostate IMRT field (two of the four segments are shown in Fig. 5). The four measurement positions (the corresponding measurement results are listed in Table 1) in these two segments are also labeled in Fig. 5. For all measured beamlets, the calculated results agree with the measurements within 0.8%.

Fluence maps

The first test was done by using a 10 × 10 cm² open beam. In this case, the desired intensity map for the test field was set to a uniform distribution of 30 MU. Table 2 lists the incident intensity maps calculated by the different leaf sequence files: (1) both transmission and head scatter were ignored (Table 2(a)), (2) only transmission was corrected (Table 2(b)), and (3) both transmission and head scatter were corrected by our method (Table 2(c)). The values listed in Table 2 are the absolute MUs for each beamlet. It could be easily obtained from Table 2 that the absolute intensity deviation between the calculated and the desired intensity map was about 1.2 MU (~ 4.0% of the desired intensity) if both head scatter and transmission were ignored, about -1.0 MU (~ -3.3% of the desired intensity) if only transmission was corrected and <0.1 MU (~ 0.3% of the desired intensity) when both effects were corrected by our method.

A six-field prostate IMRT treatment was also used to assess our algorithm. The beam incident angles were 0°, 40°, 115°, 180°, 245°, and 320°, respectively, in Varian's convention. The intensity level was set to 10, and the leaf sequences were generated using the CORVUS planning system. The numbers of segments for the six fields were 16, 15, 12, 16, 13, and 13, respectively. In Table 3(a), we show the desired intensity map for the field with gantry angle of 0°. In Table 3(b) to (d), we also show the intensity maps

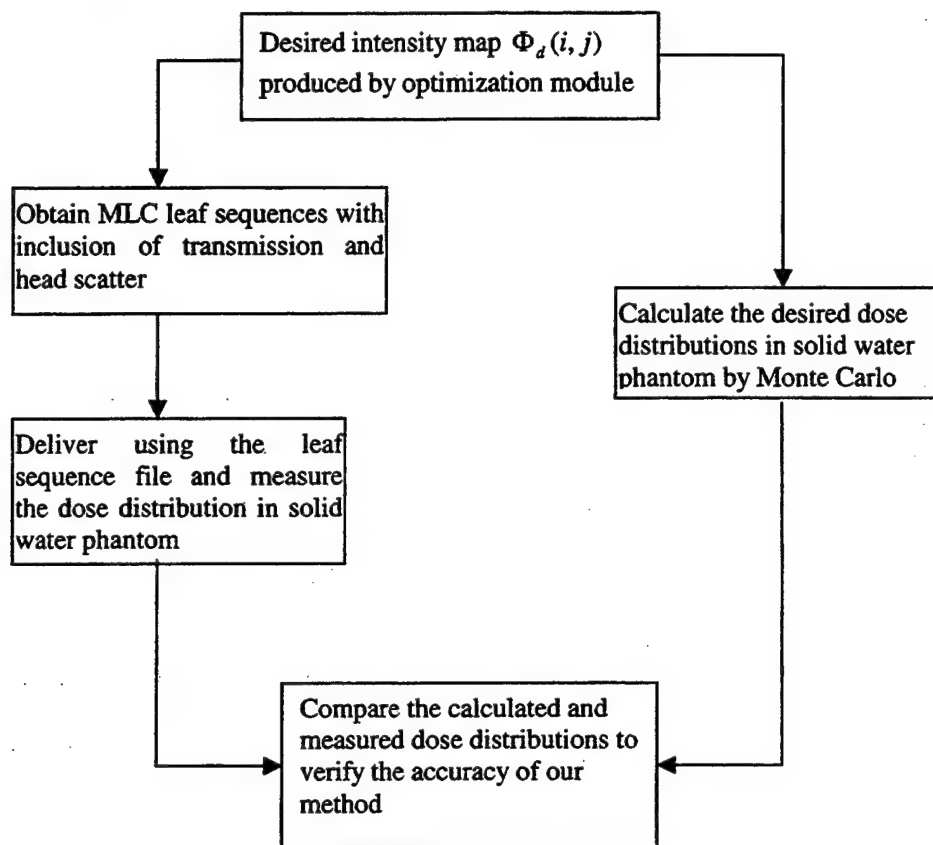
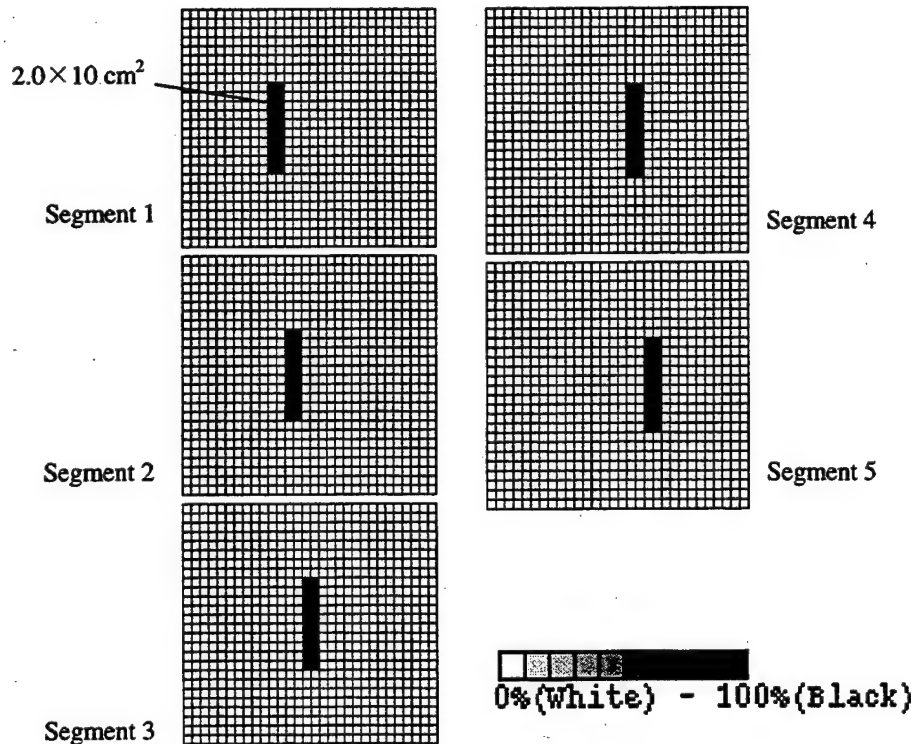


Fig. 2. The dose verification process for validating the algorithm.

Fig. 3. The schematic diagram of the intuitive test field. The field includes five consecutive $2.0 \times 10 \text{ cm}^2$ segments and attempts to produce a $10 \times 10 \text{ cm}^2$ open beam.

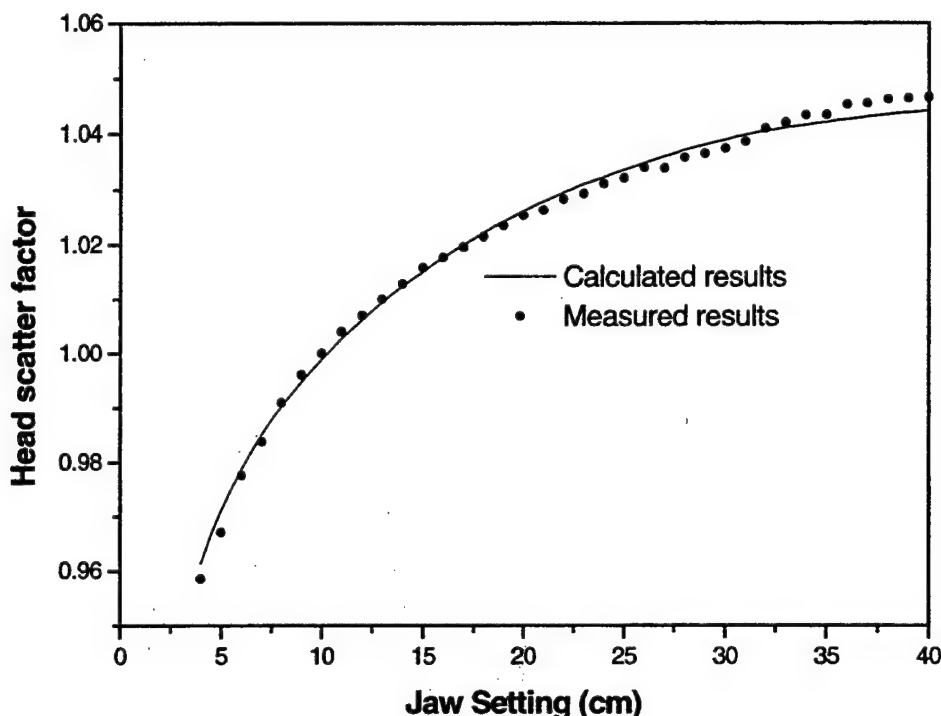


Fig. 4. The measured and calculated head scatter factors for square field size from 4 cm to 40 cm at isocenter for 15 MV photon beam. All the data are normalized to the value of a $10 \times 10 \text{ cm}^2$ field at SAD. The line and solid dots represent the calculated and measured data, respectively.

calculated by using the uncorrected, corrected, and only transmission-corrected leaf sequence files. In Table 3, we find that the maximum absolute MU differences between the calculated and desired intensity maps were about 1.5 MU ($\sim 3.0\%$ of the maximum MU in the field) if neither head scatter nor transmission was corrected, and about -2 MU ($\sim -4.0\%$ of the maximum MU in the field) if only transmission was corrected. The maximum differences between the relative intensity maps for these two situations were about 3% and 2%, respectively. After correcting for the transmission and head scatter using our algorithm, both the absolute and relative intensity maps were in agreement with desired ones within 1.0% of the maximum intensity of the field, except those beamlets whose desired intensity was zero. Table 4 lists the obtained correction factors to the fractional MUs for the IMRT field. Similar results were also found for the other five fields of the case.

Dosimetric verification

Figures 6a and 6b show the measured relative and absolute dose profiles in the isocenter plane at depth 5 cm in

solid water for the test field along the midline of the 21st leaf pair (0.5 cm from isocenter in Y2 direction). The dose profiles of the single-segment (conventional) $10 \times 10 \text{ cm}^2$ field are also shown for comparison. Although there were almost no differences between the relative dose distributions, the discrepancies between the absolute dose distributions were quite large. The absolute dose without considering the head scatter and transmission was higher than that of single-segment $10 \times 10 \text{ cm}^2$ field by about 1.2 cGy ($\sim 3.8\%$). When only the transmission was corrected, the absolute dose profile was lower than that of single-segment $10 \times 10 \text{ cm}^2$ field by about 1.1 cGy ($\sim -3.5\%$). Our leaf sequence file, which corrected for both head and transmission, generated a dose distribution very close to that of single-segment $10 \times 10 \text{ cm}^2$ field (within 1.0% deviation).

The dose distributions calculated using Monte Carlo simulation for the IMRT field with gantry angle 0° are shown in Figs. 7a and 7b as thick solid lines. The measured dose distributions delivered by the leaf sequence files with and without correcting for the transmission and head scatter are shown in

Table 1. The measured and calculated head scatter factors (S_c) for eight different beamlets in five randomly chosen segments of clinical prostate intensity-modulated fields for Varian 2300C/D 15 MV photon beam

Beamlet No.	1	2	3	4	5	6	7	8
Calculated S_c	0.948	0.954	0.945	0.965	0.979	0.962	0.976	0.961
Measured S_c	0.942	0.959	0.939	0.972	0.975	0.954	0.969	0.955
Diff (%)	0.6	-0.5	0.6	-0.7	0.4	0.8	0.7	0.4

$$\text{Diff} = (\text{Calculated } S_c - \text{measured } S_c) / \text{measured } S_c \times 100\%.$$

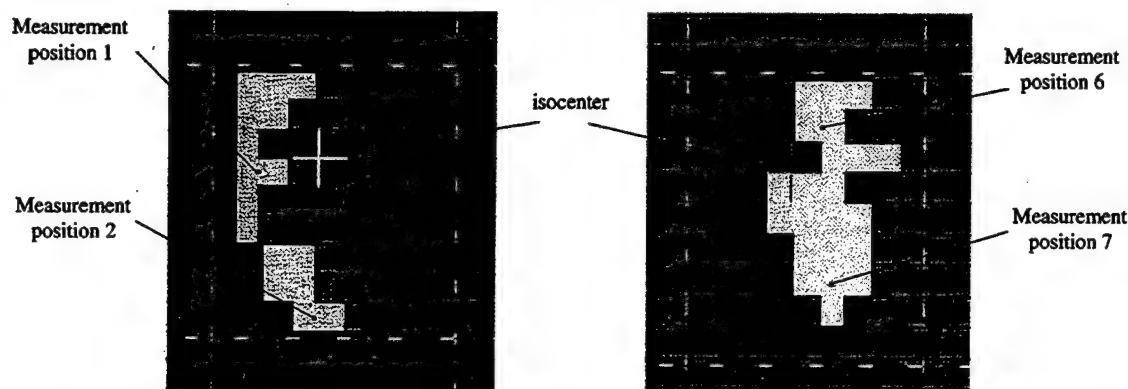


Fig. 5. Two segments of clinical prostate intensity-modulated radiation therapy fields. The four measured positions are labeled in the figure and the corresponding head scatter factors are listed data in Table 1.

Figs. 7a and 7b as thin broken lines, respectively. The calculated and measured relative and absolute dose profiles along

the leaf-moving direction at the off-axis distance of 1.5 cm (through the middle of the 22nd leaf pairs) and 0.5 cm (through

Table 2. The intensity maps for a test field. (a) The calculated intensity map without corrections of head scatter and transmission. (b) The calculated intensity map only corrected transmission. (c) The calculated intensity map corrected for both head scatter and transmission.*

(a)	-4.5	-3.5	-2.5	-1.5	0.5	0.5	1.5	2.5	4.5	4.5
4.5	30.9	30.9	31	31	31	31	31	31	30.9	30.9
3.5	30.9	30.9	31	31	31.1	31.1	31.1	31.1	31	31
2.5	31	31	31.1	31.1	31.1	31.1	31.1	31.1	31	31
1.5	31	31	31.1	31.1	31.1	31.1	31.1	31.1	31	31
0.5	31	31	31.1	31.1	31.2	31.2	31.1	31.1	31	31
-0.5	31	31	31.1	31.1	31.2	31.2	31.1	31.1	31	31
-1.5	31	31	31.1	31.1	31.2	31.2	31.1	31.1	31	31
-2.5	31	31	31.1	31.1	31.1	31.1	31.1	31.1	31	31
-3.5	30.9	30.9	31	31	31.1	31.1	31	31	31	31
-4.5	30.9	30.9	31	31	31	31	31	31	30.9	30.9
(b)	-4.5	-3.5	-2.5	-1.5	0.5	0.5	1.5	2.5	4.5	4.5
4.5	28.8	28.8	28.9	28.9	28.9	28.9	28.9	28.9	28.8	28.8
3.5	28.9	28.9	29	29	29	29	29	29	28.9	28.9
2.5	28.9	28.9	29	29	29	29	29	29	28.9	28.9
1.5	29	29	29.1	29.1	29.1	29.1	29.1	29.1	29	29
0.5	29	29	29.1	29.1	29.1	29.1	29.1	29.1	29	29
-0.5	29	29	29.1	29.1	29.1	29.1	29.1	29.1	29	29
-1.5	29	29	29.1	29.1	29.1	29.1	29.1	29.1	29	29
-2.5	28.9	28.9	29	29	29	29	29	29	28.9	28.9
-3.5	28.9	28.9	29	29	29	29	29	29	28.9	28.9
-4.5	28.8	28.8	28.9	28.9	28.9	28.9	28.9	28.8	28.8	28.8
(c)	-4.5	-3.5	-2.5	-1.5	0.5	0.5	1.5	2.5	4.5	4.5
4.5	29.9	29.9	29.9	29.9	29.9	29.9	29.9	29.9	29.9	29.9
3.5	30	30	30	30	30	30	30	30	30	30
2.5	30	30	30	30	30	30	30	30	30	30
1.5	30.1	30.1	30.1	30.1	30.1	30.1	30.1	30.1	30.1	30.1
0.5	30.1	30.1	30.1	30.1	30.1	30.1	30.1	30.1	30.1	30.1
-0.5	30.1	30.1	30.1	30.1	30.1	30.1	30.1	30.1	30.1	30.1
-1.5	30.1	30.1	30.1	30.1	30.1	30.1	30.1	30.1	30.1	30.1
-2.5	30	30	30	30	30	30	30	30	30	30
-3.5	30	30	30	30	30	30	30	30	30	30
-4.5	29.9	29.9	29.9	29.9	29.9	29.9	29.9	29.9	29.9	29.9

* The values in this table are the absolute MU for each beamlet, and the beamlets are indexed by their center positions (cm). The isocenter is at (0,0).

Table 3. The intensity maps for the clinical intensity-modulated field with gantry angle 0°. (a) The desired intensity map. (b) The calculated intensity map without corrections of head scatter and transmission. (c) The calculated intensity map corrected for both head scatter and transmission. (d) The calculated intensity map only corrected for transmission.*

(a)	-2.5	-1.5	-0.5	0.5	1.5	2.5	3.5
2.5	39.2	44.8	56	44.8	28	50.4	5.6
1.5	50.4	56	28	39.2	50.4	22.4	22.4
0.5	39.2	28	28	16.8	50.4	39.2	39.2
-0.5	56	56	50.4	56	50.4	22.4	0
-1.5	56	28	44.8	44.8	28	56	0
-2.5	16.8	5.6	16.8	44.8	56	39.2	0
-3.5	0	39.2	50.4	44.8	33.6	16.8	0
-4.5	0	44.8	56	16.8	22.4	0	0
-5.5	0	0	39.2	56	0	0	0
(b)	-2.5	-1.5	-0.5	0.5	1.5	2.5	3.5
2.5	38.9	44.3	55	44.5	28.5	49.6	7.1
1.5	49.8	55.2	28.7	39.3	49.9	23.1	23.1
0.5	39	28.5	28.8	18	50.1	39.2	39.2
-0.5	55.2	55.2	50.2	55.5	50	23.1	1.7
-1.5	55	28.8	45	45	28.8	54.9	1.7
-2.5	17.4	7.2	17.9	45.1	55.5	39.3	1.7
-3.5	1.7	38.6	49.4	44.9	34.1	17.9	1.7
-4.5	1.7	44.3	55	17.9	23.2	1.7	1.7
-5.5	1.7	1.7	38.4	54.4	1.7	1.7	1.7
(c)	-2.5	-1.5	-0.5	0.5	1.5	2.5	3.5
2.5	39.6	45.1	55.8	45.1	28.4	49.7	6.1
1.5	50.6	55.9	28.3	39.3	50	22.8	22.8
0.5	39.7	28	28.4	17.3	50.1	39.3	39.3
-0.5	55.9	55.9	50.2	56.1	50.1	22.7	1.8
-1.5	55.8	28.4	44.5	44.5	28.4	55.9	1.8
-2.5	16.8	5.6	17.3	44.5	55.9	39.7	1.8
-3.5	1.8	39.4	50.3	44.3	33.9	17.4	1.8
-4.5	1.8	45.1	55.8	17.5	22.4	1.8	1.8
-5.5	1.8	1.8	39.3	55.5	1.8	1.8	1.8
(d)	-2.5	-1.5	-0.5	0.5	1.5	2.5	3.5
2.5	37.8	43.3	54.2	43.5	27.2	48.7	5.5
1.5	48.9	54.4	27.4	38.2	49	21.9	21.8
0.5	37.9	27.2	27.5	16.6	49.2	38.1	38.1
-0.5	54.4	54.4	49.3	54.7	49.1	21.8	1.7
-1.5	54.2	27.5	44	44	27.5	54.1	1.7
-2.5	16	5.5	16.5	44	54.7	38.2	1.7
-3.5	1.7	37.5	48.5	43.9	32.9	16.5	1.7
-4.5	1.7	43.2	54.2	16.5	21.9	1.7	1.7
-5.5	1.7	1.7	37.4	53.6	1.7	1.7	1.7

* The values in this table are the absolute MU for each beamlet, and the beamlets are indexed by their center positions (cm). The intensity-modulated radiation therapy isocenter is at (0,0).

Table 4. Correction factors of the fractional MUs for the intensity-modulated radiation therapy field with gantry angle 0°*

Segment No.	1	2	3	4	5	6	7	8
C_{tr}	-0.0059	0.0201	-0.0109	-0.0025	0.0163	-0.0107	0.0007	0.0015
C_{scr}	-0.0143	0.0208	-0.0130	-0.0063	0.0163	-0.0123	-0.0001	-0.0002
Segment No.	9	10	11	12	13	14	15	16
C_{tr}	0.0016	0.0092	-0.0093	0.0042	-0.0035	-0.0014	0.0099	-0.0038
C_{scr}	0.0011	0.0075	-0.0120	0.0059	-0.0056	-0.0047	0.0079	0.0111

*The number of intensity levels is set to 10. C_{tr} = the correction factors only corrected for transmission; C_{scr} = correction factors corrected for both head scatter and transmission; + = the fractional MU of this segment should be reduced by $\Delta f = C \times MU_{tot}$; - = the fractional MU of this segment should be increased by $\Delta f = C \times MU_{tot}$; MU_{tot} = total irradiated MU for this intensity-modulated radiation therapy field.

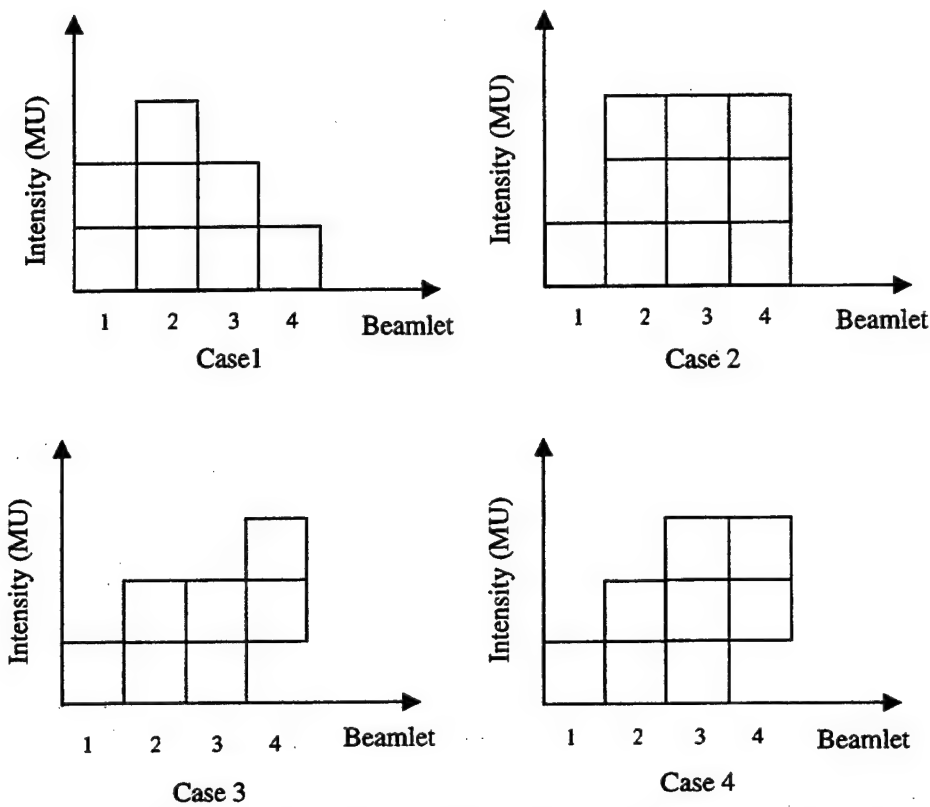


Fig. 9. Simple one-dimensional intensity-modulated radiation therapy fields consisted of four beamlets and three intensity levels. For Patients 1–3, analytic solutions can be obtained if only transmission is taken into account because the number of independent equations is less or equal to the number of correction factors (the number of variables, here is equal to 3). For Patient 4, there exists no analytic solution because the number of independent equations is larger than the number of correction factors.

For some disease sites (e.g., prostate, head-and-neck diseases), the desired intensity profiles produced by the optimization module tend to be highly complex. As a result, a large number of small segments, even potentially a single beamlet, are included in the leaf sequences. In these cases, head scatter will have significant influence on incident fluence because of the fast reduction of head scatter with the field size in the small field limit. The influence is even larger than that of transmission in some circumstances. This is why there are some regions in our measured profiles where the measured absolute doses are less than the Monte Carlo calculations even if both the transmission and head scatter have been ignored. To accurately determine head scatter distribution for each segment, we employed a three-source model.

It is interesting to confirm that transmission and head scatter usually have opposite influences on the delivered doses. The head scatter correction tends to reduce the incident intensity values and requires the leaf sequence to be modified to increase beam-on time. The transmission correction, on the contrary, tends to increase the incident intensity values and requires the leaf sequence to reduce beam-on time. If only transmission is considered in the leaf sequence algorithm, the deviations from the desired intensity maps may become larger than if none of the two factors is corrected in the leaf sequence algorithm.

because the effects of transmission and head scatter may partially cancel each other. This is especially true when there are a large number of small segments in the IMRT field. For this reason, the absolute dose discrepancies from the Monte Carlo calculation in some parts of the measured profiles (shown in Figs. 8b and 8d) are larger when only transmission is corrected than that when both effects are neglected. Similar results are also reported recently by Azcona *et al.* (11). In short, to obtain the dose distributions as close as that calculated by the inverse treatment planning system, both transmission and head scatter should be corrected accurately.

From Fig. 8, we find that the relative dose at the areas of lower dose (for example, area A in Fig. 8a) is higher than the Monte Carlo calculated dose if head scatter and transmission are not corrected. This is because these areas are blocked by MLC much longer than in other areas and receive the largest transmission contributions. In addition, as shown in Fig. 8, our measured and calculated results also indicate that the head scatter and transmission corrections have larger influences on the absolute dose (or intensity) distributions than on the relative dose (or intensity) distributions. As a consequence, if the details of head scatter and transmission relative distributions are ignored, the averaged effects for head scatter and transmission can be approximately corrected by an experimentally

determined adjusting factor, which is similar to the empiric scaling factor used by Azcona *et al.* (11) and by the CORVUS inverse planning system. The deviations in absolute dose distributions can be reduced greatly by using an empiric scaling factor if an accurate head scatter calculation model is not available or only transmission is taken into account.

When the number of intensity levels used to stratify the intensity profiles is increased, we observe that the deviations between the incident intensity map calculated by the corrected leaf sequences and the desired one decrease. This is because the number of segments usually increases with the number of intensity levels, providing more adjustable variables in the leaf sequence file.

The proposed algorithm is an optimization process, and it is not necessary to start the calculation with a leaf sequence generated without correcting the transmission and head scatter effects. Any leaf sequence with inaccurate corrections can be used as the starting point. In this sense, our program can be

used as a tool for postplan repairing. In addition, the algorithm is quite general and can be used for any step-and-shoot delivery and for any type of MLC.

CONCLUSIONS

Unlike conventional radiation treatment with static MLC fields, there are significant dosimetric issues that must be addressed when IMRT delivery is used. In this article, an algorithm for correcting the effects of the transmission and head scatter in step-and-shoot leaf sequences is presented. The experimental data indicate that the deviations of the delivered fluence (dose) corrected using the algorithm from the desired ones are significantly decreased for both the relative and absolute distributions. Although the proposed technique was applied to the Varian MLC, the methodology can be easily extended to deal with IMRT deliveries of other vendors.

REFERENCES

- Bortfeld TR, Kahler DL, Waldron TJ, *et al.* X-ray field compensation with multileaf collimators. *Int J Radiat Oncol Biol Phys* 1994;28:723–730.
- Ma L, Boyer AL, Xing L, *et al.* An optimized leaf-setting algorithm for beam intensity modulation using dynamic multileaf collimators. *Phys Med Biol* 1998;43:1629–1643.
- Que W. Comparison of algorithms for multileaf collimator field segmentation. *Med Phys* 1999;26:2390–2396.
- Dai JR, Zhu YP. Minimizing the number of segments in a delivery sequence for intensity-modulated radiation therapy with a multileaf collimator. *Med Phys* 2001;28:2113–2120.
- Convey DJ, Rosenbloom ME. The generation of intensity-modulated fields for conformal radiotherapy by dynamic collimation. *Phys Med Biol* 1992;37:1359–1374.
- Spirou SV, Chui CS. Generation of arbitrary intensity profiles by dynamic jaws or multileaf collimators. *Med Phys* 1994;21:1031–1041.
- Svensson R, Kallman P, Brahme A. An analytical solution for the dynamic control of multileaf collimators. *Phys Med Biol* 1994;39:37–61.
- Stein J, Bortfeld T, Dorschel B, *et al.* Dynamic X-ray compensation for conformal radiotherapy by means of multi-leaf collimation. *Radiat Oncol* 1994;32:163–173.
- Xing L, Li JG. Computer verification of fluence maps in intensity modulated radiation therapy. *Med Phys* 2000;27:2084–2092.
- LoSasso T, Chui CS, Ling CC. Physical and dosimetric aspects of a multileaf collimation system used in the dynamic mode for implementing intensity modulated radiotherapy. *Med Phys* 1998;25:1919–1927.
- Azcona JD, Siochi RAC, Azinovic I. Quality assurance in IMRT: Importance of the transmission through the jaws for an accurate calculation of absolute doses and relative distributions. *Med Phys* 2002;29:269–274.
- Seco J, Evans PM, Webb S. Analysis of the effects of the delivery technique on an IMRT plan: Comparison for multiple static field, dynamic and NOMOS MIMIC collimation. *Phys Med Biol* 2001;46:3073–3087.
- Chui CS, Chan MF, Yorke E, *et al.* Delivery of intensity-modulated radiation therapy with a conventional multileaf collimator: Comparison of dynamic and segmental methods. *Med Phys* 2001;28:2441–2449.
- LoSasso T, Chui CS, Ling CC. Comprehensive quality assurance for the delivery of intensity modulated radiotherapy with a multileaf collimator used in the dynamic mode. *Med Phys* 2001;28:2209–2219.
- Dirkx ML, Heijmen BJ, van Santvoort JP. Leaf trajectory calculation for dynamic multileaf collimation to realize optimized fluence profiles. *Phys Med Biol* 1998;43:1171–1184.
- Holmes TW. A method to incorporate leakage and head scatter corrections into tomotherapy inverse treatment planning algorithm. *Phys Med Biol* 2000;45:1211–1227.
- Mohan R, Arnfield M, Tong S, *et al.* The impact of fluctuations in intensity patterns on the number of monitor units and the quality and accuracy of intensity modulated radiotherapy. *Med Phys* 2000;27:1226–1237.
- Convey DJ, Webb S. Generation of discrete beam-intensity modulation by dynamic multileaf collimation under minimum leaf separation constraints. *Phys Med Biol* 1998;43:2521–2538.
- Convey DJ, Webb S. Calculation of the distribution of head-scattered radiation in dynamically-collimated MLC fields. In: Leavitt DD, Starkschall G, editors. XIth International Conference on the Uses of Computers in Radiation Therapy. Madison, WI: Medical Physics Publishing, 1997: 350–353.
- Liu HH, Mackie TR, McCullough EC. A dual source beam model used in convolution/superposition dose calculations for clinical megavoltage x-ray beams. *Med Phys* 1997;24:1960–1974.
- Kim S, Palta JR, Zhu TC. The equivalent square concept for the head scatter factor based on scatter from flattening filter. *Phys Med Biol* 1998;43:1593–1604.
- Arnfield MR, Siebers JV, Kim JO, *et al.* A method for determining multileaf collimator transmission and scatter for dynamic intensity modulated radiotherapy. *Med Phys* 2000;27:2231–2241.
- Xing L, Curran B, Hill R, *et al.* Dosimetric verification of a commercial inverse treatment planning system. *Phys Med Biol* 1999;44:463–478.
- Siochi RA. Minimizing static intensity modulation delivery time using an intensity solid paradigm. *Int J Radiat Oncol Biol Phys* 1999;43:671–680.

25. Xia P, Verhey LJ. Multileaf collimator leaf sequencing algorithm for intensity modulated beams with multiple static segments. *Med Phys* 1998;25:1424–1434.
26. Ma CM, Pawlicki T, Jiang SB, et al. Monte Carlo verification of IMRT dose distributions from a commercial treatment planning optimization system. *Phys Med Biol* 2000;45:2483–2495.
27. Keall PJ, Siebers JV, Arnfield MR, et al. Monte Carlo dose calculations for dynamic IMRT treatments. *Phys Med Biol* 2001;46:929–941.
28. Liu HH, Verhaegen F, Dong L. A method of simulating dynamic multileaf collimators using Monte Carlo techniques for intensity-modulated radiation therapy. *Phys Med Biol* 2001;46:2283–2298.

IMRT dose shaping with regionally variable penalty scheme

Cristian Cotrutz and Lei Xing^a

Department of Radiation Oncology, Stanford University School of Medicine, Stanford, California 94305-5304

(Received 18 June 2002; accepted for publication 7 January 2003; published 24 March 2003)

A commonly known deficiency of currently available inverse planning systems is the difficulty in fine-tuning the final dose distribution. In practice, it is not uncommon that just a few unsatisfactory regions in the planning target volume or an organ at risk prevent an intensity modulated radiation therapy (IMRT) plan from being clinically acceptable. The purpose of this work is to introduce a mechanism for controlling the regional doses after a conventional IMRT plan is obtained and to demonstrate its clinical utility. Two types of importance factors are introduced in the objective function to model the tradeoffs of different clinical objectives. The first is the conventional structure-dependent importance factor, which quantifies the interstructure tradeoff. The second type is the voxel-dependent importance factor which "modulates" the importance of different voxels within a structure. The planning proceeds in two major steps. First a conventional inverse planning is performed, where the structure-dependent importance factors are determined in a trial-and-error fashion. The next level of planning involves fine-tuning the regional doses to meet specific clinical requirements. To achieve this, the voxels where doses need to be modified are identified either graphically on the isodose layouts, or on the corresponding dose-volume histogram (DVH) curves. The importance value of these voxels is then adjusted to increase/decrease the penalty at the corresponding regions. The technique is applied to two clinical cases. It was found that both tumor hot spots and critical structure maximal doses can be easily controlled by varying the regional penalty. One to three trials were sufficient for the conventionally optimized dose distributions to be adjusted to meet clinical expectation. Thus introducing the voxel-dependent penalty scheme provides an effective means for IMRT dose distributions painting and sculpting. © 2003 American Association of Physicists in Medicine. [DOI: 10.1118/1.1556610]

Key words: IMRT, dose optimization, importance factors, inverse planning

I. INTRODUCTION

Treatment planning requires the calculation of a set of parameters for the delivery of a certain radiation dose to the tumor. If IMRT is to be used, the number of physically feasible plans is huge, and efforts have been focused on the determination of the beamlet weights for preselected beam energies and beam configurations. Inverse planning is often used to derive the beam parameters with an objective function as the ranking criterion. Many attempts have been made in trying to construct clinically relevant objective functions, in linear, quadratic, and nonlinear forms. They can be classified as dose-based^{1–11} and biological-based models.^{12–14} The former is concerned with accurate dose distributions and the latter argues that optimization can be guided by estimates of biological effects on considered tissues. In principle, the biologically based models are most relevant for plan ranking. However, the dose-response function of various structures is not sufficiently understood. At this point, the dose-based approach is still widely employed in practice whereas biological models are more often used for research. This is also evidenced by the fact that all commercial IMRT planning systems have chosen dose-based ranking as the starting point.

There exist many algorithms for inverse planning. In all cases, the optimizations are reported to be successful. To a large extent, the success is of a mathematical nature. Indeed,

while investigating a few commercial IMRT planning systems at Stanford, we found that the plans computed by what are called optimization systems are not always within the expectation of the planner and that several trial-and-error adjustments of the system parameters might be required to achieve a clinically acceptable plan. Given a patient, the obtained plan can vary widely from one planer to the next, even within a department. Furthermore these IMRT treatment plans are often suboptimal for patient treatments. If IMRT is to have a genuine and broad impact on radiation therapy, a more adaptable and "intelligent" inverse planning must be developed.

In our opinion, the underlying reason for the inverse planning to be an intractable process lies in the existence of multiple free parameters (e.g., the prescribed doses to the target and sensitive structures, the importance factors of various structures, beam orientations) in the current IMRT dose optimization formalisms, and the lack of a more explicit relation between these parameters and the final dose distribution. The determination of these parameters is essentially a "guessing" game and multiple trial-and-errors are often needed. The influence of the free parameters on the final solution is not known until the optimization is performed.

With the development of fast inverse planning algorithms and the advancement of computer technology, it is possible to computationally determine an optimal set of importance factors¹⁵ or even to establish a computational environment in

which the importance factors are adjusted interactively during the optimization process.¹⁶ While facilitating the planning process, this approach is still not intuitive and transparent because of the implicit relation between the final plan and the parameters. On one hand, our plan selection decision making is based on the visual evaluation of the isodose distribution or DVHs. On the other hand, in order to modify the dose at a region or to change the shape of a DVH curve, we need to go back to the beginning of plan optimization process and modify some parameters whose role to the dose in the region of interest is known only vaguely. In reality, it is this vagueness or ambiguity that makes the inverse planning process difficult to control and tedious. If we proceed along the above procedure, the best we can achieve is to lower/increase the overall dose to a structure. Therefore, lack of control over the local doses within a structure has been considered as one of the major problems in inverse planning.

The question that we ask here is knowing the region(s) that is "hot" or "cold" for a given solution, or knowing the part of a DVH curve that we wish to modify, is it possible to directly identify the responsible parties in the parameter space and then vary them accordingly so that the dose distribution is improved toward our expectation? The difficulty is that the location of the hot/cold region that needs to be "tweaked" is not known until the "optimal" plan is obtained. Consequently, an "on-the-fly" mechanism is highly desirable to adaptively fine-tune the dose distribution after a solution close to the optimum is obtained. When this process is realized manually (that is, visually identifying the "hot" or "cold" regions on isodose plots or identifying the unsatisfactory part of a DVH curve using a computer mouse), it provides us with a natural adaptive planning environment. Toward establishing such an interactive planning environment, we introduce a new inverse-planning scheme in which the importance factors are defined on a voxel specific basis rather than on an anatomical structure basis. The new scheme provides an adaptive mechanism to fine-tune the local doses and enables us to adaptively search for plans that otherwise would be unreachable.

This paper is organized as follows. In Sec. II we provide some background knowledge on the modeling of the tradeoff strategies in inverse planning and summarize the useful features of the voxel-dependent tradeoff scheme. Issues related to the implementation of the voxel-dependent penalty scheme are also described. To demonstrate the utility of the new inverse planning scheme, we have applied it to study two clinical cases. The results will be summarized in Sec. III along with some in-depth discussion. We conclude in Sec. IV.

II. METHODS AND MATERIALS

In inverse planning, dose optimization is performed under the guidance of an objective function, which is defined as a global quantity derived from general physical considerations. Because the clinical objectives are usually multifaceted and potentially incompatible with one another, a set of structure-dependent importance factors^{15–18} is often incorporated in

the objective function to parametrize the trade-off strategies. After an "optimal" plan is computed for a trial set of importance factors, there are generally two types of dose modifications that may be needed in the target volume or a sensitive structure. One is the overall dose in a structure and the other is the dose in one or more sub-volumes of a structure. The former modification is generally handled by the trial-and-error adjustments of structure-specific importance factors. The latter situation occurs quite frequently in clinical IMRT planning and is problematic. In practice, it is not uncommon that just a few unsatisfactory regions of the target volume or a sensitive structure prevent an optimized plan from being clinically acceptable. For instance, in a prostate IMRT treatment, one may wish to control more freely the dose to the urethra and perhaps the dose at the prostate-rectum boundary. Unfortunately, with the structure-specific importance factors, the system is under-determined and the best we can do is to adjust the structure specific importance that influence not only the dose in the region of concern, but also in other part of the system.

The key to enhance the degree of controllability over the regional doses is to establish a more effective link between the local dosimetric behavior of the system and the system variables. According to the current inverse planning designs, parameters like importance factors, prescription doses, maximum doses, etc., are used to control the dosimetric behavior at an anatomical structure level. Although some degree of controllability is achievable, the option to influence purposely dose at specific points within structures is hardly possible. To solve this dilemma, we introduce voxel-dependent importance factors into the inverse planning as a means to control the infrastructural tradeoffs and describe a manual planning method in which the local importance factors are adaptively modified to meet our clinical requirements. With the use of the voxel-based penalty scheme, the regional penalty will not depend only on the dose discrepancy between prescription and calculated doses but also on the local importance information, which is based on *a priori* or *a posteriori* knowledge.

To proceed along the line described above, we write the importance factor at a voxel n as a product of two factors, an overall factor specific to the structure σ , r_σ , and a voxel dependent component describing the relative weighting of different voxels inside the structure, r_n . The r_σ 's parametrize the overall tradeoff strategy of different structures, whereas r_n 's characterize the inner-structural weightings. The conventional quadratic objective function now reads

$$F = \sum_{\sigma=1}^{N_\sigma} \left[\frac{1}{N_\sigma} \sum_{n=1}^{N_\sigma} r_\sigma \cdot r_n \cdot [D_c(n) - D_0(n)]^2 \right], \quad (1)$$

where N_σ represents the total number of voxels of a structure, $D_0(n)$ is the prescription dose and $D_c(n)$ is the calculated dose at each iteration. The dose calculation algorithm has been described in Ref. 19. While a quadratic objective function is used in this work, the methodology of using voxel-dependent importance factors to fine-tune an IMRT

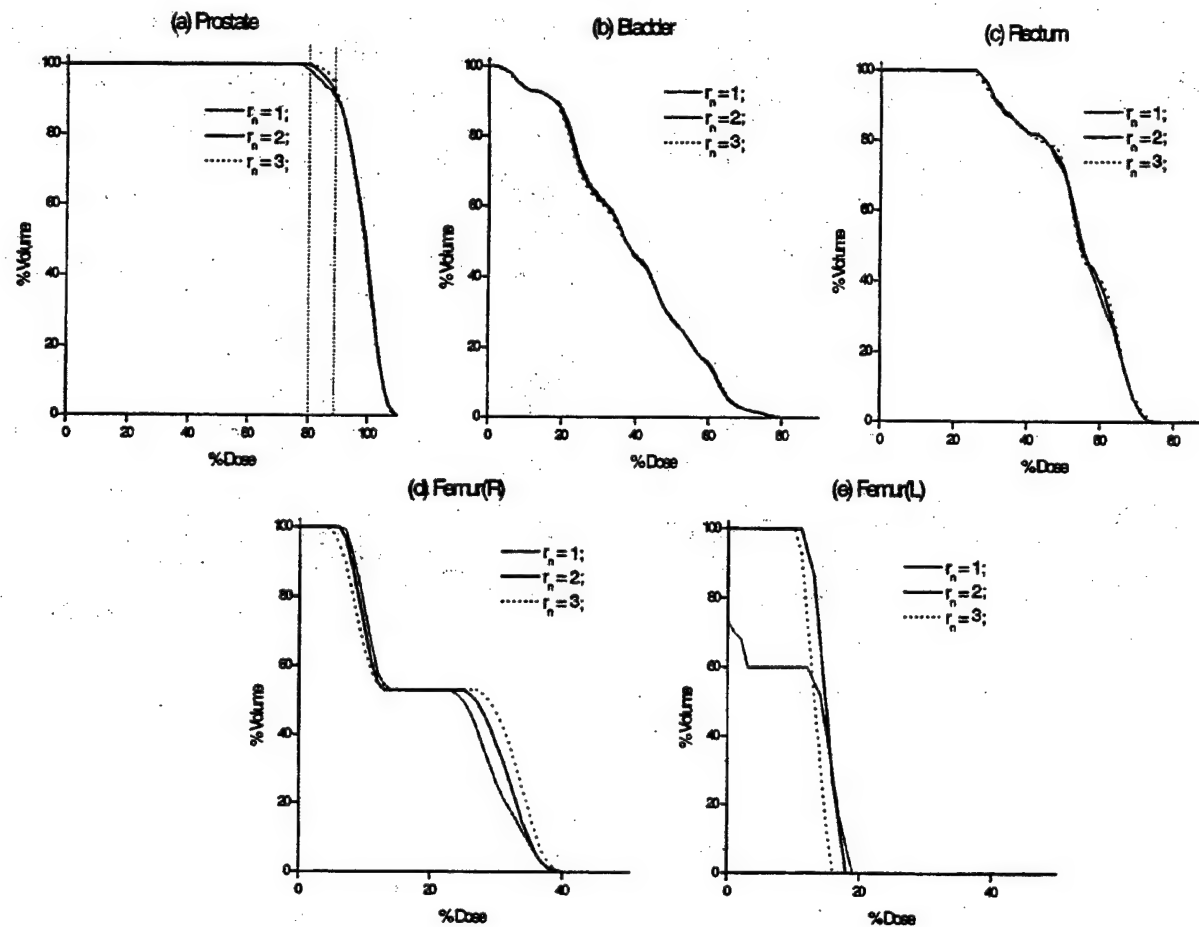


FIG. 2. DVHs of prostate (a), bladder (b), rectum (c), right femoral head (d), and left femoral head (e). The gray lines represent the conventional IMRT plan; the black solid and dotted lines correspond to plans optimized with regional importance factors of 2 and 3, respectively. These values were assigned for those voxels accounted within the vertical lines in (a).

and assigned to them a higher importance, $r_n = 2.0$. The black solid lines in Fig. 2 show the optimization results after this trial. The second attempt was made to further improve the prostate coverage. For this purpose, we reidentified the voxels that were still under dosed (below 88%) after the first trial and further increase the importance of the newly identified voxels to 3.0. The results after reoptimization are shown as dotted lines. Figures 2(b)–2(e) show the effect of increasing the local importance factors on the DVHs of the involved sensitive structures. As can be seen from Fig. 2, by using the local importance factors we were able to fine-tune the target doses flexibly. For instance, the prostate volume covered by the 85% isodose curve was increased by 5% after the two trials. In Fig. 3 we show the 85% isodose lines corresponding to the three optimized plans. The isodose line corresponding to the plan obtained with the largest voxel-based importance factors has the best target coverage and this is most distinct at the left posterior part of the prostate target.

A noticeable fact is that the bladder and rectum suffered minor but practically insignificant changes when the local importance factors in prostate were increased. The differences in the femoral head doses might be important, espe-

cially in the left one, where approximately 40% more of its volume got irradiated as the prostate dose coverage was improved. However, the dose increase to the left femoral dose did not violate any constraints, and is clinically acceptable. Physically, this effect was produced by the intensity increase in a set of beamlets in the left anterior beam (gantry angle 55 degree). This phenomenon is interesting and reminds us that, in dose optimization, there is generally no net gain. That is, the improvement in the dose to a structure is often accompanied by the dosimetrically adverse effect(s) at other points in the same or different structures. The important point to note is that from the clinical point of view, some dose distributions are more acceptable than others, and our goal is to find the solution that most improves the plan, with a clinically insignificant or acceptable sacrifice. In order to achieve this, it is necessary to have a direct control degree over the regional doses. In this sense we believe that the hereby-proposed method of dose shaping is valuable.

III. A. 2. Dose layout-based fine-tuning of hot spots in the prostate target

The second scenario considered here was the reduction of a hot spot within the prostate target. Inspecting the target

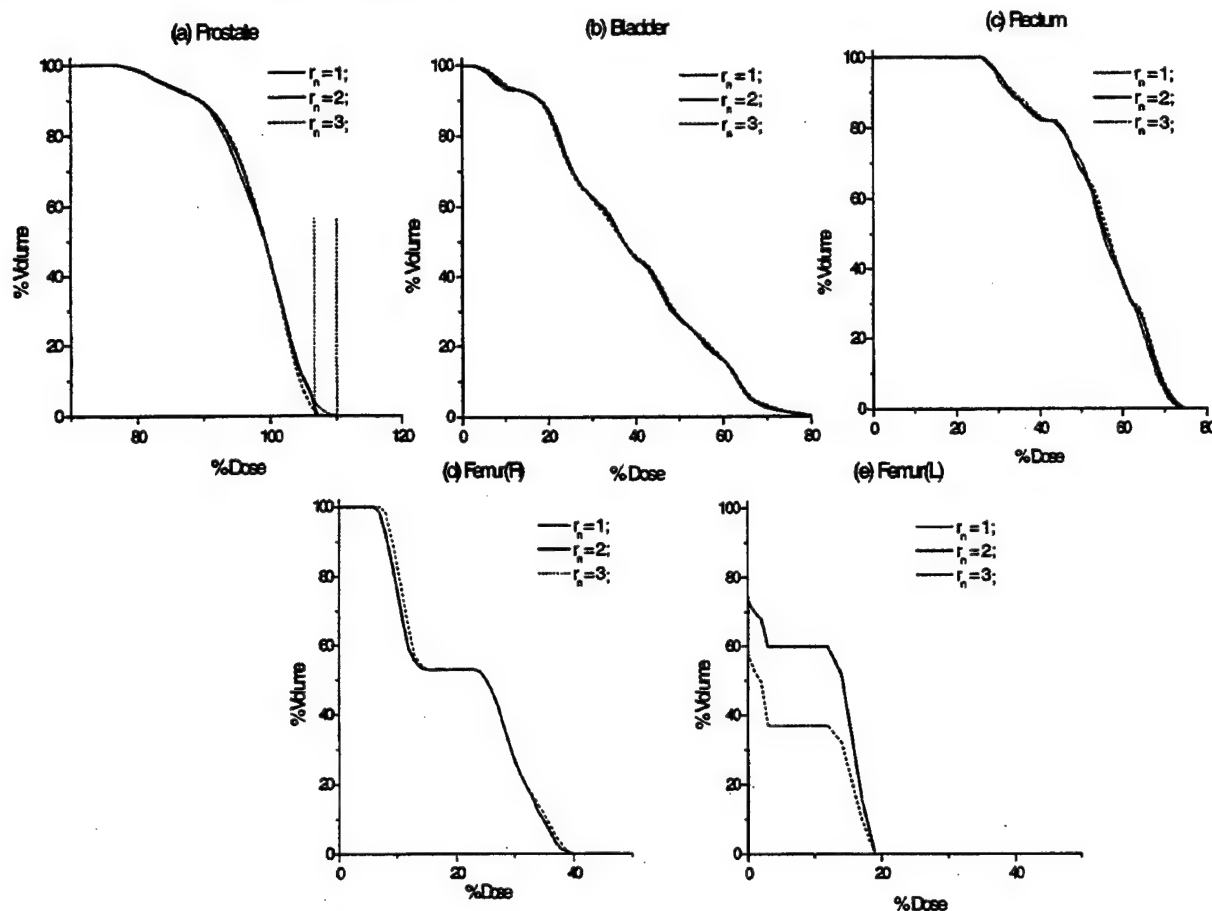


FIG. 6. DVHs of prostate (a), bladder (b), rectum (c), right femoral head (d), and left femoral head (e) for three IMRT plans. The gray lines represent the conventional plan; the black solid and dotted lines correspond to plans optimized with voxel importance factors of 2 and 3, respectively. These values were assigned for those voxels accounted within the 105–110 % dose interval [vertical lines in (a)].

cause the patient had already been treated with conventional techniques without cord sparing. In this study, five 6 MV nonequally spaced coplanar beams (95, 140, 175, 225, and 275 degrees—respecting the IEC convention) were used for the treatment. The structure specific importance factors and the prescription doses are shown in Table II. The DVHs of the conventional IMRT plan are plotted with gray lines in Fig. 8 (conventional optimization I).

As the patient was treated previously, one of the clinical concerns was to reduce the dose of the spinal cord to no more than 10 Gy (60% of the target prescription dose). Considering the results of the conventional optimization I, one way to achieve this goal would be to increase the overall importance factor of the spinal cord. The results of this approach are shown with black dashed lines in Fig. 8 DVH plot (conventional optimization II), where concomitantly to the target's homogeneity deterioration, the spinal cord DVH is entirely shifted towards lower doses. The maximum dose to the spinal cord with the new set of structure-dependent importance factor set is reduced with 6 units. A reduction of approximately 10 dose units of the spinal cord maximum dose can be achieved when instead, the fine-tuning scheme is used (see the black lines in Fig. 8). This improvement is

realized at the same expense for target homogeneity, as for the IMRT optimized plan II, and insignificant changes of the liver and kidney doses. The fine-tuning proceeded by identifying the corresponding voxels that received doses in the 60–70 % interval (marked with vertical lines in Fig. 8) and assigning them with a higher importance, $r_n = 3.0$. After re-optimization we obtained the DVHs shown by the black solid lines in Fig. 8. While the maximum spinal cord dose was reduced by 10% and the DVHs of the other two structures (liver and kidney) suffered only slightly. The tumor coverage becomes worse than that of the conventional optimized plan, as a consequence of reducing the spinal cord dose. This is similar to the scenario discussed in Sec. III A 1.

We would like to emphasize here that the introduction of the voxel-dependent importance factors changes the IMRT objective function. Consequently, the optimization algorithm is allowed to explore regions of the objective space that were inaccessible when only uniform importance factors were used. In this sense the number of the accessible solutions of the conventional IMRT optimization is increased when local importance factors are used.

To give an example, we used the conventional inverse planning regime to reduce the spinal cord dose by simply



FIG. 7. Isodose distribution of a paraspinal IMRT treatment plan.

increasing the overall importance of the spinal cord. For fair comparison, we have attempted to make the tumor DVH the same as for the plan fine-tuned by modulating local importance factors (e.g., dotted lines in Fig. 8). The two sets of DVHs are shown in Fig. 8 along with the original IMRT plan. In general, the voxel-based planning scheme produced a solution that follows more closely our expectation, that is, to differentially reduce the fractional cord volume that receives a dose higher than 60% of the prescription. This is reflected by two things: (1) for the same tumor coverage, the reduction of the maximum spinal cord dose is greater in the plan obtained using voxel dependent importance factors; and (2) in comparison to the new plan with structure specific importance (dotted line), the DVH curve obtained using voxel-based importance factors deviated less from the original plan (black solid line) in the part that is specified (implicitly) not to change.

IV. CONCLUSIONS

Inverse planning is at the foundation of IMRT and its performance critically determines the success of an IMRT treatment. Unfortunately, the currently available IMRT dose optimization formalism is deficient and the solutions resulting from the so-called "optimization" systems are often sub-optimal or even not optimal at all. Considerable effort may

TABLE II. Summary of the parameters used for obtaining the paraspinal tumor conventional optimized plan.

Relative importance factors	Target prescription and OAR tolerance doses	
	GTV	1.00
Spinal cord	0.030	0.30
Liver	0.005	0.40
Kidney	0.050	0.30
Tissue	0.055	0.75

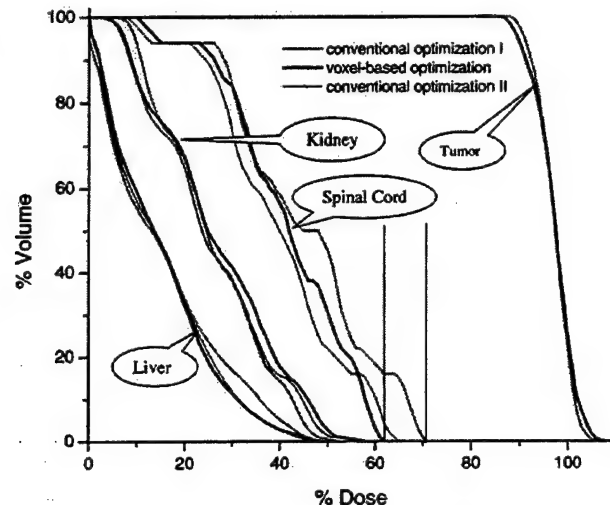


FIG. 8. Comparison of three IMRT plans: gray solid lines show the DVHs for a conventional IMRT plan which was subsequently reoptimized using regional importance factors (black solid lines). The third plan (dotted lines) is obtained conventionally, by raising the importance of the spinal cord structure, until the target DVH became similar to the re-optimized plan (black solid lines).

be required to compute a clinically acceptable plan and the final results may strongly depend on the planner's experience and understanding of the planning system. We have proposed and demonstrated an interactive inverse-planning scheme with voxel-dependent importance factors. The approach offers the planner an effective tool to fine-tune an IMRT dose distribution and makes the dose optimization process more tractable and controllable. While the local penalty was varied by the local importance factors, in practice we believe that it is also possible to achieve the same or similar effect by other means, e.g., by changing the form of the penalty function, or the prescription values. In order to modify the dose at a specific region, in principle, one can also use ray-tracing to find the beamlets that intercept the considered volume and adjust their intensities accordingly. The problem is that there are numerous ways to change and the optimal arrangement of the beamlet intensities is not obvious. We have, for the first time, pointed out that the local dosimetric behavior can be more effectively controlled by introducing a voxel-dependent penalty scheme and demonstrated the utility of the approach using a model system as well as clinical examples. Finally, we mention that the inverse planning formalism proposed in this paper might be used to other variants of IMRT, such as tomotherapy and intensity modulated arc therapy. Furthermore, it may be worthwhile to be tested for other modalities like prostate implants, gamma knife, micro-MLC based stereotactic treatments.

ACKNOWLEDGMENTS

We wish to thank Dr. Steven Hancock, Dr. Sarah Donaldson, Dr. Quynh-Thu Le, Dr. Christopher King, Dr. Arthur Boyer, and Dr. Gary Luxton for many useful discussions on the subject. This work was partly supported by a Research

Scholar Award from the American Cancer Society (RSG-01-022-01-CCE) and a research grant from the Department of Defense (BC996645).

- ^aAuthor to whom correspondence should be addressed. Electronic mail: lei@reyes.stanford.edu
- ¹T. Bortfeld, J. Burkhardt, R. Boesecke, and W. Schlegel, "Methods of image reconstruction from projections applied to conformation radiotherapy," *Phys. Med. Biol.* **35**, 1423–1434 (1990).
 - ²S. Webb, "Optimisation of conformal radiotherapy dose distributions by simulated annealing [published erratum appears in *Phys. Med. Biol.* **35**, 297 (1990)]," *Phys. Med. Biol.* **34**, 1349–1370 (1989).
 - ³S. M. Morill, R. G. Lane, J. A. Wong, and I. I. Rosen, "Dose-volume considerations with linear programming optimization," *Med. Phys.* **18**, 1201–1210 (1991).
 - ⁴I. I. Rosen, R. G. Lane, S. M. Morill, and J. A. Belli, "Treatment plan optimization using linear programming," *Med. Phys.* **18**, 141–152 (1991).
 - ⁵L. Xing and G. T. Y. Chen, "Iterative algorithms for inverse treatment planning," *Phys. Med. Biol.* **41**, 2107–2123 (1996).
 - ⁶S. V. Spirou and C. S. Chui, "A gradient inverse planning algorithm with dose-volume constraints," *Med. Phys.* **25**, 321–333 (1998).
 - ⁷G. H. Olivera, D. M. Shepard, P. J. Reckwerdt, K. Ruchala, J. Zachman, E. E. Fitchard, and T. R. Mackie, "Maximum likelihood as a common computational framework in tomotherapy," *Phys. Med. Biol.* **43**, 3277–3294 (1998).
 - ⁸Q. Wu and R. Mohan, "Algorithms and functionality of an intensity modulated radiotherapy optimization system," *Med. Phys.* **27**, 701–711 (2000).
 - ⁹T. Holmes and T. R. Mackie, "A comparison of three inverse treatment planning algorithms," *Phys. Med. Biol.* **39**, 91–106 (1994).

- ¹⁰G. Starkschall, A. Pollak, and C. W. Stevens, "Treatment planning using a dose-volume feasibility search algorithm," *Int. J. Radiat. Oncol., Biol., Phys.* **49**, 1419–1427 (2001).
- ¹¹P. S. Cho, S. Lee, R. J. Marks II, S. Oh, S. G. Sutlief, and M. H. Phillips, "Optimization of intensity modulated beams with volume constraints using two methods: cost function minimization and projections onto convex sets," *Med. Phys.* **25**, 435–443 (1998).
- ¹²R. Mohan, G. S. Mageras, B. Baldwin, L. J. Brewster, G. J. Kutcher, S. Leibel, C. M. Burnam, C. C. Ling, and Z. Fuks, "Clinically relevant optimization of 3D conformal treatments," *Med. Phys.* **19**, 933–944 (1992).
- ¹³A. Brahme, "Optimized radiation therapy based on radiobiological objectives," *Semin Radiat. Oncol.* **9**, 35–47 (1999).
- ¹⁴X. H. Wang, R. Mohan, A. Jackson, S. A. Leibel, Z. Fuks, and C. C. Ling, "Optimization of intensity-modulated 3D conformal treatment plans based on biological indices," *Radiother. Oncol.* **37**, 140–152 (1995).
- ¹⁵L. Xing, J. G. Li, A. Pugachev, Q. T. Le, and A. L. Boyer, "Estimation theory and model parameter selection for therapeutic treatment plan optimization," *Med. Phys.* **26**, 2348–2358 (1999).
- ¹⁶L. Xing, J. G. Li, S. Donaldson, Q. T. Le, and A. L. Boyer, "Optimization of importance factors in inverse planning," *Phys. Med. Biol.* **44**, 2525–2536 (1999).
- ¹⁷L. Xing, C. Pelizzari, F. T. Kuchnir, and G. T. Chen, "Optimization of relative weights and wedge angles in treatment planning," *Med. Phys.* **24**, 215–221 (1997).
- ¹⁸C. Cotrutz, M. Lahanas, C. Kappas, and D. Baltas, "A multiobjective gradient-based dose optimization algorithm for external beam conformal radiotherapy," *Phys. Med. Biol.* **46**, 2161–2175 (2001).
- ¹⁹C. Cotrutz, C. Kappas, Y. Theodorakos, C. Makris, and R. Mohan, "Development in a Windows environment of a radiation treatment planning system for personal computers," *Comput. Methods Programs Biomed.* **56**, 261–272 (1998).

Modulated Electron Radiation Therapy (MERT): A Comparative Dosimetric Study of MERT and IMRT for Parotid Cancers

Yulin Song, Ph.D.¹, Todd Pawlicki, Ph.D.¹, Lei Xing, Ph.D.¹, Michael C. Lee, Ph.D.³,
Steve Jiang, Ph.D.², Yulong Yan, Ph.D.¹, C-M Charlie Ma, Ph.D.⁴, and Arthur L. Boyer, Ph.D.¹

Departments of Radiation Oncology,

¹Stanford University School of Medicine, Stanford, CA 94305

²Massachusetts General Hospital

Harvard Medical School, Boston, MA 02114

³University of California at San Francisco, CA 94115

⁴Fox Chase Cancer Center, Philadelphia, PA 19111

Running Title Header: Radiotherapy for Parotid Cancers

Keywords: Monte Carlo, IMRT, MERT, EMLC, MLC, and Parotid Cancer

Address Correspondence to:

Arthur L. Boyer, Ph.D., Director
Division of Radiation Physics
Department of Radiation Oncology
300 Pasteur Dr., Room H0144
Stanford University School of Medicine
Stanford, CA 94305-5304
Tel: (650)-723-5549
Fax: (650)-498-5008
E-mail: boyer@reyes.stanford.edu

ABSTRACT

In this study, we investigated treating parotid cancers using modulated electron radiation therapy (MERT) and compared MERT plans with photon beam intensity-modulated radiation therapy (IMRT) in terms of target dose coverage and normal tissue sparing. To deliver MERT plans effectively, we developed a MERT delivery device – an electron multileaf collimator (EMLC) for routine clinical implementation of MERT.

A prototype electron multileaf collimator was fabricated by modifying a conventional $25 \times 25 \text{ cm}^2$ electron applicator (Varian Medical Systems, Palo Alto, CA). Electron beams produced by a linac (Clinac 2100C, Varian Medical Systems, Palo Alto, CA) and collimated by this EMCL were simulated using the EGS4/BEAM code. The simulations were based on the manufacturer's specifications of the beam production system and the electron applicator design. The MERT plans with three coplanar beams (205° , 235° , and 255°) and five nominal energies (6, 9, 12, 16, 20 MeV) were created using modified EGS4/MCDOSE code. The corresponding IMRT plans with five coplanar beams were computed using a commercial treatment planning system (CORVUS, NOMOS Corp, Sewickley, Pennsylvania). Our preliminary data indicated that MERT was able to provide at least similar or better target dose coverage and uniformity compared with photon beam IMRT. However, MERT can significantly reduce the dose to critical structures. In the cases we studied, the maximum doses to the orbits, brainstem, optic chiasm, and spinal cord were reduced by 3.0, 16.2, 11.5, and 19.6 Gy, respectively, for a 50 Gy target dose, suggesting a distinct normal tissue sparing advantage for MERT.

INTRODUCTION

Each year, about 70,000 new head and neck cases were diagnosed in the United States [1] and tumors of the parotid gland are the most frequently encountered salivary gland tumors, accounting for about 3% of total head and neck cancers [2]. Currently, the most widely used treatment is a combination of surgery and adjuvant postoperative radiotherapy for the malignant salivary tumors [3, 4]. The minimally required operation for tumors of the parotid gland is a superficial parotidectomy with careful identification and preservation of the facial nerve [5]. The parotid gland has two lobes, a superficial lobe and a deep lobe. Most tumors are located in the superficial lobe of the parotid gland and can be excised easily. Retrospective studies have indicated that this combined modality treatment can reduce the local recurrence rate by 5 - 40% [6, 7].

However, in certain situations, such as high surgical risk of damage to the facial nerve, advanced inoperable cancers, unfavorable cosmetic outcome after surgery, lymph node metastases, and deep-lobe malignant tumors, radiotherapy should be the preferred treatment [5]. Because of its proximity to many critical structures, such as the brainstem, spinal cord, optical nerves, and the lenses of the eyes, parotid cancer treatment using radiation still remains a very challenging task. Currently, the most commonly used radiotherapy techniques for the treatment of the parotid cancers are: 1) an ipsilateral wedged pair of 6 MV photon beams oriented at oblique angles to encompass the entire parotid bed, 2) an ipsilateral field treated with high energy electrons (12, 16 or 20 MeV), and 3) a combination of high energy photon and electron beams (6 MV + 12 or 16 or 20 MeV) with proper weighting [8, 9, 10] (**Figure 1**). However, all these techniques have drawbacks. The first technique gives a low radiation dose to the contra-lateral parotid gland and high doses to oral cavity, brainstem, cochlea, optical nerves, the lenses of the eyes, and spinal cord. In addition, because relatively high energy photon beams are used, the slow build-up effect of the photon beams results in a low skin dose. This is not acceptable for the treatment of the majority of the parotid cancers because most parotid

cancers are located in the superficial lobe of the parotid gland. Although the second technique may be the best in terms of normal tissue sparing, it is impossible to achieve depth dose conformity with single electron energy only. The third technique typically employs a high energy electron beam (12-20 MeV) and a single 6 MV photon beam. However, good matching of photon and electron beams is not easy to achieve and poor matching may produce areas of highly inhomogeneous tumor dose distribution.

Recently, with rapid advances in photon beam intensity modulated radiation therapy (IMRT) and the computer-controlled multileaf collimator (MLC), there has been a trend towards using photon beam IMRT to treat the head and neck cancers and the parotid cancers in particular [9, 11-16]. A common feature of the head and neck cancers is their complex geometry. IMRT has the great potential to produce highly conformal dose distribution around the concave-shaped target volumes and steep dose gradient near the organs at risk (OAR), thus it can spare radiosensitive normal structures and reduce complication rates [17-19]. In addition, IMRT can improve local-regional tumor control through dose escalation. Now, many commercial inverse treatment planning systems and MLCs are available.

Although the photon beam IMRT is a very powerful tool for treating the parotid tumors that extend deeply into tissue below the skin surface, it is not suitable to treat very shallow targets due to the low surface doses and large depth of photon beam penetration. For photon beam IMRT, the slow attenuation of photon beams can still deliver a high dose to the critical structures that are far from the target. A promising alternative approach is modulated electron radiation therapy (MERT) [20-21]. The rapid dose falloff of electron beams makes the electron therapy an ideal treatment modality for some shallow targets like parotid tumors. In general, each MERT plan consists of multiple ports (gantry angles) with different electron energies (energy modulation) and optimized beam intensity (intensity modulation). Dose conformity in the depth direction may be achieved by electron energy modulation, which is unique to MERT. Dose conformity and

uniformity in the lateral direction may be achieved by intensity modulation using an electron-specific MLC (EMLC), which is similar to photon beam IMRT. Through both intensity and energy modulations, MERT is capable of delivering highly conformal doses to targets with complex shapes and sparing surrounding and, particularly, the distal critical structures.

However, because of severe electron in-air scattering, conventional photon beam MLC is not suitable for the delivery of MERT plans. To deliver MERT plans effectively, we designed and manufactured a prototype EMLC based on the results of our Monte Carlo simulations and a conventional Varian 25 x 25 cm² electron applicator [22]. Based on the manufacturer's specifications of the beam production system and the EMLC design, electron beams collimated by this EMLC were simulated for a Varian Clinac 2100C linear accelerator using the EGS4/BEAM code [23, 24]. Subsequently, using the simulated electron beams, MERT plans for parotid cancers were created. In the present study, we investigated the possibility of treating parotid tumors using modulated electron radiation therapy by comparing MERT plans with corresponding photon beam IMRT plans in terms of target dose coverage and normal tissue sparing.

MATERIALS AND METHODS

Electron MLC

We have previously reported a prototype manually-driven electron specific MLC for the delivery of MERT plans [20, 21]. Ideally, the EMLC leaves should be placed in such a position that the bottom of the leaves is as close to the patient skin as possible in order to produce a clinically acceptable field. However, because of the existing electronic circuitry used to detect the insertion of the electron cutout at the last scraper of a standard Varian 25 x 25 cm² electron applicator, it was impossible to place the EMLC leaves at that position without changing the existing electron applicator design significantly. Thus, initially, the steel frame of the EMLC leaves was temporally inserted into the electron

cutout mount and the leaves were placed about 1 cm above the last scraper. This configuration resulted in a 10 cm air gap between the bottom of the EMLC leaves and the patient skin for a nominal 100 cm source-surface distance (SSD) (**Figure 2 (A)**). To further lower the EMLC leaves and, thus, reduce in-air electron scattering and the penumbra, we have now removed the entire last scraper of the electron applicator and its electronic accessories. The EMLC frame was placed at the bottom of the modified electron applicator and stabilized with eight screws. This modification greatly reduced the air gap (5.0 cm) between the bottom of the EMLC leaves and the patient skin (**Figure 2 (B)**). Since the electronic circuitry for detecting the electron cutout was completely removed, we were able to avoid activating interlocks associated with electron beam accessory malfunction while inserting the EMLC assembly into the linac treatment head. Thus, even if the linac was in the electron mode, the gantry could still be rotated, making the delivery of MERT plans with multiple beam angles possible.

MERT Plans

Based on manufacturer's specifications of the beam production system and the electron applicator design, electron beams produced by a Varian Clinac 2100C linear accelerator and collimated by the EMLC were simulated using the EGS4/BEAM code. Monte Carlo simulations were carried out using a group of 22 Pentium Pro CPUs (200 MHz) and 10 Pentium III CPUs (450 MHz), all running EGS4/BEAM, MCDOSE [23, 24], and their utilities under the Linux operating system. All simulation parameters, such as the electron and photon energy cutoffs (ECUT and PCUT), the maximum fractional energy loss per electron step (ESTEPE), and the number of initial electron histories, were specified in the EGS4/BEAM input file. In this study, we used ECUT = 700 KeV and PCUT = 10 KeV, below which all remaining energy was assumed to deposit on the spot. ESTEPE was set to 0.04. The EMLC was included in the EGS4/BEAM simulations as an MLC component module. The number of initial electron histories ranged from 2-30 million, depending on the electron energy. Phase space data were scored at a plane of 100 cm SSD after the particles had transported through the linac treatment head, the EMLC,

and the air gap beneath it. Based on this simulated electron beam, the MERT plans were then created using our modified EGS4/MCDOSE code.

The CT scans of representative parotid cancer patients were obtained from our department's patient database. The CT images were acquired with the patients in supine position. During CT scanning, a thermoplastic facial mask with three fiducials was used for the purpose of patient immobilization and target localization for the subsequent treatments. For each patient, about 90 images with a slice thickness of 3 mm were acquired over the entire treatment area. Each CT image had 512 x 512 voxels, with each being $0.94 \times 0.94 \times 3 \text{ mm}^3$ in size. The CT images were transferred to an AcQSim system (Marconi Medical Systems, Inc., Cleveland, OH) for further processing. The clinical tumor volume (CTV) and critical structures were contoured on the axial CT images by a radiation oncologist using AcQsim. The gross tumor volume (GTV) was defined based on diagnostic imaging and clinical findings. It consisted of gross primary and nodal tumors. The CTV was constructed by expanding GTV 1.0 cm in all directions to cover microscopic extension of the tumor. Like photon beam IMRT, any structures whose dose needs to be kept below a certain limit or whose statistics must be calculated in the MERT plan must be contoured. Only those targets and structures that have been contoured will be planned for and included in the final statistics. In addition, in order for our MERT inverse planning programs to work properly, all regions of interest must be delineated as separate structures. No structure overlapping is allowed for the current version of our programs. In this study, the critical structures to be protected were the spinal cord, brainstem, optical chiasm, optical nerve, and orbits. The CT images, along with the outlined structures, were converted from the DICOM 3.0 format into a format that was compatible with EGS4/MCDOSE code and then sent to our designated Monte Carlo treatment planning machines. The final CT images used in MERT planning had an in-plane resolution of 128 x 128 with a voxel size of $0.35 \times 0.35 \times 0.30 \text{ cm}^3$ in order to reduce the Monte Carlo dose calculation time. Additionally, the CT numbers were converted into mass densities and material types for Monte Carlo simulations. Based on

the CT numbers, each voxel was designated as being one of the three materials: air, tissue or bone. This provided the appropriate effective atomic numbers, cross-sections, and stopping powers for each voxel.

Figure 3 shows the simplified MERT planning flowchart. To facilitate the description of the flowchart, we will use the term *field* to specify each beam orientation/electron energy combination and reserve the term *port* to indicate a single beam orientation (gantry angle). Thus, a plan in which five electron energies are delivered at a single gantry angle may be said to have one port and a total of five fields. In this study, the MERT plans consisted of three ports and a total of fifteen fields, as summarized in **Tables 1 and 2**. Like the photon beam IMRT, the first step in creating a MERT plan was to select a set of suitable beam orientations, i.e., gantry angles, to fully cover the target volume while sparing the adjacent critical structures as much as possible. Each port was then divided into $1.0 \times 1.0 \text{ cm}^2$ beamlets, i.e., the smallest beam elements for dose calculation. This means that beam intensity within a $1.0 \times 1.0 \text{ cm}^2$ beamlet could not be further differentiated. The beamlet size was defined at the isocenter plane. The goal of this step was to determine how many beamlets were required to simulate for each port. The user specified the isocenter, gantry, collimator, and couch angles, the desired beamlet size, and the dimension of the search space. A program calculated which beamlets intersected the target and created a text file containing these beamlets and their coordinates. This file was used by MCDOSE to pre-calculate the beamlet dose kernels. The total number of beamlets was the sum of the beamlets over all ports. A beamlet could be turned off, i.e., assigned a weight of zero, but continued to remain active throughout optimization. After the selection of a proper set of beam angles, we needed to decide which electron energies to use for each beam angle. To do so, we computed a tumor depth map for each beam angle, whose pixel size was the same as that of a beamlet, i.e., $1.0 \times 1.0 \text{ cm}^2$. Based on the tumor depth distribution and electron losing energy at about 2 MeV/cm in tissue, we were able to determine a suitable set of electron energies for each beam angle. Since, in most of the cases, the target was not spherical in shape, different

beam angles could have different sets of electron energies. The obvious advantage of this approach was the removal of those electron energies that contributed less to the target dose and, thus, the reduction in the number of fields used and delivery time.

The next step was to calculate beamlet dose kernels using MCDOSE. The beamlet dose kernel was the Monte Carlo calculated dose array for all structures due to a single beamlet. Each element of the dose kernel represented the dose delivered to a dose calculation point or voxel assuming a unit beamlet weight. These values are also called dose deposition coefficients. Thus, the purpose of this step was, given a set of unit beamlet weights, to calculate the dose distribution in every structure that we were interested in. As mentioned earlier, every structure of interest must be delineated, including normal tissues, in order to be included in the subsequent optimization process and dose statistics. To optimize beamlet weights or intensity maps, a quadratic objective function augmented with dose-volume constraints was constructed. This was based on the assumption that there existed a quadratic relationship between the delivered dose and the biological effect. The overall objective function contained a linear component for each structure. Within each structure, each of the individual constraints contributed linearly to the objective function. Following the construction of the objective function, the optimization of beamlet weights was initiated. The core of the optimization procedure was the well-known conjugate gradient search algorithm. The complete descriptions of the technique may be found in any number of sources. The major advantage of the gradient search technique was its fast convergence speed, as compared to stochastic optimization techniques, such as simulated annealing. We believe that the gradient search algorithm was a good choice for our future routine clinical implementation of MERT. During the optimization, care was exercised to avoid negative weights. These non-physical results were eliminated by scaling step sizes to avoid stepping over the boundary of the acceptable solution space and by projecting gradients onto the boundaries.

Following the beamlet weight optimization, the resulting fifteen optimized continuous intensity maps were stratified into five discrete intensity levels in preparation of leaf sequencing. The fifteen discrete intensity maps were then converted to fifteen step-and-shoot leaf sequences [26] based on the technique proposed by Bortfeld et al. [27]. Since the dose distribution delivered by the ideal beamlets could be different from that delivered by the leaf sequences, Monte Carlo dose calculation was performed again based on the fifteen discrete intensity maps reconstructed from the corresponding fifteen leaf sequences. With these new dose kernels, the leaf sequence segment weights were re-optimized. This second optimization differed from the first one in two aspects. The first optimization was entirely based on idealized beamlets, without considering the EMLC geometry, while the second optimization took not only the EMLC geometry, but also leaf end transmission and Bremsstrahlung leakage into account. Thus, the first optimization produced the best dose distribution possible, while the second one gave the actual delivered dose.

The MERT plans with three coplanar beams (gantry angles: 205^0 , 235^0 , and 255^0) were created using our modified EGS4/MCDOSE treatment planning system. The PTV was obtained by adding a 0.5 cm margin uniformly to CTV to account for patient setup uncertainty and organ shift. The schematic layout of the beam orientations is shown in **Figure 4A**. The beam orientations were selected based on the goodness of target coverage by the beams. Each gantry angle or port was treated with five nominal electron energies (6, 9, 12, 16, and 20 MeV) separately. The intensities of each energy for each particular gantry angle were determined by the optimizer. The prescribed dose to the target was 50.0 Gy, with a conventional fractionation scheme of 2.0 Gy per fraction, 5 fractions per week, and 25 fractions in total. The goal of the treatment planning was to cover the entire target with isodose lines between 95% and 107% of the prescribed dose as recommended by ICRU Report No. 50 [25]. Isodose lines were normalized to 55.0 Gy for all plans.

IMRT Plans

The CT images, together with the outlined structure set, were transferred from the AcQSim system to a commercial treatment planning system (CORVUS, NOMOS Corp, Sewickley, Pennsylvania). The corresponding photon beam IMRT plans were computed using our standard clinical protocol. As in the MERT planning, the PTV was defined by adding a 0.5 cm immobilization and localization uncertainty to the CTV. CORVUS IMRT system allows the target volume to grow based on a user-specified positional uncertainty caused by tissue motion and setup errors. The isocenter of the beams was placed approximately at the geometric center of the target. The goal dose to the target was 50.0 Gy, with the minimum and maximum doses being 49.0 Gy and 54.0 Gy, respectively. CORVUS IMRT system also allows the user to specify a percent target volume allowed below the goal dose. In this study, we used 4% for this value. For the critical structures, the limit dose ranged from 37.0 to 42.0 Gy, with the volume allowed above the limit dose being 5%. The maximum allowable dose to the critical structures was set to be 40.0 Gy. IMRT plans using other combinations of the dose volume constraints were also tried. It was found that above-described constraints gave a fairly good plan in terms of target dose coverage and conformity and critical structure sparing. The final IMRT plans consisted of five coplanar gantry angles, each being treated with a 4 MV photon beam. The gantry angles and beam energy were selected in such a way as to minimize unnecessary normal tissue and critical structure irradiation. However, in this study, beam orientations were not optimized. IMRT plans of different beam number and angle combinations were generated. Each of the plans was carefully reviewed and evaluated on the basis of target dose coverage and normal tissue sparing. Plan evaluation indicated that the plans with coplanar beams : 0° , 205° , 235° , 270° , and 320° gave the best results. Therefore, this beam arrangement was used in this study. Isodose lines were also normalized to 55.0 Gy for all IMRT plans. **Figure 4B** shows the IMRT beam orientations.

Tissue heterogeneity correction was performed during the beamlet intensity optimization and final dose calculation. Like the MERT planning system, CORVUS IMRT system also uses an integral dose volume histogram-based cost function. The current version of CORVUS IMRT software supports only one optimization technique, simulated annealing [28]. To obtain the best possible beamlet intensities and thus, the optimal dose distribution, the optimizer mode was set to continuous. This mode determines the internal representation of the beamlet intensities and is, in general, the best choice for most treatment plans. All IMRT plans used in this study were created based on a Varian Clinac 2100C linear accelerator and delivered in step-and-shoot mode. The machine was equipped with a standard 26-leaf pair photon MLC, capable of producing $1.0 \times 1.0 \text{ cm}^2$ beamlets.

RESULTS AND DISCUSSION

Electron MLC

Figure 5 shows a photo of the EMLC assembly inserted on the treatment head of a Varian Clinac 2100C linear accelerator. The EMLC had 30 steel leaf pairs, with each leaf being 0.476 cm wide, 20.0 cm long, and 2.54 cm thick. Both sides and ends of the leaves were made parallel with the central beam axis. The maximum opening was $14.2 \times 15.5 \text{ cm}^2$ when all leaves were completely retracted, giving the largest radiation field of $15.0 \times 16.3 \text{ cm}^2$ projected at 100 cm SSD. The EMLC leaves can be pushed in and pulled out easily. For each of the beam segments, the corresponding field shape was obtained by manually positioning the leaves according to their coordinates, which were computed from our electron beam leaf-sequencing program. To set the field shapes more efficiently, currently, we first drew the field shapes on a piece of hard cardboard at a ratio of 1:1 and cut them out. The field shapes were then set using these pre-cut cardboards. In the near future, we will develop a faster and more accurate technique of setting field shapes. To evaluate the functionalities of this newly modified EMLC, preliminary experimental measurements were also performed and the results will be reported in a separate report.

In the past, people have attempted to use a photon MLC for electron beam collimation [30]. Using a photon MLC in this circumstance has its obvious advantages. On one hand, treatment planners could easily make plans that consist of both photon and electron beams. On the other hand, the plans could be delivered using the existing linear accelerators without any further capital investment. Unfortunately, because of the severe electron scattering in the air, the quality of the electron beam collimated by a photon MLC is significantly degraded and is no longer clinically useful. Here, we present a practical and viable approach to the electron beam collimation — an electron-specific MLC. Our results indicated that the newly modified EMLC was able to provide sufficient beam collimation for MERT plan delivery.

Intensity Maps

Figure 6A shows a 3-D beam's eye view of a representative parotid tumor viewed at the beam angle of 235^0 . **Figure 6B** shows the corresponding tumor depth map, in which different pixel gray scale levels represent different depths of the target. Darker pixels indicate the area where the tumor extended deeper into the tissue at this particular beam angle. As clearly demonstrated in the tumor depth map, this case was a good candidate for a MERT treatment because the target was superficial and, in addition, it had an irregular boundary. Based on the tumor depth map, a histogram was created, showing the tumor depth distribution (**Figure 7**). Out of 189 pixels, 99 pixels had a depth of greater than or equal to 5.0 cm, accounting for more than 50% of the total pixels. 37 pixels had a depth of 4.0 cm, 21 pixels had a depth of 3.0 cm, and 32 pixels had a depth of below 2.0 cm. Thus, the electron beams of 12, 16, and 20 MeV would be the best choices for this case in terms of depth dose conformity at this angle.

However, for this preliminary study, we chose to use all available electron energies. **Figures 8A to 8E** show representative beam intensity maps for a MERT plan for the 6, 9, 12, 16, and 20 MeV fields at the beam angle of 235^0 . In all figures, each pixel represents a $1 \times 1 \text{ cm}^2$ beamlet projected at the isocenter. Darker pixels indicate higher

beam intensity levels, which correspond to a longer beam on time. White background indicates zero beam intensity. These are the areas where beams were blocked all the time by the EMLC leaves. In reality, however, there was about 1% radiation leakage through the EMLC leaves. As can be seen in the intensity maps, the optimizer gave significant weights to the 12, 16, and 20 MeV fields, while small weights were assigned to the 6 and 9 MeV fields. It was these different electron energy weights that brought about the energy modulation. By carefully examining the intensity maps and the tumor depth map, we noticed that the MERT intensity maps largely reflected the tumor depth distribution. The superposition of these intensity maps yielded not only the optimal lateral dose conformity, but more importantly the optimal depth dose conformity. The numbers of segments needed to produce these intensity maps were 18, 18, 12, 18, and 14 for the 6, 9, 12, 16, and 20 MeV fields, respectively, giving a total of 80 segments for this port. This number was comparable to the number of segments for a photon field in a typical IMRT head and neck plan. For comparison, the corresponding optimized photon beam IMRT intensity map for the 4 MV field at the same beam angle is shown in **Figure 8F**. This intensity map, actually consisting of two separate maps, was combined together manually. This was because the size of the target in the anterior-posterior direction was fairly large, the MLC leaves could not cover the entire target with one field only. Thus, this 235^0 port split into two sub-fields. Like the MERT intensity maps, each pixel in the photon beam IMRT map represents a $1 \times 1 \text{ cm}^2$ beamlet projected at the isocenter. Compared to its MERT counterparts, the photon beam IMRT intensity map shows a relatively uniform intensity distribution, indicating a lack of depth dose modulation. The combined photon beam IMRT intensity map required a total of 120 segments to deliver, divided into 62 and 58 segments for each sub-field, respectively. For both the MERT and the IMRT plans, we counted both “step” and “shoot” that were listed in the step-and-shoot leaf sequence files as a segment. Thus, in the case of the combined photon beam IMRT intensity map, it required 60 steps and 60 shoots to produce. Since the delivery time is linearly proportional to the number of segments in a leaf sequence file, thus, we can say that the MERT plan required relatively less time to deliver. It is worth pointing

out that in this study, we used all five available electron energies, which, in most cases, is not necessary. Let us take the 6 and 9 MeV electron beams as examples. As shown in **Figures 8A and 8B**, the optimizer gave them very low weights. Their contributions to the dose distribution in the final MERT plan were not significant. Therefore, they could have been deleted from the plan, leaving only three electron beams in the plan. The final three leaf sequence files would have had less number of segments. The total delivery time would have been even less.

Dose Distributions

Figures 9A and 9D show the comparison of the MERT and IMRT isodose distributions for the central axial slices from a representative parotid cancer case. **Figures 9B and 9E** show the comparison of the isodose distributions for the central coronal slices from the same example. **Figures 9C and 9F** show the comparison of the isodose distributions for the central sagittal slices also from the same example. The isodose distributions are shown in color lines. In both plans, the isodose curves were normalized to 55 Gy, representing 10, 20, 30, 40, 50, 60, 70, 80, 90, and 100%, respectively. Only selected isodose lines are labeled in the figures. The red colored target in the IMRT plan represents the PTV, while the red colored target in the MERT plan represents the CTV. The final MERT dose distribution was computed based on 15 intensity maps reconstructed from corresponding 15 step-and-shoot leaf sequences. The beamlet size was $1 \times 1 \text{ cm}^2$ for both plans. It is evident from the isodose distributions that higher isodose lines covered the target fairly well in terms of conformity in both plans, with the MERT plan showing an overall better conformity for all isodose lines in all three anatomical planes. As to the lower isodose lines, the photon beam IMRT plan exhibited a relatively poor conformity. In addition, excessively high exit doses of the photon beams penetrated much deeper regions. This resulted in significant, but unnecessary doses to distal areas, including some of the critical structures. This was clearly demonstrated in the axial and coronal slices of the IMRT plan, in which the 30% isodose line fully and the 40% isodose line partly covered the spinal cord, the brain stem, and the orbits. In

contrast, the corresponding MERT plan showed an excellent critical structure sparing because of the rapid falloff of the electron beams. The 30% isodose line covered only small portions of the spinal cord, the brain stem, and the right orbit. The left orbit was almost completely spared, as shown in **Figures 9D and 9E**. Thus, it is very clear that the MERT plan provided a better target dose coverage and homogeneity than the photon beam IMRT plan.

Dose-Volume Histograms (DVH)

To evaluate the plans objectively, we analyzed the cumulative dose-volume histograms (DVH) of the plans. The cumulative dose-volume histograms displayed quantitative statistical information about the target dose coverage and homogeneity and normal tissue sparing. Each cumulative DVH curve represents the fractional volume that received a particular dose or higher for that structure. It provides radiation oncologists and medical physicists with a very effective tool to evaluate completing treatment plans created with different parameters or even with different treatment planning systems (TPS). The DVHs for the target and the critical structures considered in this study from a representative parotid cancer case are shown in **Figure 10**. Based on the DVHs, it is evident that the MERT plan provided a more homogenous dose coverage to the target than the corresponding photon beam IMRT plan as the former's DVH is more vertical than the latter's. In the MERT plan, the maximum, minimum, and mean doses delivered to the CTV were 55.82, 40.50, and 50.32 Gy, respectively, while the corresponding doses delivered to the CTV in the IMRT plan were 60.38, 17.30, and 50.24 Gy, respectively, resulting in some undesirable hot and cold spots. Obviously, the photon beam IMRT plan exhibited some degree of dose inhomogeneity. In addition, in the photon beam IMRT plan, about 3% of the CTV received a dose of greater than or equal to 55 Gy and 5 % of the CTV received a dose of less than or equal to 45 Gy. In contrast, the MERT plan gave much better statistics. Less than 0.5% of the CTV received a dose of greater than or equal to 55 Gy and approximately 1.5% of the CTV received a dose of less than or equal to 45 Gy. All these suggest that the MERT plan provide a better dose homogeneity. It has been

known that conventional treatment modalities using electron beams exhibit a higher degree of dose inhomogeneity in comparison with photon beam techniques. In part, this is caused by tissue heterogeneity and skin surface irregularity. Here, we see that with electron energy and intensity modulations, it is possible to reduce the degree of dose heterogeneity and achieve a satisfactory dose distribution and uniformity.

Significant differences between the two DVHs for the critical structures indicated that the MERT plan also delivered much less doses to the critical structures than the photon beam IMRT plan. It is undoubtedly clear from **Figure 10** that the MERT plan showed a superior normal tissue sparing. The maximum, minimum, and mean doses to the spinal cord in the MERT plan were 16.62, 0.02, and 5.24 Gy, respectively, while the corresponding doses in the photon beam IMRT plan were 36.22, 0.60, and 17.50 Gy. Only 16% of the spinal cord volume in the MERT plan received a dose of greater than or equal to 10 Gy compared to 97% in the IMRT plan. Similar sparing for other structures were also observed in the MERT plan. The maximum, minimum, and mean doses given to the brainstem in the MERT plan were 13.65, 0.45, and 2.66 Gy, respectively. In contrast, the corresponding doses given in the photon beam IMRT plan were 29.88, 8.45, and 16.66 Gy, significantly higher than the doses delivered in the MERT plan. As to the orbits, both the MERT and the photon beam IMRT plans gave very low doses. Especially, the MERT plan delivered an extremely low dose to the contra-lateral orbit, with the maximum, minimum, and mean doses being 0.15, 0.01, and 0.05 Gy, respectively. This is very significant and clinically relevant since the tolerance dose for the lenses is only 10 ~ 15 Gy. In the cases we studied, the contra-lateral parotid gland was not contoured as an independent critical structure. However, based on the isodose distributions shown in **Figure 9**, it is clear that the dose delivered to the contra-lateral parotid gland for the MERT plan was well under the established tolerance dose of 20 ~ 30 Gy [29]. Even if we increased the prescribed dose to 60 Gy, the dose delivered to the contra-lateral parotid gland for the MERT plan would be still kept well within the tolerance. It is very important to point out that the mean dose to the non-target tissue in

the photon beam IMRT plan was 7.54 Gy as compared with 3.75 Gy in the photo beam MERT plan. This is of clinical significance as the MERT plan could significantly reduce low radiation doses to large normal tissue volume.

For many years, parotid cancers have been largely treated using one of these three radiotherapy techniques: an ipsilateral wedged pair of photon beams oriented at oblique angles, an ipsilateral field treated with high energy electrons, and a combination of high energy photon and electron beams with carefully chosen weights. Unfortunately, because of the intrinsic limitation of the underlying physics, all these techniques are not able to produce treatment plans that provide both a high degree of target dose conformity and a significant normal tissue sparing. Recently, the photon IMRT has shown some success in treating certain head and neck cancers, but it is still not suitable to treat shallow tumors due to extremely low surface dose and excessively high exit dose. The low surface dose is not effective in killing tumor cells in superficial tissues. The high exit dose constitutes a significant risk to the normal function of the distal critical structures, such as the spinal cord and the contra-lateral orbit and parotid gland. Therefore, it would be desirable to develop a technique that can eliminate these drawbacks. As the results presented here indicate, through both electron intensity and energy modulations, MERT was able to deliver highly conformal doses to targets with complex shapes. In the mean time, it provided sufficient protection of the critical structures and substantial normal tissue sparing. Considering the radiation side effects and the quality of life limiting organs at risk like the contra-lateral parotid gland and orbit, it is necessary to keep the dose to the healthy tissue to a minimum and preserve the organ normal function as much as possible. In this respect, MERT had an undisputable advantage and a great potential.

CONCLUSIONS

Based on the results of this comparative dosimetric study, we conclude that EMLC was able to provide sufficient beam collimation for MERT treatments and for superficial targets, such as parotid cancers, MERT offered not only a better target dose coverage and

uniformity, but also a superior normal tissue sparing. Therefore, it could become the treatment of choice. As the development of the computer-controlled EMLC is underway, we believe that the widespread routine implementation of this novel technique for superficial tumors should be investigated.

ACKNOWLEDGEMENTS

This study was supported in part by grants DAMD17-00-1-0443 (Yulin Song and Steve Jiang), DAMD17-00-1-0444 (Todd Pawlicki), and DAMD17-01-1-0635 (Lei Xing) from the US Department of Defense. In addition, we would like to express our sincere thanks to Varian Medical System, Palo Alto, CA, for providing electron applicators for this study.

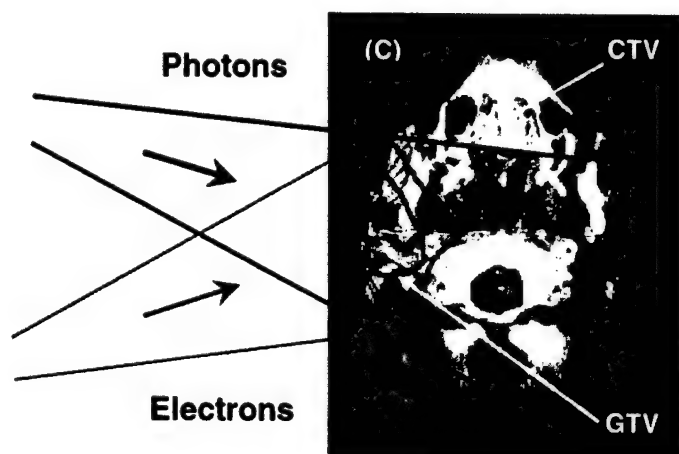
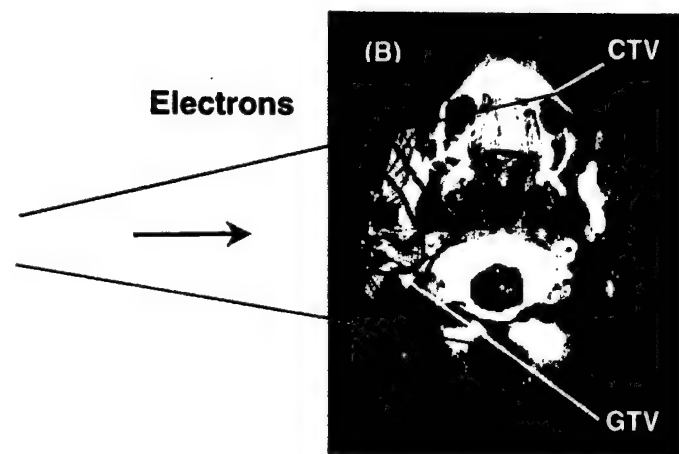
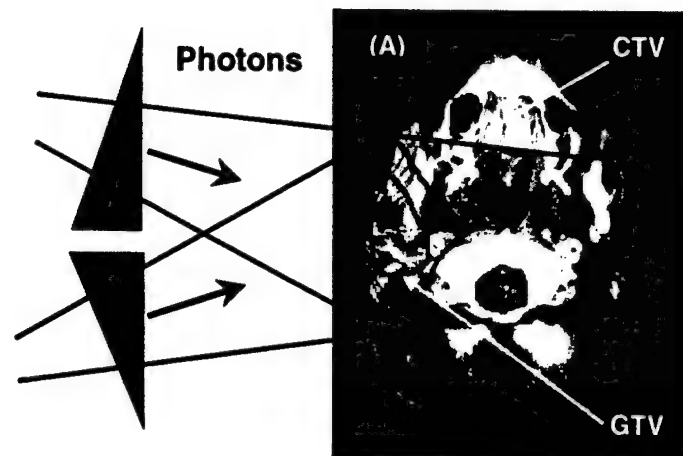


Figure 1

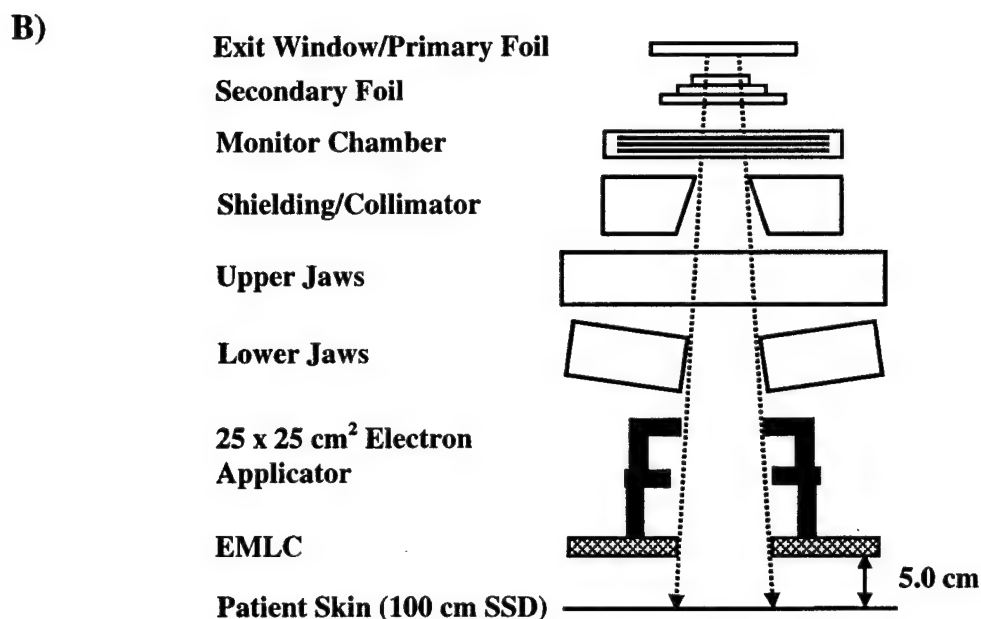
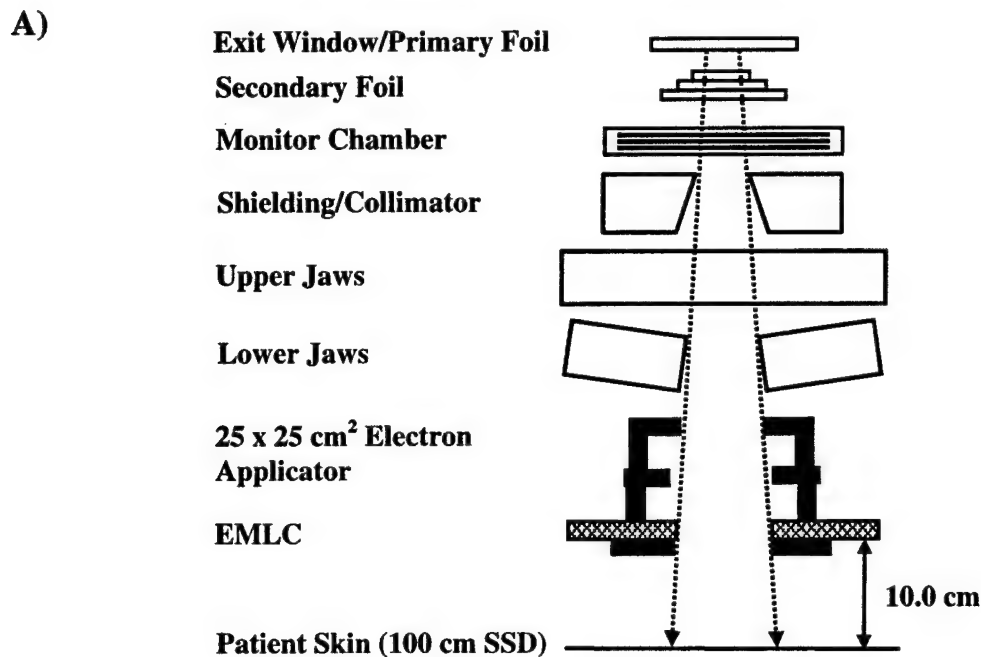


Figure 2

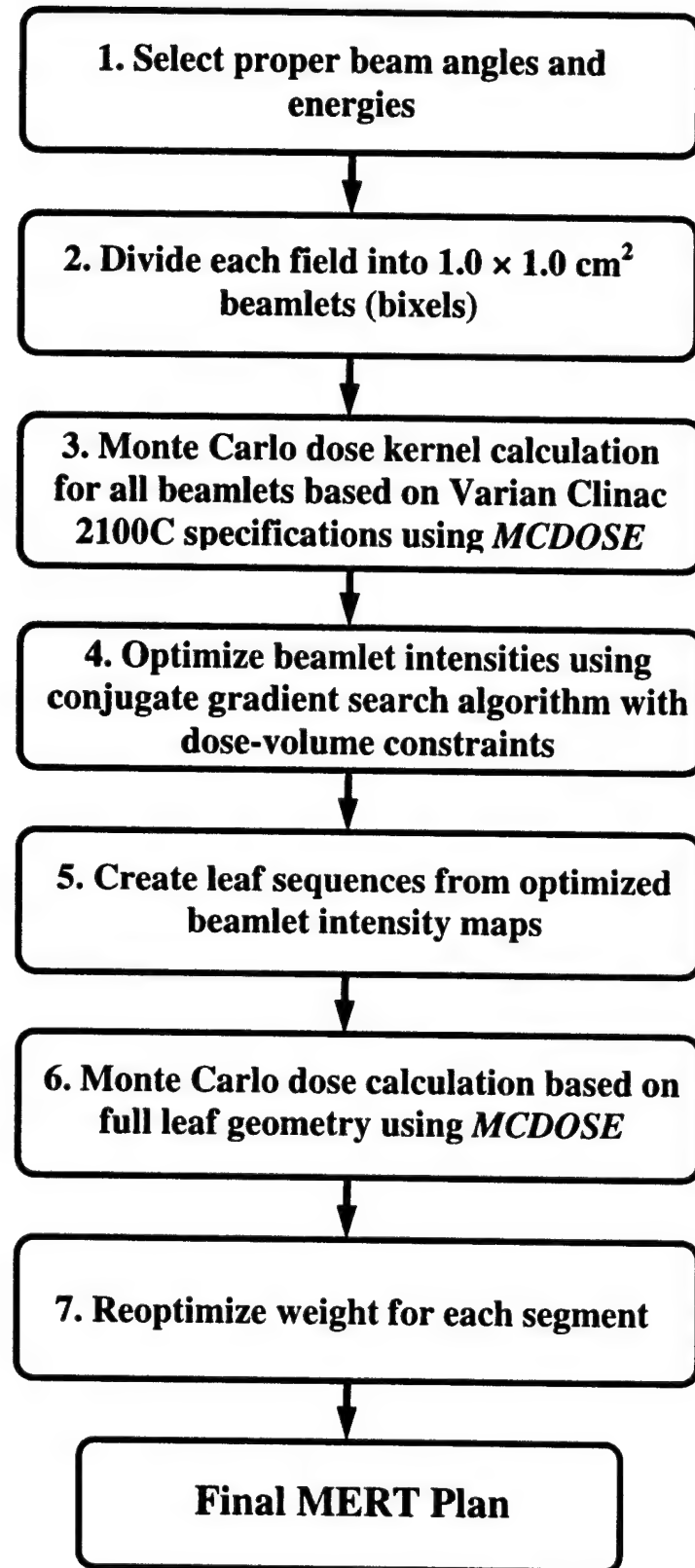


Figure 3

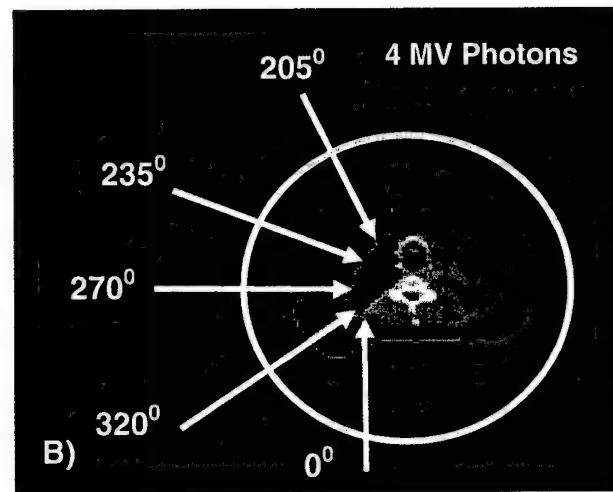
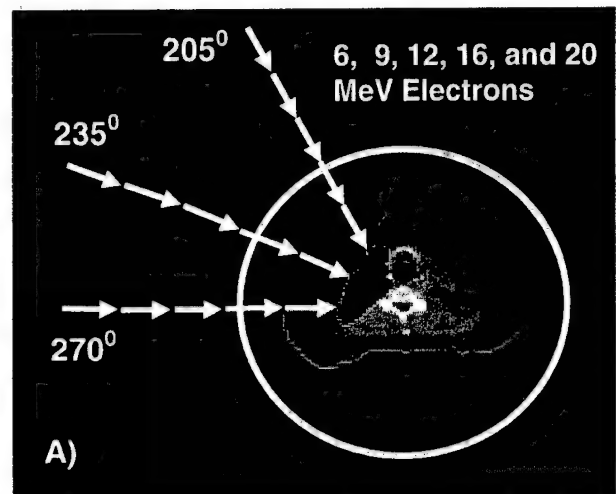


Figure 4

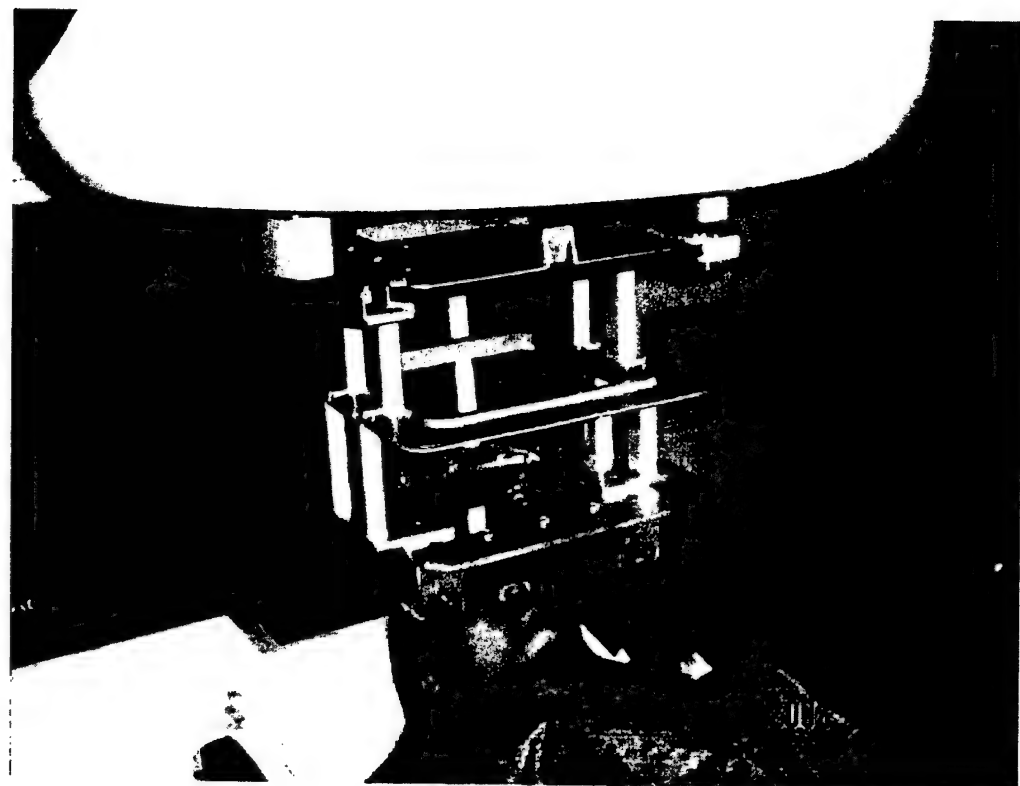
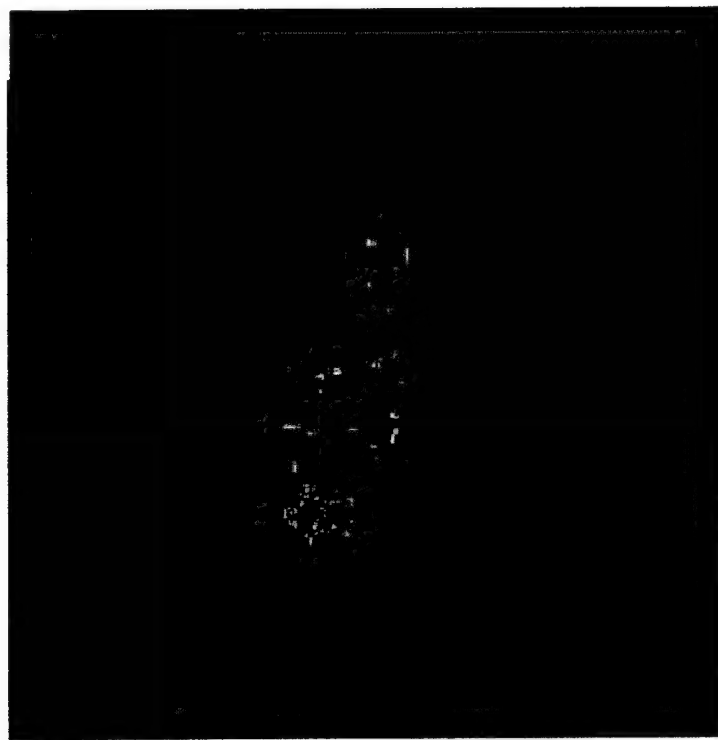


Figure 5

A



B

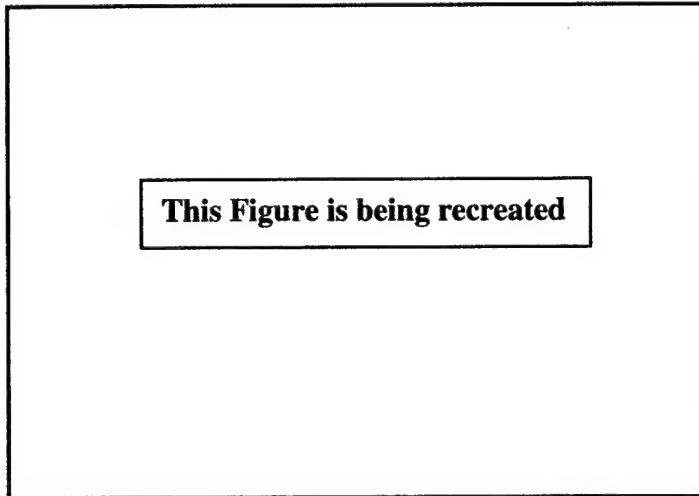


Figure 6

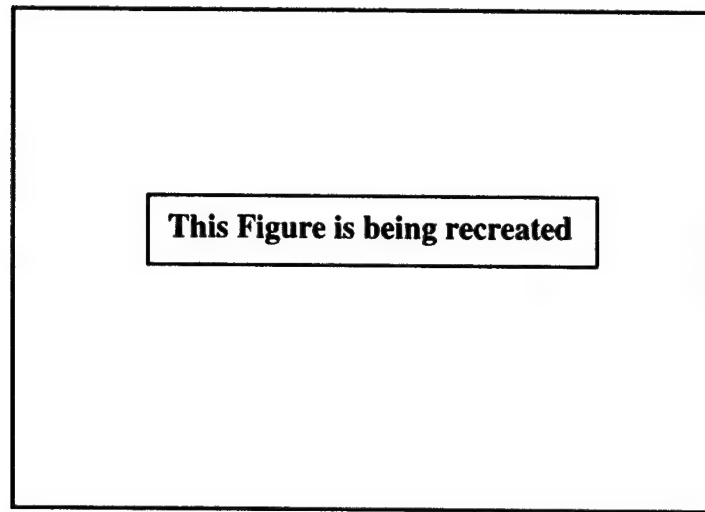
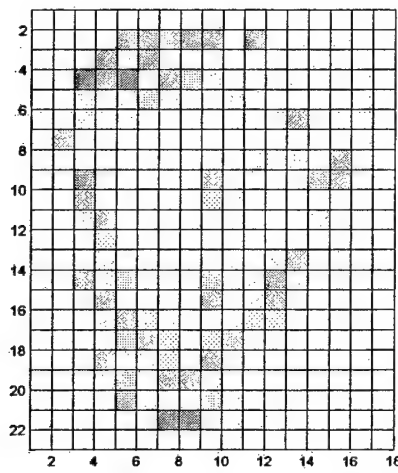
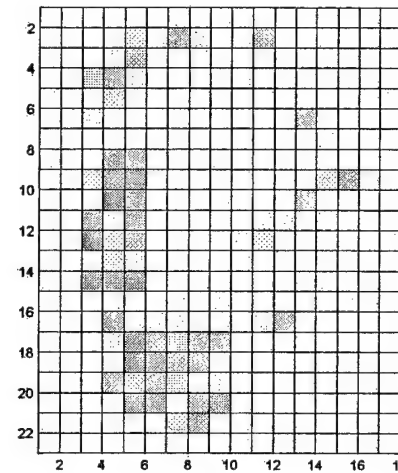


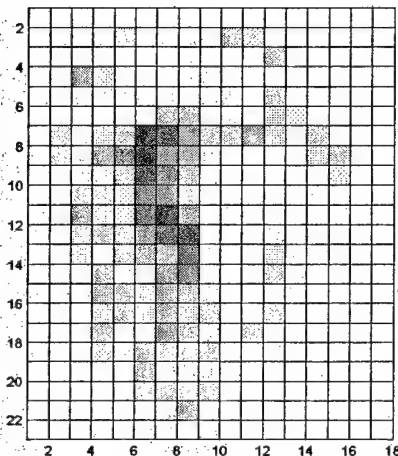
Figure 7



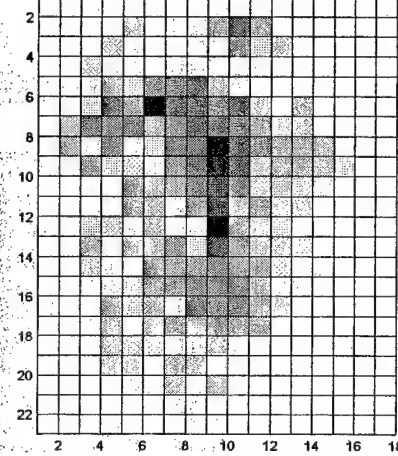
A. MERT plan 6 MeV field



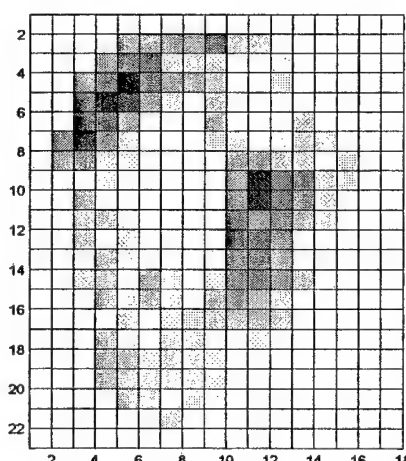
B. MERT plan 9 MeV field



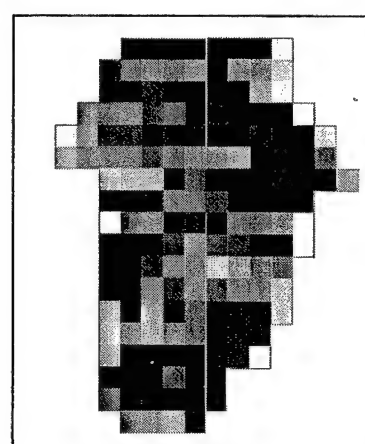
C. MERT plan 12 MeV field



D. MERT plan 16 MeV field



E. MERT plan 20 MeV field



F. IMRT plan 4 MV field

Figure 8

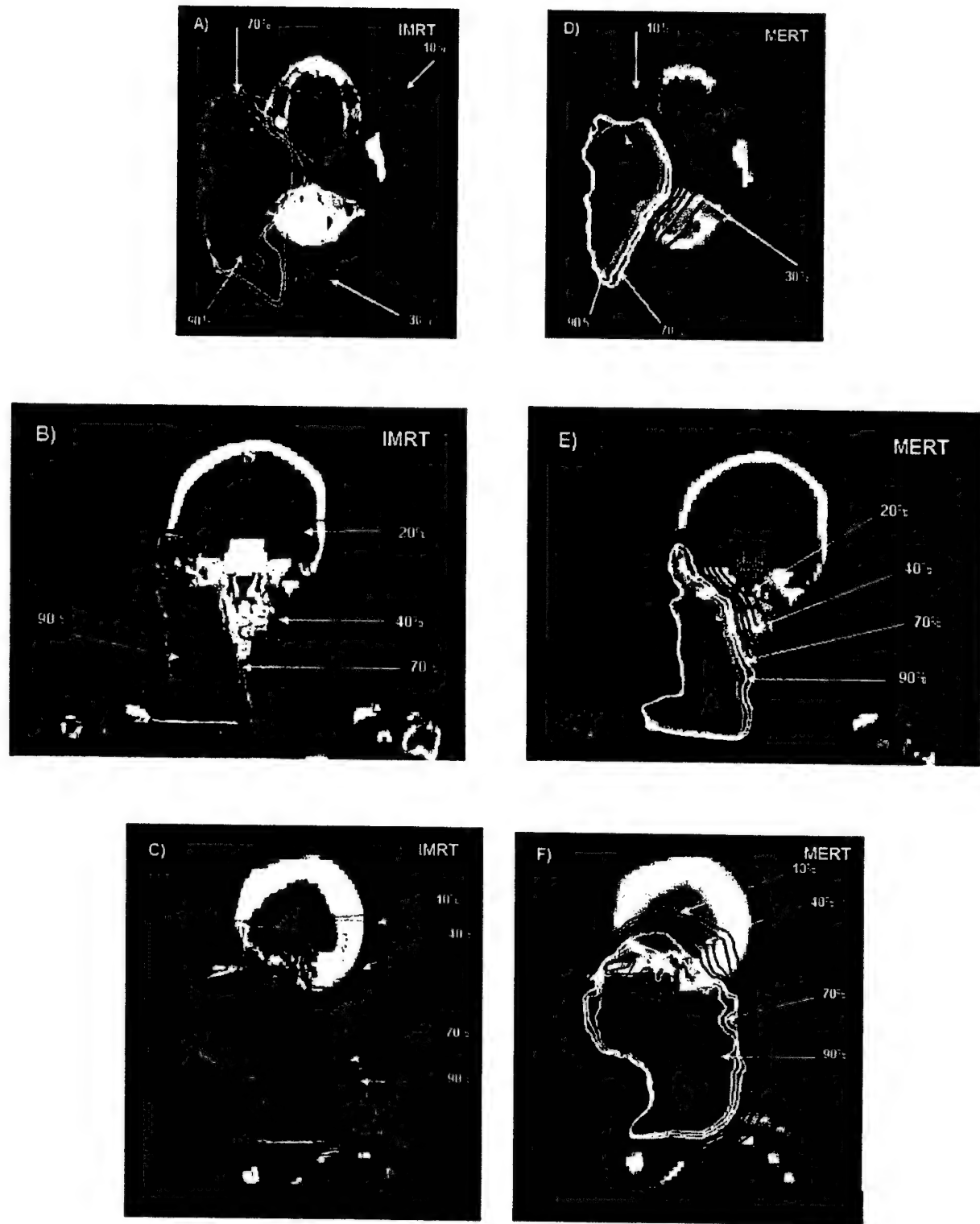


Figure 9

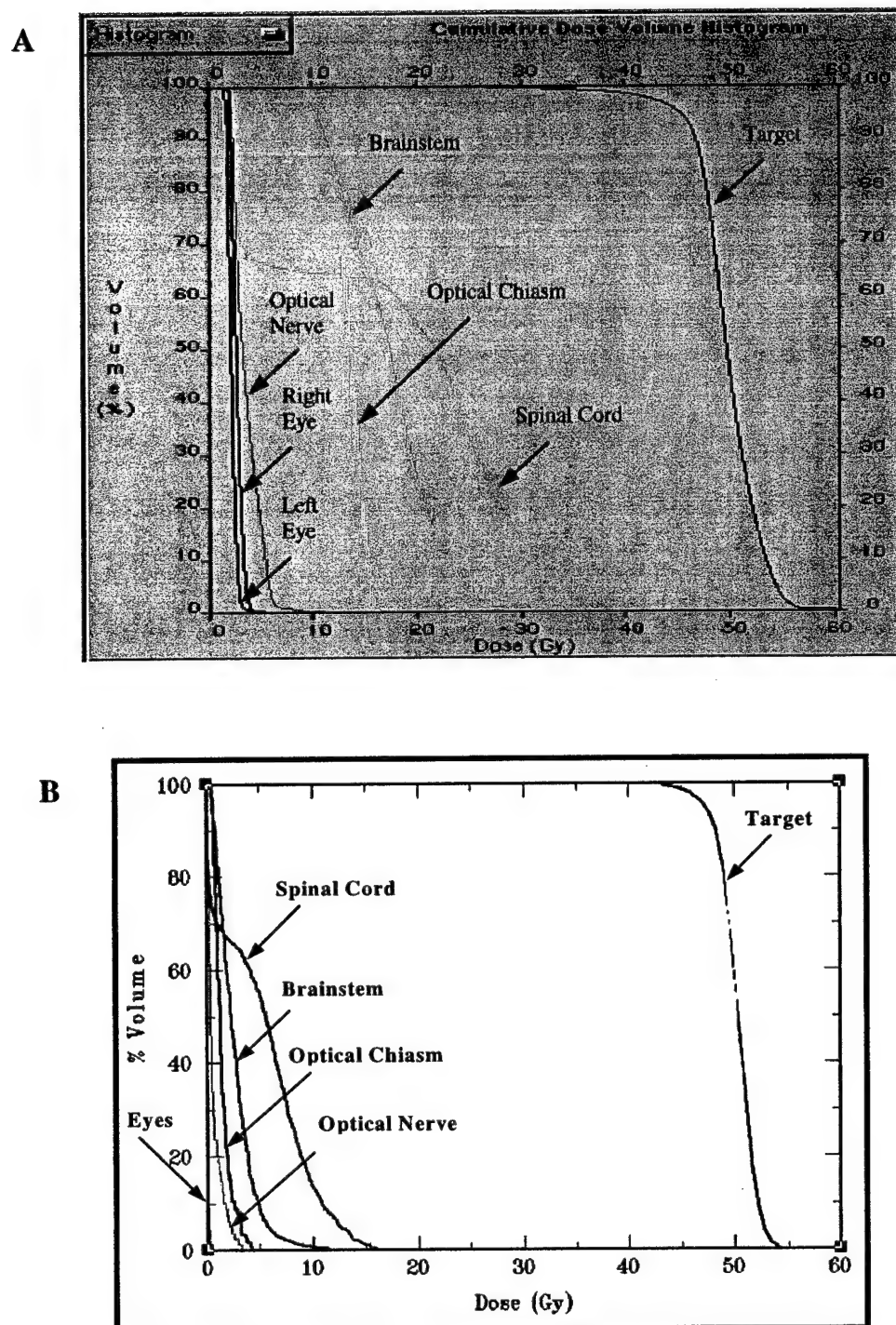


Figure 10

FIGURE LEGENDS

Figure 1

Conventional radiotherapy techniques for the treatment of parotid tumors. (A) An ipsilateral wedged pair of 6 MV photon beams oriented at oblique angles to cover the entire parotid bed, (B) An ipsilateral field treated with high energy electrons (12, 16 or 20 MeV), and (C) A combination of high energy photon and electron beams (6 MV + 12 or 16 or 20 MeV) with proper weighting.

Figure 2

Schematic drawings of the EMLC and a Varian Clinac 2100C treatment head. (A) The manually-driven EMLC was originally placed at the last scraper of a standard Varian 25 x 25 cm² electron applicator. This resulted in a considerably large air gap (10 cm) between the bottom of the EMLC leaves and the patient skin for a nominal 100 cm SSD. (B) To further lower the EMLC leaves, we have now removed the entire last scraper of the electron applicator and its electronic circuitry. The EMLC was placed immediately at the bottom of the modified electron applicator and stabilized with eight screws. This modification greatly reduced the air gap (5.0 cm) between the bottom of the EMLC leaves and the patient skin.

Figure 3

The MERT treatment planning flowchart.

Figure 4

Schematic layouts of the beam orientations. (A) Each MERT plan consisted of three coplanar ports, oriented at 205°, 235°, and 255°, respectively. Each port was treated with five nominal electron energies (6, 9, 12, 16, and 20 MeV) consecutively. (B) Corresponding photon beam IMRT plan had five coplanar ports: 0°, 205°, 235°, 270°, and 320°, with each port being treated with a 4 MV photon beam.

Figure 5

A photo of the EMLC assembly mounted on a Varian Clinac 2100C linear accelerator. The air gap between the bottom of the EMLC leaves and the patient skin was 5.0 cm.

Figure 6

A representative parotid tumor and corresponding tumor depth map. (A) A 3-D beam's eye view of a parotid tumor at the beam angle of 235^0 . (B) Corresponding tumor depth map, with darker pixels indicating the deeper parts of the tumor at this viewing angle.

Figure 7

A representative tumor depth histogram. The histogram was created based on Figure 6B, showing the number of pixels distribution as a function of tumor depth. Based on this distribution, a suitable set of electron energies were selected for this particular beam angle.

Figure 8

Representative beam intensity maps. (A-E) Intensity maps for the MERT plan for the 6, 9, 12, 16, and 20 MeV fields at the beam angle of 235^0 . (F) Corresponding photon beam IMRT intensity map for the 4 MV field at the same beam angle. This intensity map consisting of two separate intensity maps and combined together manually.

Figure 9

Comparison of the MERT and IMRT plan isodose distributions. (A, D) Isodose distributions for the central axial slices for a representative parotid cancer case. (B, E) Isodose distributions for the central coronal slices from the same case. (C, F) Isodose distributions for the central sagittal slices from the same case. The isodose curves,

normalized to 55 Gy, represent 10, 20, 30, 40, 50, 60, 70, 80, 90, and 100%, respectively. Only selected isodose lines are labeled here.

Figure 10

Comparison of dose volume histograms (DVH) for the photon beam IMRT (**A**) and MERT (**B**) plans. Clearly, the MERT plan shows a superior normal tissue sparing and a better dose distribution.

Table 1. List of ports used in the MERT plans

Port No	Gantry Angle
1	205°
2	235°
3	270°

Table 2. List of fields used in the MERT plans

Field No	Gantry Angle	Beam Energy (MeV)
1	205°	6
2	205°	9
3	205°	12
2	205°	16
5	205°	20
6	235°	6
7	235°	9
8	235°	12
9	235°	16
10	235°	20
11	270°	6
12	270°	9
13	270°	12
14	270°	16
15	270°	20

REFERENCES

1. S. Parker, T. Tong, S. Bolden, and P. Wingo, "Cancer Statistics", *CA Cancer J Clin*, **47**:5-27, 1997.
2. G. Seifert, C. Brocheriou, A. Cardesa, and J. W. Eveson, "WHO International Classification of Tumors. Tentative Histological Classification of Salivary Gland Tumors", *Pathol Res Pract*, **186**(5):555-581, 1990.
3. A. S. Garden, A. K. El-Naggar, et al, "Postoperative Radiotherapy for Malignant Tumors of the Parotid Gland", *Int J Radiat Oncol Biol Phys*, **37**:79-85, 1997.
4. I. J. Spino, C. C. Wang, and W. W. Montogmery, "Carcinoma of the Parotid Gland. Analysis of Treatment Results and Patterns of Failure After Combined Surgery and Radiation Therapy", *Cancer*, **71**:2699-2705, 1993.
5. R. E. Lenhard, Jr., R. T. Osteen, and T. Gansler, "Clinical Oncology", *American Cancer Society*, 297-329, 2001.
6. C. A. North, D-J Lee, S. Piantedosi, M. S. Zahurak, M.E. Johns, "Carcinoma of the Major Salivary Glands Treated by Surgery Plus Postoperative Radiotherapy", *Int J Radiat Oncol Biol Phys*, **18**:1319-1326, 1990.
7. A. J. Sykes, J. P. Logue, N. J. Slevin, N. K. Gupta, " An Analysis of Radiotherapy in the Management of 104 Patients with Parotid Carcinoma", *Clin Oncol*, **7**:16-20, 1995.
8. R. Yaparpalvi, D. P. Fontenla, S. K. Tyerech, L. R. Boselli, and J. J. Beitler, "Parotid Gland Tumors: A Comparison of Postoperative Radiotherapy Techniques Using Three

Dimensional (3D) Dose Distributions and Dose-Volume Histograms (DVHS)", *Int J Radiat Oncol Biol Phys*, **40**(1):1319-1326, 1990.

9. C. M. Nutting, C. G. Rowbottom, V. P. Cosgrove, J. M. Henk, D. P. Dearnaley, M. H. Robinson, J. Conway, and S. Webb, "Optimization of Radiotherapy for Carcinoma of the Parotid Gland: A Comparison of Conventional, Three-Dimensional Conformal, and Intensity-Modulated Techniques", *Radiother Oncol*, **60**:163-172, 2001.
10. A. S. Garden, A. K. El-Naggar, W. H. Morrison, D. L. Callender, K. K. Ang, and L. J. Peters, "Postoperative Radiotherapy for Malignant Tumors of the Parotid Gland", *Int J Radiat Oncol Biol Phys*, **37**(1):79-85, 1997.
11. A. L. Boyer, P. Geis, W. Grant, and M. Carol, "Modulated Beam Conformal Therapy for Head and Neck Tumors", *Int J Radiat Oncol Biol Phys*, **39**:227-236, 1997.
12. C. M. Bragg, J. Conway, and M. H. Robinson, "The Role of Intensity-Modulated Radiotherapy in the Treatment of Parotid Tumors", *Int J Radiat Oncol Biol Phys*, **52**(3):729-738, 2002.
13. Q. Wu, M. Manning, R. Schmidt-Ullrich, and R. Mohan, "The Potential for Sparing of Parotids and Escalation of Biologically Effective Dose with Intensity-Modulated Radiation Treatments of Head and Neck Cancers: A Treatment Design Study", *Int J Radiat Oncol Biol Phys*, **46**(1):195-205, 2000.
14. L. Cozzi, A. Fogliata, A. Lomax, and A. Bolsi, "A Treatment Planning Comparison of 3D Conformal Therapy, Intensity Modulated Photon Therapy and Proton Therapy for Treatment of Advanced Head and Neck Tumors", *Radiother Oncol*, **61**:287-297, 2001.

15. K. A. Vineberg, A. Eisbruch, M. M. Coselmon, D. L. McShan, M. L. Kessler, and B. A. Fraass, "Is Uniform Target Dose Possible in IMRT Plans in the Head and Neck?", *Int J Radiat Oncol Biol Phys*, **52**(5):1159-1172, 2002.
16. C. G. Rowbottom, C. M. Nutting, S. Webb, "Beam-Orientation Optimization of Intensity-Modulated Radiotherapy: Clinical Application to Parotid Gland Tumors", *Radiother Oncol*, **59**:169-177, 2001.
17. A. L. Boyer, "The Physics of Intensity-Modulated Radiation Therapy", *Phys Today*, 38-44, September 2002.
18. A. L. Boyer, *et al*, "Intensity-Modulated Radiation Therapy: Current Status and Issues of Interest", *Int J Radiat Oncol Biol Phys*, **51**(4):880-914, 2001.
19. L. Xing, C. Cotrutz, S. Hunjun, A. L. Boyer, E. Adalsteinsson, and D. Spielman, "Inverse planning for functional image-guided IMRT", *Phys Med Biol*, **47**:3567-3578, 2002.
20. M. C. Lee, J. Deng, J. Li, S. B. Jiang, and C-M Ma, "Monte Carlo Based Treatment Planning for Modulated Electron Radiation Therapy", *Phys Med Biol*, **46**:2177-2199, 2001.
21. C-M Ma, T. Pawlicki, M. C. Lee, S. B. Jiang, J. Li, J. Deng, B Yi, E. Mok, and A. L. Boyer, "Energy-and Intensity-Modulated Electron Beams for Radiotherapy", *Phys Med Biol*, **45**:2293-2311, 2000.
22. Y. Song, S. Jiang, M. C. Lee, C-M Ma, and A. L. Boyer, "A Multileaf Collimator for Modulated Electron Radiation Therapy (MERT) for Breast Cancer", the Department of Defense Breast Cancer Research Program Meeting, Proceedings Volume I, p17-5, 2002.

23. W. R. Nelson, H. Hirayama, and D. W. O. Rogers, "The EGS4 Code System", SLAC-Report-265, Stanford Linear Accelerator Center, 1985.
24. D. W. O. Rogers, B. A. Faddegon, G. X. Ding, C-M. Ma, J. Wei, and T. R. Mackie, "BEAM: A Monte Carlo Code to Simulated Radiotherapy Treatment Units", *Med Phys*, **22**:503-524, 1995.
25. ICRU, "Prescribing, Recording, and Reporting Photon Beam Therapy-Report 50", Washington, DC, *International Commission on Radiation Units and Measurements*, 1993.
26. T. Bortfeld, D. L. Kahler, T. J. Waldron, and A. L. Boyer, "X-ray Field Compensation with Multileaf Collimators", *Int J Radiat Oncol Biol Phy*, **28**:723-730, 1994.
27. A. L. Boyer and C. X. Yu, "Intensity Modulated Radiation Therapy with Dynamic Multileaf Collimators", *Semin Radiat Oncol*, **9**:48-59, 1999.
28. S. Webb, "Optimization of Conformal Radiotherapy Dose Distribution by Simulated Annealing", *Phys Med Biol*, **34**:1349-1370, 1989.
29. K. S. Clifford Chao, D. A. Low, C. A. Perez, and J. A. Purdy, "Intensity Modulated Radiation Therapy in Head and Neck Cancers: The Mallinckrodt Experience", *Int J Cancer (Radiat Oncol Invest)*, **90**:92-103, 2000.
30. M. G. Karlsson, M. K. Karlsson, and C-M Ma, "Treatment Head Design for Multileaf Collimated High-Energy Electrons", *Med Phys*, **26**:2125-2132, 1999.

Independent Dosimetric Calculation with Inclusion of Head Scatter and MLC Transmission for IMRT*

Y. Yang¹, Ph.D., L. Xing^{1,a}, Ph.D., J. G. Li², Ph.D., J. Palta², Ph.D., Y. Chen³, Ph.D.,
Gary Luxton¹, Ph.D., and A. Boyer¹, Ph.D.,

¹Department of Radiation Oncology, Stanford University School of Medicine,
Stanford, CA 94305-5304

²Department of Radiation Oncology, University of Florida,
2000 SW Archer Road, Gainesville, FL 32610-0385

³Department of Radiation Oncology, Thomas Jefferson University Hospital,
111 South 11th Street, Philadelphia, PA 19107-5097

^{a)} Author to whom correspondence should be addressed:

Department of Radiation Oncology
Stanford University School of Medicine,
300 Pasteur Drive, A0-40
Stanford, CA 94305-5304
Telephone: (650) 498-7896
Fax: (650) 498-4015
Email: lei@reyes.stanford.edu

Submitted to: Medical Physics

*This work was presented in the ASTRO 44th Annual Meeting, New Orleans, LA.

ABSTRACT

Independent verification of the MU settings and dose calculation of IMRT treatment plans is an important step in IMRT quality assurance (QA) procedure. At present, the verification is mainly based on experimental measurements, which are time consuming and labor intensive. Although a few simplified algorithms have recently been proposed for the independent dose (or MU) calculation, head scatter has not been precisely taken into account in all these investigations and the dose validation has mainly been limited to the central axis. In this work we developed an effective computer algorithm for IMRT MU and dose validation. The technique is superior over the currently available computer-based MU check systems in that (1) it takes full consideration of the head scatter and leaf transmission effects; and (2) it allows precise dose calculation at an arbitrary spatial point instead of merely a point on the central axis. In the algorithm the dose at an arbitrary spatial point is expressed as a summation of the contributions of primary and scatter radiation from all beamlets. Each beamlet is modulated by a dynamic modulation factor (DMF), which is determined by the MLC leaf trajectories, the head scatter, the jaw positions and the MLC leaf transmission. A three-source model was used to calculate the head scatter distribution for irregular segments shaped by MLC and the scatter dose contributions were computed using a modified Clarkson method. The system read in MLC leaf sequence files (or RTP file) generated by Corvus (NOMOS Corporation, Sewickley, PA) inverse planning system and then computed the doses at the desired points. The algorithm was applied to study the dose distributions of several testing intensity modulated fields and two multi-field Corvus plans and the results were compared with Corvus plans and experimental measurements. The final dose calculations at most spatial points agreed with the experimental measurements to within 3% for both the specially designed testing fields and the clinical intensity modulated field. Furthermore, excellent agreements (mostly within $\pm 3.0\%$) were also found between our independent calculation and the ion chamber measurements at both central axis and off-axis positions for the multi-field Corvus IMRT plans. These results indicate that the approach is robust and valuable for routine clinical IMRT plan validation.

Key word: dose verification, quality assurance, MU calculation, IMRT

I. INTRODUCTION

Intensity modulated radiation therapy (IMRT) is an advanced form of external beam irradiation and represents a radical change in radiation oncology practice. This new process of treatment planning and delivery shows significant potential for improving therapeutic ratio and offers a valuable tool for dose escalation and/or radiation toxicity reduction¹⁻⁹. Intensity modulation adds a new degree of freedom to the conventional radiation treatment based on open or wedged fields and allows us to modify dose distribution on an individual beamlet level, a rigorous quality assurance (QA) procedure is required to ensure what has been planned on an IMRT treatment planning system will be delivered safely and accurately¹⁰⁻¹⁴.

Among various issues related to plan validation, an important item is the verification of the monitor unit (MU) settings and the spatial dose distribution of an IMRT treatment plan. The basis for the MU calculation is the correlation between the calibrated dose under a reference condition to the dose delivered by the incident beam for the same MU. Upon completion of a patient's treatment plan, the system provides a set of MUs for the incident fields. The MU values determine the dose delivered to the tumor and are critically important for the success of radiation treatment. Little is gained if the target volume is underdosed or normal tissue is overdosed because the MUs are not accurately computed. The MU validation or a point dose check is usually performed by a manual calculation in conventional 3D radiation therapy. This calculation becomes intractable for an intensity modulated field due to the increased complexity of IMRT. In the last few years, a few groups have developed independent dose calculation algorithms¹⁵⁻¹⁸. These algorithms share two common shortcomings: (i) the influence of the head scatter factors resulting from the irregular segmented fields shaped by MLC has been ignored^{19, 20}; and (ii) the dose calculation point has been limited to the isocenter.

In this work, we present a more general independent point dose calculation algorithm with inclusion of head scatter and MLC transmission. With the improved modeling of the incident beams, the algorithm allows us to compute accurately the doses not only at the points along the central axis, but also an arbitrary point in a patient. The algorithm was applied to validate several testing IMRT fields and two Corvus treatment plans. Excellent

agreements (<3%) were found with ion chamber measurements and Corvus plans at most spatial points. Given the relative simplicity and the robustness of the algorithm, it is anticipated that the technique will have widespread application in clinical IMRT.

II. METHODS AND MATERIALS

A. Input data

In order to implement the independent dose verification algorithm, three groups of data are required: (i) primitive machine data, which include tissue maximum ratios (*TMRs*), head scatter factors (*Sc*) and phantom scatter factors (*Sp*) for square fields shaped by jaws, off axis ratios (*OARs*) for the maximum field size at several different depths, MLC transmission factors; (ii) treatment parameters, which include the jaw settings, gantry angles, collimator angles, couch angles, beam energy, the MLC leaf sequences, and the MU settings; and (iii) patient's geometry and set-up data, which include the coordinates of verification points, external contour of the patient or phantom, beam setup information (such as source-to-surface distance (SSD) for each beam). The second group of data is contained in the RTP file of the patient treatment plan.

B. Dose calculation with inclusion of head scatter and MLC transmission at an arbitrary spatial point

A few simplified algorithms have been proposed for the independent dose (or MU) calculation¹⁵⁻¹⁸. In this work, we employ the MU calculation formalism developed by Xing et al¹⁵. This method provides a clear physical picture and allows implementing the MU calculation at different level of sophistication to meet the specific requirement of different systems. For a single incident intensity modulated beam, we assume that the treatment field defined by the jaws can be partitioned into *M* beamlets and that there are *K* segments in the treatment field. The dose at a given point (*x*, *y*, *z*) in the patient can be expressed as¹⁵

$$D(x, y, z) = MU \sum_m^M C_m D_m^0 , \quad (1)$$

where the D_m^0 is the dose contribution to the calculation point per monitor unit from the m -th beamlet when it is open, MU is the total monitor unit, C_m is called the dynamic modulation factor (DMF), which represents the fractional monitor unit of the m -th beamlet in the isocenter plane perpendicular to central beamline when the beam is assigned with a monitor unit. When the MLC leaf transmission and head scatter effects are taken into account, the generalized DMF, C'_m , can be calculated by

$$C'_m = \sum_k^K [Sc_{m,k} + \alpha Sc'(1 - \delta_{m,k})] f_k , \quad (2)$$

with

$$\delta_{m,k} = \begin{cases} 1 & \text{if } m \in A_k \\ 0 & \text{if } m \notin A_k \end{cases} , \quad (3)$$

where f_k is the fractional monitor unit of the k -th segment, A_k is the radiation field shape of the k -th segment. $Sc_{m,k}$ is the head scatter factor of the beamlet m in the k -th segment, Sc' is the head scatter factor for the rectangular field defined by the jaws, and α is the average transmission factor, representing the amount of radiation passing through the MLC leaves (on average) as a percentage of the radiation of a reference open field defined by the jaws²¹. Here, we approximate the transmission for a point under the MLC (but inside the rectangular jaw field) as the product of the transmission factor, α , and the head scatter factor, Sc' , of the rectangular field set by the jaws. For a Varian machine, Sc' is a field-specific constant since the jaw settings do not change during the delivery process of an IMRT field. For the 15MV photon beam from our Clinic 2300C/D (Varian Oncology Systems, Palo Alto, CA), the average transmission factor is determined to be 1.74%.

The head scatter factor $Sc_{m,k}$ for each beamlet in a segment is calculated using a three-source model reported earlier²⁰. In this model, the photon radiation to the point of calculation is treated as if from three effective sources: one source for the primary photons from the target and two extra-focal photon sources for the scattered photons from the primary collimator and the flattening filter, respectively. The intensity distributions of the scatter sources and their positions and the off-axis difference of the scatter radiation

are taken into account in the calculation model on a machine and energy specific basis. Source parameters are determined by fitting the head scatter factors to the data of a series of square fields. Head scatter factor for an arbitrarily shaped segment is calculated by integrating the radiation contributed from areas (determined by the detector's eye view) in the two scatter sources.

A radiation beam is specified by the gantry angle, couch angle and collimator angle in the machine coordinate. On the other hand, a point in a patient is more conveniently specified by using a patient-fixed coordinate system. To calculate the absolute dose at an arbitrary point in the patient for a multiple field IMRT plan, a coordinate transform between the patient coordinate system and the machine coordinate system (shown in figure 1) is required. We assume that the coordinates of a verification point are (x, y, z) and (x', y', z') in the patient and machine coordinate systems, respectively, and that the origins of two systems are set at the isocenter. In an isocenter setup treatment, only rotation transformations are involved and the coordinates of a point in the two systems are related by

$$\begin{bmatrix} x' \\ y' \\ z' \end{bmatrix} = \begin{bmatrix} \cos \beta & \sin \beta & 0 \\ -\sin \beta & \cos \beta & 0 \\ 0 & 0 & 1 \end{bmatrix} \begin{bmatrix} \cos \theta & 0 & \sin \theta \\ 0 & 1 & 0 \\ -\sin \theta & 0 & \cos \theta \end{bmatrix} \begin{bmatrix} \cos \varphi & \sin \varphi & 0 \\ -\sin \varphi & \cos \varphi & 0 \\ 0 & 0 & 1 \end{bmatrix} \begin{bmatrix} x \\ y \\ z \end{bmatrix}, \quad (4)$$

where θ , β and φ are the gantry, collimator and couch rotation angles in the IEC convention, respectively.

We rewrite Eq. (1) as the sum of the contributions of the primary radiation and the scatter radiation:

$$D(x', y', z') = MU[\overline{C}'_{m_0} D^0_{p, m_0}(x', y', z') + \sum_{m \neq m_0}^M C'_m D^0_{s, m}(x', y', z')], \quad (5)$$

where m_0 is the beamlet contributing to the primary dose of the verification point, (x', y', z') , \overline{C}'_{m_0} is the corresponding weight-averaged DMF for this point, the $D^0_{p, m_0}(x', y', z')$ is the primary dose per monitor unit to the verification point when the beamlet m_0 is open, C'_m is the DMF for beamlet m , and the $D^0_{s, m}(x', y', z')$ is the scatter contribution to the point per monitor unit from a beamlet indexed by m . Here we should note that there are typically more than one beamlets contributing to the primary dose at a given point of

interest. In our algorithm, a finite-size pencil beam method was used to determine the primary intensity. A well-benchmarked Monte Carlo dose calculation system was used to compute the fluence distribution of a $1 \times 1\text{cm}^2$ beamlet at the d_{\max} with SSD= 97cm. It was found that the primary beam intensity at a point of interest (POI) is predominantly from the central $2 \times 2\text{cm}^2$ square. Furthermore, different points (beamlet/sub-beamlets) on the $2 \times 2\text{cm}^2$ square contribute differently to the primary intensity. Intuitively, this is understandable since the difference in their distances to the POI. In our calculation we divided each beamlet ($1\text{cm} \times 1\text{cm}$) into 4 subbeamlets ($0.5\text{cm} \times 0.5\text{cm}$) and our Monte Carlo calculation indicated that the weights in Eq. (5) for the three kinds of sub-beamlets in the central $2\text{cm} \times 2\text{cm}$ square are 0.200, 0.02 and 0.01, respectively. Therefore,

$$\bar{C}'_{m_0} = \sum_i^{16} W_i C'_i, \text{ here } W_i \text{ and } C'_i \text{ is the corresponding weight and DMF for the beamlet } i \text{ in the 16 beamlets surrounding beamlet } m_0.$$

The $D_{p,m_0}^0(x', y', z')$ can be calculated using

$$D_{p,m_0}^0(x', y', z') = \left(\frac{100}{100 - z'}\right)^2 C_f Sp(0) TMR(d_{eff}, 0) POAR(d_{eff}, x', y'), \quad (6)$$

where C_f is the calibration factor of the linac, d_{eff} is the water equivalent depth of the calculation point, $Sp(0)$ and $TMR(d_{eff}, 0)$ are the phantom scatter factor and TMR for zero field size, respectively. $POAR(d_{eff}, x', y')$ is the primary off-axis ratio at the calculation point, which can be determined using the method presented by Gibbons and Khan²². Only the standard central axis data, including output factors, TMR s, and $40 \times 40 \text{ cm}^2$ profiles, are required in the method.

A modified Clarkson integration method is used to compute the scatter dose contribution. As was done before¹⁵, we use square beamlets as the elementary calculation units, which are more natural for MLC-based IMRT. The $D_{s,m}^0(x', y', z')$ can be obtained by

$$D_{s,m}^0(x', y', z') = \left(\frac{100}{100 - z'}\right)^2 C_f [Sp(r + \Delta r) TMR(d_{eff}, r + \Delta r) - Sp(r) TMR(d, r)] POAR(d_{eff}, m), \quad (7)$$

where r is the distance between the center of the m -th beamlet and the projection of the calculation point on the isocenter plane, $\Delta r = l^2/2\pi r$, l is the beamlet size used in

calculation, $POAR(d_{eff}, m)$ is the primary off-axis ratio at the center of the m -th beamlet in water equivalent depth d_{eff} . For calculation purpose, a beamlet can be further divided into a number of sub-beamlets. We found a sub-beamlet size of $0.5 \times 0.5 \text{ cm}^2$ can yield a satisfactory accuracy.

In the case of multiple incident beams, the dose at a point can be calculated by simply summing the contributions from all beams, that is

$$D(x, y, z) = \sum_{j=1}^J D_j(x', y', z') = \sum_{j=1}^J MU_j \left(\bar{C}_{m_0, j} D_{p, m_0}^0(x', y', z') + \sum_{m \neq m_0}^M C'_{m, j} D_{s, m, j}^0(x', y', z') \right), \quad (8)$$

where index j has been added to label each individual incident beam, and J is the total number of beams.

C. Phantom description and experimental verification

In order to ensure the functionality of the point dose calculation algorithm described above, a series of measurements and Corvus calculations were carried out for several testing cases using either a cubic water equivalent phantom or a cylindrical Lucite phantom of radius 15 cm. Given a phantom and the coordinate of a validation point in the machine coordinate system, (x', y', z') , it is straightforward to obtain the effective depth, d_{eff} , defined in Eq. (6). For the cubic phantom geometry, we have

$$d_{eff} = \rho_e (100 - SSD - z') \sqrt{(100 - z')^2 + (x'^2 + y'^2)/(100 - z')}, \quad (9)$$

and for the cylindrical phantom, we have

$$d_{eff} \approx \rho_e (\sqrt{(100 - SSD)^2 - (x'^2 + y'^2)} - z') \times \sqrt{1 + \left(\frac{x'}{100 - z'}\right)^2 + \left(\frac{y'}{100 - z'}\right)^2}, \quad (10)$$

where SSD is source-skin distance of the calculation point and ρ_e is the electron density of the phantom material relative to that of water.

A Varian Clinic 2300C/D with a standard 80-leaf MLC and 15MV photon beam was used to test the independent dose calculation software. Two groups of experiments were performed. The first group includes four specifically designed testing fields and a field from a clinical IMRT plan. The four specially designed fields are: (i) $10 \times 10 \text{ cm}^2$ field formed by five consecutive $2 \times 10 \text{ cm}^2$ subfields (Fig. 2a); (ii) a wedge field (Fig. 2b); (iii) a pyramid field (Fig. 2c); and (iv) an inverse pyramid field (Fig. 2d). The MLC leaf sequence file for the first field (Fig. 2a) was generated using Varian's Shaper program.

For the rest of fields in Fig. 2, the Beam Utility Program of the Corvus system was used to take the intensity maps to compute the corresponding dose distributions in the cubic water equivalent phantom. Upon the completion of dose calculations, the leaf sequencing module of the Corvus system was used to generate the leaf sequences for the delivery of the fields.

The dose distributions for the intensity modulated fields shown in Fig. 2 were measured using Kodak XV2 films at different depths perpendicular to the incident beams. The calibration curve for the radiographic films was determined by optical densities measured at $d_{max}=3.0$ cm for different MU irradiation in the center of a $10\times 10\text{ cm}^2$ field with SSD=100 cm. The optical density distributions for the fields were then converted to dose distributions by using the calibration curve. The absolute doses were also measured with a PTW Farmer 0.6cm^3 ion chamber in the relatively flat parts of the fields for normalization purpose.

In the second group of study, we used a cylindrical Lucite phantom as a surrogate to recalculate the dose distribution of two multi-field IMRT treatments using the Corvus system. The first case was an IMRT treatment of prostate cancer, where the targets consisted of prostate and seminal vesicle of the patient. Six coplanar beams (gantry angles of these fields are 0, 55, 145, 180, 215, and 305 degrees, respectively) were used for the treatment and the corresponding intensity maps are shown in figure 3. The second case was an advanced stage prostate cancer with the involvement of pelvic lymph nodes. This plan also used six coplanar beams, two of which were split into two beams since the field widths were larger than the maximum extension of the MLC (14.5 cm). The corresponding gantry angles for this treatment are 0, 40, 115, 180, 245, and 320 degrees, respectively. The intensity maps are shown in figure 4.

The doses at different spatial points in the Lucite phantom were measured using a 0.147 cm^3 IC-10 ionization chamber (Wellhöffer Dosimetric, Schwarzenbruck, Germany) following the recommendations of the AAPM protocol. No corrections were made for the variation in the chamber replacement effect. The results of the CORVUS planning, our independent calculations and the measurements were compared for both groups of tests.

III. RESULTS

A. Single testing fields on a cubic water equivalent phantom

Figure 5 shows the comparison of the absolute dose profiles along the midline of the 21st leaf pair in the isocenter plane at the 5.0cm depth (SSD=95cm) in the cubic phantom for the four testing fields shown in Fig. 2. Except for Fig. 5a, in which no Corvus result is shown, three groups of data are presented: film measurements (solid lines), Corvus results (cross+lines) and our calculations (scattered solid circles). The three sets of data agree within $\pm 3.0\%$ in most parts of the high dose regions. It is also intriguing to note that good agreement is found in the low dose and penumbra regions of the fields, which indicates that the head scatter radiation has been modeled adequately in our algorithm since the doses in these regions arise mainly from the head scatter and phantom scatter. The absolute dose profiles at depth 10.0cm with SSD= 95cm along the midline of the 21st leaf pair for the wedge (Fig. 2b), pyramid (Fig. 2c), and inverse pyramid (Fig. 2d) shaped field are shown in Fig. 6. Similar levels of agreement are found for these fields.

Figure 7a shows the intensity map of a treatment field from a clinical IMRT case. The absolute dose profiles along the four lines marked in Fig. 7a were computed using our algorithm in isocenter plane at 3.0cm depth (SSD=97cm) in the cubic water equivalent phantom and the results are shown in Fig. 7b, 7c, 7d, and 7e as solid dots. The film measurements and Corvus calculations were also performed in the phantom. While the overall agreement between our calculations, the Corvus plans and the ion chamber measurements is excellent, there are regions (region A, B, C in figure 7) where the dosimetric discrepancies between the three are more than 5%. In these regions, it seems that our program yielded closer doses to the measured values in comparison with that of the Corvus calculation. Furthermore, as can be seen from Fig. 7, the penumbra regions are modeled adequately by our calculation.

B. Multi-field IMRT Plans

The dosimetric validation for the two multi-field IMRT plans was performed on the cylindrical Lucite phantom. Using the RTP files of the surrogate Lucite phantom plans,

we independently computed the doses at eight pre-selected spatial points inside the phantom for each plan. In selecting the calculation points, we have intentionally distributed them in high, medium and relatively low dose regions, respectively, in order to have a complete coverage of all possible scenarios. The coordinates of the points of interest relative to the isocenter are listed in Table I and II for both cases.

Table I summarizes the absolute doses from our calculations, Corvus plans and the measurements for the first case. Our calculations agree with the measurements to within 3.0% for all the eight verification points. The agreement between our calculations and the Corvus plans are also within 3.0% for all the points except point 5. At the point 5, the deviation of the Corvus dose from the measurement was found to be 5.6%, whereas our calculated dose for the point is only 0.6% different from the measured value.

Table II lists the three sets of data for the case 2. In this case, it was found that our calculations agreed with ion chamber measurements to within 3% for five out of the eight points. The relative errors of our independent calculations with respect to the measurements at the rest three points were above 3.0% but less than 5.0%. We also noticed that there are three points (point 3, 4, 5 in Table II) where the errors of the Corvus calculations against the measurements were quite large: 5.6%, 11.8% and 7.8%, respectively. The discrepancies of our calculations from the measurements for the three points are -4.6%, 1.1% and -4.6%, respectively, which are much closer to the measurements. We attribute the superior performance of our system to the better modeling of head scatter contributions. We note that the point 4 is located in a region where dose gradient is high, which may explain the large deviation of Corvus calculation from the measurement.

We also compared the calculated doses with and without head scatter correction for the all test points for the two cases and found that the average difference is about 4% for the points in the case 2 (large field IMRT) and about 2% for those in the case 1 (small field IMRT). These results indicate the importance of head scatter in IMRT, in particularly IMRT with large fields, and strongly suggest that the head scatter correction should be included in plan validation algorithm.

IV. DISCUSSION

The dose verification is mainly done by experimental measurements in current practice. A drawback of the approach is that it is time consuming and manpower intensive. Clinically, the task of carrying out the patient specific plan validation becomes quite burdensome as the number of IMRT patients increases to more than two or three per week and this has become a major bottle-neck problem in IMRT implementation. Just like that in the conventional 3D conformal radiation therapy, an independent dose calculation may be more practical approach for patient-specific QA of IMRT. While the basic philosophy is similar, there are a few issues specific to IMRT that must be resolved in order to have a truly reliable computer-based plan validation tool.

First of all, we wish to stress that the conventional approach based on point dose verification is not enough to validate an IMRT plan¹⁴. To have a comprehensive understanding of the issue here, let us start by discussing the independent dosimetric verification procedure in conventional 3D conformal radiation therapy (CRT). In CRT, the verification is mainly concerned with the MU calculation for each incident field. An independent calculation of the dose or MU at a point based on primitive machine data is recommended by AAPM TG-40²³. Because the fluence of a uniform/wedged field is spatially correlated, information of the dose at a spatial point can in principle be used to estimate the dose in other spatial points provided that the off-axis information is known. This is, however, not the case for an intensity modulated field since the weights of the beamlets across the field are independent. The correctness of the dose at a spatial point only warrants, at most, the correctness of the beamlets passing through or nearby that point. As shown in Table I and Table II, although the dose discrepancies between the Corvus calculations and the measurements are all within 2.0% at isocenter for the two clinical cases, the dose discrepancies in the off-axis positions may be much larger. To ensure that the final dose distribution adheres to the plan, a dosimetric check at multiple points should be an integral part of patient-specific QA to take consideration of the independence of the beamlets. An independent fluence map measurement/calculation would also be useful to remedy the uncertainty caused by the insufficient number of validation points and provide additional assurance.

In order to compute the spatial doses of an IMRT field, it is critical to model the MLC transmission and head scatter accurately because beamlet intensities are varied by moving MLC leaves across the irradiation field and a spatial point may often be at the edge(s) of one or more segmented fields. In this work, the head scatter contribution is calculated by using a well-established three-source model. This makes it possible to accurately compute the point doses at an arbitrary spatial point in a phantom or patient.

V. CONCLUSION

The level of quality in IMRT treatment is the result of many factors, but at this point, perhaps no factor has such a far-reaching effect as the timely development of computer based QA tools. With more and more hospitals starting their IMRT programs, it becomes increasingly important to have effective QA tools ready in the clinics. Otherwise, the gain from IMRT may be lost in non-optimal QA procedure and/or be offset by the increased cost of treatment. In this paper, an effective dose verification algorithm has been developed for IMRT treatment plan validation. The algorithm separates the primary and scatter radiation calculations. A modified Clarkson method is employed to compute the scatter dose contributions. A salient feature of the algorithm is the accurate inclusion of head scatter and MLC transmission. The inclusion of head scatter allows us to compute the IMRT dose not only at the central-axis point but also an arbitrary off-axis point. Given the relative simplicity and accuracy, the algorithm seems to balance the practicality and precision required by an IMRT plan validation tool and is thus valuable to greatly facilitate the routine clinical IMRT QA process.

Acknowledgment

This work was partly supported by a grant from the Department of Defense (DAMD17-01-0635) and a Research Scholar Award from the American Cancer Society (RSG-01-022-01-CCE).

Table I Absolute doses measured and calculated in a Lucite phantom for the case 1

Number of Calc point	Coordinates of Calc points (cm)	Current Calc dose (cGy)	Corvus calc dose (cGy)	Ion chamber measurement (cGy)	Deviation with Corvus (%)	Deviation with measurement (%)
1	(0,0,0)	218.5	217.0	216.7	0.7	0.8
2	(2,0,0)	212.2	215.0	216.7	-1.3	-2.1
3	(0,2,0)	211.4	209.0	210.9	0.9	0.2
4	(0,0,2)	210.6	211.0	207.2	-0.2	1.6
5	(0,0,6)	78.6	74.0	78.1	6.2	0.6
6	(-6,0,6)	78.5	80.0	79.2	-0.6	-0.9
7	(6,0, -5)	97.8	96.0	100.6	1.9	-2.8
8	(-6,2, -5)	102.5	103.0	104.3	-0.5	-1.7

Table II Absolute doses measured and calculated in a Lucite phantom for the case 2

Number of Calc point	Coordinates of Calc points (cm)	Current Calc dose (cGy)	Corvus calc dose (cGy)	Ion chamber measurement (cGy)	Deviation with Corvus (%)	Deviation with measurement (%)
1	(0,0,0)	206.2	207.0	209.8	-0.4	-1.7
2	(2,0,0)	223.4	218.0	224.5	2.5	0.5
3	(0,6,0)	122.3	121.0	128.2	1.1	-4.6
4	(0,0,8)	91.7	80.0	90.7	14.6	1.1
5	(0,5,2)	84.8	82.0	88.9	3.3	-4.6
6	(-5,9,0)	187.9	191.0	186.9	-1.1	0.5
7	(-4,5,2)	180.0	180.0	178.3	0	1.0
8	(4.5,7.5, -2)	171.8	175.0	178.0	-1.8	-3.5

Legends

Fig.1. Patient coordinate system ($X-Y-Z$) and the machine coordinate system ($X'-Y'-Z'$). θ , β and ϕ are the gantry, collimator and couch rotation angles in the IEC convention, respectively. The line 1 is in the $X-Y$ plane with a rotation angle ϕ along Z -axis. The line 2 is the corresponding line of line1 after the gantry rotation of θ angle.

Fig.2. The intensity maps for four testing intensity modulated fields: (a) a uniform field formed by five consecutive $2 \times 10 \text{ cm}^2$ subfields; (b) a wedge field; (c) a pyramid field; and (d) an inverse pyramid field. The beamlet size is $1 \times 1 \text{ cm}^2$. Intensity level of a beamlet is characterized by its gray level, ranging from 0 (white) to 100 (black).

Fig. 3. The intensity maps for a six-field IMRT prostate treatment. Intensity level of a beamlet is characterized by its gray level, ranging from 0 (white) to 100 (black).

Fig. 4. The intensity maps for a six-field IMRT treatment of an advanced stage prostate cancer with the involvement of the pelvic lymph nodes. Intensity level of a beamlet is characterized by its gray level, ranging from 0 (white) to 100 (black).

Fig. 5. Dose profiles along the midline of the 21st leaf pair obtained by using film measurements, Corvus planning system, and the current independent calculation for the four test intuitive fields: (a) a uniform open field formed by five $2 \times 10 \text{ cm}^2$ subfields; (b) a wedge field formed by MLC; (c) a pyramid field; and (d) an inverse pyramid field. The measurements and calculations were done in the isocenter plane at depth 5.0cm in water equivalent phantom.

Fig. 6. Dose profiles at depth 10.0cm with SSD= 95cm in solid water along the midline of the 21st leaf pair for three test intuitive fields: (a) a wedge field; (b) a pyramid field; and (c) an inverse pyramid field.

Fig. 7. Comparison of our calculations with ion chamber measurements and Corvus plan for a clinical intensity modulated field. The intensity map of the field and the four lines along which the doses were compared are shown in (a). The absolute dose profile for line-1, -2, -3, and -4 are shown in panel b, c, d, and e, respectively.

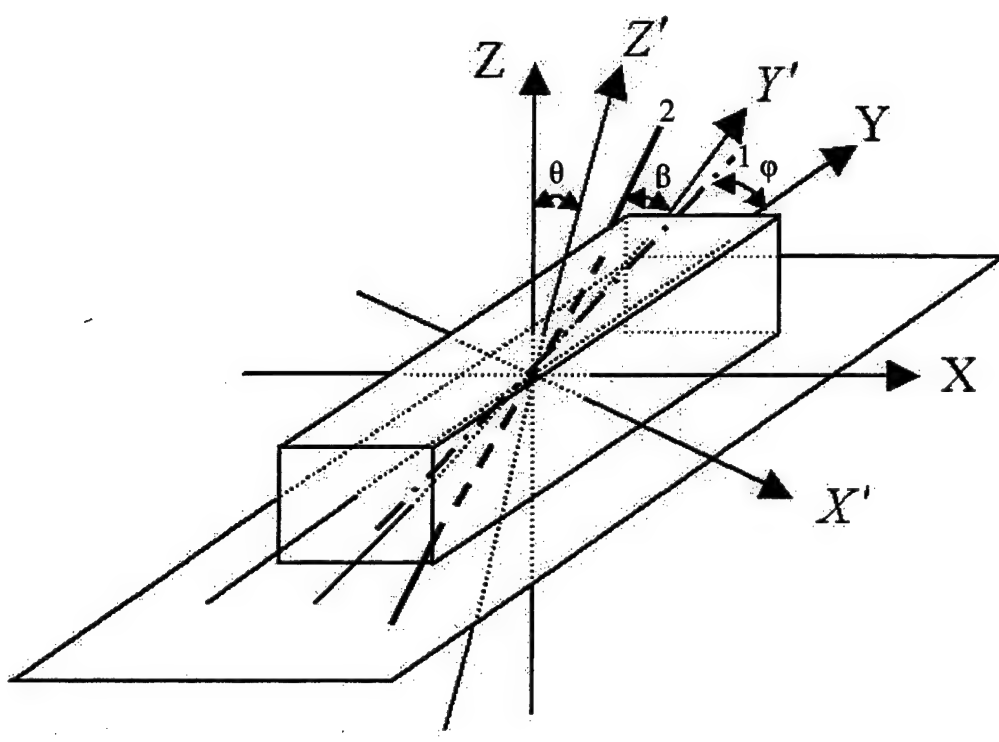
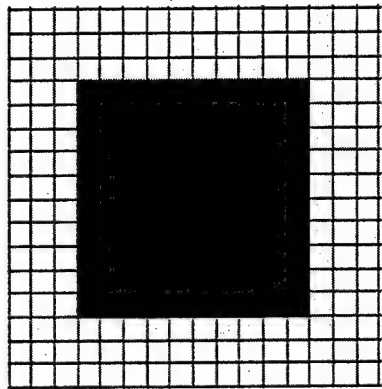
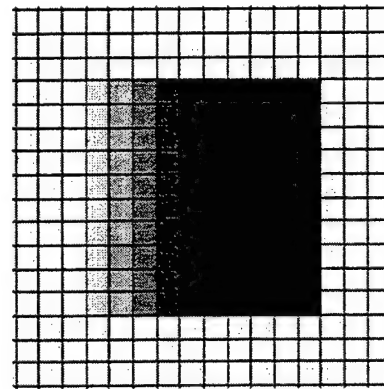


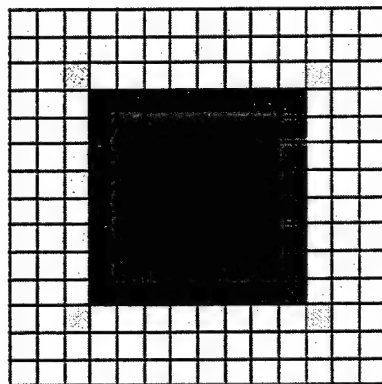
Figure 1



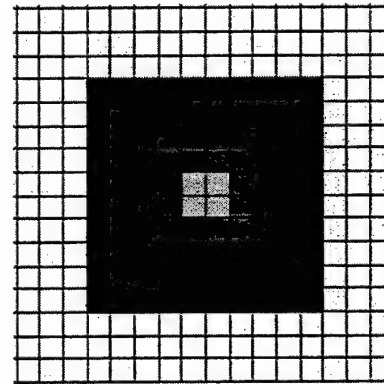
a. Uniform field



b. Wedge field



c. Pyramid field

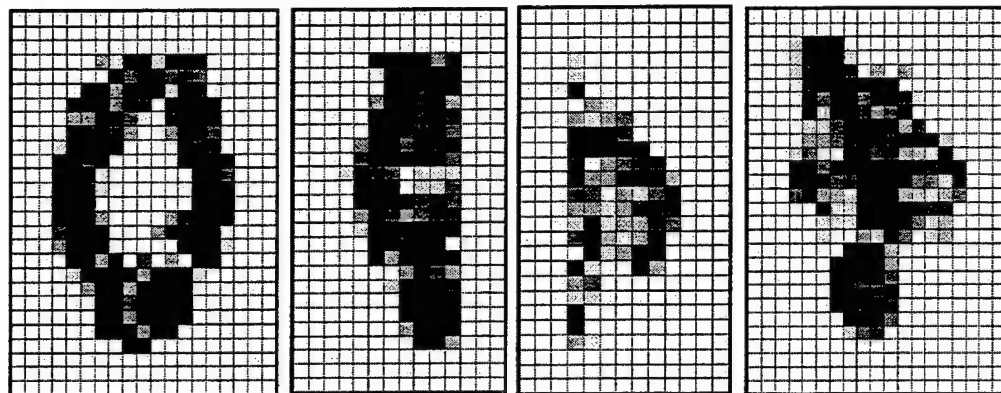


d. Inverse pyramid field

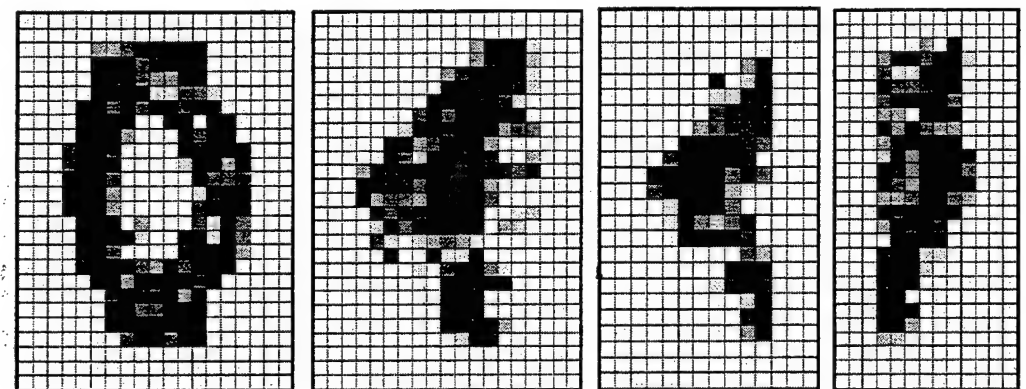


0% (white) – 100% (black)

Figure 2



Gantry = 0° Gantry = 40° a Gantry = 40° b Gantry = 115°

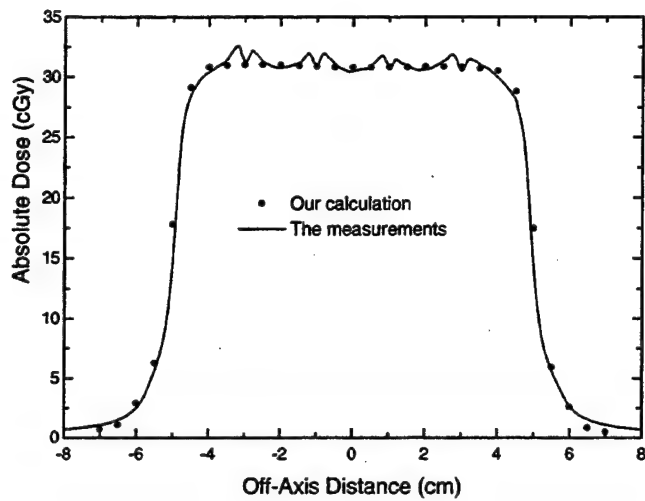


Gantry = 180° Gantry = 245° Gantry = 320° a Gantry = 320° b

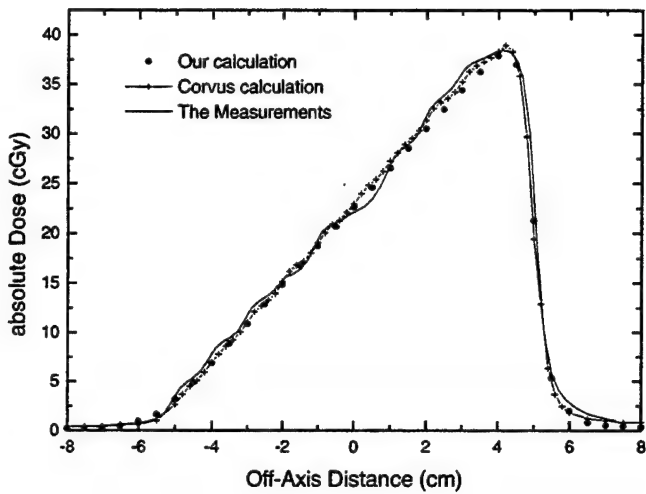


0% (white) – 100% (black)

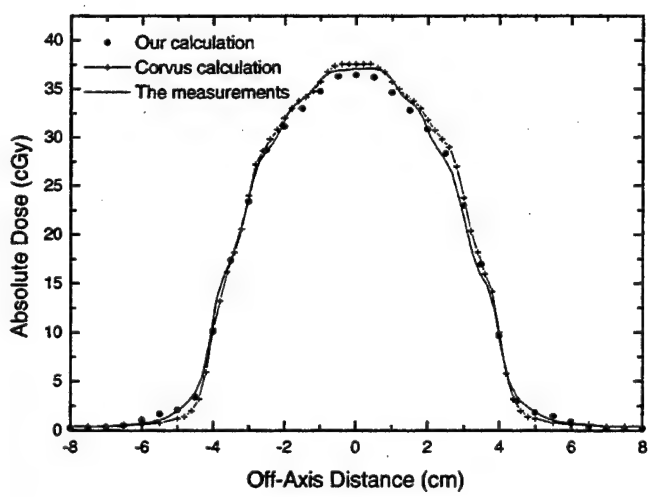
Figure 4



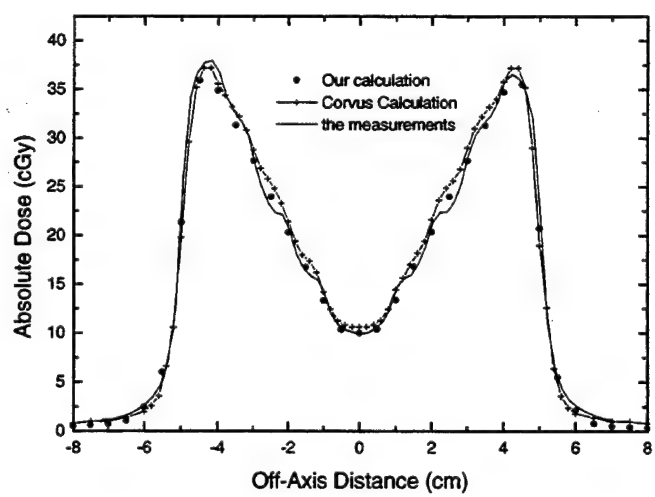
a



b



c



d

Figure 5

References

1. IMRT Collaborative Working Group. Intensity-modulated radiotherapy: current status and issues of interest. *International Journal of Radiation Oncology, Biology, Physics* 2001; 51:880-914.
2. Ling CC, Burman C, Chui CS, et al. Conformal radiation treatment of prostate cancer using inversely-planned intensity-modulated photon beams produced with dynamic multileaf collimation. *International Journal of Radiation Oncology, Biology, Physics* 1996; 35:721-30.
3. Xing L, Cotrutz C, Hunjan S, Boyer AL, Adalsteinsson E, Spielman DM. Inverse Planning for Functional Image-Guided IMRT. *Physics in Medicine & Biology* 2002; 47:3567-3578.
4. Tsai JS, Wazer DE, Ling MN, et al. Dosimetric verification of the dynamic intensity-modulated radiation therapy of 92 patients. *International Journal of Radiation Oncology, Biology, Physics* 1998; 40:1213-30.
5. Wu Q, Manning M, Schmidt-Ullrich R, Mohan R. The potential for sparing of parotids and escalation of biologically effective dose with intensity-modulated radiation treatments of head and neck cancers: a treatment design study. *International Journal of Radiation Oncology, Biology, Physics* 2000; 46:195-205.
6. Mundt AJ, Lujan AE, Rotmensch J, et al. Intensity-modulated whole pelvic radiotherapy in women with gynecologic malignancies. *International Journal of Radiation Oncology, Biology, Physics* 2002; 52:1330-7.
7. Huang E, Teh BS, Strother DR, et al. Intensity-modulated radiation therapy for pediatric medulloblastoma: early report on the reduction of ototoxicity. *International Journal of Radiation Oncology, Biology, Physics* 2002; 52:599-605.
8. Le QT, Xing L, Boyer AL. Head and Neck IMRT. In: Purdy J. GI, and Palta J, ed. *3D Conformal Radiation Therapy & Intensity Modulated Radiation Therapy in the Next Millennium*. Madison, WI: Medical Physics Publishing, 1999:190-95.
9. Chao KS, Deasy JO, Markman J, et al. A prospective study of salivary function sparing in patients with head-and-neck cancers receiving intensity-modulated or

- three-dimensional radiation therapy: initial results. International Journal of Radiation Oncology, Biology, Physics 2001; 49:907-16.
10. Low DA, Chao KS, Mutic S, Gerber RL, Perez CA, Purdy JA. Quality assurance of serial tomotherapy for head and neck patient treatments. International Journal of Radiation Oncology, Biology, Physics 1998; 42:681-92.
 11. Low DA, Harms WB, Mutic S, Purdy JA. A technique for the quantitative evaluation of dose distributions. Medical Physics 1998; 25:656-61.
 12. LoSasso T, Chui CS, Ling CC. Comprehensive quality assurance for the delivery of intensity modulated radiotherapy with a multileaf collimator used in the dynamic mode. Medical Physics 2001; 28:2209-2219.
 13. Xing L, Curran B, Hill R, et al. Dosimetric verification of a commercial inverse treatment planning system. Physics in Medicine & Biology 1999; 44:463-78.
 14. Xing L, Lin Z, Donaldson SS, et al. Dosimetric effects of patient displacement and collimator and gantry angle misalignment on intensity modulated radiation therapy. Radiotherapy & Oncology 2000; 56:97-108.
 15. Xing L, Chen Y, Luxton G, Li JG, Boyer AL. Monitor unit calculation for an intensity modulated photon field by a simple scatter-summation algorithm. Physics in Medicine & Biology 2000; 45:N1-7.
 16. Kung J, Chen G. A monitor unit verification calculation in intensity modulated radiotherapy as a dosimetric quality assurance. Medical Physics 2000; 27:2226-2230.
 17. Watanabe Y. Point dose calculations using an analytical pencil beam kernel for IMRT plan checking. Physics in Medicine & Biology 2001; 46:1031-8.
 18. Chen Z, Xing L, Nath R. Independent monitor unit calculation for intensity modulated radiotherapy using the MIMiC multileaf collimator. Medical Physics 2002; 29:2041-51.
 19. Zhu TC, Bjarnegard BE, Xiao Y, Yang CJ, Kim S. Modeling the output ratio in air for megavoltage photon beams. Medical Physics 2001; 28:925-37.
 20. Yang Y, Xing L, Boyer AL, Song Y, Hu Y. A three-source model for the calculation of head scatter factors. Medical Physics 2002; 29:2024-2033.

21. Arnfield MR, Siebers JV, Kim JO, Wu Q, Keall PJ, Mohan R. A method for determining multileaf collimator transmission and scatter for dynamic intensity modulated radiotherapy. *Medical Physics* 2000; 27:2231-41.
22. Gibbons JP, Khan FM. Calculation of dose in asymmetric photon fields. *Medical Physics* 1995; 22:1451-1457.
23. Kutcher GJ, Coia L, Gillin M, et al. Comprehensive QA for radiation oncology: report of AAPM Radiation Therapy Committee Task Group 40. *Medical Physics* 1994; 21:581-618.



PHYSICS CONTRIBUTION

INCORPORATING PRIOR KNOWLEDGE INTO BEAM ORIENTATION OPTIMIZATION IN IMRT

ANDREI PUGACHEV, M.S., AND LEI XING, PH.D.

Department of Radiation Oncology, Stanford University School of Medicine, Stanford, CA

Purpose: Selection of beam configuration in currently available intensity-modulated radiotherapy (IMRT) treatment planning systems is still based on trial-and-error search. Computer beam orientation optimization has the potential to improve the situation, but its practical implementation is hindered by the excessive computing time associated with the calculation. The purpose of this work is to provide an effective means to speed up the beam orientation optimization by incorporating *a priori* geometric and dosimetric knowledge of the system and to demonstrate the utility of the new algorithm for beam placement in IMRT.

Methods and Materials: Beam orientation optimization was performed in two steps. First, the quality of each possible beam orientation was evaluated using beam's-eye-view dosimetrics (BEVD) developed in our previous study. A simulated annealing algorithm was then employed to search for the optimal set of beam orientations, taking into account the BEVD scores of different incident beam directions. During the calculation, sampling of gantry angles was weighted according to the BEVD score computed before the optimization. A beam direction with a higher BEVD score had a higher probability of being included in the trial configuration, and vice versa. The inclusion of the BEVD weighting in the stochastic beam angle sampling process made it possible to avoid spending valuable computing time unnecessarily at "bad" beam angles. An iterative inverse treatment planning algorithm was used for beam intensity profile optimization during the optimization process. The BEVD-guided beam orientation optimization was applied to an IMRT treatment of paraspinal tumor. The advantage of the new optimization algorithm was demonstrated by comparing the calculation with the conventional scheme without the BEVD weighting in the beam sampling.

Results: The BEVD tool provided useful guidance for the selection of the potentially good directions for the beams to incident and was used to guide the search for the optimal beam configuration. The BEVD-guided sampling improved both optimization speed and convergence of the calculation. A comparison of several five-field IMRT treatment plans obtained with and without BEVD guidance indicated that the computational efficiency was increased by a factor of ~10.

Conclusion: Incorporation of BEVD information allows for development of a more robust tool for beam orientation optimization in IMRT planning. It enables us to more effectively use the angular degree of freedom in IMRT without paying the excessive computing overhead and brings us one step closer to the goal of automated selection of beam orientations in a clinical environment. © 2002 Elsevier Science Inc.

IMRT, Inverse planning, Intensity modulation, Optimization, Beam orientation.

INTRODUCTION

Beam configuration may have significant influence on intensity-modulated radiotherapy (IMRT) dose distribution, and an individualized beam configuration is frequently needed to achieve the best possible treatment (1, 2). Clinically, beam orientations are usually selected based on trial-and-error search. Considerable effort may be required to come up with a set of acceptable beams. The final results

may strongly depend on the planner's experience and understanding of the planning system. An ideal solution is to incorporate the beam orientation optimization into the planning system to automate the beam placement process. With currently available techniques, unfortunately, this would take a prohibitive amount of computing time, even on a high-end workstation. Generally speaking, to optimize beam configuration, one can add the degree of freedom of beam angles to the objective function and optimize them

Reprint requests to: Lei Xing, Ph.D., Stanford University School of Medicine, Department of Radiation Oncology, 300 Pasteur Drive, Stanford, CA 94305-5304. Tel: (650) 498 7896; Fax: (650) 498 4015; E-mail: lei@reyes.stanford.edu

This work was supported in part by a research scholar grant award from the American Cancer Society and research grants from the U.S. Department of Defense, the Whitaker Foundation, and the Information Technology Systems and Services of Stanford University.

Acknowledgments—We thank our colleagues at Stanford University—S.S. Donaldson, A.L. Boyer, G. Luxton, T. Pawlicki, S.M. Crooks, C. Cotrutz, S. Hunjan, J. Lian, and D.Y. Yang—for many useful discussions.

Received May 7, 2002, and in revised form Aug 8, 2002.
Accepted for publication Aug 12, 2002.

together with the beamlet weights. Although this does not pose any conceptual challenge, the search space is greatly enlarged, because of the coupling between beam profiles and beam configuration (1, 3–8). Improving the computational efficiency is a key to having a clinically practical beam orientation optimization tool.

A stochastic algorithm used for beam orientation optimization involves testing a large number of beam configurations. In the current algorithms, the beam orientations are sampled randomly and, for every sampled beam configuration, the beam profiles must be optimized to obtain the value of the objective function for determining whether the trial should be accepted. In practice, some beam directions are better/worse than others, and this information is available through an independent evaluation based on the system's geometric and dosimetric information (2, 9, 10). Incorporation of this type of prior knowledge can potentially make the angular search more intelligent and greatly facilitate the calculation. The prior knowledge here acts like a filter that prescreens the search space by identifying the potential "good" and "bad" gantry angles. In this way, the simulated annealing algorithm can heavily sample the region where the potential for a beam to be placed is high and avoid spending valuable computing time exploring the beam configurations that are less likely to be the optimal solution.

We have recently introduced a beam's-eye-view dosimetry (BEVD) to rank the beam orientations (2, 9). The central point of the technique is that the figure of merit of a beam direction should be measured by what that beam could achieve dosimetrically without exceeding the dose constraints of the system. Application of the BEVD technique to several model systems and clinical cases clearly showed its advantage in IMRT (2, 9). In this study, we point out that the BEVD represents the prior knowledge of the system, and an effective use of the information can provide a computationally intelligent algorithm for beam orientation optimization. In our calculation, the BEVD score was first evaluated for every possible beam orientation, and the simulated annealing optimization of beam orientations was then followed under the guidance of BEVD score. The probability of a beam orientation being sampled in the BEVD-guided calculation depended on the corresponding BEVD score. The new optimization scheme was tested using a clinical case, and the results indicated that this approach significantly reduced the computational time and greatly facilitated the IMRT beam orientation selection process.

METHODS AND MATERIALS

BEVD as a priori knowledge for beam orientation optimization

Relative merit of a single beam can be obtained before beam orientation optimization. An appealing approach is along the line of the beam's-eye-view (BEV), which was originally used in three-dimensional treatment planning as an interactive tool to assist the oncologists in defining

radiation portal entry angles that exclude critical structures while fully encompassing the target volume (2, 9, 11). The binary beam orientation scoring was further improved by the introduction of BEV volumetrics (12–15). The volume of normal structures intersected by a specified aperture/portal direction was calculated for all possible incident directions, permitting the planner to evaluate quantitatively the relative merit of a given portal field. In this approach, the good beam directions were those minimizing the volume of normal tissue intersected. Although the technique worked well for conventional three-dimensional radiation therapy, radical modifications must be made for it to be suitable for IMRT.

Generally speaking, an intensity-modulated beam that intercepts a large volume of sensitive structure(s) is not necessarily a bad beam. The dose tolerances of the involved sensitive structures should be considered also when constructing a metric for measuring the quality of incident beam directions (Note that the BEV volumetrics approach is based *purely* on the geometric information of the patient). We have recently derived a BEVD that ranks a beam direction by what the beam could achieve dosimetrically without violating the dose constraint of the system. To compute the BEVD score of a given gantry angle, a ray tracing is performed for each involved beamlet, and the sensitive structure(s) along the path of the beamlet is located. The maximum achievable weight of a beamlet, which depends on the tolerance(s) and location(s) of the sensitive structure(s), determines the width of the radiation "window" of the beamlet. The score of the beam is calculated according to Eq. 1, as follows (2, 9):

$$S_i = \frac{1}{N_T} \sum_{n \in \text{Target}} \left(\frac{d_{ni}}{D_T^P} \right)^2, \quad (1)$$

where d_{ni} is the maximum dose delivered to the voxel n by the beam from the direction indexed by i , N_T is the number of voxels in the target, and D_T^P is the target prescription dose.

The BEVD score described above is obtained under the assumption of a single incident beam. It is capable of identifying potentially "good" and "bad" directions and can be used as a useful guidance for beam placement in either manual planning or computer optimization. The optimal beam configuration for an IMRT treatment balances the BEVD score and the beam interplay as a result of the overlap of radiation fields. In the following section, we describe how to use the BEVD information to facilitate the beam orientation optimization calculation.

BEVD-guided beam orientation optimization

For simplicity, only coplanar beams were considered in this paper. Noncoplanar beams could be similarly included in the search space by adding the degree of freedom of couch angle (1, 2, 16). We also assumed that the number of beams to be used for the treatment had already been selected

based on clinical consideration. Beam orientation was specified by the gantry angle, varying from 0° to 360° in 5° increments. All calculations were done on a Silicon Graphics O₂ R5000 workstation (Silicon Graphics, Inc., Mountain View, CA) using the PLUNC treatment planning system (University of North Carolina, Chapel Hill, NC).

System variables were divided into two groups: gantry position and beam profile (beamlet weights). Simulated annealing (17–20) was used for beam orientation optimization and the simultaneous iterative inverse treatment planning algorithm for beam intensity profile optimization (21, 22). However, the beam profile optimization could also be done using other existing inverse planning algorithms (23–26). A quadratic objective function defined by:

$$F = \sum_i w_i (D_i - D_i^p)^2 \quad (2)$$

was used in this study, where D_i is the calculated dose value in voxel i , D_i^p is the desired dose, and w_i is the structure-specific importance factor. The values of the importance factors were determined empirically (27–31). D_i^p was the prescribed dose for the target and zero for sensitive structures. The zero prescription dose to the sensitive structures ensured that the optimization continuously improved the dose to the sensitive structures when there was room for improvement, instead of stopping at an *a priori* nonzero value.

In previously reported algorithms, the gantry angles underwent random changes to explore different combinations of beam orientations. The corresponding dose distribution was then calculated, and the objective function evaluated. The trial beam configuration was accepted with the probability

$$P = \begin{cases} 1 & \text{If } \Delta F < 0 \\ \exp\left(-\frac{\Delta F}{T}\right) & \text{Otherwise} \end{cases} \quad (3)$$

where ΔF is the change of the objective function, and T the system temperature. The temperature was gradually lowered according to an exponential cooling schedule, in which the temperature at each iteration step was reduced by a predetermined factor to ensure adiabatic cooling (32, 33). Typically, ~3,000–5,000 sets of beam orientations were sampled in the optimization of coplanar beams to find the solution. The conventional approach is brute force in nature. Given a patient, the geometric characteristics and dose tolerances of sensitive structures are known. The angular search space can be prereduced using BEVD, and this ranking can be used to assist the optimization process.

Ideally, the integration of BEVD into beam orientation optimization algorithm should be done in two steps. First, we use the BEVD information to prescreen the search space

to eliminate the “bad” gantry angles. A computer optimization is then used to individualize the beam orientations by searching the reduced solution space. Although conceptually simple, the situation is more complicated here. The issue is that the BEVD score is obtained under the assumption of a single incident beam. Therefore, it reflects only one facet of the beam configuration selection problem. The final beam configuration depends also on the interplay between the incident beams, because of the overlap of radiation fields. The optimal beam configuration needs to balance between the BEVD scores and the beam interplay. Even though less likely from the perspective of the BEVD, a beam direction with a low but nonzero BEVD score may show up in the final solution if it is angularly well separated from others. In other words, our prior BEVD knowledge about the angular space is “fuzzy” and incomplete. The goal here is to develop a formal and robust approach to incorporating the partial information into the beam orientation optimization.

In conventional beam orientation optimization, the most time-consuming part of the computation is the optimization of beam profiles for every trial beam configuration. Before proceeding to optimize the beam profiles of a trial beam configuration, the strategy here is to evaluate first the likelihood that the trial beam configuration is the final solution, based on prior knowledge of the angular variables (e.g., BEVD). If the likelihood is small that the trial configuration is the final solution, the algorithm will most likely not continue to the next step (i.e., to optimize the beam profiles). Instead, a new sampling of trial beam configuration will be performed. Although our requirement for the general behavior of the BEVD-based likelihood function for accepting a trial beam is clear, its specific form is a matter of experimenting. We found that fast convergence was achieved when the likelihood was proportional to the square of the BEVD score. That is,

$$P(\theta) = \left(\frac{\text{BEVD}(\theta)}{\text{BEVD}_{\text{MAX}}} \right)^2, \quad (4)$$

where $\text{BEVD}(\theta)$ is the score corresponding to the gantry angle (θ), and BEVD_{MAX} is the normalization factor equal to the maximum value of the score function. Several other expressions, including linear and cubic forms, were tested. Even though they all led to the same optimal solution and speeded up the conventional simulated annealing calculation, the level of improvement was less significant than that from Eq. 4. It is possible to incorporate any other type of relative measures of the beam orientation, such as entropy measure (10), into the expression for the probability of acceptance given by Eq. 4.

The overall calculation process, along with the conventional simulated annealing algorithm, is outlined in Fig. 1. The starting temperature was chosen to be higher than the largest value of the objective functions calculated for several sets of randomly sampled beam orientations. During an

A. Simulated annealing (SA) optimization B. BEVD-Guided Optimization

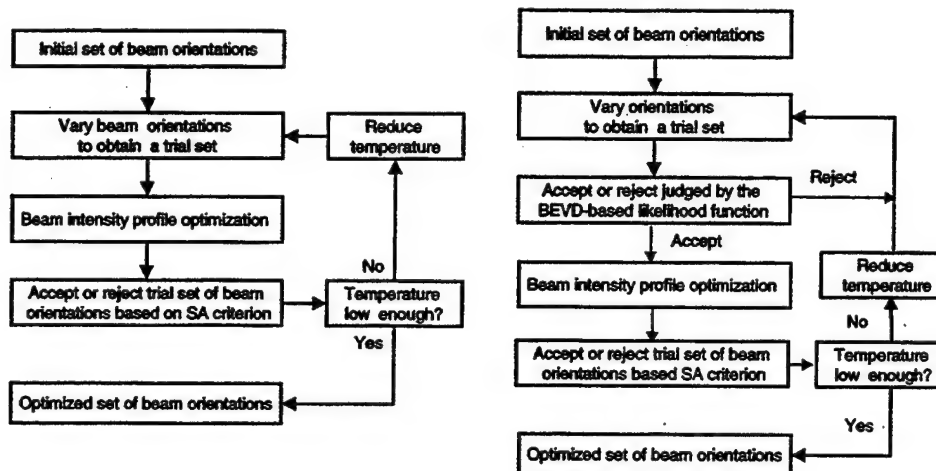


Fig. 1. (A) Flow chart of the conventional simulated annealing beam orientation optimization algorithm. (B) Flow chart of the BEVD-guided simulated annealing sampling algorithm.

iteration, a trial beam configuration was introduced by randomly selecting a set of beams and varying the directions of the beams using a predesigned distribution function. In our algorithm, the probability of selecting an arbitrary number of beams from the total number of beams is set to be equal (i.e., $1/K$ for each possibility, where K is the total number of beams used for treatment). The sampling probability of an angular variation of a beam was determined by a symmetrical exponential distribution function (i.e., proportional to the reciprocal of the exponential of the angular increment).

As stated earlier, a trial set of angular variations has only a certain chance to be accepted and evaluated by the simulated annealing algorithm. Before proceeding to beam profile optimization, we sequentially determine the acceptance of every beam within the configuration based on the value of the precalculated BEVD-based likelihood function (4). If not accepted, a new sampling was done for the beam. Only when all the beams within the set were accepted was the beam profile optimization carried out and the trial further checked by the simulated annealing acceptance probability defined in Eq. 3. In a sense, the overall acceptance probability for a trial beam orientation sampling can be viewed as a product of the traditional acceptance probability and the BEVD-based probability distribution.

Because of the prescreening of the BEVD-based likelihood function, we reduced the chance for the algorithm to spend valuable computing time on those trials that were less likely to be the final solution. The temperature was gradually lowered according to an exponential cooling schedule described earlier. The stopping temperature was determined by monitoring the objective function as a function of the temperature change. We would like to emphasize here that the likelihood for a trial variation of a beam to pass the BEVD-based prescreening is not zero unless the BEVD score of the trial direction is zero (corresponding to a situation in which the beam is completely blocked by the

sensitive structure[s] having zero tolerance). In other words, we do not completely eliminate a beam configuration containing one or a few beams with low BEVD score(s) from being tested by the simulated annealing algorithm. This is because BEVD represents only the partial/incomplete knowledge of the angular variable, and a beam configuration containing one or a few beams with relatively low (but not close to zero) BEVD scores may not necessarily be a bad beam configuration. This issue has been discussed already in the third paragraph of this section.

An IMRT treatment of paraspinal tumor was used here to illustrate the usefulness of prior knowledge of the system in facilitating IMRT planning. Five 15-MV photon beams were used for the treatment. To assess the computational efficiency, the convergence behavior of the new algorithm was compared with that of the conventional simulated annealing calculation. To demonstrate the improvement in plan quality, the results of the BEVD-guided optimization were compared with an IMRT plan obtained with five equiangular-spaced beams. The dose–volume histograms, as well as the dose distributions, for the target and sensitive structures were used for the evaluation of the treatment plans.

RESULTS

The BEVD-guided beam orientation optimization was applied to a five-field IMRT treatment of paraspinal tumor. The prescribed doses and importance factors of different structures are given in Table 1. In Fig. 2 we show the BEVD score as a function of gantry angle. This calculation was performed before beam orientation optimization calculation, and the result depended only on the patient's geometric information and on the dosimetric tolerances of the involved sensitive structures. Because of the dosimetric restriction of

Table 1. Relative importance factors and dose tolerances.

	Relative importance factors	Target prescription and sensitive structure tolerance doses
GTV	1.0	1.0
Spinal cord	1.0	0.6
Liver	0.01	0.4
Kidney	0.02	0.4
Skin	0.001	1.0

the liver and the long radiologic path for the photon to reach the target, the angles between 260° and 360° are considered to be in a disadvantageous region in terms of target irradiation, as reflected by the lower BEVD scores. The BEVD has a distinct peak at 225°. The optimal beam angles from the BEVD-guided beam orientation optimization are listed in Table 2. It is interesting to note that one of the optimal gantry angles (220°) is located very near the highest BEVD score (225°) in the final optimized solution. Furthermore, there is no beam located in the angularly disadvantageous region (between 260° and 360°) identified by BEVD.

The conventional simulated annealing algorithm generated the same beam configuration as listed in Table 2 for four out of five independent runs, but with much longer computing time. To assess the improvement in computing efficiency, we studied the convergence behavior of the BEVD-guidance optimization in parallel to the conventional

Table 2. Beam orientations used in equiangular treatment and the treatment with beam orientation optimization

Equiangular-spaced beam orientations
Gantry angles: 40°, 110°, 180°, 255°, 325°
Optimized beam orientations
Gantry angles: 110°, 145°, 180°, 220°, 250°

simulated annealing optimization. Two tests were done. First, we set the temperature in the simulated annealing to zero and compared the performance of the beam orientation optimizations with and without incorporation of BEVD knowledge. When the temperature is set to zero, only trial configurations with lower objective function values are accepted in both cases, and the system moves only toward the downhill direction. However, this calculation cannot be replaced by a gradient search, because it does not allow the system to jump over the barriers of a "bumpy" objective function. The evolution of the objective function as a function of iteration step for conventional simulated annealing is shown as the dashed line in Fig. 3. The solid line shows the convergence of the system when the BEVD is incorporated into the sampling using the algorithm described in the last section. The stepwise decrease of the objective function indicates that the system jumps from one "valley" of the objective function to another during the computational process. With the guidance of BEVD score, the performance of the modified simulated annealing algorithm was improved significantly. The objective function reached its minimum

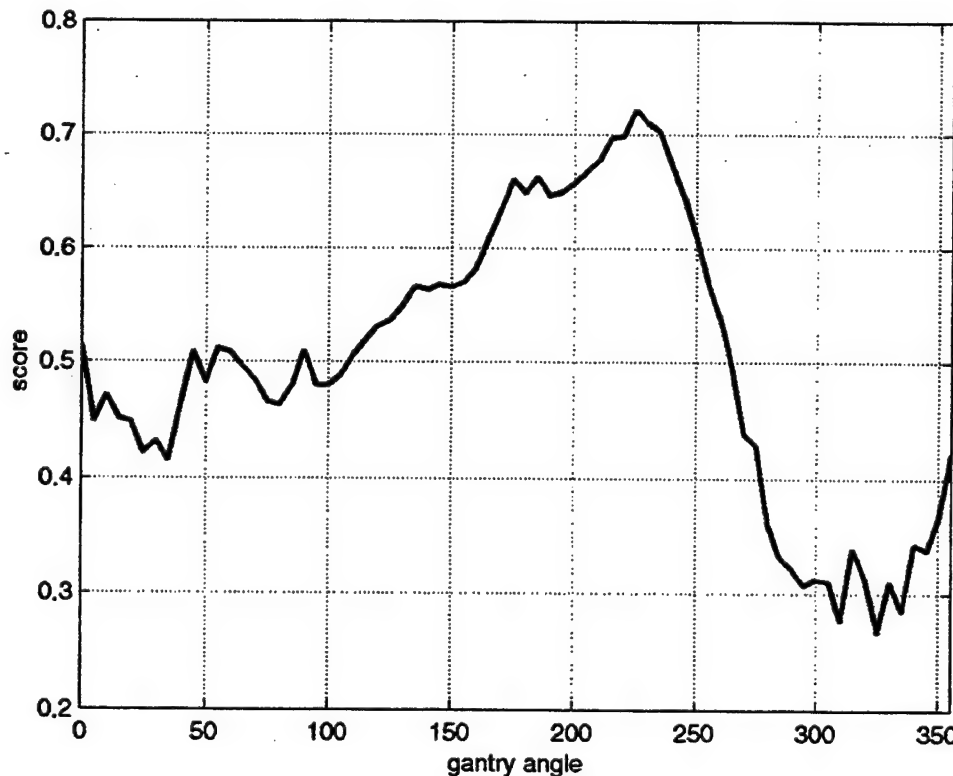


Fig. 2. BEVD score as a function of the gantry angle.

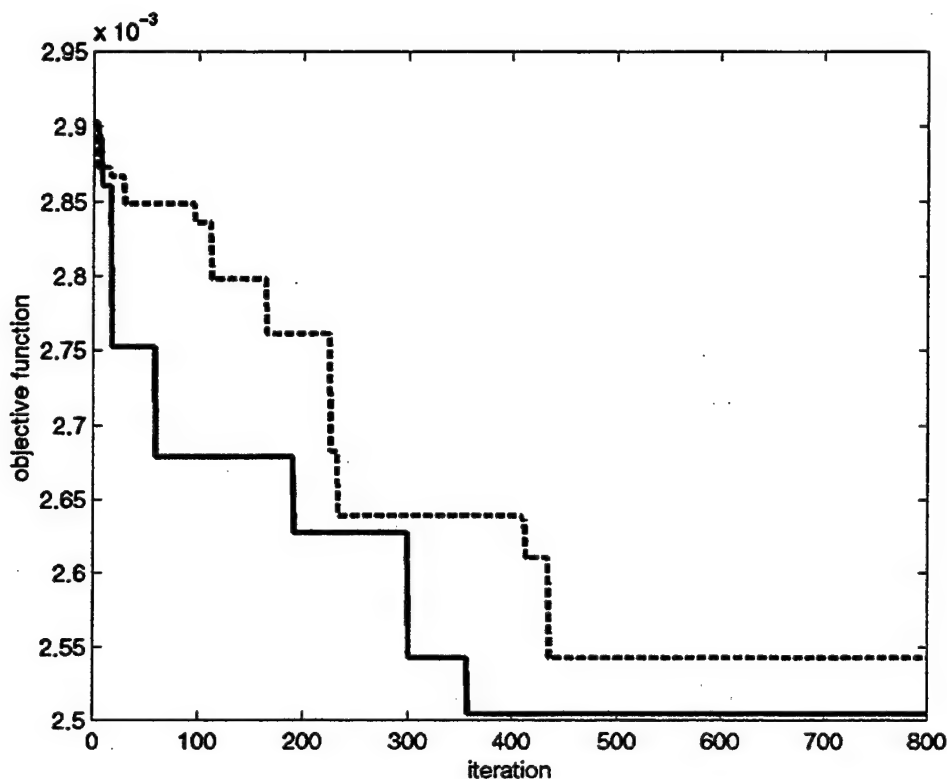


Fig. 3. The objective function vs. iteration step with the temperature set to zero during the optimization process. Dashed and solid lines correspond to the simulated annealing performed with standard sampling and the BEVD-guided sampling, respectively.

in approximately 360 iterations, whereas the conventional simulated annealing took many more iterations to converge. Theoretically, the convergence of the simulated annealing algorithm to the global minimum of the objective function is guaranteed only in the case of a very slow logarithmic cooling schedule, which is hardly realized in practice. When a realistic cooling schedule is used, it is possible that some optimization runs get "stuck" in a local minimum (19). The result indicated that the incorporation of prior BEVD knowledge not only increases the calculation speed but also improves the convergence behavior of the simulated annealing calculation based on a realistic cooling schedule.

The next level of test involved a comparison of the BEVD-guided optimization and the conventional simulated annealing optimization with an exponential cooling schedule (32, 33). Figure 4 shows the objective function as a function of iteration step for the two types of calculations. In each case, an average was taken over five independent runs to reduce the "noisy" behavior of the evolution of the objective function. Comparing Figs. 3 and 4, it can be seen that switching on the annealing in both cases speeds up the convergence and decreases the number of iterations required for the system to reach the ground state. From Fig. 4, it is seen that the BEVD-guided simulated annealing significantly outperformed the standard simulated annealing. All five BEVD-guided optimization calculations reached the global minimum within 300 iterations. With 400 iterations, only one out of five runs of standard simulated an-

nealing was able to get to the ground state. All four other simulations led to suboptimal solutions with higher objective function values. Generally, it took about 5,000 iterations for the standard simulated annealing calculations to converge to the optimal solution.

For comparison, in Fig. 4 we plotted also the value of the objective function (dashed horizontal line) for a five-field IMRT plan with equally angled beams listed in Table 2. The dose distribution corresponding to the five equally angled beams is shown in Fig. 5a. The improvement in dose distribution after BEVD-guided optimization is shown in Fig. 5b. Figure 6 shows comparisons of dose-volume histograms for plans obtained using the equiangular-spaced beam configuration and the BEVD-guided optimization. Whereas the target dose-volume histogram was improved slightly, the fractional dose-volume of the spinal cord, kidney, and liver were all lowered by moderate to significant amounts. Considering the large volumes of the kidney and liver and the reduction in radiation doses, the improvement should be considered as clinically significant.

On average, it took slightly more than 2 hrs for the SGI 02 workstation to carry out 300 iterations. However, with state-of-the-art computer hardware now available on the market, as well as improved programming, it is likely that the calculation efficiency will be enhanced to a level where BEVD-guided beam orientation becomes practically achievable in a clinical environment.

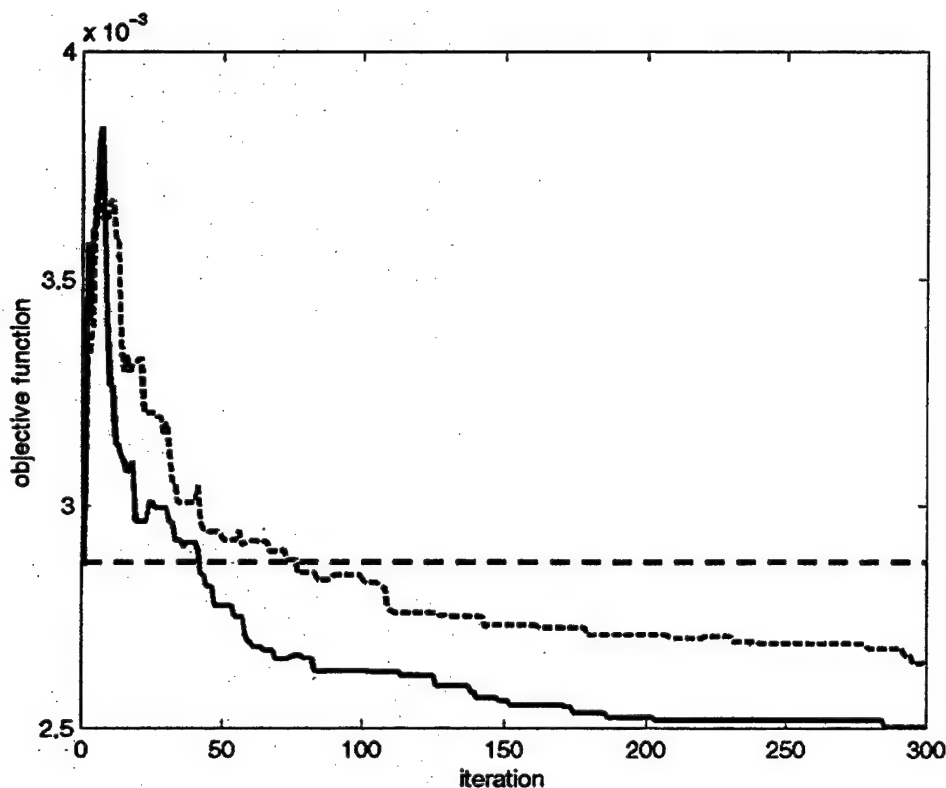


Fig. 4. The objective function vs. iteration step for simulated annealing with the exponential cooling schedule. Dashed and solid lines correspond to the simulated annealing performed with standard sampling and the BEVD-guided sampling, respectively. Horizontal dashed line indicates the objective function value of an IMRT plan with 5 equiangular beams.

DISCUSSION

In this study, we have proposed incorporating the BEVD information into the beam orientation optimization algorithm to guide the angular search. The BEVD ranking is a single beam score function available before inverse treatment planning. Generally speaking, an intensity-modulated beam that intercepts one or more sensitive structures is not necessarily a bad beam. In reality, it is the dose and/or dose-volume that determines the damage to a sensitive structure. The BEVD score measures the dosimetric capability of a given beam direction. Although it does not provide the optimal beam configuration, because of the absence of beam interplay, it points out the location of the potentially good and bad directions for beam placement and represents prior partial knowledge of the system. This is supported by our optimization results, presented in "Results." Indeed, all the beams in the final optimal solution have high BEVD scores, and in particular, one of the beams appears very near the peak position of the BEVD function. We observed that, even in a suboptimal solution resulting from the conventional simulated annealing calculation, none of the beams took a position in the disadvantageous region of the BEVD function.

We have shown that incorporation of the valuable BEVD information greatly facilitated the beam orientation optimization. The approach proposed here is different from other

beam orientation optimization algorithms, for example those described in Refs. 34, 35 in the way the available information is used. Instead of adding to the objective function used to evaluate the "fitness" or "energy" of a trial configuration, we use the BEVD at the step of designing the trial configuration. In our calculations, the gantry angles were sampled according to a simulated annealing algorithm with consideration of BEVD. During an iteration step, the angle of an arbitrarily chosen beam was varied by a random amount. The trial was prescreened by the BEVD according to Eq. 4. Instead of performing beam profile optimization for every trial beam configuration, we performed the conventional simulated annealing calculation (optimizing beam profiles and computing the corresponding value of the objective function) only for those trials that passed the prescreening, as depicted in Fig. 1. The prescreening allowed us to eliminate those beam configurations that were less likely to be the candidates for the optimal solution and saved a large amount of computing time. Application of the technique to clinical cases clearly showed its advantage. It reduced the sampling rate for those angles that were less likely to appear in the final solution and saved a large amount of computing time.

The inclusion of BEVD makes the computation more intelligent and can bring the system into the vicinity of the optimal solution more rapidly. As a result, the BEVD-

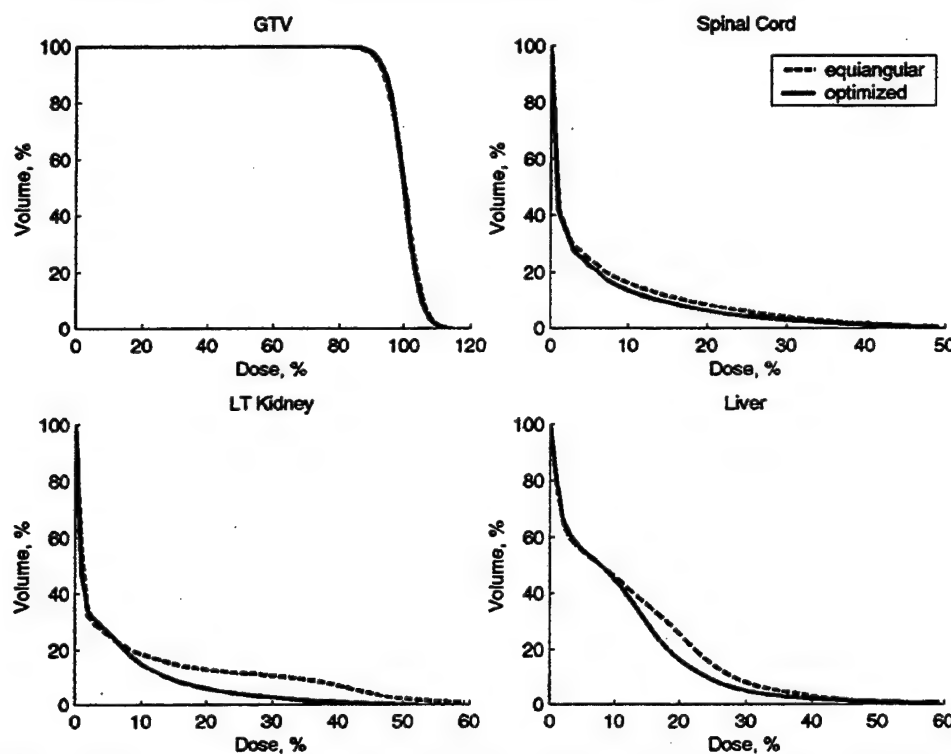


Fig. 6. Target and sensitive structure dose–volume histograms of the IMRT treatment plans for a paraspinal tumor. The dashed curves and solid curves correspond to the plans with 5 equiangular-spaced beams and 5 beams obtained using BEVD-guided optimization.

Finally, in this article we have assumed that the number of beams was given before beam orientation optimization. The optimal choice of the number of beams represents another important issue in IMRT planning and should be addressed in future research. In general, the sensitivity of an

IMRT treatment plan with respect to the number of beams varies from site to site. A systematic study of the beam number dependence for a variety of clinical cases should be helpful in obtaining important insight and in providing practical guidance on this important issue.

REFERENCES

- Pugachev A, Li JG, Boyer AL, et al. Role of beam orientation optimization in intensity-modulated radiation therapy. *Int J Radiat Oncol Biol Phys* 2001;50:551–560.
- Pugachev A, Xing L. Pseudo beam's-eye-view as applied to beam orientation selection in intensity-modulated radiation therapy. *Int J Radiat Oncol Biol Phys* 2001;51:1361–1370.
- Stein J, Mohan R, Wang XH, et al. Number and orientations of beams in intensity-modulated radiation treatments. *Med Phys* 1997;24:149–160.
- Bortfeld T, Schlegel W. Optimization of beam orientations in radiation therapy: Some theoretical considerations. *Phys Med Biol* 1993;38:291–304.
- Rowbottom CG, Oldham M, Webb S. Constrained customization of non-coplanar beam orientations in radiotherapy of brain tumours. *Phys Med Biol* 1999;44:383–399.
- Sailer SL, Rosenman JG, Symon JR, Cullip TJ, Chaney EL. The tetrad and hexad—maximum beam separation as a starting point for noncoplanar 3d treatment planning—prostate cancer as a test case. *Int J Radiat Oncol Biol Phys* 1994;30:439–446.
- Sherouse GW. A mathematical basis for selection of wedge angle and orientation. *Med Phys* 1993;20:1211–1218.
- Soderstrom S, Brahme A. Which is the most suitable number of photon beam portals in coplanar radiation therapy? *Int J Radiat Oncol Biol Phys* 1995;33:151–159.
- Pugachev A, Xing L. Computer assisted beam orientation selection in IMRT. *Phys Med Biol* 2001;46:2467–2476.
- Soderstrom S, Brahme A. Selection of suitable beam orientations in radiation therapy using entropy and Fourier transform measures. *Phys Med Biol* 1992;37:911–924.
- Pugachev A, Xing L. Computer assisted selection of beam energy and orientations in IMRT. *Int J Radiat Oncol Biol Phys* 2001;51:74.
- Chen GT, Spelbring DR, Pelizzari CA, et al. The use of beam's eye view volumetrics in the selection of non-coplanar radiation portals. *Int J Radiat Oncol Biol Phys* 1992;23:153–163.
- Myrianthopoulos LC, Chen GT, Vijayakumar S, Halpern HJ, Spelbring DR, Pelizzari CA. Beam's eye view volumetrics: An aid in rapid treatment plan development and evaluation. *Int J Radiat Oncol Biol Phys* 1992;23:367–375.
- McShan DL, Fraass BA, Lichter AS. Full integration of the beam's eye view concept into computerized treatment planning. *Int J Radiat Oncol Biol Phys* 1990;18:1485–1494.
- McShan DL, Kessler ML, Fraass BA. Advanced interactive planning techniques for conformal therapy: High level beam descriptions and volumetric mapping techniques. *Int J Radiat Oncol Biol Phys* 1995;33:1061–1072.
- Meyer J, Mills JA, Haas OC, Burnham KJ, Parvin EM. Accommodation of couch constraints for coplanar intensity

- modulated radiation therapy. *Radiother Oncol* 2001;61:23–32.
17. Webb S. Optimisation of conformal radiotherapy dose distributions by simulated annealing. *Phys Med Biol* 1989;34:1349–1370.
 18. Rosen II, Lam KS, Lane RG, Langer M, Morrill SM. Comparison of simulated annealing algorithms for conformal therapy treatment planning. *Int J Radiat Oncol Biol Phys* 1995; 33:1091–1099.
 19. Winkler G. Image analysis, random field and dynamic Monte Carlo methods. Berlin: Springer-Verlag; 1995.
 20. Li J, Boyer A, Xing L. Clinical implementation of wedge filter optimization in 3D radiotherapy treatment planning. *Radiother Oncol* 1999;53:257–264.
 21. Xing L, Chen GTY. Iterative algorithms for inverse treatment planning. *Phys Med Biol* 1996;41:2107–2123.
 22. Xing L, Hamilton RJ, Spelbring D, Pelizzari CA, Chen GT, Boyer AL. Fast iterative algorithms for three-dimensional inverse treatment planning. *Med Phys* 1998;25:1845–1849.
 23. Wu Q, Mohan R. Algorithms and functionality of an intensity modulated radiotherapy optimization system. *Med Phys* 2000; 27:701–711.
 24. Olivera GH, Shepard DM, Reckwerdt PJ, et al. Maximum likelihood as a common computational framework in tomotherapy. *Phys Med Biol* 1998;43:3277–3294.
 25. Rosen II, Lane RG, Morrill SM, Belli JA. Treatment plan optimization using linear programming. *Med Phys* 1991;18: 141–152.
 26. Cho PS, Lee S, Marks RJ, 2nd, Oh S, Sutlief SG, Phillips MH. Optimization of intensity modulated beams with volume constraints using two methods: Cost function minimization and projections onto convex sets. *Med Phys* 1998;25:435–443.
 27. Mohan R, Wang X, Jackson A, et al. The potential and limitations of the inverse radiotherapy technique. *Radiother Oncol* 1994;32:232–248.
 28. Xing L, Li JG, Donaldson S, Le QT, Boyer AL. Optimization of importance factors in inverse planning. *Phys Med Biol* 1999;44:2525–2536.
 29. Xing L, Li JG, Pugachev A, Le QT, Boyer AL. Estimation theory and model parameter selection for therapeutic treatment plan optimization. *Med Phys* 1999;26:2348–2358.
 30. Cotrutz C, Lahanas M, Kappas C, Baltas D. A multiobjective gradient-based dose optimization algorithm for external beam conformal radiotherapy. *Phys Med Biol* 2001;46:2161–2175.
 31. Gopal R, Starkshall G. Plan space: Representation of treatment plans in multidimensional space. *Med Phys* 2001;28: 1227.
 32. Kirkpatrick S, Gelatt CDJ, Vecchi MP. Optimization by simulated annealing. *Science* 1983;220:671–680.
 33. Press WP, Saul A, Teukolsky SA, Vetterling WA, Flannery BP. Numerical Recipes in C. Cambridge: Cambridge University Press; 1993.
 34. Rowbottom CG, Nutting CM, Webb S. Beam-orientation optimization of intensity-modulated radiotherapy: Clinical application to parotid gland tumours. *Radiother Oncol* 2001;59: 169–177.
 35. Haas OC, Burnham KJ, Mills JA. Optimization of beam orientation in radiotherapy using planar geometry. *Phys Med Biol* 1998;43:2179–2193.
 36. Deasy JO. Multiple local minima in radiotherapy optimization problems with dose-volume constraints. *Med Phys* 1997;24: 1157–1161.
 37. Llacer J, Deasy J. Multiple extrema in inverse radiation therapy planning. *Phys Med Biol* 2002, submitted.
 38. Winkler RL. An introduction to Bayesian inference and decision. New York: Holt, Rinehart & Winston, Inc.; 1972.

A Comprehensive Method of Breast-Conserving Radiation Therapy using Forward Multiple-Segment Planning and Step-and-Shoot Delivery

L. Xing¹, Ph.D., T. Pawlicki¹, Ph.D., L. Yuen¹, C.M.D., S. Crooks¹, Ph.D., J. Dugan², B.S., C. Li², Ph.D., F. Halberg², M.D., C. Cotrutz¹, Ph.D., J. Lehmann¹, Ph.D., Vivek Metha, M.D., Sarah S. Donaldson, M.D., G. Luxton¹, Ph.D., A. L. Boyer¹, Ph.D., D. R. Goffinet¹, M.D.

¹Department of Radiation Oncology, Stanford University School of Medicine,
Stanford, California 94305-5304

²Department of Radiation Oncology, Marin Cancer Institute, Greenbrae, CA 94904

Address correspondence to:

Lei Xing, Ph.D.
Department of Radiation Oncology
Stanford University School of Medicine
300 Pasteur Drive
Stanford, CA 94305-5304

Phone: (650) 498-7896
FAX: (650) 498-4015
E-mail: lei@reyes.stanford.edu

In preparation.

Purpose: To establish the multiple segment radiation therapy (MSRT) as a general technique for the treatment of breast cancer, to demonstrate its superiority over the standard opposed tangential-field (OTF) technique, and to illustrate why forward planning is more efficient than beamlet-based inverse planning approach for breast irradiation.

Methods and Materials: The patient setup and target definition were the same as that used in the standard OTF treatment. The MSRT treatment plan was obtained using a conventional 3D planning system with manual trial-and-error forward planning method. The approach utilized additional MLC segments stacking on top of the original OTF to improve the dose distribution. The aperture and weight of the added segment were chosen in such a way that the dose was most uniform in the breast target. After the plan was completed, the static MLC fields of each gantry angle were concatenated together for step-and-shoot delivery. An algebraic method was used to minimize the MLC transmission in the delivery process. As a standard QA procedure, the fluence map and MU of each field were independently checked before a patient treatment. Ten patients with early-stage breast tumors were planned with the MSRT and the results were compared with those using OTF.

Results: The MSRT plans significantly improved target dose uniformity in comparison with the standard OTF plans. The overall planning and treatment delivery overhead of the MSRT was found to be minimum. Our results for ten breast cases revealed that the target dose uniformity could easily be reduced from 109%~117% to 106% to 112%. The volume of receiving high dose irradiation in the breast target was also markedly reduced. It was also possible to use MSRT to reduce the dose to the ipsilateral lung/heart.

Conclusions: The current IMRT planning, delivery, and QA deviate significantly from the conventional approach and requires additional steps in the treatment process. MSRT bridges the gap, both conceptually and operationally, between the conventional and IMRT treatments. The underlying reason for this method to be a viable choice is that the initial OTF plan have already brought the system to the vicinity of optimal solution. As a result, it is often sufficient to add 1~3 segments to substantially improve the dose distribution. For breast cancer, MSRT is a natural extension of standard treatment and improves the dosimetry without paying excessive overhead associated with the current IMRT. It does not rely on an inverse planning system, nor require

explicit delineation of the breast target. Furthermore, each segment is a standard field and conventional dose calculation and checking methods can be used for QA of MSRT.

Key Words: breast cancer, treatment planning, IMRT, inverse planning, step-and-shoot.

I. INTRODUCTION

Radiation therapy is accepted as an effective treatment modality in the management of both invasive and non-invasive breast cancer [1-4]. Conventional breast radiotherapy utilizes two opposed tangential photon beams with either uniform or wedged shaped fluence profiles. A certain volume of the ipsilateral lung and, in the case of the left breast, a small volume of the heart is inevitably included in the tangential field, resulting in high radiation dose to this part of the lung and heart. For large sized breast, the technique is frequently incapable of producing homogeneous dose distribution in the target volume. Consequently, breast irradiation has been associated with a number of potential complications, including radiation induced pneumonitis, cardiac toxicity, rib fracture, arm edema, severe breast or chest wall fibrosis, and soft tissue or bone necrosis, and radiation induced secondary cancer [4]. Adjuvant treatment with chemotherapy may further aggravate these effects.

Many approaches have been proposed to improve the current OTF treatment which aims at achieving more homogeneous dose distributions in the breast target volume and limit radiation dose to normal structures to reduce cardiac and pulmonary toxicity. Karlsson and Zackrisson [5, 6] and Jansson et al. [7] proposed the use of matched electron and photon beams to reduce dose to the underlying structures. The medial part of the breast is treated with an electron beam, which is matched to two opposed photon beams used to treat the most lateral part of the breast. However, large dose inhomogeneity was seen in the matched region between the electron and photon beams. As was demonstrated in recent theoretical and experimental studies by Li et al. [8, 9], the matching was improved by using intensity-modulated photon beams because of effective penumbra broadening. A drawback of the approach is that the beam setup and treatment procedure becomes less straightforward. Smitt et al. [10] examined the potential of fan-beam IMRT for breast cancer. While the volumes of the ipsilateral lung and the heart that received high doses were smaller as compared to the conventional plans, it was found that significantly larger volume of the two structures as well as the contralateral lung and the contralateral breast received low doses. Williams et al. [11] studied the feasibility of using multiple (3~7) intensity-modulated beams for breast cancer. The technique can treat the breast target as well as the nodal sites with a single set of IMRT fields, simplifying thus the treatment when the regional lymph nodes (supraclavicular, axillary and internal mammary nodes) are involved and eliminating the

potential overdosing/underdosing caused by matching the supraclavicular/axillary field with the tangential fields. But the adjacent sensitive structures are exposed to low, or moderate or even high dose of radiation because of the exiting and scatter photons. This is similar to that seen in breast cancer treatment using fan-beam IMRT [10] and cone-beam IMRT with multiple beams [8, 9]. The increase in the volumes of normal structures receiving a low dose of radiation is detrimental to the clinical application of these techniques. Breast irradiation using modulated electron radiotherapy (MERT), which attempts to achieve conformal dose distributions by intensity- and/or energy-modulation of an electron beam, has also been proposed [12]. While it is straightforward to simulate MERT on a computer, there are a number of serious engineering and physics problems that must be overcome before its practical implementation.

Tangential field treatment using intensity-modulated fields offers a viable choice for breast cancer treatment [13]. This technique has been recently evaluated on 10 breast patients and notable improvement in the doses to critical structures was achieved. Compared with standard OTF plans, there is a significant reduction in the dose to the coronary artery region (for patients treated to the left breast), the mean dose to the contra-lateral breast, and the ipsilateral lung and soft tissue volumes receiving more than prescribed dose. The dose homogeneity within the target volume was also improved (~8%), especially in the superior and inferior regions of the breast. Similar results were also reported by McCormick [14], Chang et al.[15], Donovan et al [16], Kestin et al. [17], Lo et al [18], and van Asselen et al. [19].

While the dosimetric advantage of IMRT with opposed tangential beam configuration for breast cancer is clear, an important question is how to efficiently implement the technique in a busy clinical environment. The current IMRT planning and treatment process deviates significantly from the conventional approach and requires additional steps in planning, delivery and quality assurance [15, 20-23]. When applied to breast irradiation, the current beamlet-based IMRT has two additional limitations: (1) it is required to segment explicitly the target volume, which adds a large amount of extra work to physicians; and (2) a tangential treatment field is often split into two separate fields for delivery because of the large field width and the disintegration of the dose optimization and the MLC leaf sequencing in the planning process. Characteristics that are special to breast cancer treatments are not incorporated in the current inverse planning system

design and the inverse planning algorithms are by no means the most efficient optimization scheme for breast cancer. In addition, the procedure of dosimetric verification of an arbitrarily shaped intensity-modulated beam is not well established and the QA is of a great concern [20, 22, 24-26]. If intensity modulation is to have truly impact on breast treatment, it has to be more adaptive and efficient than it is today.

In this paper we establish a variant of IMRT, multiple segment radiation therapy (MSRT) [27-29], for breast cancer treatment and illustrate its utility by using several clinical cases. While a few research groups have reported the use of MSRT for breast treatment [20, 22, 24-26], the focus of this work is on developing a clinically practical procedure and providing intuitive explanation on why forward planning with multiple segment delivery is more competitive than the conventional IMRT. We address several untouched clinical issues related to the technique, including the use different types of wedges (physical or dynamic), field width problem, incorporation of MLC transmission into the step-and-shoot delivery, and QA related issues. We have applied the technique to ten clinical cases and our results indicated that the MSRT markedly improved breast irradiation and provided superior dose distributions needed to reduce radiation side effects and complications. The technique is especially valuable for radiation treatment of large-breasted women, where it is difficult to achieve homogeneous target dose distribution. In addition, the methodology developed here should be useful also for radiation treatment of other diseases (such as Hodgkins disease, lung cancer), where isodose shaping at the field boundary can be realized by beam shaping with a simple beam configuration.

II. METHODS AND MATERIALS

II.1 CT data acquisition and target definition

Five right-sided and five left-sided breast cancer patients with invasive carcinomas of the breast, who had previously undergone lumpectomy, were selected for the study. The patients underwent computed tomography (CT) in the conventional treatment position supported by an Alpha Cradle immobilization device (Smithers Medical Products, Tallmadge, Ohio). Radiopaque markers were

placed on the patients' chest to indicate the medial and lateral borders of the palpable breast tissue and the location of the lumpectomy scar. All ten breast patients underwent MSRT planning for the whole breast.

The radiation-sensitive structures included the left and right lungs, the heart, and the contralateral breast. For this study, the contours of the skin, target volume and the sensitive structures were outlined using the segmentation tools provided by the AcQSim virtual simulation workstation (Marconi Medical System, Cleveland, OH). It is, however, not required to outline the structures in general MSRT treatment, similar to that in the routine OTF breast irradiation. The tangential fields were determined by the routine virtual simulation procedure performed on an AcQSim workstation. The fields may be adjusted at the stage of treatment planning according to the actual treatment objective for each patient with considerations concerning tumor bed coverage, in-field lung and cardiac volume, if for left breast irradiation. Figure 1a shows an example of the OTF setup for the treatment of a left breast cancer patient. A flash region of 2 cm was used in the anterior field border to account for patients' respiration motion and setup uncertainty.

II.2 Treatment planning

Treatment planning was done with the FOCUS 3D treatment planning system (Computerized Medical System, St. Louis, MO). A uniform dose of 4,500 cGy or 5,040 cGy was prescribed to the target volume in 180-cGy fractions. For comparison, three plans were generated for each patient. One was the standard opposed OTF plan and the other two were the MSRT plans with different constraints. Standard plans involved a medial and lateral tangential field with 6 or 15 MV photon energy. A wedge filter was used in lateral direction. When a physical wedge was used, we avoided placing it in the medial field to reduce the scatter dose to the lung/heart and the contra-lateral breast. In this case, both fields were modulated with multiple segments (MSRT-B). The segmented fields in the lateral direction were delivered concurrently with the physical wedge in place. For treatment involved dynamic wedge(s), a slightly different approach was used and this will be described in Section II.3. All plans were obtained through manual trial-and-error process.

For intermediate or large sized breast patients, a standard OTF plan is frequently incapable of generating homogeneous dose distribution. MSRT affords an effective way to improve the dose distribution. The MSRT planning started with a standard OTF plan. After the initial wedged plan was obtained, we proceeded to introduce an additional MLC field segment to one or both beam directions to boost the “cold” region(s) under the guidance of dose distributions in the plane perpendicular to the incident beam direction. For MSRT-B, multiple segment modulation was allowed for both beams. All segments in the lateral beam were planned and delivered with the physical wedge in place. Figures 1d-1i show the three segments of the lateral and the medial fields for a MSRT-B treatment. The weights and MLC apertures of the segments were adjusted manually to achieve a uniform dose distribution. Our experience indicated that, for intermediately complex cases, it was often sufficient to introduce one or two additional segments to the original opposed tangential fields. For complex cases, two or three additional segments were frequently used. A segment with ipsilateral lung or heart blocked by MLC (the third segment in either medial or lateral MRST field) was also helpful in reducing the dose to these structures.

II.3 MSRT plan with dynamic wedge

In the MSRT-B treatment described above, both lateral and medial fields were modulated by multiple segments. Upon the completion of the MSRT-B planning, the sequential MLC shapes from the same gantry angle were stacked together for step-and-shoot delivery (see Sec. II.4). For the lateral field, the multiple segments were delivered with a physical wedge in place. If dynamic wedge is to be employed for treatment, the above planning and delivery procedure needs be modified.

The complication with dynamic wedge based MSRT arises from the interplay between the MLC leaf movement and the dynamic jaw motion. In reality, there are two ways to proceed. The first one is to plan the treatment using the MSRT-B scheme described in Sec. II.2 and then deliver the segmented MLC fields and the dynamic wedge field separately. If this scheme is to be used, each segment is an MLC-shaped uniform field which must not be modified by the wedge filter. This is different from the delivery based on a physical wedge, where the fluence of each segment was modified by a physical wedge (unless one chooses to deliver the wedged field and the multiple

segments separately). The major disadvantage of this approach was that it doubled the number of delivery fields and prolonged the treatment. To facilitate the treatment, we restricted one of the incident beam to be modulated with only dynamic wedge and the other beam with only MLC-shaped segmented fields (MSRT-S). This approach enabled us to take advantage of the MSRT treatment yet avoiding the separated delivery of the dynamic wedge field and the multiple segmented fields. The overall treatment planning procedure for this delivery scheme was similar to that described in the Section II.2. In figure 2 we show an example of such a treatment with three segments in the medial direction and a 30° enhanced dynamic wedge in the lateral direction.

II.4 Step-and-shoot delivery

The MLC movement trajectories (or leaf sequences) were known upon the completion of MSRT plan and there was no need for a leaf sequencing algorithm to convert an optimal fluence map into MLC sequences. The static MLC file of each segment was exported as an ASCII file from the FOCUS treatment planning system. For each gantry angle, the segmented fields were stacked together to form a step-and-shoot delivery using a simple software tool, developed in-house, which read in each individual MLC segment and output the step-and-shoot delivery file according to the MLC manufacturer's specifications. In addition, a step-and-shoot delivery file for portal verification was also generated (see Sec. II.5).

A step-and-shoot delivery is perhaps the simplest scheme from the delivery and QA points of view. In this modality, MLC leaf movements and dose deliveries are done at different instances [30-33]. A leaf sequence file consists of alternatives of dose-only and motion-only instances. Figure 3 shows an example, which corresponds to the delivery of the MSRT-B treatment outlined in Fig. 1. In figure 3 f_k and $a f_k$ are the fractional MU of the k^{th} instance and the accumulated fractional MU, respectively. If the treatment planning system has already considered the MLC transmission in treatment plan, we have

$$f_k = MU_k / MU, \quad (1)$$

where MU_k ($k=1, 2, 3, \dots$) are the monitor units of the k -th segment from the treatment planning system and $MU = \sum_k MU_k$ is the total MU of the field. Equation (1) was applied directly to the treatment plan obtained using FOCUS 3D planning system since the MLC transmission has been

already taken into account in the dose calculation of each segment. Otherwise, it is desirable to take the MLC transmission into account during the delivery process. The influence of MLC transmission can be compensated by adjusting the values of $\{f_k\}$ in the step-and-shoot delivery file. A general method of incorporating the MLC transmission into the step-and-shoot delivery has been established [34, 35]. Assuming that the average MLC transmission coefficient is α , the transmission fluence of a segment with fractional monitor unit of f_k is given by $MU(1-f_k)\alpha$. To the first order approximation, the f_k used in the MLC leaf file should be replaced by $\tilde{f}_k = f_k - (1-f_k)\alpha$, where f_k is given by Eq. (1). It has been shown in Ref. [35] that this algebraic relation offers an effective way to compensate the MLC transmission for the step-and-shoot delivery.

The step-and-shoot file must have correct CRC (computer redundancy check) code attached at the end of the file in order to be executable by the MLC workstation. The subroutine generating CRC code was implemented into the in-house software that concatenated a series of static MLC segments into a step-and-shoot file.

For Varian's accelerators, the upper and lower jaws are fixed during the whole step-and-shoot delivery process. At a given segment, some pairs of leaves may need to be closed. In order to avoid unnecessary exposure from the ends of a pair of closed leaves, it is desirable to move the leaf ends to a position under the lower jaw protection, as shown in the third segment in Fig. 2c. A MLC configuration for the same segment shown in Fig. 4 is not acceptable. Otherwise, a large amount of leakage (~25%) will be resulted in the region of closed leaf ends.

II.5 Quality assurance

Quality assurance is of practical importance. MSRT is a modality in between a conventional conformal radiation therapy and IMRT. The patient specific pre-treatment QA of MSRT consisted of two integral parts: MU and fluence map checks. We used an in-house MU calculation program to check independently the MU settings [36]. The MU setting of each segment could also be easily checked using a manual calculation procedure. But this does not check the functionality of the software module that concatenates the individual MLC segments together for step-and-shoot delivery. After a MLC leaf sequence file was obtained, we used the

file as input and re-computed the fluence map using a software described in an earlier publication [22]. This independent calculation ensured that the step-and-shoot MLC files were executable and generated the intended fluence map.

The on-treatment QA included isocenter setup verification and the verification of treatment portals relative to the patient's anatomy [37]. Different from an IMRT field, an MSRT field consists of, generally, two or three segments for most cases. Hence it is practically possible to obtain the portal image of each segment on a single film. In principle, the step-and-shoot treatment file created with Eq. (1) is usable for the portal verification. However, the fractional MU for some segments could be very small, leading to unclear segmental images. We thus created a step-and-shoot file specific for portal verification for each MSRT field. This file was essentially the same as the original MSRT treatment delivery file except that an equal fractional MU was assigned to each segment. Multiple segment portal film was then obtained by executing this file at the time of portal verification. The total MU was set to $2K$, where K is the number of segment in the MSRT field.

III. RESULTS

Ten patients with various breast sizes have been studied using MSRT. In Table 1 we summarize the treatment plans obtained using the standard OTF technique, MSRT-B, and MSRT-S. Minimum, maximum, and mean doses in the breast target volume and critical structures are given for each treatment plan. For these cases, the prescribed dose was specified to a point ~3 cm anterior to the isocenter and it was desired that the 100% isodose curve to cover the breast target volume. For comparison, we have scaled the prescription dose of all treatment plans to 5,040 cGy. The hot spots of the standard OTF plans in the breast volume ranged from 109% to 118% when normalized to the prescription dose. These plans represented typical clinical cases that fell into the category of intermediately complicated or complicated cases.

Figure 1 shows the standard setup of the opposed fields (top row) and the segmented fields in the medial (middle row) and lateral (bottom row) direction of an MSRT-B treatment for the first

patient listed in Table I. Figure 2 shows the same setup obtained with an MSRT-S treatment technique, in which the lateral field was generated using a 30° dynamic wedge. The isodose distributions in the central transverse section and in a plane perpendicular to the incident beams for the standard OTF, MSRT-B, and MSRT-S treatments are plotted in figure 5, and the corresponding cumulative dose-volume histograms (DVHs) are displayed in figure 6. As can be seen from figures 5 and 6, the dose inhomogeneity in the target volume was significantly reduced with both MSRT-B (figure 5b) and MSRT-S (figure 5c) techniques, as well as reduction in the high dose to the ipsilateral lung and heart when compared with the OTF plan. The target maximum dose was reduced from 117.7% to 112.2% for the MSRT-B plan, and to 111.9% for the MSRT-S plan. Furthermore, the target volume receiving high dose irradiation was significantly reduced. In order to include the mammary nodes into the radiation field, ~10% of the heart volume and the left lung were included in the tangential fields, resulting for these parts of the heart and lung receiving high radiation dose. The high doses to the heart was reduced by almost 6% using MSRT-B technique as a result of adding one additional segment in each incident beam (figures 1f and 1i), together with ~5% improvement in the maximum target dose in the target volume. The heart volume and ipsilateral lung volumes receiving high dose irradiation were also markedly reduced for MSRT-B treatment. As can be seen from figures 5 and 6, the MSRT-S also showed moderate improvement in the lung/heart doses in comparison with the standard OTF plan.

In Table II we list the MU setting of each segment of the MSRT-B and MSRT-S plans for the patient discussed above. In addition, the MU values from the independent calculation are also presented. We have also recomputed the fluence map based on the MLC leaf sequences and compared it with the intended fluence map for each beam. The independent fluence maps were found to be the same as the intended maps from the planning system.

IV. DISCUSSION

IV.1 Forward planning vs. inverse planning

There are two aspects in conformal radiation treatment planning: conformance of a certain isodose-curve to the target volume and the dose uniformity inside the target. For simple beam configurations (eg., OTF, AP/PA), the isodose-curve shaping is usually realized through beam shaping based on the initial MLC segments. In this case, a field-in-field technique obtained by adding a few segments to the original incident beams is often a viable choice to significantly improve the target dose uniformity. Breast irradiation using OTF belongs to this category of treatments. The isodose-curve shaping here is realized by the proper choice of the two initial tangential fields. The main purpose of introducing additional segments is to improve the dose homogeneity inside the target volume and/or to spare the sensitive structure(s) located along the path of the beams. Previous studies and our results clearly showed the dosimetric advantage of the MSRT for breast treatment.

MSRT is a convenient scheme of IMRT. For breast irradiation, MSRT is superior over IMRT for a few reasons. First, it is possible to obtain a MSRT treatment plan through a manual procedure using a conventional 3D treatment planning system. In practice, when the isodose curve shaping can be accomplished by MLC shaping of the initial segments, a manual forward planning is a competitive approach to inverse planning. In inverse planning, an objective function is constructed based on general physical/dosimetric or biological considerations and is defined as a global quantity [38]. In constructing an objective function, the voxel-dependent local information is "compressed" into a global quantity. Hence, one loses, to a certain extent, control over them. When a desired dose distribution is not attainable, a compromised solution is found using the algorithm's ranking. In reality, the compromised distribution may not necessarily be what the planner wants and several trial-and-error adjustment of prescription and relative importance factors of different anatomical structures may be needed to obtain a clinically sensible plan. For a simple beam configuration, the inverse planning approach may not necessarily be more efficient than a manual MSRT planning with the aperture weights and shapes adjusted in a trial-and-error fashion. After all, the final dose distribution has to be evaluated by the planner in either inverse or forward method. The manual planning is more direct in fine-tuning the doses in the target when isodose shaping is already achieved with the initial segments.

For a simple beam configuration, *a priori* knowledge can be incorporated into a manual forward planning process more efficiently as compared with computerized inverse planning. The feedback mechanism (or the trial-and-error) is more natural and straightforward. Based on the empirical experience, a planner can quickly find a suitable wedge filter to lead him/her to the vicinity of an optimal solution. The planner can then fine-tune the dose distribution with additional segmented field(s). The whole planning process was found not much more complex than the standard OTF planning process. Note that a wedged field in MSRT planning represents a "hidden" intensity modulated field. It would require at least ten segmented fields to produce a wedged field. Plus the added segments, the "effective" modulation in MSRT should be comparable to that of beamlet-based IMRT. The use of a wedge filter in planning provides a way for us to take a "shortcut" to find the optimal solution. Of course, the forward planning is efficient only when the number of system variables is not large and when the optimal solution is not "far" from the conventional OTF solution. The types of clinical cases that can potentially benefit from the proposed method include, but not limited to, tangential breast irradiation, AP/PA or oblique-field treatment of lung and Hodgkins disease. When the number of system variables increases and/or when the isodose-curve shaping cannot be achieved by simply changing the initial MLC leaf positions, the computer based inverse planning becomes more efficient. That is, the inverse planning technique becomes necessary for cases in which both isodose-curve shaping and dose uniformity need to be accomplished through intensity modulation.

IV.2 Field width problem

Inverse planning system obtains the solution by optimizing an objective function. The hardware limitations are usually not considered in the plan optimization process. A major limitation is the maximum spread of the MLC leaves, which restricts the maximum achievable field width without cartridge movement. Currently, the maximum field spread is 14.5cm for Varian accelerators. Other vendors have similar constraints. With beamlet-based IMRT, the maximum usable field width without abutting two or more photon fields is often smaller than the maximum field width achievable using conventional treatments.

For large-sized breast patient, we found that, when an inverse planning system was used for breast planning, a tangential treatment field was sometimes split into two intensity-modulated sub-fields for delivery due to the MLC physical limitations. An implicit feature of MSRT is that the MLC and jaw setting constraints have been taken into account during the manual treatment planning process. For a given jaw setting, the planning system would not allow for any MLC configuration that violates the machine constraints to happen at any stage of the planning process. It thus ensured that all the MLC segments were deliverable with a single step-and-shoot delivery upon completion of the MSRT plan.

IV.3 Miscellaneous

We emphasize that the MSRT planning does not require explicit delineation of the target volume and sensitive structures. This is another major advantage of MSRT over the current IMRT inverse planning approach, in which one must outline the breast target slice-by-slice in order for the automated inverse planning algorithm to perform dose optimization. Clinically, there exists a class of radiation treatment where the target volume is often defined on radiographic films or empirically without explicit delineation for the target. MSRT provides a natural solution to improve the dose distribution of this type of treatment.

IMRT represents a major deviation from conventional radiation therapy. Currently, IMRT with inverse planning is still in its early stage of clinical implementation and much educational training in planning, QA and the overall process are needed to bring the new modality into routine clinical practice. MSRT, on the other hand, combines the useful features of conventional radiation therapy and intensity-modulation and bridges the "gap" between what seemingly to be two different processes. It affords a valuable educational mechanism to familiarize the staff with IMRT and makes it possible to evolve gradually instead of going through a paradigm change in planning, delivery, and QA. MSRT provides thus a timely solution to improve not only breast irradiation but also the clinical implementation of IMRT. At the implementation level, each segment in MSRT is a conventional field and the dose calculation can be done using standard methods developed over the years in 3D conformal radiation therapy. In addition, there is no

need for a leaf sequencing algorithm since the MLC sequences are known upon the completion of the MSRT plan.

V. CONCLUSION

Despite of the well-appreciated fact that intensity-modulation could lead to significantly improved dose distributions in breast irradiation, its clinical implementation has been hindered by the deficiencies in the current inverse planning system and by the lack of a comprehensive treatment procedure. This is evidenced by the fact that very few institutions are using IMRT routinely for breast cancer treatment. A clinical challenge in IMRT breast treatment is how to modulate breast irradiation without increasing the treatment complexity. In this work we have described MSRT treatment of breast cancer in details and demonstrated its utility using several examples. Two different delivery schemes (MSRT-B and MSRT-S) have been discussed to meet the requirements of different clinical environments. We have also attempted to illustrate the pros and cons for the forward and inverse planning techniques. We pointed out that when isodose shaping can be realized using MLC beam shaping devices, the addition of a few extra segments can often improve the dose distribution significantly. In this case, the manual forward planning technique is a competitive approach in comparison with computerized inverse planning. MSRT is particularly efficient in incorporating prior and posterior knowledge and physical constraints into the treatment planning process. In addition, it allows us to take advantage of intensity-modulation without changing the conventional procedure of patient setup and tumor volume definition and even without relying on an inverse planning system. It is thus a more natural way to evolve from conventional radiation therapy to the more sophisticated IMRT treatment. MSRT is likely to be beneficial for any radiation treatment where a simple beam configuration is used and where it is difficult to achieve a homogeneous dose distribution within the target volume.

ACKNOWLEDGEMENT

We thank J. Kung and M. Murphy for useful discussion on how to incorporating the MLC leaf transmission into a step-and-shoot delivery. This work was supported in part by Research Grants from the Department of Defense (BC996645) and the American Cancer Society.

Table 1

Doses for ten breast cases. Five left breasts (#1-5) and five right breasts (#6-10) were studied. Results of three different treatment techniques, including standard tangential-field treatment, MSRT-B, and MSRT-S, are listed here. The breast size is defined by the dimension of the medial field (the first number is the inferior-superior dimension and the 2nd one measures the distance in the posterior-anterior direction), and the distance between the entrance points of the medial and the lateral fields.

Patient #	Breast size (cm ³)	Standard plan					MSRT-B					MSRT-S				
		D ^T _{max}	D ^T _{min}	D ^T _{ave}	D ^L _{max}	D ^H _{max}	D ^T _{max}	D ^T _{min}	D ^T _{ave}	D ^L _{max}	D ^H _{max}	D ^T _{max}	D ^T _{min}	D ^T _{ave}	D ^L _{max}	D ^H _{max}
1	13.0x20.6x26.7	5932	3235	5212	5494	5312	5653	3247	5240	5342	4989	5639	3240	5177	5464	5296
2	9.5x22.0.x19.1	5692	3497	5155	5314	4501	5536	3465	5111	5232	4140	5521	3344	5147	5220	4492
3	14.0x19.0x24.1	5861	3593	5236	5363	4658	5630	3579	5117	5122	4452	5500	3479	5074	4985	4015
4	8.0x16.5x17.7	5513	3738	5028	4867	4408	5369	3783	5047	4847	4427	5462	3742	5162	5109	4676
5	10.0x19.2x16.8	5686	4497	4886	5467	4908	5421	4639	4792	5203	4824	5385	3452	4948	5235	4828
6	9.0x20.0x21.1	5703	3940	5230	5101	*	5532	3939	5195	5015	*	5542	3948	5214	5081	*
7	8.0x18.2x17.0	5590	4066	5111	5172	*	5408	4053	5082	5099	*	5402	3809	5105	5057	*
8	7.0x14.0x17.9	5630	4175	5113	5542	*	5433	4125	5043	5345	*	5502	4205	5148	5387	*
9	8.5x19.0x19.0	5838	4027	5185	5257	*	5471	4005	5120	5207	*	5545	4018	5148	5236	*
10	9.0x17.5x20.2	5799	3823	5217	5424	*	5535	3808	5148	5268	*	5522	4044	5155	5258	*

Table 2 Parameters of MSRT-B and MSRT-S treatment of a left breast case. For MSRT-B, three segments were used in each incident beam direction. The MU setting of each segment was provided by the FOCUS treatment planning system. The fractional MU, f_k of the k -th segment was obtained using $f_k = MU_k / \sum_k MU_k$.

Tx technique	MSRT-B						MSRT-S			
Beam direction	Medial field			Lateral field			Medial field			Lateral field
Wedge filter	None			30° physical wedge			None			30° enhanced dynamic wedge
Segment	1	2	3	1	2	3	1	2	3	1
Segment MU	96	11	7	183	10	9	76	31	6	143
Independent cal.	97	11	7	178	10	9	73	32	6	147
f_k	0.8431	0.0980	0.0588	0.9056	0.0500	0.0444	0.6733	0.2772	0.0495	1.0000

Figure Caption

Figure 1. Standard tangential field arrangement for treatment of a left breast cancer patient (top row). The middle and bottom rows are the MLC shapes of the three segments of the medial and lateral MSRT fields, respectively. A physical wedge of 30° was used in the lateral field.

Figure 2. MLC shapes of the medial field (a-c) of a MSRT-S plan. The lateral field (d) in the MSRT-S treatment is a 30° enhanced dynamic wedge field.

Figure 3. Instances in a step-and-shoot delivery scheme for the medial and lateral MSRT fields shown in figure 1. Here $a f_k$ represents the accumulated fractional MU at a given instance and varies from zero to unity. Subtraction of the two consecutive segments gives the fractional MU delivered when the system goes from one instance to the subsequent one. For convenience, the fractional MU, f , of each segment are specified for each segment (a "step" instance plus a "shoot" instance makes a segment).

Figure 4. When one or more pairs of leaves inside the rectangular field extended by the jaws needs to be closed, the leaf ends should be moved to a position under the lower jaw protection, as shown in Fig. 2c. This figure shows an unacceptable leaf configuration.

Figure 5. Comparison of the isodose distributions of the treatment plans of the left-sided breast case using the tangential field technique (a), MSRT-B (b), and MSRT-S (c). Target volume includes the whole breast and the internal mammary nodes. Isodose levels are shown at 110%, 100%, 90%, 70%, 50%, 30%, and 10%.

Figure 6. Dose-volume histograms for the targets and normal structures for the treatment plans of the left-sided breast cancer patient shown in Fig. 5. The build-up region of 0.5cm is excluded from the breast tissue. Dash-dotted lines: OTF plan. Dashed lines: MSRT-B plan. Solid lines: MSRT-S plan.

References

1. Fisher, B., et al., *Eight-year results of a randomized clinical trial comparing total mastectomy and lumpectomy with or without irradiation in the treatment of breast cancer*, New England Journal of Medicine, 1989. **320**(13): p. 822-8.
2. Harris, J.R., et al., *Breast Diseases*, ed. 2nd. 1991, Philadelphia, PA: J.B. Lippincott Co.
3. Rutqvist, L.E., D. Pettersson, and H. Johansson, *Adjuvant radiation therapy versus surgery alone in operable breast cancer: long-term follow-up of a randomized clinical trial*. Radiotherapy & Oncology, 1993. **26**(2): p. 104-10.
4. Dobbs, H.J., *Radiation therapy for breast cancer at the millennium*. Radiotherapy & Oncology, 2000. **54**: p. 191-200.
5. Karlsson, M. and B. Zackrisson, *Matching of electron and photon beams with a multi-leaf collimator*. Radiotherapy & Oncology, 1993. **29**(3): p. 317-26.
6. Zackrisson, B., M. Arevarn, and M. Karlsson, *Optimized MLC-beam arrangements for tangential breast irradiation*. Radiotherapy & Oncology, 2000. **54**(3): p. 209-12.
7. Jansson, T., et al., *Radiotherapy of breast cancer after breast-conserving surgery: an improved technique using mixed electron-photon beams with a multileaf collimator*. Radiotherapy & Oncology, 1998. **46**(1): p. 83-9.
8. Li, J.G., L. Xing, et al., *Matching photon and electron fields with dynamic intensity modulation*. Medical Physics, 1999. **26**(11): p. 2379-84.
9. Li, J.G., et al., *Breast-conserving radiation therapy using combined electron and IMRT technique*. Radiotherapy & Oncology, 2000. **56**: p. 65-71.
10. Smitt, M.C., et al., *Breast-conserving radiation therapy: potential of inverse planning with intensity modulation*. Radiology, 1997. **203**(3): p. 871-6.
11. Williams, S.S., et al., *Intensity modulated treatment of breast cancer with inclusion of supraclavicular and internal mammary lymph nodes*. International Journal Radiation Oncology, Biology, Physics, 1998. **42**(1): p. 370.
12. Hyodynmaa, S., A. Gustafsson, and A. Brahme, *Optimization of conformal electron beam therapy using energy- and fluence-modulated beams*. Medical Physics, 1996. **23**(5): p. 659-66.

13. Hong, L., *et al.*, *Intensity-modulated tangential beam irradiation of the intact breast*. International Journal of Radiation Oncology, Biology, Physics, 1999. **44**(5): p. 1155-64.
14. McCormick, B., *et al.*, *Breast IMRT: The potential for treatment improvement with intensity modulation in left-breast disease*. International Journal of Radiation Oncology, Biology, Physics, 2000. **48**(3): p. 298.
15. Chang, S.X., *et al.*, *A comparison of different intensity modulation treatment techniques for tangential breast irradiation*. International Journal of Radiation Oncology, Biology, Physics, 1999. **45**(5): p. 1305-14.
16. Donovan, E.M., *et al.*, *Evaluation of compensation in breast radiotherapy: a planning study using multiple static fields*. International Journal of Radiation Oncology, Biology, Physics, 2000. **46**(3): p. 671-9.
17. Kestin, L.L., *et al.*, *Intensity-modulation to improve dose uniformity with tangential breast radiotherapy: initial clinical experience*. International Journal of Radiation Oncology, Biology, Physics, 2000. **48**: p. 1559-1568.
18. Lo, Y.C., *et al.*, *Intensity modulation for breast treatment using static multi-leaf collimators*. International Journal of Radiation Oncology, Biology, Physics, 2000. **46**(1): p. 187-94.
19. van Assen, B., *et al.*, *An improved breast irradiation technique using three-dimensional geometric information and intensity modulation*. Radiotherapy & Oncology, 2001. **58**: p. 341-347.
20. Burman, C., *et al.*, *Planning, delivery, and quality assurance of intensity-modulated radiotherapy using dynamic multileaf collimator: a strategy for large-scale implementation for the treatment of carcinoma of the prostate*. International Journal of Radiation Oncology, Biology, Physics, 1997. **39**(4): p. 863-73.
21. Low, D.A., Z. Li, and E.E. Klein, *Verification of milled two-dimensional photon compensating filters using an electronic portal imaging device*. Medical Physics, 1996. **23**(6): p. 929-38.
22. Xing, L. and J.G. Li, *Computer verification of fluence maps in intensity modulated radiation therapy*. Medical Physics, 2000. **27**: p. 2084-92.
23. Xing, L., *et al.*, *Dosimetric verification of a commercial inverse treatment planning system*. Physics in Medicine & Biology, 1999. **44**(2): p. 463-78.

24. Wang, X., et al., *Dosimetric verification of intensity-modulated fields*. Medical Physics, 1996. **23**(3): p. 317-27.
25. Low, D.A., et al., *A technique for the quantitative evaluation of dose distributions*. Medical Physics, 1998. **25**(5): p. 656-61.
26. Tsai, J.S., et al., *Dosimetric verification of the dynamic intensity-modulated radiation therapy of 92 patients*. International Journal of Radiation Oncology, Biology, Physics, 1998. **40**(5): p. 1213-30.
27. Fraass, B.A., et al., *Optimization and clinical use of multisegment intensity-modulated radiation therapy for high-dose conformal therapy*. Seminars in Radiation Oncology, 1999. **9**(1): p. 60-77.
28. Xiao, Y., et al., *An optimized forward-planning technique for intensity modulated radiation therapy*. Medical Physics, 2000. **27**(9): p. 2093-9.
29. Klein, E.E., et al., *Differential dosing of prostate and seminal vesicles using dynamic multileaf collimation*. International Journal of Radiation Oncology, Biology, Physics, 2000. **48**(3): p. 1447-1456.
30. Bortfeld, T., et al., *Realization and verification of three-dimensional conformal radiotherapy with modulated fields*. International Journal of Radiation Oncology, Biology, Physics, 1994. **30**(4): p. 899-908.
31. Svensson, R., P. Kallman, and A. Brahme, *An analytical solution for the dynamic control of multileaf collimators*. Physics in Medicine & Biology, 1994. **39**(1): p. 37-61.
32. Ma, L., et al., *An optimized leaf-setting algorithm for beam intensity modulation using dynamic multileaf collimators*. Physics in Medicine & Biology, 1998. **43**(6): p. 1629-43.
33. Boyer, A., L. Xing, and P. Xia, *Beam shaping and intensity modulation in modern technology of radiation oncology*. Modern Technology of Radiation Oncology, ed. J. Van Dyk . 1999, Madison, WI: Medical physics publishing.
34. Dirkx, M.L., B.J. Heijmen, and J.P. van Santvoort, *Leaf trajectory calculation for dynamic multileaf collimation to realize optimized fluence profiles*. Physics in Medicine & Biology, 1998. **43**(5): p. 1171-84.
35. Kung, J., M. Murphy, and L. Xing, *An algebraic method to incorporate collimator leakage into step-and-shoot leaf sequences for intensity-modulated radiation therapy*. Physics in Medicine and Biology, 2001: submitted.

36. Xing, L., et al., *Monitor unit calculation for an intensity modulated photon field by a simple scatter-summation algorithm*. Physics in Medicine & Biology, 2000. **45**(3): p. N1-7.
37. Chen, Y., et al. *A multi-purpose quality assurance tool for MLC-based IMRT*. in *ICCR*. 2000. Heidelberg, Germany: Springer-Verlag.
38. Xing, L., et al., *Estimation theory and model parameter selection for therapeutic treatment plan optimization*. Medical Physics, 1999. **26**(11): p. 2348-58.

Fig. 1

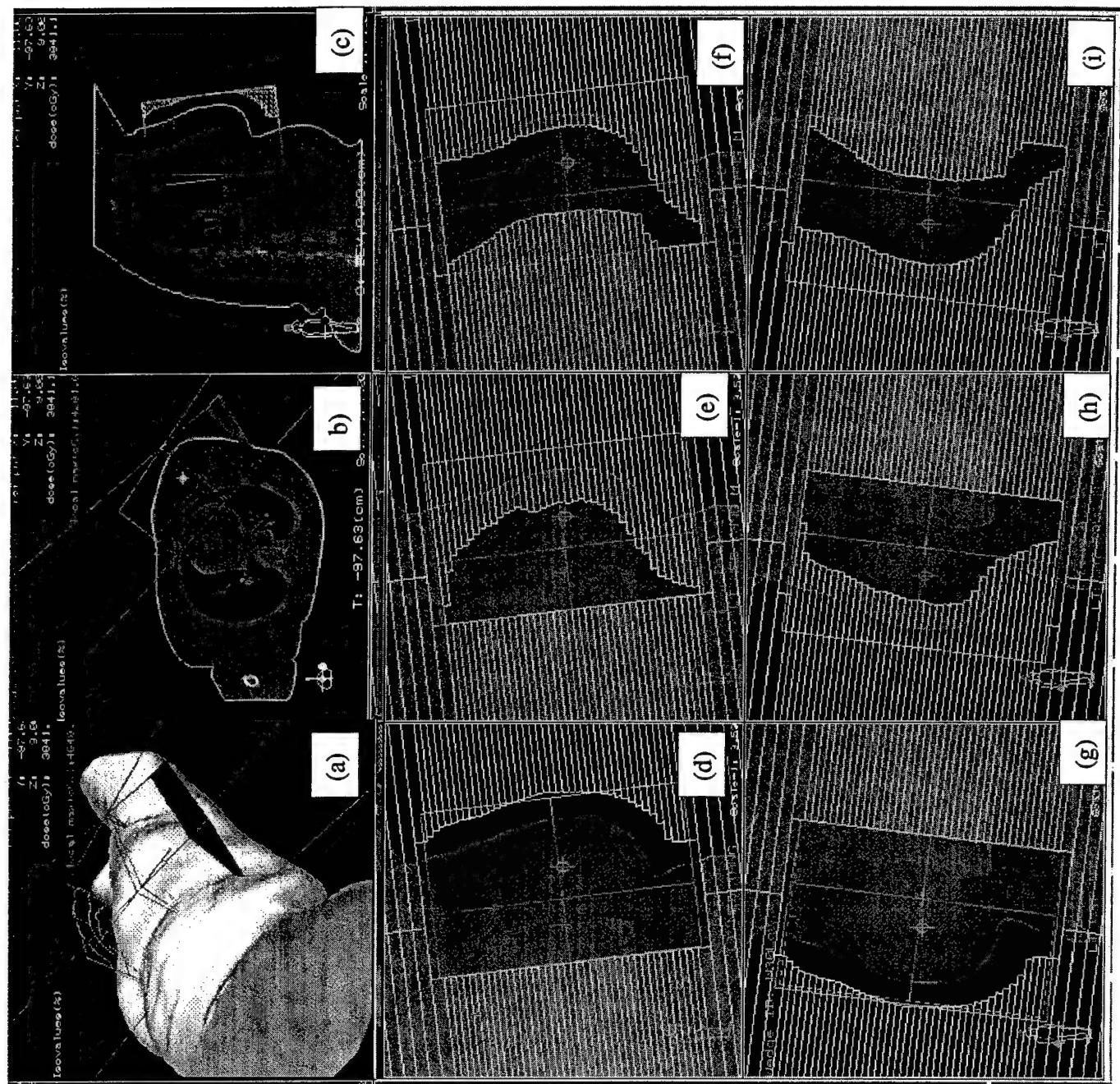
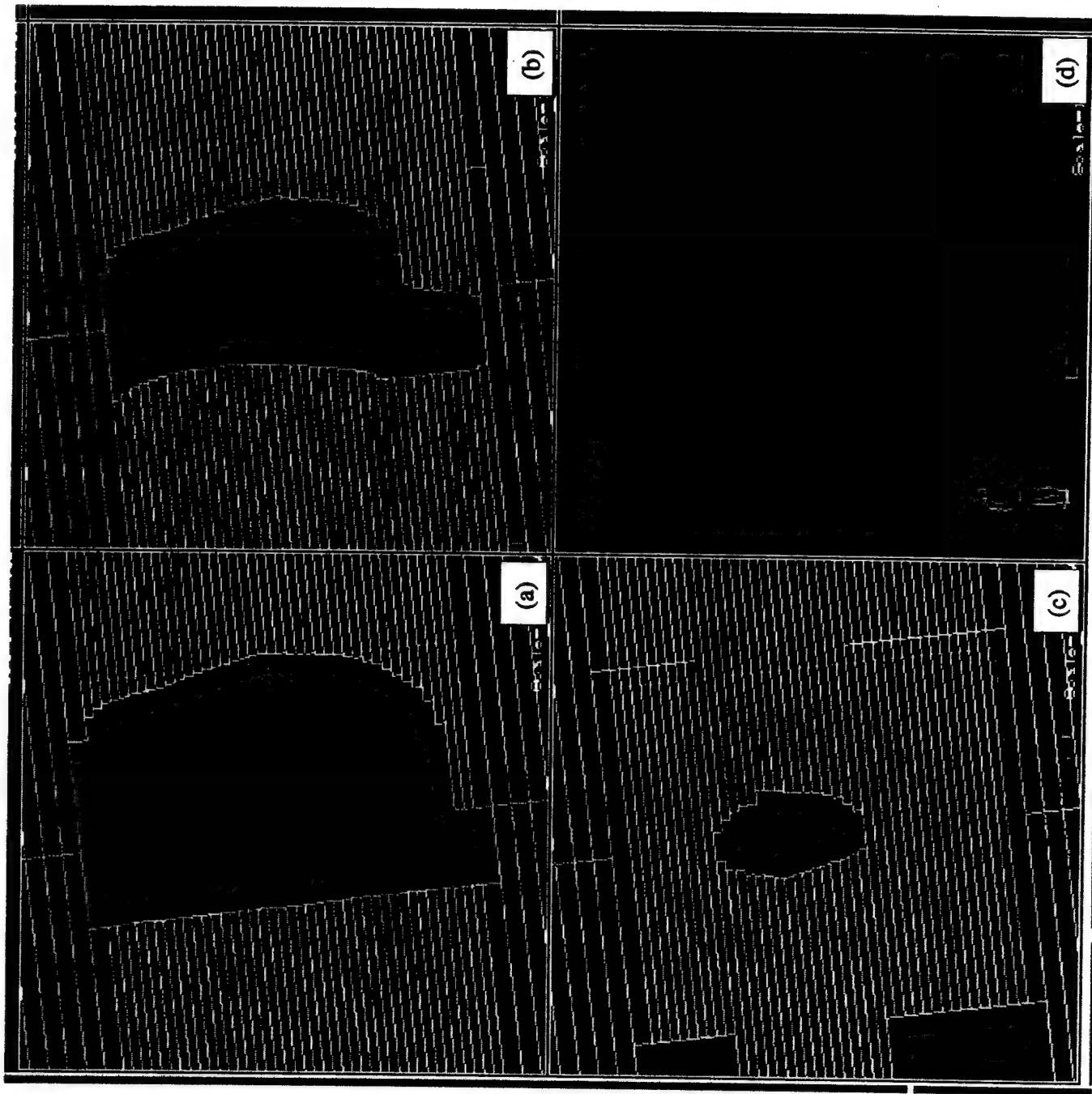


Fig. 2



Step-and-shoot Delivery

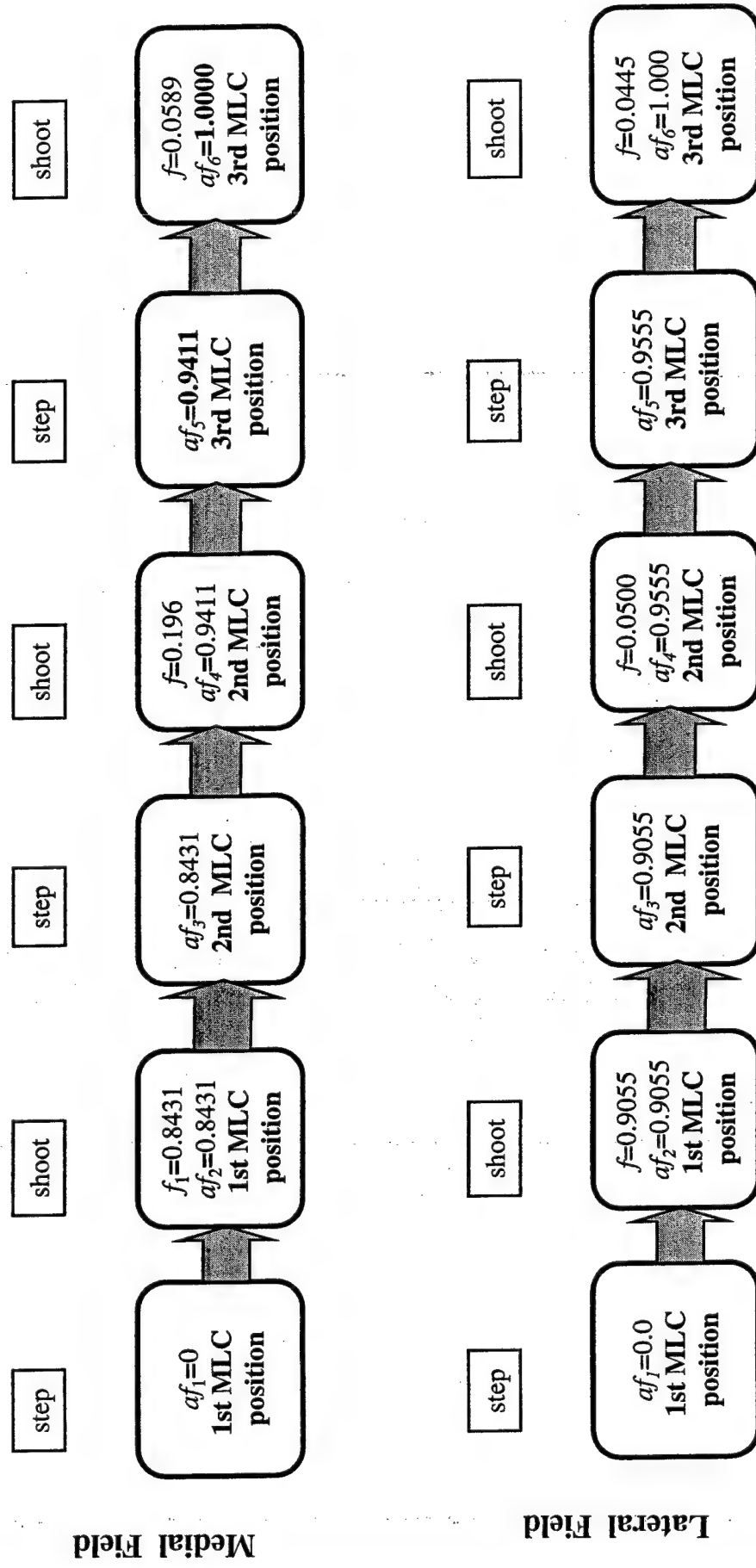


Fig. 3

Fig. 4

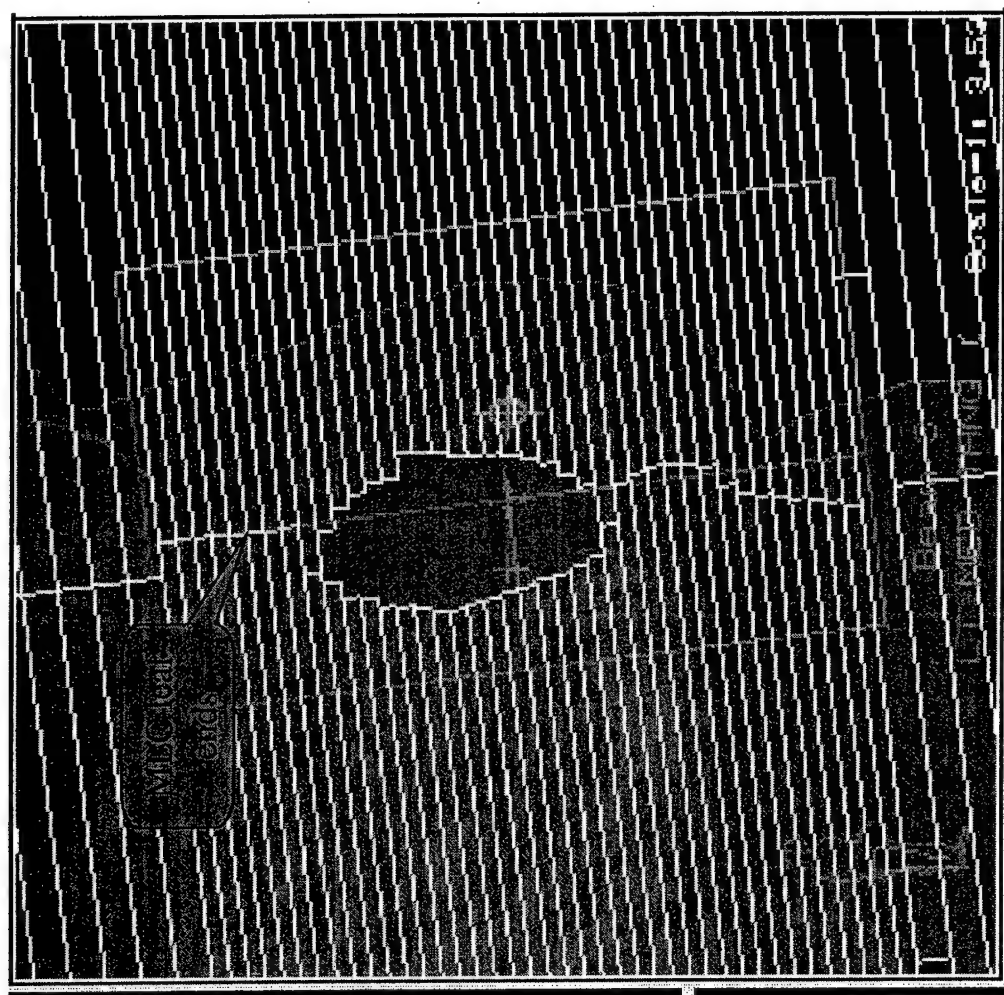
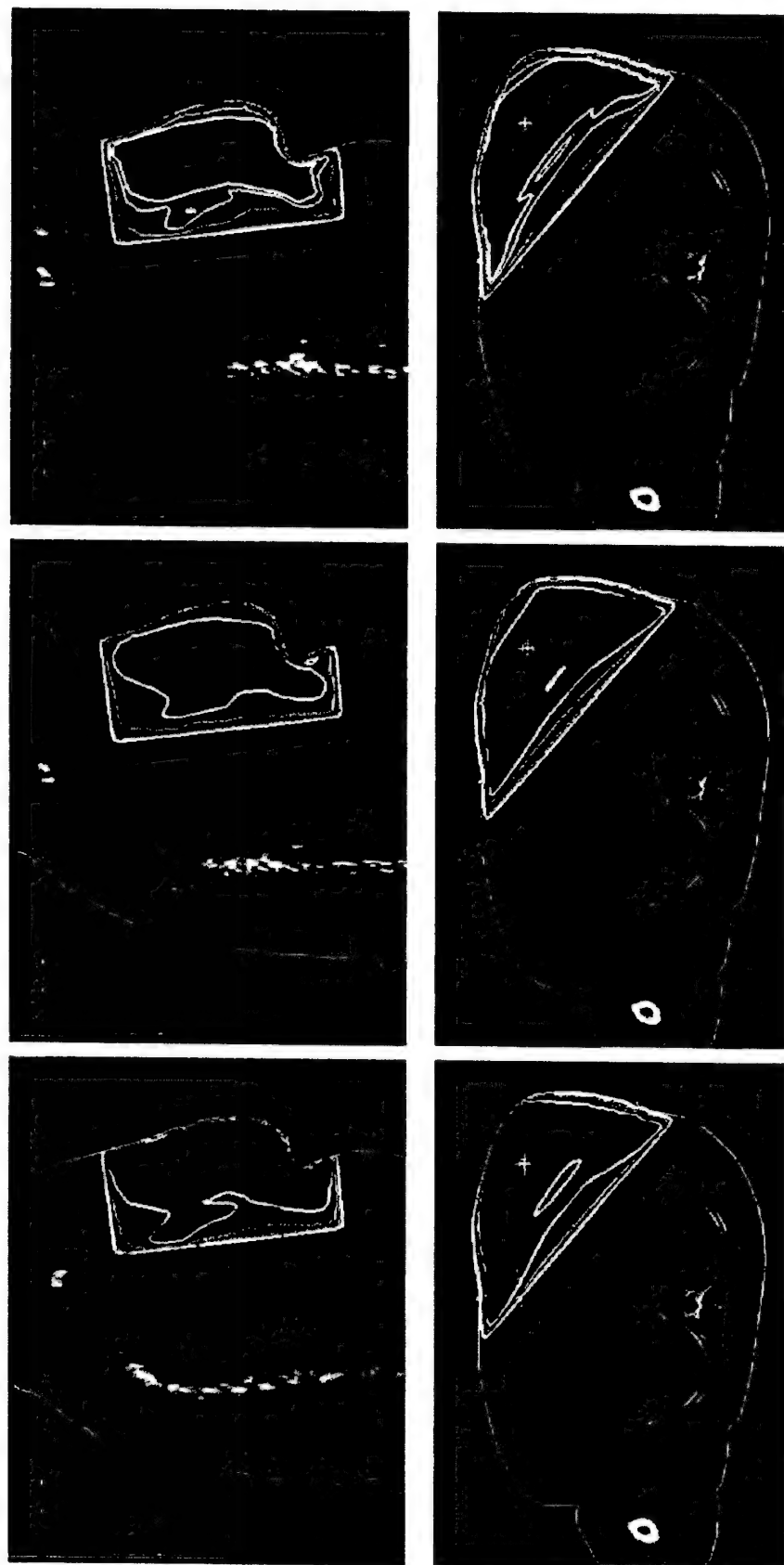


Fig. 5

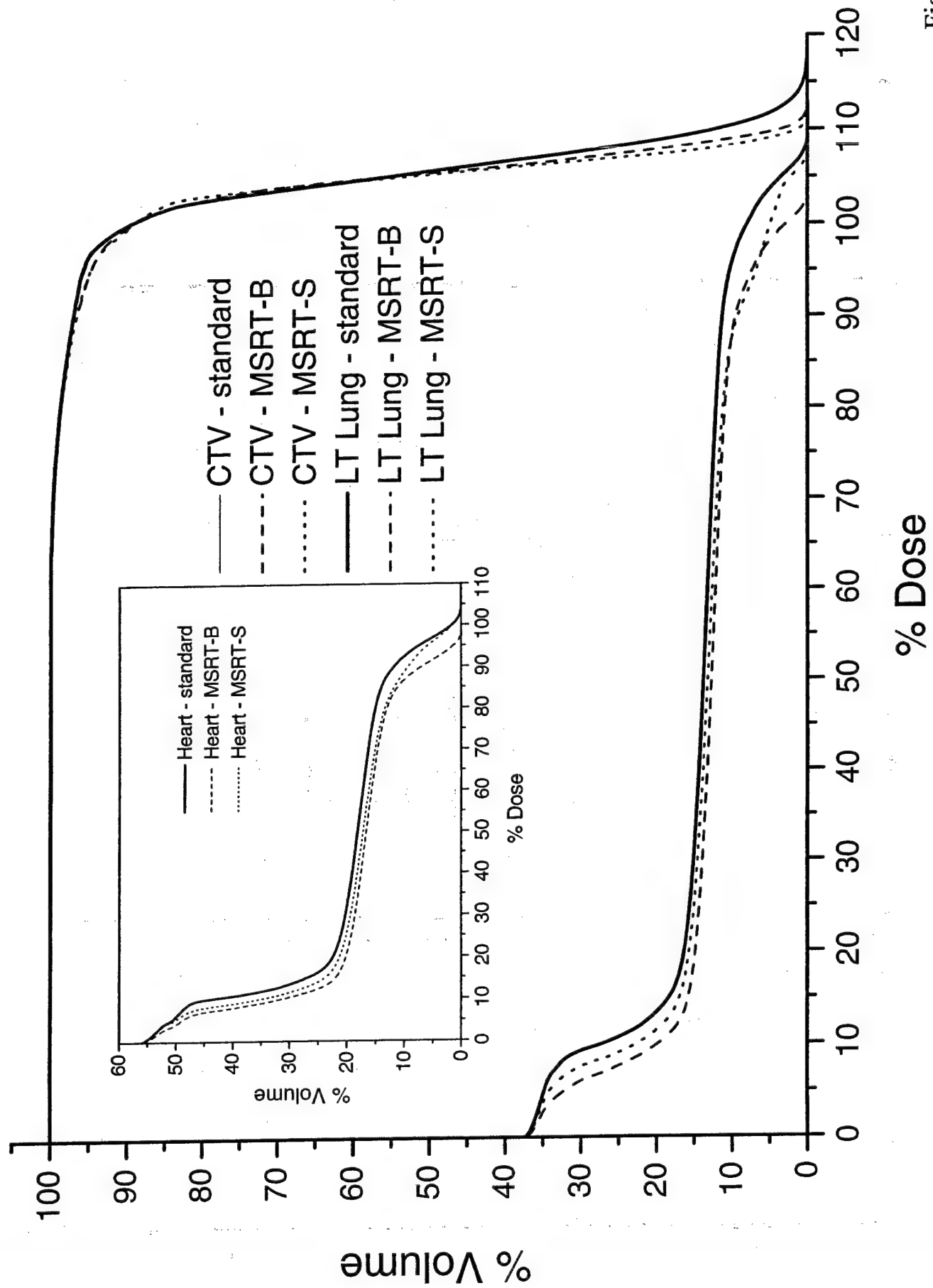


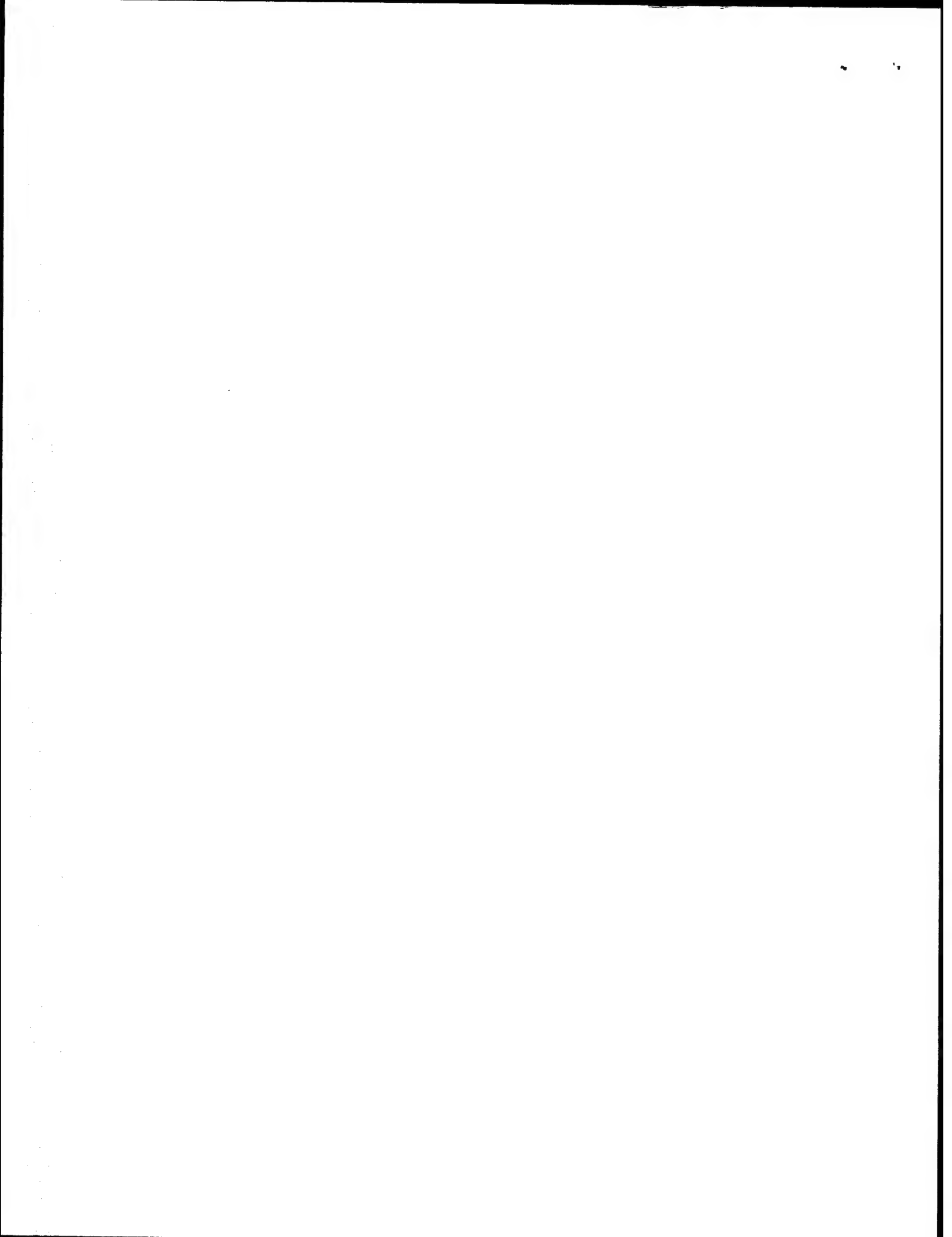
(c)

(b)

(a)

Figure 6





U.S. PATENT APPLICATION

BY

5

Cristian Cotrutz and Lei Xing

FOR

Method for determining a dose distribution in radiation therapy

CROSS-REFERENCE TO RELATED APPLICATIONS

This application is cross-referenced to and claims priority from U.S Provisional application

15 60/363,913 filed 3/12/2002, which is hereby incorporated by reference.

**STATEMENT REGARDING FEDERALLY SPONSORED
RESEARCH OR DEVELOPMENT**

This invention was supported in part by grant number Army DAMD 17-01-1-0635 from the
20 U.S. Department of Defense. The U.S. Government has certain rights in the invention.

Monitor Unit Calculation And Plan Validation For Intensity-Modulated Radiation Therapy

**Lei Xing, Ph.D.¹, Yong Yang, Ph.D.¹, Jonathan G. Li, Ph.D.², Yan Chen, Ph.D.³,
Gary Luxton, Ph.D.¹, Zhe Chen, Ph.D.⁴, Y. Song¹, and Arthur L. Boyer, Ph.D.¹**

¹Department of Radiation Oncology, Stanford University School of Medicine,
Stanford, California

²Department of Radiation Oncology, University of Florida,
Gainesville, Florida

³Department of Radiation Oncology, Thomas Jefferson University Hospital,
Philadelphia, Pennsylvania

⁴Department of Radiation Oncology, Yale University School of Medicine,
New Haven, Connecticut

Introduction	515
Review Of IMRT Dose Validation Algorithms.....	516
Dose Calculation For IMRT	516
A General Formalism For MU Or Point Dose Check	517
Point Dose Calculation For Multifield IMRT	520
Role Of Scatter From MLC Segments	522
Inverted Field And Point Dose Calculation In A Low-Dose Region	522
Is A Point Dose Enough For Validating	
An IMRT Treatment Plan?	526
Necessity Of Multiple Points Validation For IMRT	526
Independent Fluence Map Calculation And Its Utility	
For IMRT Plan Validation	526
Conclusion	528
Acknowledgments	528
References	528

Introduction

Intensity-modulated radiation therapy (IMRT) is being developed into an important radiation therapy modality (Ling et al. 1996; Wang et al. 1996; Tsai et al. 1998; Xing et al. 2000b; Webb 2001; IMRTWG 2001; Cheng and Das 2002; Xia et al. 2000) and methods for the plan optimization and delivery have evolved to a high level of sophistication (Xing et al. 1999; Lian, Cotrutz, and Xing 2002; Wu et al. 2002; Pugachev and Xing 2002; Shepard et al. 1995; Hou et al. 2003). However, the development of means for quality assurance (QA) has lagged behind. At present, the verification of IMRT treatment plans remains a labor-intensive and institution-dependent process. Considerable confusion exists regarding what dosimetric tests are needed to validate an IMRT plan and how to efficiently execute these tests in a routine

clinical environment. Generally, the methods of IMRT plan validation can be classified into two categories: experimental measurement and independent calculation. While the former method is, in principle, more reliable, the latter approach has a number of advantages and may be more suitable for routine application. Instead of using ionization chamber and/or radiographic films to actually perform the dosimetric measurements, it attempts to simulate the treatment on a computer and independently calculates the dosimetric quantities, such as the spatial doses or fluence maps. The philosophy here is similar to that used in plan validation in three-dimensional (3-D) conformal radiation therapy (3DCRT), where a manual or simple computer calculation is employed to double check the monitor units (MUs) of a treatment. In this chapter, we review different techniques used for computer-based IMRT plan validation and summarize our experience in implementing the technique.

Review Of IMRT Dose Validation Algorithms

Dose Calculation In IMRT

It is useful to first summarize the dose calculation algorithms that are widely used in IMRT treatment planning systems. There are two major types of dose calculation algorithms: correction-based and model-based (IMRTCWG 2001). Correction-based models compute the dose distributions in patients by correcting the dose distributions of similar geometries in a homogeneous water phantom for the beam modifiers, patient contours, tissue heterogeneities, and volume scattering effect. The type of heterogeneity corrections includes the 1-D method, in which only densities along the primary photon path are considered, and the equivalent tissue-air ratio method. The volume scattering effects (scatter dose as a function of field size and shape) are often computed by using the equivalent square field method and/or Clarkson integration. Some pencil beam methods, like the finite-size pencil beam algorithm (Bourland and Chaney 1992), are also classified as the correction-based models.

Model-based models can directly calculate the dose distributions in a patient for a given beam energy, geometry, beam modifiers, patient contour, and tissue heterogeneities. The kernel-based convolution/superposition (Mackie, Scrimger, and Battista 1985; Mackie et al. 1988; Boyer and Mok 1985; Boyer et al. 1989) and Monte Carlo method (Ma et al. 2000; Jeraj and Keall 1999; Solberg et al. 1998) are representatives of the kind. In the convolution/superposition techniques, the dose deposition is viewed as a superposition of appropriately weighted kernels to point irradiations and the superposition can be efficiently evaluated by means of convolution if the kernels are considered as spatially invariant. The kernels, representing the energy transport and dose deposition of secondary particles stemming from a point irradiation, can be calculated by Monte Carlo simulation. Monte Carlo method computes the dose distributions by simulating particle transport in a patient. Model-based models are capable of accounting for the electronic disequilibrium effects and therefore are more accurate in dealing with the tissue inhomogeneity and calculating the dose in the electron disequilibrium regions.

Despite the fact that kernel-based models are superior to the correction-based models in calculation accuracy, the correction-based models are still useful, especially as a means for independent check of the treatment planning calculations because of their simplicity and efficiency. Pencil beam algorithms, which are the hybrid of the two approaches, are also useful for IMRT dose optimization and for independent IMRT dosimetric check because of their flexibility to model lateral fluence variations and their computational efficiency.

A General Formalism For MU Or Point Dose Check

A few simplified algorithms have been proposed for the independent dose (or MU) calculation (Xing et al. 2000a; Kung and Chen 2000; Watanabe 2001; Chen, Xing, and Nath 2002). Here we briefly review a general algorithm developed by our group (Xing et al. 2000a; Yang et al. 2003). This method provides a clear physical picture and allows implementation of the MU calculation at a different level of sophistication to meet the specific requirements of different systems. For a single incident beam, the dose at a given point, (x, y, z) , can be expressed as a sum of the contributions from all beamlets (Xing et al. 2000a),

$$D(x, y, z) = MU \sum_m^M C_m D_m^0, \quad (1)$$

where MU is the total monitor unit of the field, D_m^0 is the dose per unit MU from the m th beamlet when it is open, C_m is called the dynamic modulation factor (DMF), which represents the fractional MU of the m th beamlet when the beam is assigned with a unit MU, and M is the total number of beamlets. The DMF, C_m , can be calculated by

$$C_m = \sum_k^K [S_{c,m,k} + \alpha S'_c (1 - \delta_{m,A_k})] f_k, \quad (2)$$

with

$$\delta_{m,A_k} = \begin{cases} 1 & \text{if } m \in A_k \\ 0 & \text{if } m \notin A_k \end{cases}, \quad (3)$$

where K is the number of segments of the field, f_k is the fractional MU of the k -th segment, A_k is the field boundary defined by the k -th segment, $S_{c,m,k}$ is the head scatter factor of the beamlet m in the k th segment, S'_c is the head scatter factor for the rectangular field defined by the jaws, and δ is the average transmission factor (Arnfield et al. 2000). Here we have ignored the tongue-and-groove and MLC leaf end effects. When the head scatter is negligible, equation (2) becomes (Xing et al. 2000a)

$$C_m = \sum_k^K [\delta_{m,A_k} + \alpha(1 - \delta_{m,A_k})] f_k \quad (4)$$

To accurately compute the dose, it is also required to know the beamlet kernel, D_m^0 . The formalism described above is general enough and allows using beamlet kernels derived from any method. We have implemented a Clarkson summation method, in which equation (1) is re-written as the sum of the contributions of the primary radiation and the scatter radiation:

$$D(x, y, z) = MU[C_{m_0} D_{p,m_0}^0(x, y, z) + \sum_{m \neq m_0}^M C_m D_{s,m}^0(x, y, z)], \quad (5)$$

where the first term is the primary dose and the second one is the scatter contribution. We treat the primary dose by a weighted average of the intensities in the surrounding 16 beamlets (a 2×2 cm 2 square). The $D_{p,m_0}^0(x, y, z)$ can be calculated using

$$D_{p,m_0}^0(x, y, z) = \left(\frac{100}{100 - z}\right)^2 C_f S_p(0) TMR(d_{eff}, 0) POAR(d_{eff}, x, y), \quad (6)$$

where C_f is the calibration factor of the linac, d_{eff} is the water equivalent depth of the calculation point, $S_p(0)$ and $TMR(d_{eff}, 0)$ are the phantom scatter factor and tissue-maximum ratio (TMR) for zero field size, respectively. $POAR(d_{eff}, x, y)$ is the primary off-axis ratio at the calculation point (Gibbons and Khan 1995). As was described earlier (Xing et al. 2000a), the scatter dose contribution is computed by summing over the contributions from all the scatter sources. We use 0.5×0.5 cm 2 sub-beamlets as the elementary calculation units. The $D_{s,m}^0(x, y, z)$ can be obtained by

$$D_{s,m}^0(x, y, z) = \left(\frac{100}{100 - z}\right)^2 C_f [S_p(r + \Delta r) TMR(d_{eff}, r + \Delta r) - S_p(r) TMR(d, r)] POAR(d_{eff}, m), \quad (7)$$

where r is the distance between the center of the m th sub-beamlet and the projection of the calculation point on the isocenter plane, $\Delta r = 0.5^2/2\pi r$, $POAR(d_{eff}, m)$ is the primary off-axis ratio at the center of the m th sub-beamlet in water equivalent depth d_{eff} .

Figure 1 shows the intensity map of a clinical IMRT treatment field (figure 1a) and the absolute dose profiles along the four lines marked in figure 1a were computed using the above algorithm in isocenter plane at 3.0 cm depth in the cubic water equivalent phantom. The results are shown in figures 1b, 1c, 1d, and 1e as solid dots. The film measurements and CORVUS® calculations were also performed in the phantom using a Varian Clinic 2300C/D with 80-leaf MLC and 15 MV photon beam. The results are shown in figure 1. While the overall agreement between our calculations, the CORVUS plans and the ion chamber measurements is excellent, there are regions (region A, B, C in figure 1) where the dosimetric discrepancies between the three are more than 5%.

In these regions, it seems that our program yielded closer doses to the measured values in comparison with that of the CORVUS calculation. Furthermore, as can be seen from figure 1, the penumbra regions are modeled adequately by our calculation.

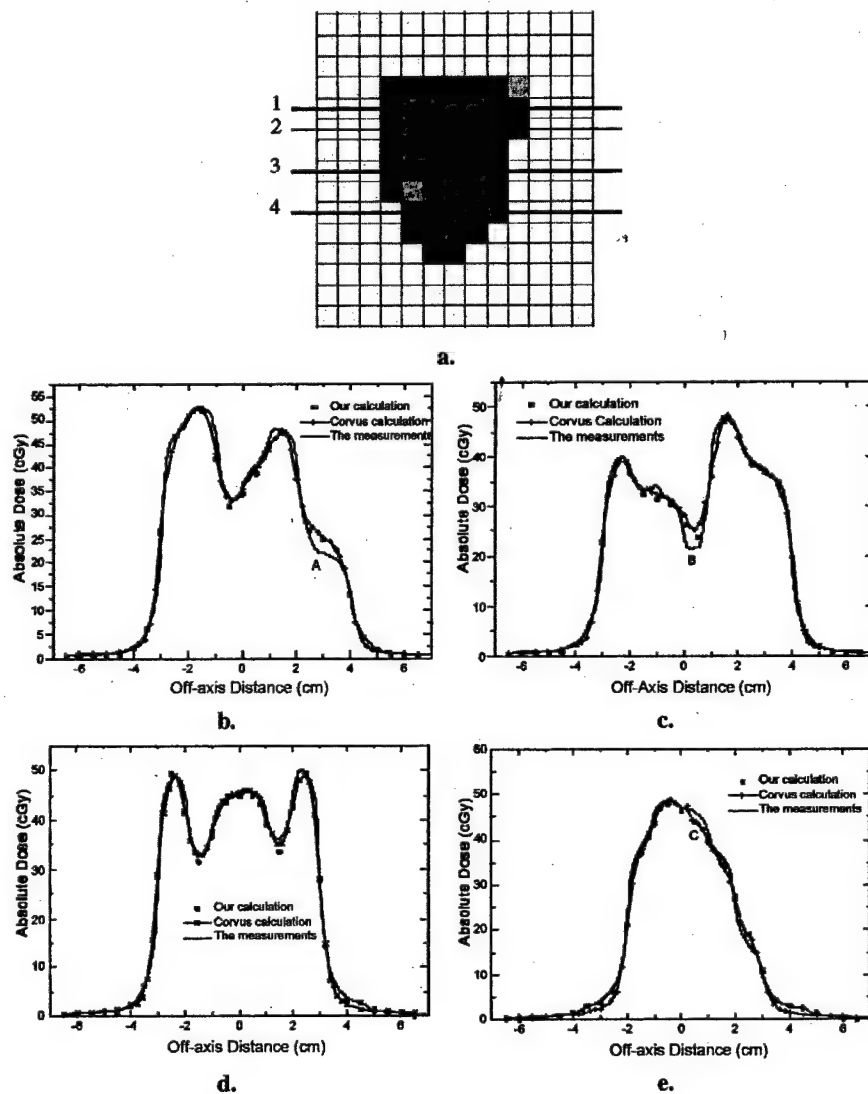


Figure 1. Comparison of our calculations with ion chamber measurements and CORVUS® plan for a clinical intensity-modulated field. The intensity map of the field and the four lines along which the doses were compared are shown in (a). The absolute dose profile for line-1, -2, -3, and -4 are shown in panels b, c, d, and e, respectively. [Reprinted from *International Journal of Radiation Oncology Biology Physics*, Y. Yang, J. G. Li, J. Palta, Y. Chen, G. Luxton, A. Boyer, and L. Xing, "Independent dosimetric calculation with inclusion of head scatter and MLC transmission for IMRT," Submitted for publication. © 2003, with permission from Elsevier.]

Point Dose Calculation For Multifield IMRT

A point of interest (POI) is conveniently specified using a patient-fixed coordinate system and a radiation beam is usually described in the machine coordinate. To calculate the dose at an arbitrary point in the patient for a multiple field IMRT treatment, a coordinate transform between the two systems is required. We assume that the coordinates of a verification point are (x, y, z) and (x', y', z') in the patient and machine coordinate systems, respectively, and that the origins of two systems are set at the isocenter. In an isocenter treatment, only rotation transformations are involved and the dose at a point can be calculated by simply summing the contributions from all beams, that is

$$D(x, y, z) = \sum_{j=1}^J D_j(x', y', z') = \sum_{j=1}^J M U_j \left(C'_{m_0, j} D_{p, m_0, j}^0(x', y', z') + \sum_{m \neq m_0}^M C'_{m, j} D_{s, m, j}^0(x', y', z') \right), \quad (8)$$

where index j has been added to label each individual incident beam, and J is the total number of beams.

Table 1. Absolute Doses Measured and Calculated in a Lucite™ Phantom for the Case 1

Number of Calc Point	Coordinates of Calc Points (cm)	Current Calc Dose (cGy)	CORVUS Calc Dose (cGy)	Ion Chamber Measurement (cGy)	Deviation with CORVUS	Deviation with Measurement (%)
1	(0,0,0)	218.5	217.0	216.7	0.7	0.8
2	(2,0,0)	212.2	215.0	216.7	-1.3	-2.1
3	(0,2,0)	211.4	209.0	210.9	0.9	0.2
4	(0,0,2)	210.6	211.0	207.2	-0.2	1.6
5	(0,0,6)	78.6	74.0	78.1	6.2	0.6
6	(-6,0,6)	78.5	80.0	79.2	-0.6	-0.9
7	(6,0,-5)	97.8	96.0	100.6	1.9	-2.8
8	(-6,2,-5)	102.5	103.0	104.3	-0.5	-1.7

[Reprinted from *International Journal of Radiation Oncology Biology Physics*, Y. Yang, J. G. Li, J. Palta, Y. Chen, G. Luxton, A. Boyer, and L. Xing, "Independent dosimetric calculation with inclusion of head scatter and MLC transmission for IMRT," Submitted for publication. © 2003, with permission from Elsevier.]

The dosimetric validation of the above algorithm for a six-field IMRT prostate treatment plans was performed on the cylindrical Lucite™ phantom. The gantry angles of the six beams are 0° , 55° , 145° , 180° , 215° , and 305° , respectively, and the corresponding intensity maps are shown in figure 2. We independently computed the doses at eight pre-selected spatial points inside the phantom. The coordinates of the points

of interest relative to the isocenter are listed in table 1, along with the results from the CORVUS calculation and the ion chamber measurements. Our calculations agree with the measurements to within 3.0% for all eight verification points. The agreement between our calculations and the CORVUS plans are also within 3.0% for all the points except point 5. At point 5, the deviation of the CORVUS dose from the measurement was found to be 5.6%, whereas our calculated dose for the point is only 0.6% different from the measured value. We attribute the superior performance of our system to the better modeling of head scatter contributions.

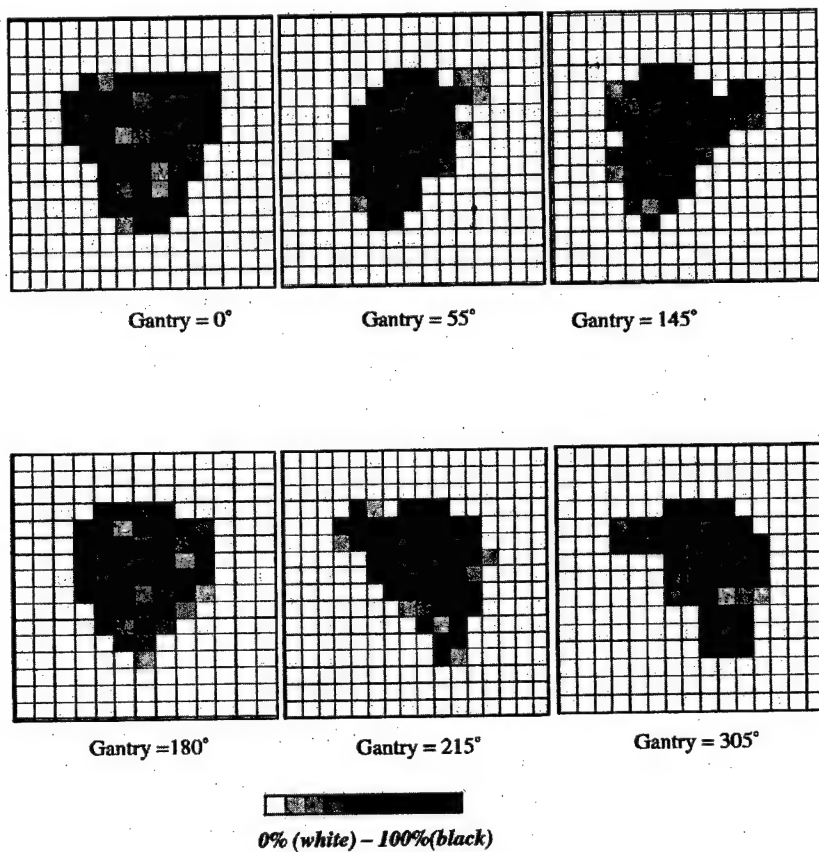


Figure 2. The intensity maps for a six-field IMRT prostate treatment. Intensity level of a beamlet is characterized by its gray level, ranging from 0 (white) to 100 (black). [Reprinted from *International Journal of Radiation Oncology Biology Physics*, Y. Yang, J. G. Li, J. Palta, Y. Chen, G. Luxton, A. Boyer, and L. Xing, "Independent dosimetric calculation with inclusion of head scatter and MLC transmission for IMRT," Submitted for publication.]

© 2003, with permission from Elsevier.]

Role Of Scatter From MLC Segments

To compute the spatial doses of an IMRT field, it is critical to model the MLC transmission and scatter accurately. The calculation of head scatter for irregularly shaped MLC segments is challenging and, up to this point, its effect has not been accounted for adequately in many commercial systems. Recently, Yang et al. (2002) have reported an effective three-source model for the calculation and it is claimed that less than 0.3% of accuracy can be achieved for the measured and calculated head scatter factors for a variety of testing fields. In this model, the photon radiation to the point of calculation is treated as if from three effective sources: one source for the primary photons from the target and two extra-focal photon sources for the scattered photons from the primary collimator and the flattening filter, respectively. The intensity distributions of the scatter sources and their positions and the off-axis difference of the scatter radiation are taken into account in the calculation model on a machine- and energy-specific basis. Source parameters are determined by fitting the head scatter factors to the data of a series of square fields and no backscatter measurements are needed. Head scatter factor for an arbitrarily shaped segment is calculated by integrating the radiation contributed from areas in the two scatter sources. Using this model, Yang and Xing (Yang et al. 2002) have recently investigated the influence of head scatter on IMRT delivery for a Varian 2100 C/D accelerator and showed that an error of 3% to 5% error can result if the head scatter from a MLC shaped segment is ignored. It is anticipated that the inclusion of head scatter will be even more crucial for Siemens and Elekta machines due to their specific MLC designs.

Inverted Field And Point Dose Calculation In A Low-Dose Region

Our experience with IMRT dose validation in high-dose regions indicated that dose agreement within 3%~5% is adequate and reflects the current standard of practice. Implementation of the criterion for all IMRT cases is complicated, however, by the fact that the beam intensity is modulated and frequently, the POI is located in the low-dose region of one or more treatment fields. The relative dosimetric error can be as high as 5% to 30% in a low-dose region when the data are normalized to the dose at the POI. In reality, a large relative error may rise from a true dosimetric error or simply from the "amplification" effect in the low-dose region. One method to better portray the dosimetric impact is to normalize to the maximum dose (see the chapter herein by Xia and Chuang, *Patient-Specific Quality Assurance in IMRT*). Another way is to be able to draw a more decisive conclusion based on the independent dose calculation; it is desirable to have a unified QA criterion for both high- and low-dose regions.

We introduce a useful concept of the inverted field for IMRT. For each intensity-modulated field (primal field), there exists a unique inverted field whose beamlet weights are defined as

$$W_i(n) = W_{\max} - W_p(n) , \quad (9)$$

where $W_i(n)$ and $W_p(n)$ are the weights of the n th beamlet in the inverted and primal fluence maps, respectively, and W_{\max} is the maximum beamlet weight of the primal beam. By convention, we set the maximum beamlet weight of the primal field to be 100. The inverted field plus the primal field constitutes a uniform open field defined by setting the weights of all beamlets under the collimator jaws to be 100. As a result of the inversion relation defined by equation (9), the low-dose region of the primal field corresponds to the high-dose region of its inverted field, and vice versa. This complementary relation bridges what appears to be two independent schemes and allows us to validate the MU setting of the primal field by using the dosimetric data of the inverted field. That is, instead of directly evaluating the primal field, we may proceed by assessing the dose of the inverted field when the POI is located in a low-dose region of the primal field. Because the POI is in the high-dose region of the inverted field, the commonly used QA criterion can be readily employed for QA decision-making. Without the criterion based on the inverted field, it would be difficult to judge whether a QA action should be taken if we were to rely only on a relative dose error of the primal field dose.

Three intensity maps, consisting of a wedged field and two well-shaped fields, are shown in figure 3 to illustrate the inverted field approach. The dose distributions of the three intensity-modulated beams in a circular Lucite phantom were computed using the CORVUS planning system. The gray scale intensity maps of the inverted fields are plotted in figures 3d through 3f. The total MUs of each beamlet from the two fields were set to 100 MU. In table 2 we list the isocenter dose for the three primal and inverted fields. In these three cases, the sum of the primal and inverted fields constituted a 10×10 cm square field. In table 2, we also list the results of ion chamber measurement. For comparison, we have also computed directly the dose distributions of the three inverted fields using the CORVUS system. The CORVUS isocenter doses for the three sets are listed in the table.

The wedged field represents an intuitive example and it is easy to conceive that, when the positive and negative wedges shown in figures 3a and 3d are combined, a uniform open field is the result. Indeed, as shown in table 2, the summation of the isocenter doses of the primal and inverted wedged fields is equal to that of the uniform 10×10 cm field to within 2.0% for both ion chamber measurements and theoretical calculations. The two well-shaped fields are similar except that the central four beamlets are zero for the field shown in figure 3c. The isocenter is located in a low-dose region in both cases. Once again, the sum of the primal and inverted field doses for the two cases was found to be equal to that of the open field dose to within 2.5% for both energies. For the third case shown in figure 3c, the isocenter dose is completely from scatter and transmission. The disagreement between the ion chamber measurements and the direct calculations was found to be large, ~5.1% for 6 MV photon beam and 13.2% for 15 MV photon beam when normalized to the measurement data. The relative discrepancy between the independent calculation and the CORVUS calculation was also found to be excessive (~18%) for the 15 MV photon beam. Similarly, for the 6 MV photon beam shown in figure 3b, the relative discrepancy between the

independent calculation and the CORVUS calculation was found to be ~11%. As we have mentioned earlier, in reality, a large relative error may rise from a true dosimetric error or simply because the point is in a low-dose region which "enhances" the relative error. The concept of the inverted field provides an effective method to properly evaluate the error. For these two particular cases, we found that the relative discrepancies were all within 4.0% when normalized to the inverted field dose. It is thus concluded that the CORVUS calculation for these fields meets the QA criterion

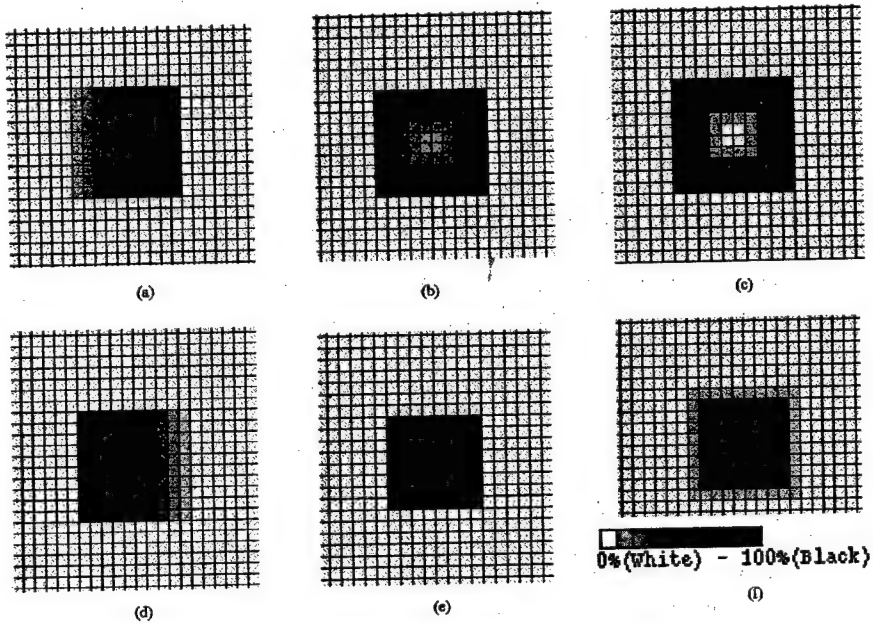


Figure 3. Fluence maps of a wedged field (a) and two well-shaped fields [(b) and (c)]. The intensity levels for the wedged field are 10, 20, 30, 40, 50, 60, 70, 80, 90, and 100 from right to left. The intensity levels for figure 1b are 0, 10, 30, 60, and 100 from inside to outside. The For figure 3c, the intensity levels are 10, 20, 30, 60, and 100 from inside to outside. The inverted fields for the primal fields are shown in 3d, 3e, and 3f.

Table 2. Measured and Calculated Doses at the Center of a Cylindrical Lucite™ Phantom for the Intensity-Modulated Beams Shown in Figure 3

The top of each row shows the 6 MV data and the bottom row shows the data for 15 MV photons. The data shown in the third column is obtained using the complementary relation of the primary and inverted fields. The dose of the 10×10 cm open field at the center of the phantom is 0.627 Gy for 6 MV photon beam and 0.781 Gy for 15 MV photon beam, which is consistent with an ion chamber measurement and a simple hand calculation

Field Name	Direct Calculation (Gy)	Calculation Using Inverted Field (Gy)	Ion Chamber Measurement (Gy)	CORVUS Calculation (Gy)
6 MV Photon				
Wedged field (fig. 3a)	0.315	0.311	0.314	0.318
Inverted wedged field (fig. 3d)	0.316	0.312	0.318	0.321
Well-shaped field (fig. 3b)	0.100	0.091	0.106	0.111
Inverted well-shaped field (fig. 1e)	0.536	0.527	0.522	0.528
Well-shaped field (fig. 3c)	0.074	0.066	0.078	0.071
Inverted well-shaped field	0.561	0.553	0.548	0.565
15 MV Photon				
Wedged field (fig. 3a)	0.399	0.383	0.391	0.399
Inverted wedged field (fig. 3d)	0.398	0.381	0.394	0.398
Well-shaped field (fig. 3b)	0.111	0.092	0.116	0.115
Inverted well-shaped field (fig. 3e)	0.689	0.670	0.665	0.672
Well-shaped field (fig. 3c)	0.072	0.056	0.083	0.059
Inverted well-shaped field (fig. 3f)	0.725	0.709	0.712	0.731

Is A Point Dose Enough For Validating An IMRT Treatment Plan?

Necessity Of Multiple Points Validation For IMRT

Let us start by discussing the independent dosimetric verification procedure in conventional 3-D conformal radiation therapy (3DCRT). In 3DCRT, the verification is mainly concerned with the MU calculation for each incident field. An independent calculation of the dose or MU at a point based on primitive machine data is recommended by AAPM Task Group 40 (Kutcher et al. 1994). Because the fluence of a uniform/wedged field is spatially correlated, information of the dose at a spatial point can in principle be used to estimate the dose in other spatial points provided that the off-axis information is known. This is, however, not the case for an intensity-modulated field since the weights of the beamlets across the field are independent. The correctness of the dose at a spatial point only warrants, at most, the correctness of the beamlets passing through or nearby that point. Because of the independence of the beamlets, the doses at multiple points must be verified to ensure the correctness of the whole field. An independent fluence map check is also highly recommended to ensure the integrity of the field. This is addressed in the following.

Independent Fluence Map Calculation And Its Utility For IMRT Plan Validation

The fluence map check can yield valuable information about the spatial correlation of the beamlets and thus complements the point dose check. In the past, the verification of a fluence map has been done using radiographic film, an electronic portal imaging device (EPID) (Pasma et al. 1999; Curtin-Savard and Podgorsak 1999; Partridge et al. 1998) or a beam imaging system (BIS) (Ma, Geis, and Boyer 1997) by actually delivering the leaf sequence file. While the measurement provides a reliable test on whether the leaf sequence file is deliverable and whether the execution of the file reproduces the intended fluence map, it is a labor-intensive and time-consuming process. Furthermore, the electronic devices are suitable only for a step-and-shoot delivery. They may have difficulty in verifying dynamic delivery because of finite dead-time of the electronics. Xing and Li (2000) have pointed out that it is more practical to use a computer simulation for the independent verification of the leaf sequences or fluence map. It is proposed to separate the IMRT treatment plan verification and the QA of the dynamic MLC. In the independent fluence map calculation, the program reads in the leaf sequence file generated by the planning system and recalculates the fluence map. The calculation is then compared quantitatively with the intended fluence map from the treatment planning system. The goal of the simulation is to warrant that, assuming that a rigorous independent QA of the MLC system has been performed so that the dynamic MLC can accurately execute the instruction of a leaf sequence file, the execution of

the leaf sequence will generate the desired fluence map should it pass the simulation test. This eliminates the experimental verification for each treatment field and each patient and significantly simplifies the QA procedure. The philosophy here is similar to that of using an independent dose calculation to replace the ion chamber or film measurements.

We consider the QA of dynamic MLC delivery a separate important issue. In practice, the point doses and fluence maps should be verified for every patient treatment. The frequency and the extent of the MLC QA are, on the other hand, independent issues and should be determined by the need to maintain the normal operation of dynamic delivery. This does not require an actual delivery check for every IMRT patient treatment field, similar to that we do not usually check dynamic jaw movement for every treatment involved with a dynamic wedge in conventional radiation therapy.

The fluence map calculation for both step-and-shoot and dynamic deliveries has been discussed by Xing and Li (2000). Computationally, the fluence map of a field can simply be obtained by normalizing the DMF distribution with respect to its maximum value. To quantitatively compare the independently computed fluence map and the intended fluence map from the treatment planning system, we have introduced two indices. The first one is the maximum difference between the two maps. The pixel value difference is reported. In addition, a global quantity that has proved useful in IMRT is the correlation coefficient defined as (Ma, Geis, and Boyer 1997; Xing and Li 2000)

$$r = \frac{\sum_n (F_n - \bar{F})(R_n - \bar{R})}{\sqrt{\sum_n (F_n - \bar{F})^2} \sqrt{\sum_n (R_n - \bar{R})^2}}, \quad (10)$$

where F_n and R_n are the pixel values of the computed and the reference images, respectively, \bar{F} is the average of F_n and \bar{R} is the average of R_n . The correlation coefficient measures the strength of the association between the two images and tests the linear predictability of the calculation from its reference image, and vice versa. The correlation coefficient is not very sensitive to the variation of the individual pixel value, but may provide valuable information on the global behavior of the fluence map.

Depending on the MLC manufacturer, different MLCs may have different specifications and constraints. These physical restrictions also need to be checked by the software to ensure that the leaf sequences not only reproduce the intended fluence map in a computer simulation, but also meet the machine constraints. A warning should be issued if these limitations are exceeded in an MLC file. This will prevent scheduling an undeliverable treatment from taking place since the MLC application cannot load a faulty file.

Conclusions

In this chapter we have discussed the rationale and methods for independent point dose and fluence map check. From the IMRT dosimetry point of view, we believe that it is necessary to perform these two tests to validate an IMRT treatment plan. The validation of fluence map is unique to IMRT and ensures the integrity of the IMRT field (or the correctness of the relative planar distribution of the beamlets). Furthermore, we have argued that both types of tests can be more efficiently done using a computer and summarized our previous work on how to carry out these calculations. We emphasize that the proposed computer verification of the MU and fluence map is not intended to replace the QA of the MLC delivery system. A rigorous QA procedure for MLC must be established independent of the proposed software development to achieve the desired fluence/dose distribution through the actual delivery. The QA items for a dynamic MLC delivery system should include various mechanical and dosimetric properties as well as the proprietary software that controls the movement of the MLC leaves during radiation delivery.

Acknowledgments

This work was partly supported by a Research Scholar Award from the American Cancer Society (RSG-01-022-01-CCE) and Department of Defense (DAMD17-01-0635). Table 1 and figures 1 and 2 are from a submitted manuscript to the *International Journal of Radiation Oncology, Biology, Physics*. We would like to thank Elsevier Science for permission to use the figures and the table.

References

- Arnfield, M. R., J. V. Siebers, J. O. Kim, Q. Wu, P. J. Keall, and R. Mohan. (2000). "A method for determining multileaf collimator transmission and scatter for dynamic intensity modulated radiotherapy." *Med. Phys.* 27:2231–2241.
- Bourland, J. D., and E. L. Chaney. (1992). "A finite-size pencil beam model for photon dose calculations in three dimensions." *Med. Phys.* 19:1401–1412.
- Boyer, A., and E. Mok. (1985). "A photon dose distribution model employing convolution calculations." *Med. Phys.* 12:169–177.
- Boyer, A. L., Y. P. Zhu, L. Wang, and P. Francois. (1989). "Fast Fourier transform convolution calculations of x-ray isodose distributions in homogeneous media." *Med. Phys.* 16:248–253.
- Chen, Z., L. Xing, and R. Nath. (2002). "Independent monitor unit calculation for IMRT using MIMiC multileaf collimator." *Med. Phys.* 29:2041–2051.
- Cheng, C. W., and I. J. Das. (2002). "Comparison of beam characteristics in intensity modulated radiation therapy (IMRT) and those under normal treatment condition." *Med. Phys.* 29:226–230.
- Curtin-Savard, A.J., and E. B. Podgorsak. (1999). "Verification of segmented beam delivery using a commercial electronic portal imaging device." *Med. Phys.* 26:737–742.
- Gibbons, J. P., and F. M. Khan. (1995). "Calculation of dose in asymmetric photon fields." *Med. Phys.* 1995; 22:1451–1457.

- Hou, Q., J. Wang, Y. Chen, and J. Galvin. (2003). "An optimization algorithm for intensity modulated radiotherapy—The simulated dynamics with dose–volume constraints." *Med. Phys.* 30: 61–68.
- IMRTWG (Intensity Modulated Radiation Therapy Collaborative Working Group). "Intensity-modulated radiotherapy: Current status and issues of interest." *Int. J. Radiat. Oncol. Biol. Phys.* 51:880–914.
- Jeraj, R., and P. Keall. (1999). "Monte Carlo-based inverse treatment planning." *Phys. Med. Biol.* 44:1885–1896.
- Kung, J., and G. Chen. (2000). "A monitor unit verification calculation in intensity modulated radiotherapy as a dosimetric quality assurance." *Med. Phys.* 27:2226–2230.
- Kutcher, G. J., L. Coia, M. Gillin, W. F. Hanson, S. Leibel, R. J. Morton, J. R. Palta, J. A. Purdy, L. E. Reinstein, G. K. Svensson, M. Weller, and L. Wingfield. (1994). "Comprehensive QA for radiation oncology: Report of AAPM Radiation Therapy Committee Task Group 40." *Med. Phys.* 21:581–618.
- Lian, J., C. Cotrutz, and L. Xing. (2002). "Therapeutic treatment plan optimization with probabilistic dose prescription." *Med. Phys.* 27: In press.
- Ling, C. C., C. Burman, C. S. Chui, G. J. Kutcher, S. A. Leibel, T. LoSasso, R. Mohan, T. Bortfeld, L. Reinstein, S. Spirou, X. H. Wang, Q. Wu, M. Zelefsky, and Z. Fuks. (1996). "Conformal radiation treatment of prostate cancer using inversely-planned intensity-modulated photon beams produced with dynamic multileaf collimation." *Int. J. Radiat. Oncol. Biol. Phys.* 35:721–730.
- Ma, L., P. B. Geis, and A. L. Boyer. (2000). "Quality assurance for dynamic multileaf collimator modulated fields using a fast beam imaging system." *Med. Phys.* 24:1213–1220.
- Ma, C.-M., T. Pawlicki, S. B. Jiang, J. S. Li, J. Deng, E. Mok, A. Kapur, L. Xing, L. Ma, and A. L. Boyer. (2000). "Monte Carlo verification of IMRT dose distributions from a commercial treatment planning optimization system." *Phys. Med. Biol.* 45:2483–2495.
- Mackie, T. R., J. W. Scrimger, and J. J. Battista. (1985). "A convolution method of calculating dose for 15-MV x rays." *Med. Phys.* 12:188–196.
- Mackie, T. R., A. F. Bielajew, D. W. Rogers, and J. J. Battista. (1988). "Generation of photon energy deposition kernels using the EGS Monte Carlo code." *Phys. Med. Biol.* 33:1–20.
- Partridge, M., P. M. Evans, A. Mosleh-Shirazi, and D. Convery. (1998). "Independent verification using portal imaging of intensity-modulated beam delivery by the dynamic MLC technique." *Med. Phys.* 25:1872–1879.
- Pasma, K. L., M. L. Dirkx, M. Kroonwijk, A. G. Visser, and B. J. Heijmen. (1999). "Dosimetric verification of intensity modulated beams produced with dynamic multileaf collimation using an electronic portal imaging device." *Med. Phys.* 26:2373–2378.
- Pugachev, A., and L. Xing. (2002). "Incorporating prior knowledge into beam orientation optimization." *Int. J. Radiat. Oncol. Biol. Phys.* 54:1565–1574.
- Shepard, D. D., M. A. Earl, X. A. Li, S. Naqvi, and C. X. Yu. (1995). "Direct aperture optimization: A turnkey solution for step-and-shoot IMRT." *Med. Phys.* 29:1007–1018.
- Solberg, T. D., J. J. DeMarco, F. E. Holly, J. B. Smathers, and A. A. DeSalles. (1998). "Monte Carlo treatment planning for stereotactic radiosurgery." *Radiother. Oncol.* 49:73–84.
- Tsai, J. S., D. E. Wazer, M. N. Ling, J. K. Wu, M. Fagundes, T. DiPetrillo, B. Kramer, M. Koistinen, and M. J. Engler. (1998). "Dosimetric verification of the dynamic intensity-modulated radiation therapy of 92 patients." *Int. J. Radiat. Oncol. Biol. Phys.* 40:1213–1230.
- Wang, X., S. Spirou, T. LoSasso, J. Stein, C. Chui, and R. Mohan. (1996). "Dosimetric verification of intensity-modulated fields." *Med. Phys.* 23(3):317–327.

- Watanabe, Y. (2001). "Point dose calculations using an analytical pencil beam kernel for IMRT plan checking." *Phys. Med. Biol.* 46:1031–1038.
- Webb, S. *Intensity-Modulated Radiation Therapy*. Bristol, UK: Institute of Physics Publishing (IOP), 2001.
- Wu, Q., R. Mohan, A. Niemierko, and R. Schmidt-Ullrich. (2002). "Optimization of intensity-modulated radiotherapy plans based on the equivalent uniform dose." *Int. J. Radiat. Oncol. Biol. Phys.* 52:224–235.
- Xia, P., K. K. Fu, G. W. Wong, C. Akazawa, and L. J. Verhey. (2000). "Comparison of treatment plans involving intensity-modulated radiotherapy for nasopharyngeal carcinoma." *Int. J. Radiat. Oncol. Biol. Phys.* 48:329–337.
- Xing, L., and J. G. Li. (2000). "Computer verification of fluence maps in intensity modulated radiation therapy." *Med. Phys.* 27:2084–2092.
- Xing, L., J. G. Li, A. Pugachev, Q. T. Le, and A. L. Boyer. (1999). "Estimation theory and model parameter selection for therapeutic treatment plan optimization." *Med. Phys.* 26: 2348–2358.
- Xing, L., Y. Chen, G. Luxton, J. G. Li, and A. L. Boyer. (2000a). "Monitor unit calculation for an intensity modulated photon field by a simple scatter-summation algorithm." *Phys. Med. Biol.* 45:N1–7.
- Xing, L., Z. Lin, S. S. Donaldson, Q. T. Le, D. Tate, D. R. Goffinet, S. Wolden, L. Ma, and A. L. Boyer. (2000b). "Dosimetric effects of patient displacement and collimator and gantry angle misalignment on intensity modulated radiation therapy." *Radiother. Oncol.* 56(1):97–108.
- Yang, Y., L. Xing, A. Boyer, Y. Song, and Y. Hu. (2002). "A three-source model for the calculation of head scatter factors." *Med. Phys.* 29:2024–2033.
- Yang, Y., J. L. Li, J. Palta et al. (2003). "Independent dosimetric calculation with inclusion of head scatter and MLC transmission for IMRT." *Int. J. Radiat. Oncol. Biol. Phys.* Submitted.